Investigating the Performance of Geothermal Energy Piles using Coupled Thermo-Hydro-Mechanical Finite Element Analyses

by

Alitking Anongphouth

A Thesis submitted to the Faculty of Graduate Studies of

The University of Manitoba

in Partial Fulfilment of the Requirements for the Degree of

MASTER OF SCIENCE

Department of Civil Engineering

University of Manitoba

Winnipeg, Manitoba

Abstract

Harvesting shallow geothermal energy by means of energy piles coupled with ground source heat pump systems for heating and cooling buildings has increased in recent years. However, the structural integrity of such systems subjected to thermo-mechanical loads or heating-cooling cycles should be studied. Therefore, a comprehensive understanding of their structural and geotechnical performances is vital for successful applications. This thesis aims to investigate the responses of concrete energy piles subjected to thermal and thermo-mechanical loads using fully coupled thermo-hydro-mechanical (THM) finite element analyses. The axisymmetric models were carried out for two case studies of full-scale energy pile tests. Two hypothetical energy piles in Winnipeg were also analyzed to study their performances by considering local geological and climatic conditions. In general, it was found that the THM numerical models could capture considerably well the behavior of energy piles during cooling and heating cycles in comparison with the field data published in the literature. The thermo-mechanical loads did have significant effects on pile responses. From sensitivity analyses, it was found that there were considerable effects of the thermal expansion of concrete and soil stiffness on the thermo-mechanical pile responses. The pile head restrained conditions also affected the behavior of energy piles with stronger effects in the upper part of the pile near the pile head. From the simulations of the energy piles in Winnipeg, settlements of the pile head kept on increasing with increasing numbers of thermal cycles (ratcheting settlement phenomena). It was also found that the ultimate geotechnical pile capacities generally increased when the pile was heated but reduced when cooled.

Keywords: Geothermal energy pile behavior, thermo-mechanical load, heating-cooling cycles, geothermal energy pile-soil interaction, coupled THM finite element analysis.

Acknowledgments

Throughout my time as a graduate student at the University of Manitoba, many people have provided me with valuable guidance and assistance professionally and personally. First and foremost, I would like to sincerely thank both of my advisors, Dr. Pooneh Maghoul, P.Eng (advisor) and Dr. Marolo Alfaro, P.Eng (co-advisor), for their time, patience, guidance, and support academically and financially during my study. I also would like to extend my gratitude to my thesis advisory committee members: Dr. James Graham, P.Eng (Professor Emeritus) and Dr. Madjid Birouk, P.Eng, for their time and constructive comments during the research meetings. I am also grateful to Dr. Hartmut Hollaender, P.Eng, for friendly discussions and of course good coffee.

I would like to thank all my fellow graduate students of the Geotechnical Research Group for the fruitful discussions about the research and for making a cheerful, positive, and professional workplace and learning experience.

There are more than words to describe my gratitude and love for my wife, Irene Olivia Ubay-Anongphouth, for her endless encouragement and emotional support; thanks for always being on my side. I am forever thankful to the most important persons in my life, my parents, who have always been giving me unconditional love and support and to all my family members in Laos and the Philippines.

Financial assistance for purchasing the PLAXIS 2D license from the Alcantara-Ubay & Co., Inc. is also highly appreciated.

To my beloved late grandfather,

you will always be missed.

Table of Contents

List of Tables

List of Figures

Chapter 1: Introduction

1.1. Geothermal Energy Overview

Growing concerns about environmental degradation, air pollution, global warming, and the depletion of fossil fuel reserves have led to research and development of technologies that use alternative and renewable energy resources. One of these resources is geothermal energy, which is the energy stored beneath the earth's surface in the form of heat. It is considered renewable and environmentally friendly.

The geothermal energy is typically harvested using two main systems namely deep and shallow geothermal energy systems. Deep geothermal energy systems are mainly those involved in electricity productions which can go down to a few kilometers below the ground surface to reach a very high temperature (usually 150 °C or higher) within the hydrothermal aquifers, dry and hot rocks or magma (Al-Khoury, 2012).

On the other hand, shallow geothermal energy systems generally refer to the systems that use low-temperature geothermal energy found within a depth of less than 250 m below the ground surface (Al-Khoury, 2012). Ground source heat pump (GSHP) systems (see Section 2.4 for more information) are used in buildings for heating and cooling purposes. They can also be used for domestic water heating, heating greenhouses for agricultural productions and de-icing of highway and bridge surfaces in cold regions. One component of the GSHP systems is the ground heat exchanger which is buried in the ground. The ground heat exchangers can be traditional borehole heat exchangers (BHEs) or more recently the geothermal energy structures such as geothermal energy piles, as explained in more details in Section 1.2.

In general, the temperature of the shallow ground (within 50 m below the ground surface) in its natural state without any effects of human activities and other anomalies such as volcanic activities, depending on the regions, is usually ranging from 10 to 20°C (Al-Khoury, 2012). Similarly, Brandl (2006) reported the ground temperature values of 10 to 15°C and 20 to 25°C in Europe and the tropics, respectively. In Canada, as reported by Mitalas (1987), the mean annual ground temperature ranges from 4.6 to 12.3°C.

1.2. Geothermal Energy Piles

Structural elements that are installed in the ground or contact with the ground such as ground-contacted slabs, deep basement walls and diaphragm walls, tunnel linings, and deep foundations can be used as ground heat exchangers for the ground source heat pump (GSHP) system (Brandl, 2006). The structures used for this purpose are collectively called energy geostructures or geothermal structures. Amongst these energy geostructures, the geothermal energy piles are the most widely used. Many names have been used to refer to the geothermal energy piles in the literature. For instance, heat exchanger piles, thermal piles, thermo-active piles, or energy piles. This thesis, nonetheless, prefers to use the term "geothermal energy piles or simply energy piles".

The geothermal energy piles are; in fact, structural piles with heat exchange pipes (loops) attached inside the re-bar cages (reinforcements) before casting or pouring concrete. The loops can be a single U-loop or multiple U-loops or a spiral coil as shown in Figure 1.1 and Figure 1.2. The pipes are usually made of high-density polyethylene (HDPE) with diameters ranging from 19 to 32 mm and filled with the heat-carrying fluid. The energy pile is a special type of ground heat exchangers in which it does not only serve as a structural element to support the superstructure but

also as a ground heat exchanger for the GSHP system at the same time. Regarding the diameters, the energy piles are much larger (0.6 to 0.9 m or even greater) in comparison with 0.1 to 0.15 m for conventional borehole heat exchangers (BHEs). Thus, many heat exchange pipes can be installed inside the piles. As a result, it can potentially provide a greater heat exchange capacity (Amis & Loveridge, 2014). Since the piles already required for a structural reason, the cost of drilling as well as the area required for installing for separate systems for the sole purpose of heating and cooling such as the conventional BHEs are eliminated. This leads to cost savings in addition to other benefits of the GSHP system subsequently mentioned in Section 2.4.2.

Energy piles are generally made of concrete, which can be driven piles or bored cast-in-place piles (also known as drilled shafts). Concrete is known to have a good thermal conductivity as well as a superb thermal storage capacity, which makes it a preferred medium as an energy absorber (Brandl, 2006). Besides, installations of the loops inside reinforced concrete piles could also protect them from possible damages due to ground chemical attacks and ground movements. Like structural piles, energy piles can be built in any lengths. However, since their primary purpose is to support the building loads, they should be designed to meet the structural requirements first. The design for their secondary purpose which is their energy performance would then follow. In practical applications, energy pile lengths can be in the range of 10 to 50 m (Brandl, 2006). This is deep enough to reach the relatively stable ground temperature that suitable for heating and cooling of buildings with GSHP systems.

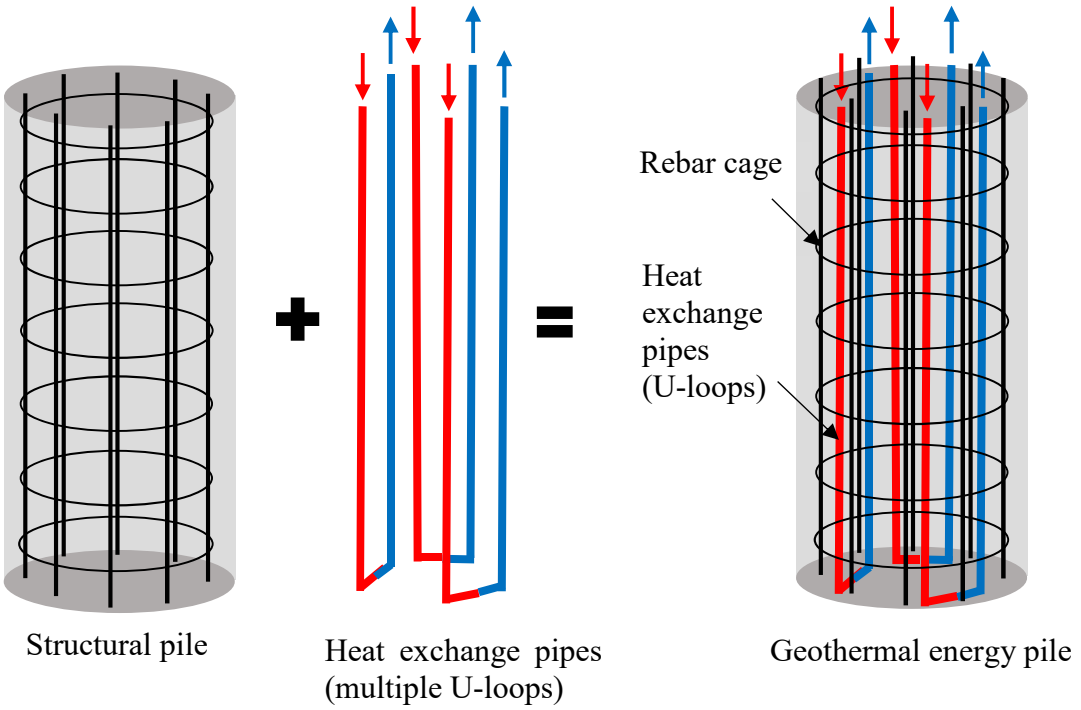

Figure 1.1. Geothermal energy pile configuration with multiple U-loop heat exchange pipes

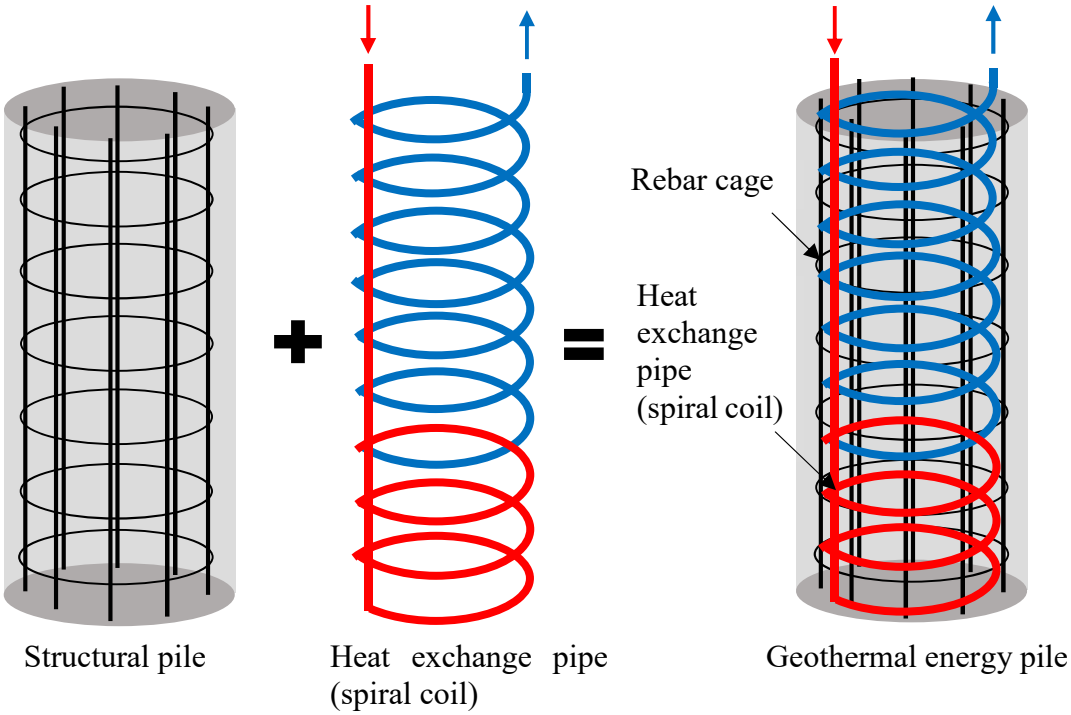

Figure 1.2. Geothermal energy pile configuration with a spiral coil heat exchange pipe

The first use of foundation piles as ground heat exchangers was in Austria. As reported by Brandl (2006), energy piles have been installed in Austria since 1984. Since then its use has spread over European countries, especially Switzerland (Laloui, Nuth, & Vulliet, 2006; Pahud & Hubbuch, 2007), Germany (Weber, Ganz, Schellschmidt, Burkhard, & Schulz, 2015), and the UK (Amis & Loveridge, 2014; Suckling & Cannon, 2004). In Austria, more than 5500 energy piles were installed in 2004 alone, and a total number installed from 1984 to 2004 was more than 22800 piles (Brandl, 2006). Similarly, in the UK, as of 2012, there were more than 5000 energy piles installed (Amis & Loveridge, 2014). Recently, other countries outside of Europe also started using energy piles. For example, the USA (Murphy & McCartney, 2015; Murphy, McCartney, & Henry, 2015), Japan (Hamada, Saitoh, Nakamura, Kubota, & Ochifuji, 2007), China (Gao, Zhang, Liu, Li, & Yang, 2008), and South Korea (Moon & Choi, 2015). Australia also has shown interest and conducted research on energy piles (Bouazza et al., 2011; Singh, Bouazza, & Wang, 2015; Wang et al., 2015).

In Canada, despite widespread and increasing implementations of GSHP systems with conventional ground loops, the use of energy piles is limited. To the best of the author's knowledge, the first building that used concrete energy piles is the 6-Story WestJet Calgary Campus located in Alberta. Here, the energy piles are bored cast-in-place concrete piles, about 20 m long and up to 1.0 m in diameter (Bererton, 2010). However, the number of energy piles used was not reported, and there were no tests performed on these piles.

1.3. Motivation and Research Objectives

In recent years, even though the use of energy piles has increased for their contributions to more renewable and sustainable energy uses, their acceptance and implementation are still slow in some

countries. This may be due to safety concerns of the building developers/owners regarding possible adverse effects of thermal loads (heating-cooling cycles) on the structural and geotechnical performance of the working piles, i.e., thermally loading the piles may lead to over-stressing of the concrete, loss of load-carrying capacities of the piles, and excessive or intolerable displacements (uplift movements and settlements). Even though energy piles have been used in the construction industry for more than three decades, there is still limited understanding of their behavior under a combined effect of thermal and mechanical loads, especially in cold regions like Canada. As it is known, pile-soil interactions under thermo-mechanical loads are very complex, and research into this area is still limited. At present, the design method considering both ultimate and serviceability limit states for energy piles are not yet available (Bourne-Webb, Burlon, Javed, Kürten, & Loveridge, 2016). In an effort to understand the energy pile behavior, some full-scale field tests were carried over the past decade. Two of the earlier energy pile tests: one at Swiss Federal Institute of Technology in Lausanne, Switzerland (Laloui et al., 2006) and the other at Lambeth College in London, the UK (Amis, Bourne-Webb, Davidson, Amatya, & Soga, 2008; Bourne-Webb et al., 2009) were reported. Numerical analyses using different methods (i.e., load-transfer method and finite element method) and different analysis tools were studied as well to try to replicate the observed behavior from the field tests. As the energy pile-soil interaction is a complex phenomenon that involves the thermo-hydro-mechanical behavior of soils, an advanced numerical model is needed for numerical simulations. Most of the numerical analyses carried out in the literature used the load-transfer method (Knellwolf, Peron, & Laloui, 2011; Ouyang, Soga, & Leung, 2011) that used springs to represent the stiffnesses of piles and the pile-soil interfaces. The load-transfer method does not take into account the real thermal interaction between the energy pile and the surrounding soils. However, this simplified method results in faster

computational time compared with the finite element method. Fully coupled thermo-hydro-mechanical (THM) finite element analyses reported in the literature are still limited. They, however, do not account for the effects of surface temperature variations and pile head restraining conditions. More research through full-scale field tests and numerical modeling using representative constitutive material models are needed to examine the behavior of energy piles built in the different ground and climatic conditions.

This thesis aims at improving understanding of the behavior of energy piles subjected to thermal and thermo-mechanical loads, especially in cold regions. The specific objectives of this research are as follows:

- To investigate the behavior of energy piles subjected to thermal and thermo-mechanical loads using coupled THM finite element models.
- To compare the numerical results with field measurement data from case studies available in the literature.
- To examine how strains and loads change in the energy piles as well as pile head uplifts and settlements.
- To examine how shaft friction and radial stresses mobilize along the pile-soil interfaces.
- To investigate the sensitivity of various model parameters on the numerical modeling results.
- To investigate the performance of energy piles under local climatic and geological conditions in Winnipeg and also examine the heating-cooling effects on their ultimate geotechnical capacities.

1.4. Research Methodology

Numerical modeling -was carried using geotechnical finite element computer software capable of simulating the fully coupled thermo-hydro-mechanical (THM) behavior of energy piles. A commercially available software program PLAXIS 2D-2018 was used as a numerical modeling platform. The first part of this study involves validating the numerical modeling setup. Numerical models were used to simulate the performance of two energy pile case studies reported in the literature. Numerical results were then compared with the observed data from the field measurements.

Numerical studies were subsequently undertaken to investigate the behavior of energy piles under geological and climatic conditions that representative in Winnipeg, Manitoba, Canada. To the best of the author's knowledge, no full-scale energy pile tests have been conducted in Winnipeg. Therefore, two hypothetical energy piles were examined. One is a friction energy pile and the other is an end-bearing energy pile.

Sensitivity analyses were then carried out to investigate important factors affecting the performance of both energy pile case studies and Winnipeg energy piles. Furthermore, the effects of temperature changes on the ultimate geotechnical capacities at the end of heating and at the end of cooling periods were investigated for the Winnipeg energy piles.

1.5. Limitations of the Thesis

It is known that research into energy piles has two distinctive aspects. First, the study of energy piles regarding their energy performance in which their heating and cooling capacities are evaluated. In other words, the amount of thermal energy that can be extracted from or injected into the piles. Second, the study of their thermo-mechanical behavior to make sure that the heating-

cooing cycles do not cause adverse effects on the structural and geotechnical performances of energy piles. In other words, to make sure that the energy piles are safe and sound during their operations. This thesis only focused on the thermal and thermo-mechanical behavior of energy piles. Only axisymmetric models were used for the analyses, excluding the full 3D models and also only concrete cast-in-place single piles were considered, not a group of piles. Furthermore, the ground freezing and thawing effects on the energy pile responses were not be taken into consideration. No field and laboratory tests were carried out. Therefore, all of the model parameters used in the numerical simulations were taken from relevant published documents.

1.6. Organization of the Thesis

This thesis consists of five (5) chapters. Chapter 1 provides the background on the geothermal energy, geothermal energy piles in civil engineering applications, motivation to carry out this research, research objectives, research methodology, and limitations of the thesis. The review of relevant information from literature is given in Chapter 2. Chapter 3 presents the procedures and numerical results of two selected case studies of energy piles. In Chapter 4, the THM finite element analyses were carried out for the hypothetical energy piles in Winnipeg, using local geological and climatic conditions. Finally, in Chapter 5, major findings from this research and recommendations for future studies were given.

Chapter 2: Background and Literature Review

2.1. Mechanisms of Heat Transfer

Physical bodies store heat or thermal energy, and they can also gain or lose heat from or to their surrounding media through a thermodynamic process called the heat transfer. The heat transfer consists of three main mechanisms, also known as modes, namely conduction, convection, and radiation. Note that, in the earth's shallow subsurface environment, the predominant form of the heat flow is the conduction (Farouki, 1981) which is through solid particles and pore fluids. There will also be the convection by means of groundwater flow (Banks, 2012). However, as Farouki (1981) mentioned, the natural convection through air and water movements in most soils is negligible in comparison to the conduction heat transfer mechanism. He also stated that heat transfer in soils due to the radiation is insignificant. Therefore, the following subsections will only describe the conduction and convection modes of heat transfer.

2.1.1. Conduction

Heat conduction describes how heat diffuses through a medium by the process of molecular interaction due to a temperature gradient (Al-Khoury, 2012). Heat transfer by conduction can occur in the soil constituents, i.e., the soil solids and the pore fluids. It should be noted that the heat or thermal energy only flows from an area with higher temperature to an area with lower temperature within a body or between two bodies that are in contact and the process would continue unless the thermal equilibrium is reached. Furthermore, the dry density and the degree of saturation of soils influence the amount of heat transferred by conduction: the higher the dry density and the degree of saturation, the larger the amount of heat transfer (Farouki, 1981).

The conductive heat transfer can be expressed using Fourier's law in a one-dimensional form as follows (Al-Khoury, 2012; Banks, 2012; Loveridge, 2012):

$$q_{cond} = Q/A = -\lambda_s (dT/dx) \quad \text{[Equation 2.1]}$$

where Q is the heat flow in (J s^{-1}), A is the cross-sectional area (m^2), Q/A= q_{cond} is the heat transfer rate per unit area normal to the direction of heat flow also known as heat flux (W/m^2), λ_s is the thermal conductivity (W m^{-1} K^{-1}), and dT/dx is the temperature gradient in the direction of the heat flow (K m^{-1}). The negative sign in the equation indicates that the heat always flows in the direction of decreasing temperature (high to low).

2.1.2. Convection

Heat transfer by means of bulk movements of liquid or gas is termed convection. There are two types of convective heat transfers: free convection and forced convection. Free convection of fluids occurs due to changes in the fluid density because of temperature changes at the contact zone. This, as a result, leads to the flow of the heat-carrying fluids. Forced convection is the convection due to the movements of heat-carrying fluids induced by an external force imposed by a mechanical device such as a heat pump. For instance, the flow of the heat-carrying fluids inside the closed loops in the GSHP systems (Banks, 2012; Loveridge, 2012). The convective heat transfer can be expressed using Newton's law of cooling as follows:

$$q_{conv} = Q/A = h\left(T_{body} - T_{fluid}\right) \quad \text{[Equation 2.2]}$$

Where q_{conv} is the heat transfer from the body to fluid in W/m^2 of the surface area, h is the heat transfer coefficient (W/m^2/K) which depends on many factors such as the nature of the fluid, its

rate of flow, and the surface properties of the body. T_{body} and T_{fluid} are the temperatures of the body and the fluid, respectively [K or °C].

2.2. Thermal Properties of Geomaterials and Concrete

2.2.1. Thermal Conductivity

A thermal conductivity (TC) is an intrinsic property of a material, which describes its ability to transfer heat by conduction. For example, copper is very good at conducting heat whereas soils and rocks are moderate, and plastics are usually poor (Al-Khoury, 2012; Banks, 2012). In this thesis, the TC is denoted by $\lambda_{s,}$ and it has a unit of J m^{-1} s^{-1} K^{-1} or W m^{-1} K^{-1}.

As the soil is a multi-phase porous material, which consists of solid particles, porewater, and poreair, its TC depends on the nature and proportions of its constituents. Amongst these three constituents, the solid particles are the most conductive followed by the water and then the air which is negligible. Note that the most conductive mineral of geomaterials is the quartz with a value of around 7.7 W m^{-1} K^{-1} (Table I.10 in Appendix I). Thus, soils and rocks that are rich in the quartz mineral will generally have the highest TC (Banks, 2012; GSHPA, 2012). The TC also depends on the degree of saturation and density. The higher the degree of saturation and the density, the higher the value of the TC. As reported by GSHPA (2012), the TC of soils and rocks ranges from 0.2 to 5.0 W m^{-1} K^{-1}. The typical values; however, tend to fall within a rather narrow range between 1.0 and 3.0 W m^{-1} K^{-1} (Banks, 2012).

Similar to soils and rocks, the thermal conductivity of concrete depends on its constituents, i.e., cement, aggregates, and additives as well as the density and moisture content. The TC of concrete ranges from about 1.0 to 3.0 W m^{-1} K^{-1} (Table I.8 in Appendix I). However, GSHPA (2012) suggested that, in the absence of specific information regarding the aggregate type and

proportions, the TC of the concrete should not be assumed to be greater than 1.5 W m^{-1} K^{-1}. Some typical values of the TC of soils, rocks, and some other materials reported in the literature are given in Table I.6, Table I.7, and Table I.9; respectively, in Appendix I.

2.2.2. Specific Heat Capacity

Materials (solid, liquid, and gas) can store heat. Their ability to store heat can be quantified in terms of their specific heat capacity (SHC), here denoted by C_s. The SHC is the amount of heat stored in the medium for every degree change in temperature, and it has a unit of J K^{-1} kg^{-1}. Most rocks have SHC values of about 800 J K^{-1} kg^{-1} (Banks, 2012). The term called volumetric heat capacity, C_{sv}, or the volume-specific heat capacity can be obtained by multiplying the specific heat capacity C_s by the density, ρ_s. Typical values of the SHC for some geomaterials, minerals, and other materials can be found in Table I.6 to Table I.10 in Appendix I.

It is to note that both the specific heat capacity and volumetric heat capacity are temperature dependent. This is partly due to changes in the mass density of the materials (Banks, 2012). However, for the GSHP system coupled with energy pile applications, the specific heat capacity and the mass density of the materials can be practically considered as constant (Al-Khoury, 2012).

2.2.3. Thermal Diffusivity

The thermal diffusivity describes the rate and extent to which the heat pulse propagates throughout a heat transfer medium (Banks, 2012). The thermal diffusivity, here denoted by α_{TD}, has a unit of m^2 s^{-1} and it is expressed as a ratio of the thermal conductivity to the volumetric heat capacity as follows:

$$\alpha_{TD} = \lambda_s / C_{SV} = \lambda_s / (\rho_s C_S) \qquad \text{[Equation 2.3]}$$

where λ_s is the thermal conductivity (W m^{-1} K^{-1}), ρ_s is the mass density (kg m^{-3}), C_s is the specific heat capacity (J K^{-1} kg^{-1}), and C_{SV} is the volumetric heat capacity (J K^{-1} m^{-3}). The equation above shows that there is a direct proportionality of the thermal diffusivity to the thermal conductivity. Therefore, materials with high thermal conductivity compared with their volumetric heat capacity will lead to high thermal diffusivity and the materials will quickly adjust their temperature to that of their surroundings.

2.2.4. Coefficient of Thermal Expansion

The linear coefficient of thermal expansion, α_L, which has a unit of K^{-1} or $^oC^{-1}$, is the fractional increase in the original length, L, in a bar of a material for one degree increase in temperature, T. The volumetric thermal expansion, α_V, is a fractional increase in volume due to one degree increase in temperature. For homogeneous materials, α_V is usually equal to 3 α_L. The coefficient of thermal expansion (CTE) values of some soils, rocks, and concrete reported in the literature are summarized in Table I.11 to Table I.13 in Appendix I.

2.3. Thermal Effects on the Properties of Geomaterials

Attention to the effect of temperature on the behavior of soils probably started in the 1960s for nuclear waste disposal technologies. Since then, many researchers have carried out experimental studies on the effect of temperature on the behavior of soils, especially on saturated clays. it is now generally agreed that the temperature effects on the behavior of soils has to be considered in the analyses and designs of the projects such as the nuclear waste disposal in which clays or backfill buffer is exposed to the decay heat (Graham, Tanaka, Crilly, & Alfaro, 2001; Hueckel & Baldi, 1990). In recent years, the use of thermo-active structures or energy geo-structures such as

geothermal energy piles also involves the thermal effects on the behavior of soils. However, the temperature range encountered in the energy pile is much lower than in the case of nuclear waste disposal applications, which is up to 100°C (Graham et al., 2001) and Gibb (1999) mentioned that the temperature in nuclear waste disposal should be below 150°C. On the other hand, the temperature of the operational energy piles is about -0.6 to 30°C (Brandl, 2006). Other researchers also reported that this temperature could range from 4 to 30°C (Knellwolf et al., 2011) or 0 to 50°C (Laloui & Di Donna, 2011).

The thermo-mechanical behavior of soils mainly depends on the type of soil and its stress history. For medium dense to dense non-cohesive (cohesionless) soils, heating and cooling caused by energy piles are not expected to have a considerable effect (GSHPA, 2012). Similarly, for rocks, a study by Wai & Lo (1982) indicated that the deformation and strength of limestone were temperature-independent up to 350°C. Therefore, for the applications of energy piles with a much lower temperature range, it may be assumed that the strength and stiffness of rocks are insensitive to temperature changes.

For clays, temperature changes induce complex behavior, which is until now still not fully understood. In general, heating the clays may change the soil properties such as pre-consolidation pressure, stiffness and strength (GSHPA, 2012) which are mainly dependent on the stress history and drainage conditions. In the energy pile applications, the thermal effects on the soils near the pile-soil interfaces are the most important because this may affect the pile behavior and its load-carrying capacity. Again, there is still limited knowledge regarding this aspect. However, in the short-term or undrained conditions, it is likely that the excess porewater pressure in the clays at and near the pile-soil interface will be generated due to heating, resulting in a decrease in shear strength. This is because of a relatively large thermal expansion of porewater in comparison with

the thermal expansion of the soil skeleton (Campanella & Mitchell, 1968; GSHPA, 2012). The thermally induced excess porewater pressure will likely dissipate with time and lead to the consolidation settlement. As a result, the shear strength of the soil may increase. In drained conditions, when a normally consolidated clay sample is heated, a volume reduction will occur and the strength and stiffness of the clay increase. Over-consolidated clays, on the other hand, shows a volume increase and the shear strength is not significantly affected.

Furthermore, the studies of the temperature on the critical state friction angle of different clays showed different results. For example, kaolin clays showed a slight dependency of the friction angle (Cekerevac & Laloui, 2004) whereas that of the illite and smectite clays seem to be temperature independent (Graham et al., 2001). In general; therefore, the effect of temperature on the friction angle is considered to be negligible and could be ignored in the framework of energy piles (Di Donna, 2014).

2.4. Ground Source Heat Pump System

A ground source heat pump (GSHP) system is the system for the heat exchange between buildings and the ground, including ground-contact bodies such as groundwater, lakes, ponds, and rivers. The system is also known as an earth energy system or ground energy system and geo-exchange system (GXS) in Canada (CGC, 2009). The system is used to exchange heat or geothermal energy stored in the ground beneath and adjacent to buildings to heat and cool building spaces in winter and summer, respectively. The GSHP system takes advantage of the fact that the undisturbed ground temperature at about 10 to 15 m beneath the ground surface is not affected by daily and seasonal changes of ambient air temperature (Brandl, 2006). In other words, the ground temperature at these depths stays relatively constant throughout the year, which is usually at about

a few degrees above the long-term mean annual air temperature (Banks, 2012; CGC, 2009). At these depths, the ground temperature is cooler than the air temperature in summer and warmer in winter. Therefore, the ground provides a convenient heating source in winter and cooling source in summer. Because of these conditions, the GSHP system is much better than the air-source heat pump system in terms of heat exchange efficiency. For example, in Manitoba, Canada, the extreme outdoor air temperatures limit the effectiveness of the air-source heat pump units for heating in the coldest months. On the other hand, the GSHP system can extract the heat from the ground that provides a stable source of heat in the winter time (Manitoba Hydro, 2018).

2.4.1. Basic Components of the GSHP System

The GSHP system typically consists of three main components (Manitoba Hydro, 2018): a ground heat exchanger (loop), a heat pump unit, and a distribution system inside the building as explained below.

2.4.1.1. *Ground Heat Exchanger*

The first component is a ground heat exchanger or a ground loop, some publications (Brandl, 2006; Loveridge, 2012) referred this as a primary circuit, which is used to extract/inject the heat from/into the ground. There are mainly two types of loops: open loops and closed loops. In an open loop system, an aquifer is needed to supply the groundwater, and this groundwater is pumped up from one well and then forced to flow through the heat pump. After the heat is extracted, then the groundwater is pumped back into another well (a return well) installed at some distance away.

In the closed loop system, the loop usually made of high-density polyethylene (HDPE) pipes with diameters ranging from 19 to 32 mm (CGC, 2009) are buried in the ground beneath or adjacent to the buildings. The pipes are filled with heat-carrying fluid that circulates through a heat

pump that extracts heat from it. Because this system circulates the same heat-carrying fluid through the loop repeatedly and the fluid is not open to the environment, it is named the closed loop system. The closed-loop system can have many configurations such as a horizontal closed loop, lake or pond closed loop and vertical closed loop configurations. CGC (2009) provides good explanations and details of these different configurations.

For vertical closed loop configuration, U-shaped loops are installed in vertically drilled holes in the ground and then grouted with neat cement paste. This conventional configuration is also known as a borehole heat exchanger (BHE) which has a borehole depth ranging from 15 to 150 m with 0.10 to 0.15 m in diameter (CGC, 2009). For example, at Manitoba Hydro Place (a commercial hi-rise building in downtown Winnipeg, Manitoba), 280 BHEs with a diameter of 0.15 m (6 inches) and about 120 m (400 feet) deep were installed in an interspersed manner among foundation piles (Kuwabara, Auer, Gouldsborough, Akerstream, & Klym, 2009). Data collected from 2008 to 2010 showed that the vertical closed loop configuration or the BHE is the most widely used configuration in Manitoba Province, Canada (CGC, 2009). This may be due to the presence of soft clay deposits (Glacial Lake Agassiz Clay), more than 15 m thick, in the southern part of this province. The main advantages of the vertical closed loop compared with the horizontal one are that a land area needed for installation of the loop is much smaller; and therefore, it is an inevitable choice for buildings in urban areas where the land is scarce. Furthermore, because the vertical closed loop is buried in the ground at a greater depth that is less influenced by the ambient air temperature variation, it could be more efficient in terms of energy performance.

Although the GSHP systems with conventional ground loops as ground heat exchangers are now quite well established and widely used in Europe, North America, and East Asia, the initial cost of investment of the systems is still higher than other systems; for example, the air-source

heat pump systems for heating and cooling. The high initial cost of the GSHP systems is mainly due to the borehole drilling and installing of the ground loops. To reduce the cost and to eliminate spaces needed for the conventional BHEs, engineers have come up with an ingenious idea; they use structural piles already required for structural reasons for ground heat exchangers by installing the vertical closed-loops (U-loops or spiral coil) directly inside the piles. However, since the energy piles are also used for supporting the structures, many concerns regarding their structural integrity during operation under temperature variations have been raised. The review on their behavior under thermo-mechanical loads is given in Section 2.5.

2.4.1.2. ***Heat Pump Unit***

The second component is a heat pump which the GSHP system needs in order to be functional. Canadian GeoExchange Coalition (CGC, 2009) defines the heat pump as "*A device at the heart of a GXS designed to extract heat from a low-grade source (like the earth) by way of an open or closed loop and concentrate it for use to heat a space*". In other words, it modifies the unsuitable temperature drawn from the ground by circulating the heat-carrying fluid inside the heat exchange pipes (loops) to a level that is suitable for heating or cooling of building spaces. With a reversing valve, the heat pump can function for both heating and cooling modes of the GSHP system. Nonetheless, the heat pump does need a minimal amount of electricity to run.

2.4.1.3. ***Distribution System***

The third component is the distribution system. Some publications (Brandl, 2006; Loveridge, 2012) referred to this component of the GSHP system as a secondary circuit. This distribution system can be the forced air system, in which a fan in the heat pump furnace unit blows air over a fan coil, and the heated or cooled air is distributed inside the buildings through the network of

ducts. In a hydronic heating system; on the other hand, hot water is circulated through radiators or a network of the underfloor pipes.

2.4.2. Benefits of the GSHP System

There are many reasons why the GSHP systems provide attractive sources of heating and cooling for buildings compared with traditional heating and cooling systems (i.e., air source heat pump and fossil-based furnaces). First, the operation and maintenance costs of the GSHP systems are relatively low, leading to substantial long-term cost savings. A reduction in the annual heating costs for homes can range from 50% to 70 % and up to 20% decrease in domestic water heating costs (Manitoba Hydro, 2018). Second, GSHP systems have low environmental impacts in terms of CO_2 emissions. Unlike burning oil and coal, the GSHP systems themselves do not produce CO_2 emissions; however, they still need a minimal amount of electricity to run. This electricity may come from power plants; for example, a coal power plant that expels CO_2. The GSHP systems can be considered as a zero-CO_2 heat source if a renewable source of electricity (e.g., solar power) is used to power them. Hence, the GSHP systems is indeed an environmentally friendly technology because they help the world to reduce greenhouse gas emissions and other harmful effects to the environment. Other benefits may be the fact that GSHP systems are hidden in the ground, which can be particularly attractive in the areas where planning regulations restrict the visual impact of new developments (Banks, 2012) such as the objections to wind turbine installations in some areas. Moreover, it is also relatively quiet to run the GSHP systems.

2.5. Thermo-Mechanical Behavior of Geothermal Energy Piles

Even though the use of energy piles began in the early 1980s (Brandl, 2006), research into their thermo-mechanical behavior only started in recent years. Many pioneering works regarding this aspect of energy piles have been carried out in Europe through full-scale field tests as reported in the literature (Amatya, Soga, Bourne-Webb, Amis, & Laloui, 2012; Bourne-Webb et al., 2009; Brandl, 2006; Laloui et al., 2006). Based on the observed thermal and thermo-mechanical responses of these tests, a simplified conceptual framework has been established and published in a series of publications (Amatya et al., 2012; Bourne-Webb et al., 2009; Bourne-Webb, Amatya, & Soga, 2013). This descriptive framework mainly focuses on the axial stress and strain changes in the pile, and also how the side shear stresses developed at the pile-soil interface during heating and cooling of the pile. The framework was established under the assumptions that (a) the pile is a linear elastic material and has a constant cross-sectional area, (b) the soil surrounding the pile has a uniform strength (c) The neutral plane of thermal expansions and contractions of the pile is located at the mid-depth of the pile, and (d) changes in temperature is uniform over the whole body of the pile.

To understand the behavior of energy piles subjected to different mechanical and thermal load combinations, it is essential to understand at first the behavior of piles under a mechanical load and a thermal load separately. As in reality, the energy piles are generally loaded with the mechanical or structural loads from the buildings first before thermally loaded in terms of temperature changes induced by the heating-cooling operations. The following sections explain, based on a simplified framework mentioned earlier, how the energy pile responds under the mechanical, thermal, and thermo-mechanical loads.

2.5.1. Pile Response under Mechanical Loads only

A typical pile subjected to only a mechanical or structural load, which is the load transferred to the pile head from the overlying structure, is shown in Figure 2.1. In this case, the mechanical load causes the pile to move downwards (negative) and these downward displacements are resisted by the surrounding soils through the shaft friction acting upwards (positive) and the toe stress (resistance). The axial stress induced by the mechanical load varies along the pile length with the highest value at the pile head and reduces gradually as the stress in the pile is transferred into the surrounding soils through the shaft (skin) friction at the pile-soil interface, and the remaining stress then transferred at the pile toe. Depending on the amount of load transferred to the pile shaft and the pile toe, the pile is called a friction (or floating) pile if it mainly resists the load through its shaft resistance. Otherwise, if the pile mainly resists the load at the pile toe by toe-bearing (or end-bearing) resistance, then it called the toe-bearing (or end-bearing pile).

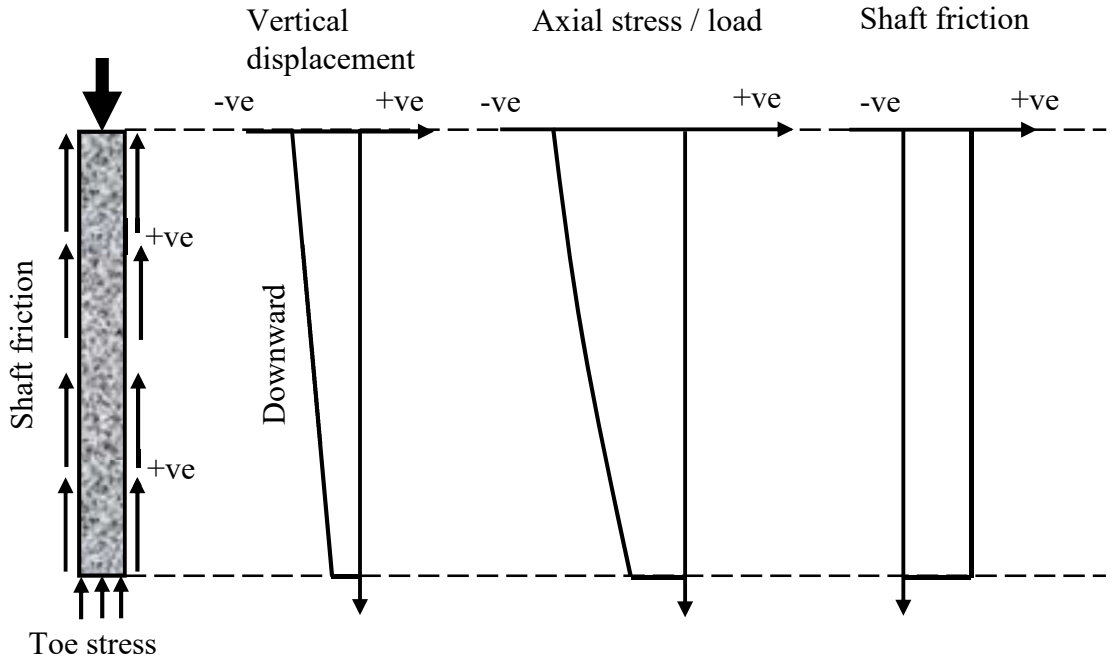

Figure 2.1. Simplified pile response subjected to the mechanical load only (drawn based on Amatya et al. (2012); Bourne-Webb et al. (2013))

2.5.2. Pile Response under Thermal Loads only

If both ends (head and toe) of the pile are not restrained, cooling (pile temperature decrease) the pile will lead to pile contraction. The upper part of the pile above a neutral plane (NP), assumed to be located at the mid-depth of the pile, moves downwards. The lower part below the NP; however, moves upwards. In reality, the NP may not always be at the mid-depth of the pile if the pile is installed in non-homogenous or layer soils. The location of the NP also varies with different head restrained conditions. The pile contraction induces tensile axial stress or load (positive) in the pile, and the side shear stress (shaft friction) is mobilized at the upper portion of the pile in the same upwards direction (positive) as that mobilized by the mechanical load (downwards direction is negative). In the lower half of the pile, the opposite occurs (Figure 2.2).

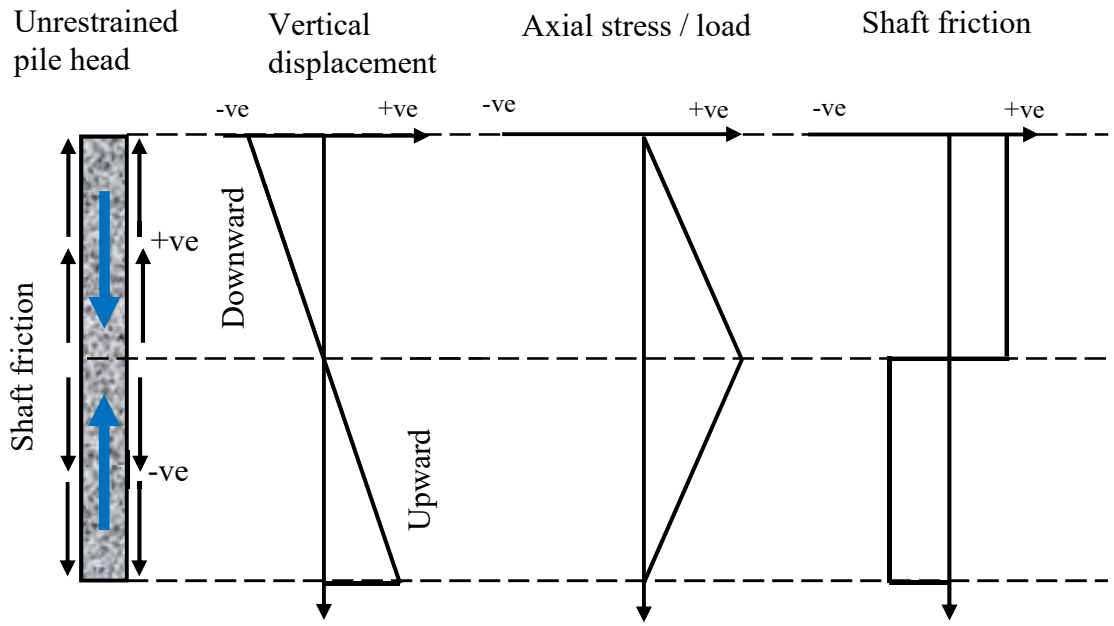

Figure 2.2. Simplified pile response subjected to the thermal load (cooling) only (drawn based on Amatya et al. (2012); Bourne-Webb et al. (2013))

As shown in Figure 2.3, in contrary to cooling, heating (pile temperature increase) causes the pile to expand or elongate in relation to the NP. The upper part of the pile above the NP moves

up while the lower part below the NP moves down. The expansive deformation will be resisted by shaft restraint along the pile-soil interface; therefore, the compressive stress (negative) will develop in the pile. The pile-soil interface shear stress generated at the upper part and the lower part of the pile will be in the opposite and the same direction as that mobilized by the mechanical load, respectively.

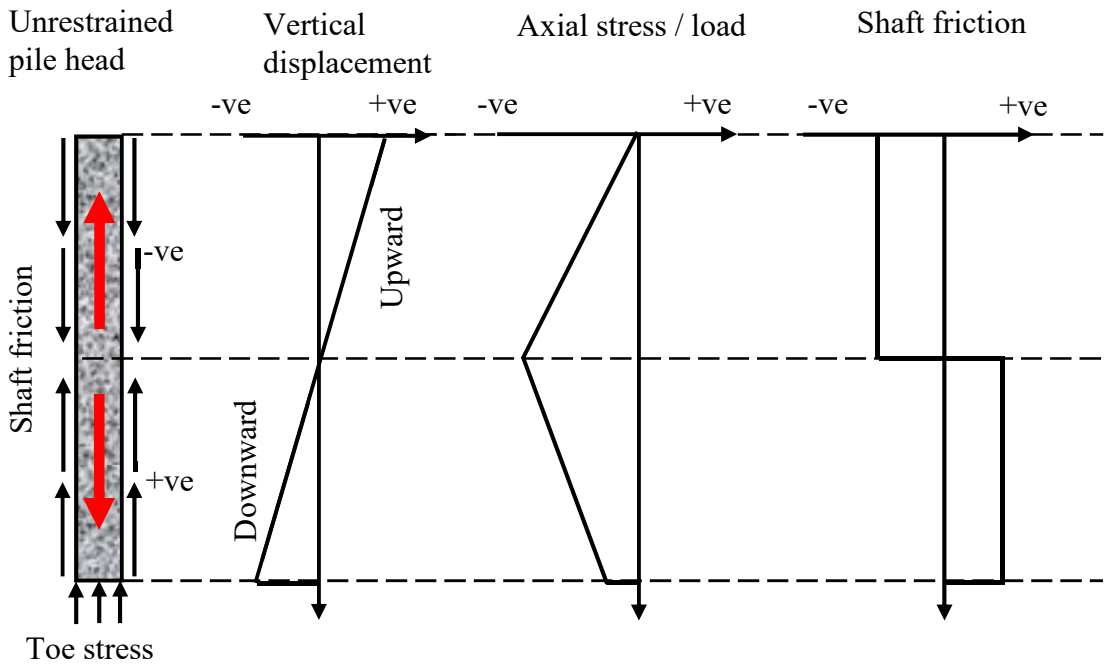

Figure 2.3. Simplified pile response subjected to the thermal load (heating) only (drawn based on Amatya et al. (2012); Bourne-Webb et al. (2013))

2.5.3. Pile Response under Thermo-Mechanical Loads

This section describes the pile response under a combination of mechanical and thermal loads (aka thermo-mechanical loads). Figure 2.4 shows the response of the energy pile subjected to both the mechanical load and the decrease in temperature (cooling). As mentioned previously, the thermal cooling induces axial tensile stress along the pile opposite to the mechanical load. This leads to

the pile to be less compressive for their combined effects. In some cases with a higher decrease in temperature and the lower mechanical load applied at the pile head, the axial tensile stress or load may develop at the lower part of the pile. Furthermore, due to contraction at the pile toe, there is a reduction in the toe stress. For the pile-soil interface shear stress or friction, the additional shear stress will be mobilized at the upper part of the pile whereas at the lower part of the pile there is a decrease and may be negative (negative skin friction) in some cases; for example, the case with a large decrease in temperature.

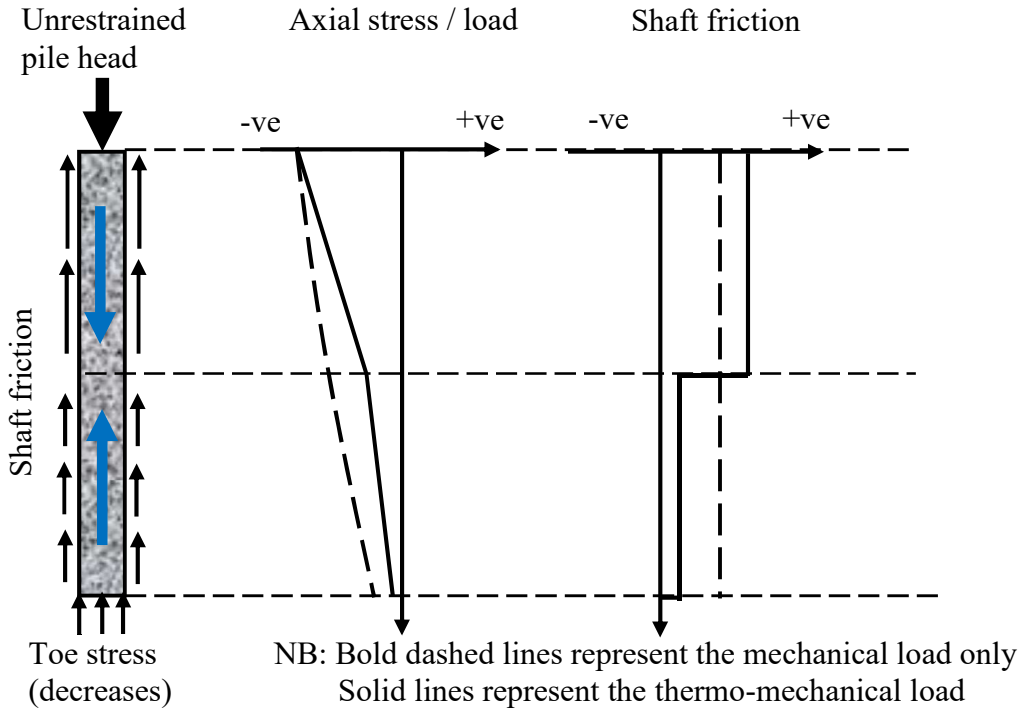

Figure 2.4. Simplified pile response subjected to both the mechanical load and cooling load (drawn based on Amatya et al. (2012); Bourne-Webb et al. (2013))

The pile response subjected to a combination of the mechanical load and the increase in temperature (heating) is shown in Figure 2.5. Again, as mentioned before, the thermal heating causes axial compressive stress or load along the pile the same way as the mechanical load. As a

result, there is an overall increase in the axial compressive stress along the pile. Moreover, due to the elongation at the pile toe, the stress at the pile toe increases. In contrary to the thermal cooling, the mobilized pile-soil shear stress is reduced in the upper part of the pile. This occurs because of the upward displacement of the pile. At the same time, at the lower part of the pile, the shaft friction is increased because of the downward movement of the pile. In the case of lower applied mechanical load, the higher negative shaft friction may be produced due to heating and therefore overcome the positive shaft friction induced by the mechanical load. This may result in the overall negative shaft friction in the upper portion of the pile under the thermo-mechanical load during heating.

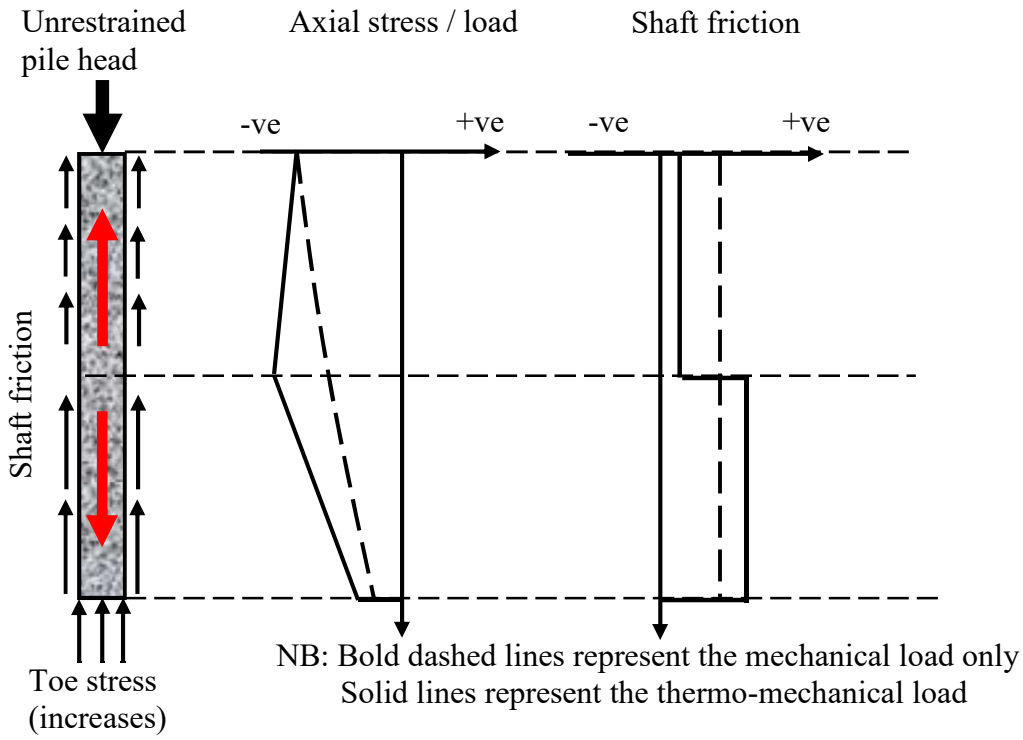

Figure 2.5. Simplified pile response subjected to both the mechanical load and heating load (drawn based on Amatya et al. (2012); Bourne-Webb et al. (2013))

2.5.4. Thermally Induced Displacement, Strain, Stress in the Pile

The magnitude of a vertical pile displacement at the pile head depends on the restrained conditions and relative displacements between the pile and its surrounding soils. As suggested by the Ground Source Heat Pump Association (GSHPA, 2012), a conservative estimation of the vertical pile movement can be made by assuming that there are no pile restraints along the pile shaft and pile ends (Figure 2.6). Therefore, the pile is free to move, which leads to full development or mobilization of the thermally induced axial strain that can be calculated using the following equation. Note that, in this case, because the thermal strain is fully mobilized, there is no thermally induced stress in the pile.

$$\Delta L = L_O \varepsilon_{T-Free} \quad \text{[Equation 2.4]}$$

$$\varepsilon_{T-Free} = \alpha_L \Delta T \quad \text{[Equation 2.5]}$$

where ΔL is the change in length (m), ΔT is the change in temperature (°C), L_O is the original length, and α_L is the coefficient of linear thermal expansion of the pile material or concrete (1/°C), and $\varepsilon_{T\text{-}Free}$ is the free axial thermal strain (-).

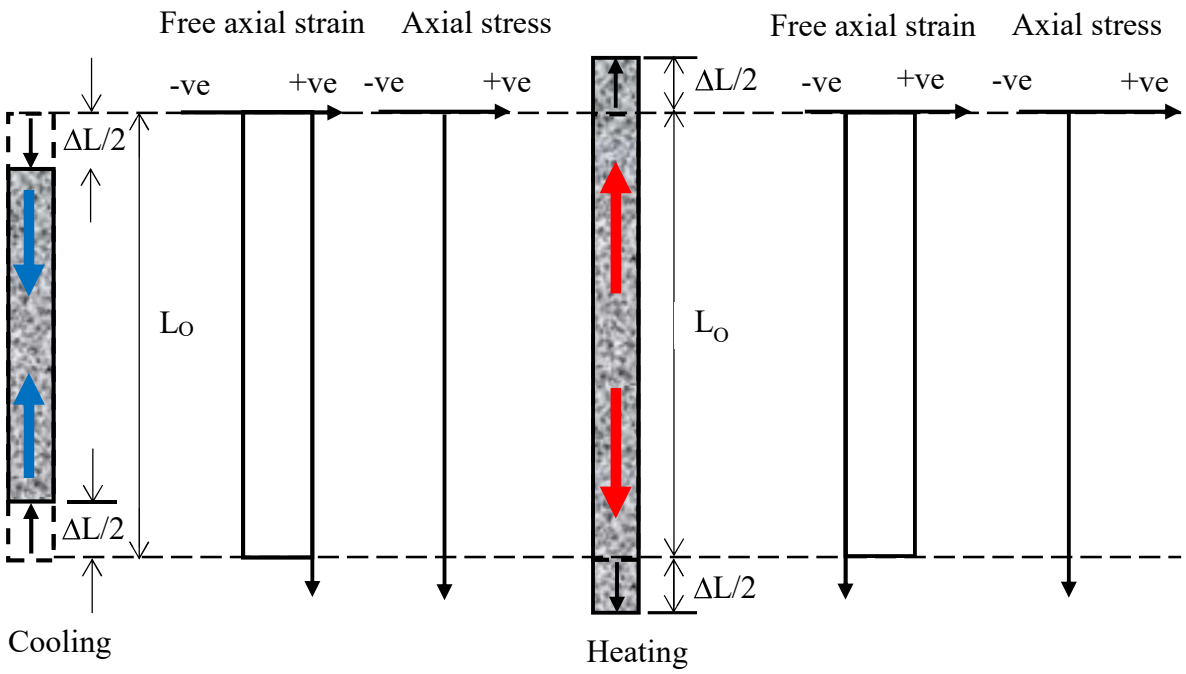

Figure 2.6. Thermal response of an unrestrained pile or free body (drawn based on Bourne-Webb et al. (2013); GSHPA (2012))

As suggested by the GSHPA (2012), an extreme case for the thermally induced stress in the pile can be made by assuming that the pile is fully restrained as shown in Figure 2.7. In other words, the movements of the pile at both ends are completely restricted. Therefore, the strain potential is converted to the axial thermal stress or load. The thermally induced stress or load can then be calculated using the following equation:

$$\sigma_T = \varepsilon_{T-Rstr} E \qquad \text{[Equation 2.6]}$$

$$P_T = \sigma_T A \qquad \text{[Equation 2.7]}$$

$$P_T = EA\ \varepsilon_{T-Rstr} \qquad \text{[Equation 2.8]}$$

where σ_T is the thermally induced stress (kPa), $\varepsilon_{T\text{-}Rstr}$.is the restrained axial strain (-) which is the axial strain potential that could not be mobilized due to restrictions and in the case fully restrained

pile the $\varepsilon_{T\text{-}Rstr}$ is equivalent to the $\varepsilon_{T\text{-}Free}$, E is the elastic or Young's modulus of pile material or concrete (kPa), and A is the cross-sectional area of the pile (m^2).

It is important to note that Figure 2.6 and Figure 2.7 only show the two most extreme restrained conditions of the pile: the free body and the fully restrained body, correspondingly. These conditions rarely occur in reality. Because in reality, the pile will be restrained to some degree (partially restrained) by the surrounding soils and the overlying structure. Therefore, a more realistic estimation of the thermally induced displacements, strains, and stresses in the pile could be done by the use of numerical methods of analyses and by carrying out full-scale field tests.

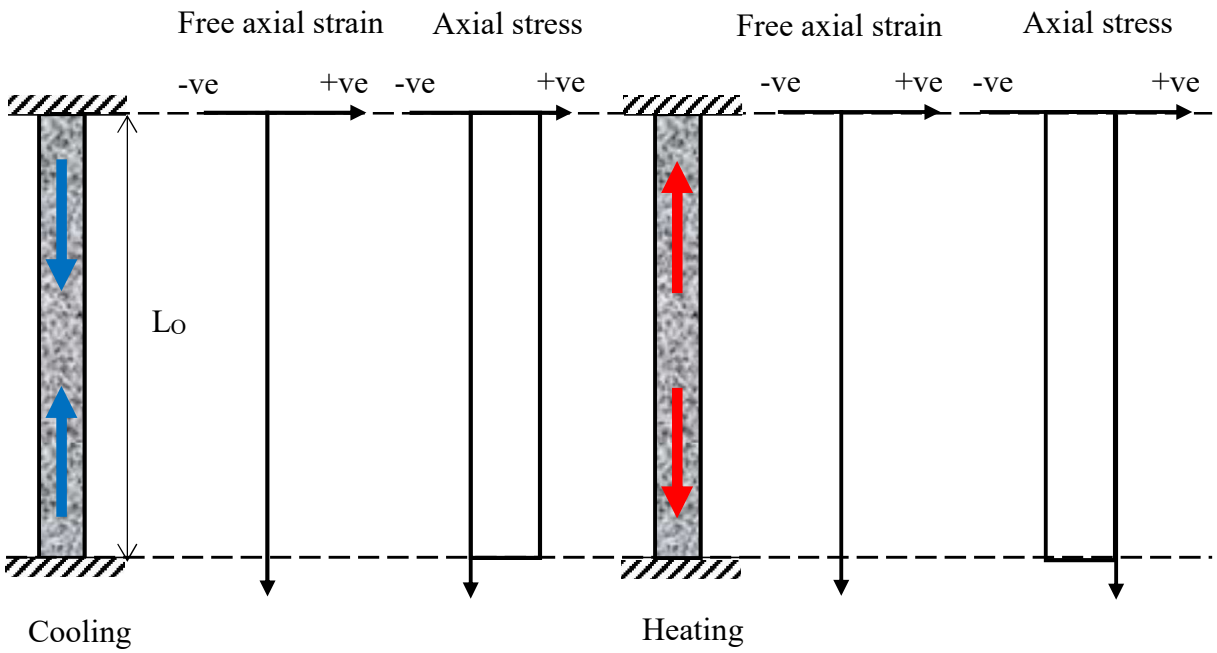

Figure 2.7. Thermal response of a fully restrained pile or restrained body (drawn based on Bourne-Webb et al. (2013); GSHPA (2012))

2.6. Full-Scale Field Tests of Geothermal Energy Piles

Experimental observations of thermo-mechanical responses of energy piles are, until now, still very limited. Most of the early full-scale field tests were carried out in Europe as summarized in (Amatya et al., 2012). These full-scale field tests are: (a) energy pile test at Bad Schallerbach, Austria, which is a part of an operational GSHP system of 143 piles used for a rehabilitation center (Amatya et al., 2012; Brandl, 2006). (b) energy pile test at the Swiss Federal Institute of Technology in Lausanne (EPFL), Switzerland, which is the only pile underneath a four-story building used to study the thermo-mechanical response (Laloui et al., 2006). (c) energy pile test at Lambeth College, London, the United Kingdom, which is not a part of the building, constructed for the sole purpose of thermo-mechanical testing (Amis et al., 2008; Bourne-Webb et al., 2009).

Recently, in other parts of the world outside Europe, full-scale field tests to observe the thermo-mechanical behavior of the concrete energy piles have also been performed. For example, the test at Monash University, Melbourne, Australia (Bouazza et al., 2011; Singh et al., 2015) Some tests have also been done in the USA such as the one carried out at the US Air Force Academy, Colorado (Murphy et al., 2015), which is a working pile supporting a one-story building. Also, three full-scale in-situ tests were performed in Houston, Texas, as reported in (Sutman, Brettmann, & Olgun, 2018), to study the response of energy piles with different end-restrained conditions.

It is noted that, even though the energy pile tests mentioned above provided important findings and insight knowledge of the behavior of the energy pile itself when subjected to thermo-mechanical loadings such as thermally induced stress and strain in the concrete pile, some data is still incomplete. For instance, how thermo-mechanical loading affects the load-carrying capacity

of the pile, changes in porewater pressure in the soils at the pile-soil interface and near the pile, soil deformation, and long-term behavior of the energy piles.

This thesis focuses on the thermo-mechanical behavior of bored cast-in-place concrete energy piles, especially their responses to the field conditions. Therefore, attention was paid to the two full-scale energy pile tests that were carried out at the Swiss Federal Institute of Technology and Lambeth College, and these were selected as the case studies for validating the THM finite element analyses carried out in this thesis. Information about these case studies is given in Sections 2.6.1 & 2.6.2 below. Note that the reasons for selecting these two tests are that they seem to be the most recognized field tests in the literature and good data from the field measurements are available. Furthermore, these two tests have been used for establishing the simplified conceptual framework for understanding energy pile behavior (Amatya et al., 2012; Bourne-Webb et al., 2009, 2013). Other researchers such as Knellwolf et al. (2011) also used these tests to validate their numerical modeling based on the load-transfer approach that assesses the main effects of temperature changes on pile behavior. Thermo-elastic finite element analyses reported in Laloui & Nuth (2009) and Laloui et al. (2006) used the experimental test results from the Swiss Federal Institute of Technology to compare with the results from their numerical simulations.

2.6.1. Energy Pile Test at Lambeth College, London, UK

This energy pile case study will be used for the numerical simulations as the case study 1 given in Section 3.2. Detailed information about this test site can be found in a series of publications (Amatya et al., 2012; Amis et al., 2008; Bourne-Webb et al., 2009). The energy pile test at Lambeth College was a trial test for the purpose of improving knowledge and understanding the thermo-mechanical loading on the pile in terms of stresses, strains, pile head movements and heat propagation from the energy pile. The piles constructed at the site include anchor piles, heat sink

pile, and the main test pile (pile used for thermo-mechanical response test). Note that at 0.5 m away from the main test pile, an instrumented borehole was also installed to allow for near-field temperature measurements. The test pile was designed as a friction pile and it mostly embedded in London clay except for the upper 4 m to 4.5 m of made ground and river terrace deposits (sand & gravel). The groundwater table was about 3 m below the ground surface. The main test pile has a nominal diameter of 0.6 m and 23 m long. The as-built diameter of the pile, however, varies from 0.61 m at the top 5 m and 0.55 m below this depth (Figure 2.8). This variation of pile diameter was due to the temporary casing used during the pile installation.

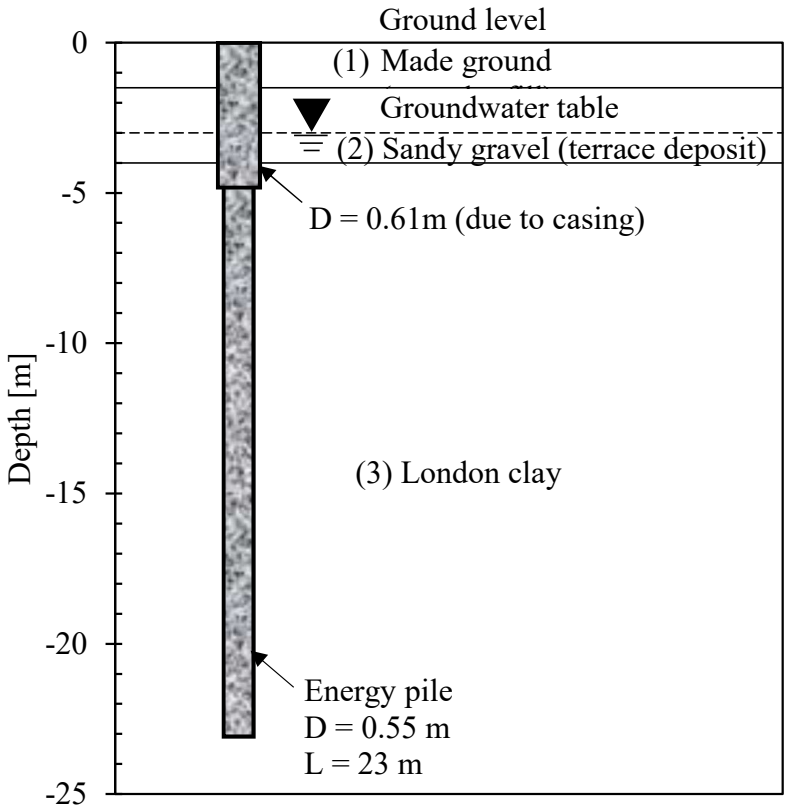

Figure 2.8. Geological profile and dimensions of the tested pile at the Lambeth College (drawn based on Bourne-Webb et al. (2009))

During the thermo-mechanical response test of the main test pile at Lambeth College, a mechanical load of -1200 kN applied at the pile head was maintained. The mechanical load was provided by a hydraulic jack which was in turn supported by a loading frame and anchor piles. During this testing period, the pile was cooled for about 31 days with an inflow-fluid temperature of -6 °C, and heated for 12 days with the inflow-fluid temperature of 40°C. The temperature of the heat-carrying fluid was controlled by the 8 kW heat pump. As noted by Bourne-Webb et al. (2009), the range of the inflow-fluid temperature was considered as an extreme case. Normally, during the operation of the GHSP system, the range of the inflow-fluid temperature is more likely to be within -1 to 30°C.

2.6.2. Energy Pile Test at the Swiss Federal Institute of Technology, Switzerland

This energy pile case study will be used for the numerical simulations as the case study 2 given in Section 3.3. Complete information about this test site can be found in the papers written by Laloui & Nuth (2009 and Laloui et al. (2006). The energy pile was a working pile (pile used to support the superstructure) located at the side of a 4-story building, which was at that time under construction. The nominal pile diameter was 0.88 m, and the length was 25.8 m. However, the as-built diameter of the pile varied from about 0.96 m to 1.20 m. The average diameter was about 1.0 m (Laloui et al., 2006). The tested pile was one of the 97 piles underneath the building with 100 m x 30 m in dimension, but only one pile was used as a ground heat exchanger while the rest were used solely as load-carrying piles. The geological profile at the site consists of five layers, and the groundwater table in this particular site was very close to the ground surface. The pile toe was embedded in the sandstone (molasse) about 0.5 m as shown in Figure 2.9. Heat-carrying fluid pipes (absorber pipes) were U-shaped polyethylene (PE) pipes which were attached to a rebar cage before lowering down into the drilled hole and pouring concrete.

The tested pile was then subjected to both thermal and mechanical loads. Because this pile was a working pile, the superstructure provided the mechanical (structural) load whereas the thermal load was provided by the heat pump. In Test 1, there was no superstructure yet. Therefore, the pile was subjected to thermal load only. In contrast, Test 7 was carried out when the construction of the building reached the top floor. Therefore, the pile was subjected to the maximum mechanical load at the pile head of -1300 kN as well as the thermal load. Note that the highest change in temperature in the pile at the end of heating was about 21°C and 18°C ($\Delta T \approx$ 21°C and 18°C) for Test 1 and Test 7, respectively.

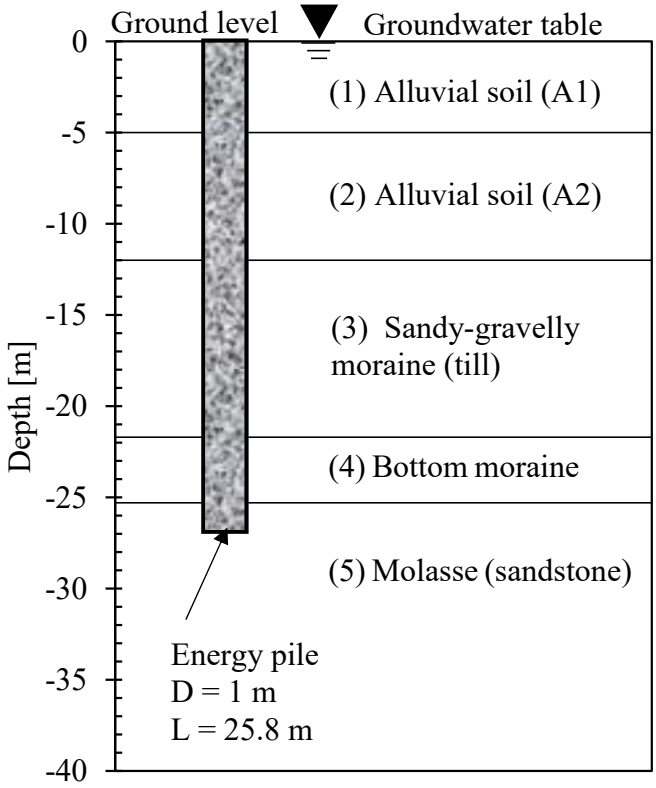

Figure 2.9. Geological profile and dimensions of the tested pile at the Swiss Federal Institute of Technology (drawn based on Laloui et al. (2006))

Chapter 3: THM Modeling of Geothermal Energy Piles

3.1. Introduction

Thermo-hydro-mechanical (THM) finite element analyses were conducted to study the behavior of energy piles subjected to thermal loads and a combination of thermal and mechanical loads. PLAXIS 2D-2016, which is a commercially available finite element software, was chosen as the modeling platform. This software has the capability to model transient thermo-hydro-mechanical (THM) coupling problems. It takes into account the time-dependent effects of temperature changes on stress, deformation, and groundwater flow in a fully coupled manner. The fully coupled THM implementation in PLAXIS 2D is an extension of the fully coupled hydro-mechanical (HM) analysis. Details of the formulation of the governing equations can be found in the PLAXIS documentation for thermal and coupled THM analysis (PLAXIS, 2015). It should be noted that the current version of PLAXIS has some limitations in which it does not consider the effect of temperature on the retention curve and mechanical properties of soils. However, these limitations are considered not to affect the conclusions given in this study.

The previously mentioned computer software has many constitutive models readily available, ranging from a simple model that only needs a few input parameters to sophisticated models that require many input parameters (PLAXIS 2D, 2018). In this thesis, two constitutive models were selected for the materials: linear elastic model (LEM) and hardening soil with small strain stiffness model (HSSM). The LEM requires only two parameters: Young's or elastic modulus (E) and Poisson's ratio (ν). Whereas, the HSSM needs 11 input parameters: reference secant stiffness from the standard triaxial test (E_{50}^{ref}), reference tangent stiffness from the

unloading/reloading primary oedometer loading (E_{eod}^{ref}), unloading/reloading Poisson's ratio (ν_{ur}), exponential power (m), failure ratio (R), reference shear stiffness at very small strain (G_0^{ref}), threshold shear strain ($\gamma_{0.7}$), and the Mohr-Coulomb failure parameters: cohesion intercept (c') and internal friction angle (φ' or ϕ') for the strength of soils, and an angle of dilatancy (ψ). More information about this soil constitutive model can be found in PLAXIS material manual (PLAXIS 2D, 2018).

It should be noted that this computer software currently uses sign conventions in that tension is positive (+ve) and compression is negative (-ve). Therefore, in all of the output data, compressive strains, stresses, and forces, including porewater pressures are taken to be negative (-ve). Expansive or tensile strains, stresses, and forces are taken to be positive (+ve).

The main objectives of this chapter are to validate the coupled THM numerical computations with the full-scale field measurements data and to perform sensitivity analyses to determine important model parameters that affect the behavior of energy piles. Two published case studies of energy piles were used to validate the model, the London energy pile and the Lausanne energy pile. These two case studies have distinctive features in which one is a friction energy pile installed in the London clay while the other is an end-bearing pile socketed into sandstone bedrock. Results from the numerical simulations were compared with experimental measurements of energy pile responses under the thermal and thermo-mechanical loadings, as follows.

3.2. THM Modeling of the London Energy Pile

The energy pile tested at Lambeth College in London, the United Kingdom, was selected as case study 1 (CS1). This energy pile was a trial pile, not a working pile (a structural pile underneath the building).

3.2.1. Material Characteristics

The soil stratigraphy at the site is given in Table 3.1 which is based on the information reported in the literature (Amatya et al., 2012; Amis et al., 2008; Bourne-Webb et al., 2009). The soil profile consists of three layers: (1) made ground (granular fill) from 0.0 to 1.5 m below ground level (bgl) (2) sandy gravel (terrace deposit) from 1.5 to 4.0 m bgl (3) London clay at a depth greater than 4.0 m bgl. The groundwater table is located within the sandy gravel layer, at about 3.0 m bgl.

Table 3.1. Soil stratigraphy at the London energy pile test site, U.K (CS1)

Concrete pile		Soil profile			
Diameter [m]	Length [m]	Layer	Depth [m]	Description	Thickness [m]
		1	0.0 - 1.5	Made ground (granular fill)	1.5
0.55	23	2	1.5 - 4.0	Sandy gravel (terrace deposit)	2.5
		3	> 4.0	London clay	

Note: Groundwater table is at 3.0 m bgl

The concrete pile was modeled as a solid (non-porous) elastic material using the linear elastic constitutive model (LEM) while the hardening soil with small strain stiffness model (HSSM) was used for the soils. The interface elements were represented by the Mohr-Coulomb model (MCM). The interface properties were calculated automatically by PLAXIS software using the soil properties in the associated data set and the interface strength reduction factors (R_{inter}). For the base case analysis, the model parameters shown in Table 3.2 were considered. These parameters were based on the information reported in the published documents (see more information in Table E.1 to Table E.4 in Appendix E and also Table I.1 in Appendix I).

Table 3.2. Model parameters for the base case analysis for the London energy pile (CS1)

Parameter	Symbol	Made ground (granular fill)	Sandy gravel (terrace deposit)	London clay	Concrete pile	Unit
Material model	-	HSSM	HSSM	HSSM	LEM	-
Analysis type	-	Fully coupled	Fully coupled	Fully coupled	Non-porous	-
Unit weight (above GWL)	γ_{unsat}	18	18	18	25	[kN/m^3]
Unit weight (below GWL)	γ_{sat}	19	20	20	-	[kN/m^3]
Initial void ratio	e_{init}	0.4	0.35	0.6	-	[-]
Parameters						
Young's modulus	E'	-	-	-	4000x10^3	[kPa]
Poisson's ratio	ν'	-	-	-	0.15	[-]
Ref. secant stiffness (in standard dr. tri. test)	E_{50}^{ref}	21x10^3	77x10^3	38.5x10^3	-	[kPa]
Ref. tangent stiffness (for primary oed. loading)	E_{oed}^{ref}	21x10^3	77x10^3	38.5x10^3	-	[kPa]
Ref. un/reloading stiffness	E_{ur}^{ref}	59.4x10^3	231x10^3	115.5x10^3	-	[kPa]
Un/reloading Poisson's ratio	ν_{ur}	0.2	0.2	0.2	-	[-]
Exponential power	m	0.5	0.5	1	-	[-]
Failure ratio	R_f	0.9	0.9	0.9	-	[-]
Shear stiffness (at very small strain)	G_0^{ref}	79.2x10^3	308x10^3	154x10^3	-	[kPa]
Threshold shear strain	$\gamma_{0.7}$	0.0002	0.0002	0.0002	-	[-]
Cohesion	c'	0.5 [a]	0.5 [a]	20	-	[kPa]
Internal friction angle	φ'	33	35	25	-	[°]
Dilatancy angle	ψ	3	5	0	-	[°]
Interface strength reduction factor	R_{inter}	1	1	1	-	[-]
Hydraulic conduc. (hor.)	k_x	1	1	1x10^{-5}	-	[m/day]
Hydraulic conduc. (vert.)	k_y	1	1	1x10^{-5}	-	[m/day]
Specific heat capacity	c_s	1200	1200	1500	800	[kJ/t/°C]
Thermal conductivity	λ_s	2x10^{-3}	2x10^{-3}	1.5x10^{-3}	1.8x10^{-3}	[kW/m/°C]
Soil density	ρ_s	1.94	2.04	2.04	2.55	[t/m^3]
Linear thermal exp. coef.	$\alpha_{sL(x,y,z)}$	5x10^{-6}	5x10^{-6}	5x10^{-6}	8.5x10^{-6}	[1/°C]

LEM = Linear Elastic Model; HSSM = Hardening Soil with Small strain stiffness Model

[a] small value of c' is used to prevent the numerical complication in the Plaxis compuatation

3.2.2. Geometry and Boundary Conditions

Axisymmetric finite element models with 15-node triangular elements were used for all numerical analyses. The 15-node triangular elements provide a fourth order interpolation for displacements and numerical integrations involve 12 stress points (PLAXIS 2D, 2018). This type of elements is highly recommended to be used for the axisymmetric analysis. The pile length was 23 long with the pile diameters (D) of 0.61 m (R= 0.305 m) for the top 5 and 0.55 m (R= 0.275 m) below this depth. The model domain was set at the distance of 50 m, slightly greater than 2L, for the side boundary, and at the distance of 75 m, just larger than 3L, for the bottom boundary (Figure 3.1). These distances were set far enough to minimize or eliminate the boundary effects. Larger boundaries were used, but with no effects on the modeling results.

The model domain was divided into zones for discretization in which a very fine mesh was used for the pile body, along the pile-soil interface, and around the pile toe in order to ensure that there were enough elements to capture the correct pile behavior. The size of the mesh was coarser for the zones further away from the pile.

For displacement boundary conditions, a free displacement was allowed at the top boundary. Whereas, both vertical and horizontal displacements were restrained at the bottom boundary (i.e., pinned boundary). Only vertical displacements were allowed at the left-hand side and right-hand side boundaries which mean that, in the horizontal direction, horizontal displacements were prevented for both sides (i.e., roller boundaries).

For hydraulic boundary conditions, the drainage was allowed at the top and right-hand side boundaries. A closed flow boundary was assigned along the axisymmetric line (left-hand side boundary) and the bottom boundary.

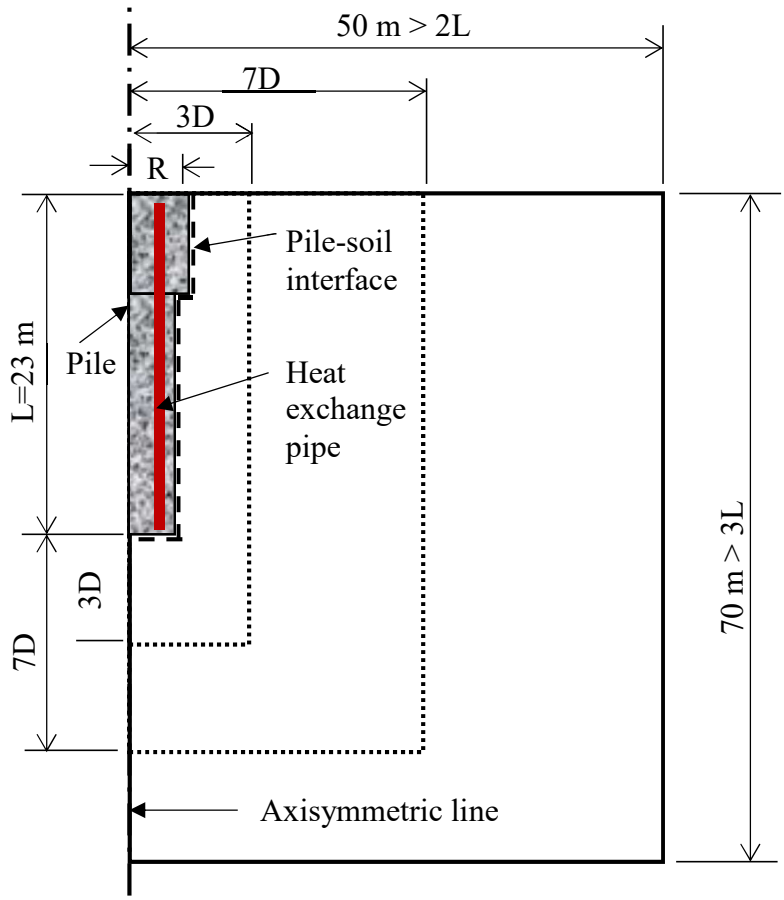

Figure 3.1. The axisymmetric geometry of the model for the London energy pile, U.K (not to scale)

For thermal boundary conditions, the heat flow was closed (adiabatic boundary condition) at the right-hand side boundary as well as at the left-hand side boundary. The latter was due to the axisymmetric condition. Since the pile test program was carried out in London during summer 2007 from June to August (Amis et al., 2008; Bourne-Webb et al., 2009), it was considered reasonable to use a constant surface temperature of 19.5°C at the top boundary. Note that the initial ground temperatures measured at this site range from 18 to 21°C (Amis et al., 2008). The average initial ground temperature of 19.5°C was used for the entire domain, and a constant temperature of 19.5°C was applied at the bottom boundary. Table 3.3 summaries the boundary conditions used for the energy pile test in London, UK.

Table 3.3. Summary of boundary conditions used for the London energy pile (CS1)

Boundary conditions	Top	Bottom	Left-hand side	Right-hand side
Displacement				
Vertical	Allowed	Not allowed	Allowed	Allowed
Horizontal	Allowed	Not allowed	Not allowed	Not allowed
Hydraulic	Open	Closed	Closed	Open
Thermal	Constant temperature of 19.5°C	Constant temperature of 19.5°C	Closed	Closed

Note: Initial ground temperature was set at 19.5°C for the entire model domain

3.2.3. Modeling Procedures

After setting up the model with all the boundary conditions mentioned above and assigning all the required model properties, the following modeling procedure was applied. The first step was to establish the initial stress conditions and initial ground temperature fields using what is called the K_o-procedure and the earth gradient, respectively. The next step was to install the concrete pile (the pile was wished in place which means that the effects of the pile installation were not taken into account on the stress states of the soils). Note that the pile-soil interface elements, represented by the Mohr-Coulomb model with a strength reduction factor of 1.0, were used for all analyses. Next, the mechanical load of -1200 kN, corresponding to a uniform distribution of the stress of -4106 kPa (with the pile head diameter of 0.61 m), was applied on the pile head in a drained manner before the start of the cooling-heating cycle. This means that the excess porewater pressure induced by the mechanical load was allowed to fully dissipate. The thermal load in terms of temperature was then applied in the pile using the line-based internal convective boundary (this implies a circular shell in the axisymmetric models) at the approximate location of the heat-carrying fluid pipe (heat exchange pipe), assumed at 70 mm from the pile shaft (edge). The thermal transmittance value (U-value) of 1.0 kW/m^2/°C was used for this convective thermal boundary condition. Note

that during the heating-cooling cycles, the mechanical load at the pile head was maintained constant throughout the test.

Pile temperature data recorded by the thermistor during the test, reported in Bourne-Webb et al. (2009) as replotted in Figure 3.2, was used as a thermal load applied internally in the pile. This temperature variation with time was from the thermistor attached to the re-bar cage at a depth of about 9 m bgl. From six thermistors installed along the pile length, it was observed that the recorded temperatures at a particular time along the pile length were practically constant, except slightly roll-offs near the pile head. From the thermistor at a depth of about 9 m bgl; as seen in the graph, the pile was cooled down for 31 days from the initial temperature of 19.5°C to just above zero (0.88°C), i.e. a change of $\Delta T \approx -18.6$°C in temperature at the end of cooling (EOC). Subsequently, heating began that lasted for about 12 days. This means the cooling-heating cycle took about 43 days. The drop-down in the temperature during the heating at about the 35th day was caused by a power interruption during the test. At the end of heating (EOH), the temperature was about 30.5°C, i.e. $\Delta T \approx +11$°C.

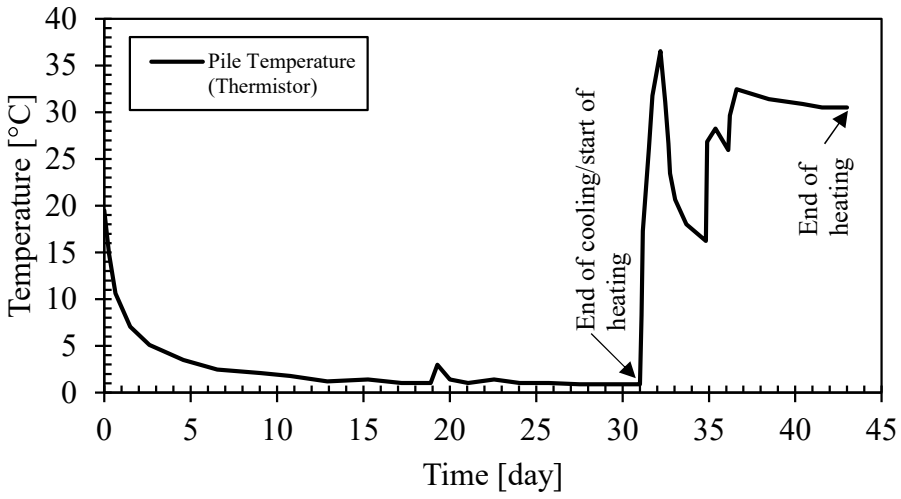

Figure 3.2. Temperature variations with time imposed on the pile for the London energy pile

3.3. THM Modeling of the Lausanne Energy Pile

The energy pile tested at the Swiss Federal Institute of Technology in Lausanne, Switzerland was chosen as case study 2 (CS2). Note that this energy pile was a part of the group of pile underneath the building. However, because only one pile was used as an energy pile, it could be considered as a single pile in the numerical model for simplicity.

3.3.1. Material Characteristics

The soil profile at the site reported in Laloui et al. (2006) was adopted, as summarized in Table 3.4. It consists of five layers namely: (1) alluvial soil (A1) from 0.0 to 5.5 m below ground level (bgl) (2) alluvial soil (A2) from 5.5 to 12.0 m bgl (3) sandy-gravelly moraine or till from 12.0 to 21.7 m bgl (4) bottom moraine from 21.7 to 25.3 m bgl, and (5) molasse or sandstone at the depth greater than 25.3 m bgl. The groundwater table was found at about the ground surface level.

Table 3.4. Soil stratigraphy at the energy pile test site in Lausanne, Switzerland (CS2)

Concrete pile		Soil profile			
Diameter [m]	Length [m]	Layer	Depth [m]	Description	Thickness [m]
		1	0.0 - 5.5	Alluvial soil (A1)	5.5
		2	5.5 - 12.0	Alluvial soil (A2)	6.5
1.0	25.8	3	12.0 - 21.7	Sandy gravelly moraine	9.7
		4	21.7 - 25.3	Bottom moraine (till)	3.6
		5	> 25.3	Molasse (sandstone)	

Note: Groundwater table is at ground level (0.0 m)

Like in the numerical analyses for the London energy pile, the coupled THM finite element simulations were also carried out. The soil properties used were mostly based on those given in Laloui et al. (2006). Some parameters such as the Poisson's ratios, hydraulic conductivities of sandstone, and coefficients of thermal expansion were taken from other papers (Di Donna, Rotta

Loria, & Laloui, 2016; Rotta Loria & Laloui, 2017) in which the author of this thesis considered to be more appropriate based on his engineering judgment. Table 3.5 shows the model parameters used for the base case analysis. Again, the concrete pile was considered as a solid and linear-elastic material and therefore was represented by the linear-elastic model (LEM). The hardening soil with small strain stiffness model (HSSM) was used for all the soil layers, except for the molasse (sandstone) layer which was represented by the LEM. The properties of soils related to those found in the Lausanne energy pile site can be found in Table F.1 to Table F.4 in Appendix F. Note that, in Laloui et al. (2006), the shear and bulk moduli (G and K) and porosities (n) of materials were given and these values were converted to elastic moduli (E) and void ratios (e) using the relationships: $E = (9KG)/(3K+G)$ and $e = n/(1-n)$, respectively.

Table 3.5. Model parameters for the base case analysis for the Lausanne energy pile (CS2)

Parameter	Symbol	Alluvial soil (A1)	Alluvial soil (A2)	Sandy-gravelly moraine(till)	Bottom moraine	Molasse (sandstone)	Concrete pile	Unit
Material model	-	HSSM	HSSM	HSSM	HSSM	LEM	LEM	-
Analysis type	-	Fully coupled	Fully coupled	Fully coupled	Fully coupled	Fully coupled	Non-porous	-
Unit weight (above GWL)	γ_{unsat}	18	18	18	20	23	24.53	[kN/m^3]
Unit weight (below GWL)	γ_{sat}	19.62	19.13	19.62	21.58	25.02	-	[kN/m^3]
Initial void ratio	e_{init}	0.11	0.11	0.54	0.43	0.05 [c]	-	[-]
Young's modulus	E'	-	-	-	-	3000x10^3	2920x10^3	[kPa]
Poisson's ratio	ν'	-	-	-	-	0.22	0.15	[-]
Ref. secant stiffness (in standard dr. tri. test)	E_{50}^{ref}	143x10^3	143x10^3	247.5x10^3	346.5x10^3	-	-	[kPa]
Ref. tangent stiffness (for primary oed. loading)	E_{eod}^{ref}	143x10^3	143x10^3	247.5x10^3	346.5x10^3	-	-	[kPa]
Ref. un/reloading stiffness	E_{ur}^{ref}	429x10^3	429x10^3	742.5x10^3	1039.5x10^3	-	-	[kPa]
Un/reloading Poisson's ratio	ν_{ur}	0.2	0.2	0.2	0.2	-	-	[-]
Exponential power	m	1	1	0.5	0.5	-	-	[-]
Failure ratio	R_f	0.9	0.9	0.9	0.9	-	-	[-]
Shear stiffness (at very small strain)	G_o^{ref}	572x10^3	572x10^3	990x10^3	1386x10^3	-	-	[kPa]
Threshold shear strain	$\gamma_{0.7}$	0.0002	0.0002	0.0002	0.0002	-	-	[-]
Cohesion	c'	5	3	6	20	-	-	[kPa]
Friction angle	φ'	30	27	23	27	-	-	[°]
Dilatancy angle	ψ	0	0	0	0	-	-	[°]
Interface strength reduction factor	R_{inter}	1	1	1	1	1	-	[-]
Hydraulic conduc. (hor.)	k_x	0.1730	0.0605	0.0860	0.0860	1.70x10^{-5} [b]	-	[m/day]
Hydraulic conduc. (vert.)	k_y	0.1730	0.0605	0.0860	0.0860	1.70x10^{-5} [b]	-	[m/day]
Specific heat capacity	c_s	1200	1231	1200	1091	784	800	[kJ/t/°C]
Thermal conductivity	λ_s	1.8x10^{-3}	1.8x10^{-3}	1.8x10^{-3}	1.8x10^{-3}	1.1x10^{-3}	2.1x10^{-3}	[kW/m/°C]
Density	ρ_s	2.00	1.95	2.00	2.20	2.55	2.50	[t/m^3]
Linear thermal exp. coef.	$\alpha_{sL(x,y,z)}$	3.33x10^{-6}	3.33x10^{-6}	3.33x10^{-6} [a]	3.33x10^{-6} [a]	2.3x10^{-6} [a]	10x10^{-6} [a]	[1/°C]

LEM = Linear Elastic Model; HSSM = Hardening Soil with Small strain stiffness Model

[a] Rotta Loria & Laloui (2017)

[b] Di Donna et al. (2016)

[c] Adjusted

3.3.2. Geometry and Boundary Conditions

According to Laloui et al. (2006), the as-built diameter of the pile varied slightly. For simplicity in the numerical model, the average pile diameter (D) of 1.0 m or a radius (R) of 0.5 m was used as well as the pile length (L) of 25.8 m. The width and the height of the model domain were set at 52 m (≈ 2L) and 78 m (≈ 3L), respectively (Figure 3.3). The model discretization was done in a similar way with that of the London energy pile. Also, the displacement, groundwater flow, and thermal boundary conditions were the same (see Section 3.2.2), except a constant temperature boundary of 13°C was used for the top and bottom boundaries (Table 3.6). Note that, the initial ground temperature of 13°C, as reported in Laloui et al. (2006), was also used in all models for the Lausanne pile.

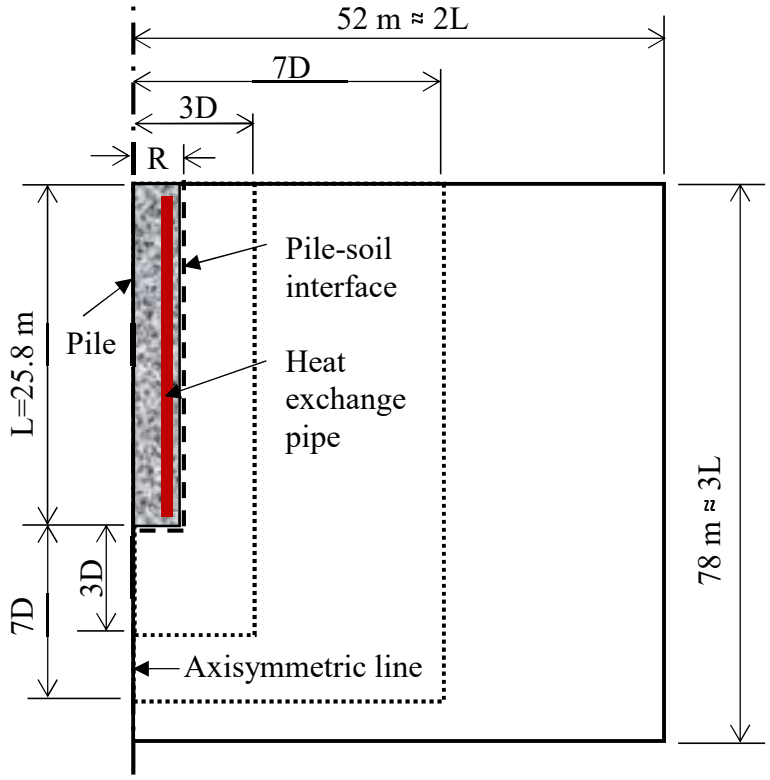

Figure 3.3. The axisymmetric geometry of the model for the Lausanne energy pile, Switzerland (not to scale)

Table 3.6. Summary of boundary conditions used for the Lausanne energy pile (CS2)

Boundary conditions	Top	Bottom	Left-hand side	Right-hand side
Displacement				
Vertical	Allowed	Not allowed	Allowed	Allowed
Horizontal	Allowed	Not allowed	Not allowed	Not allowed
Hydraulic	Open	Closed	Closed	Open
Thermal	Constant temperature of 13°C	Constant temperature of 13°C	Closed	Closed

Note: Initial ground temperature was set at 13°C for the entire model domain

3.3.3. Modeling Procedures

A detailed explanation would not be given here as the modeling procedures used for this Lausanne energy pile was similar to that of the London energy pile. There were seven tests (Test 1 to Test 7) performed periodically for the Lausanne energy pile throughout the construction period of the building. However, only Test 1 and Test 7 were considered in this study. During Test 1, there was no structure on top of the pile yet. Therefore, the energy pile was only subjected to a thermal load without any mechanical load on its head and it was first heated for 12 days, reaching the highest temperature at the end of heating (EOH) of 34°C (ΔT=+21°C). The pile was then cooled down for about 16 days to 15°C ($\Delta T \approx$+2°C) at the end of cooling (EOC), just higher than the initial ground temperature of 13°C. In Test 7, the building construction had reached the top floor; as a result; it transferred the mechanical load of -1300 kN onto the pile head corresponding to the stress of -1655 kPa (with the pile head diameter of 1.0 m). As shown in Figure 3.4, the heating-cooling cycles during Test 1 and Test 7 were slightly different. In Test 7, the heating period was approximately 22 days, reaching the temperature of 31°C ($\Delta T \approx$+18°C) at the end of heating (EOH) and the cooling period was about six days with $\Delta T \approx$+2°C at the end of cooling (EOC). These temperature variations with time in the pile were recorded using vibrating-wire extensometers that

could measure vertical strains and temperatures. There were 28 vibrating-wire extensometers that were attached to the rebar cage and located along the pile length (Laloui et al., 2006). Again, it was observed that the recorded temperatures at a particular time along the pile length were relatively constant.

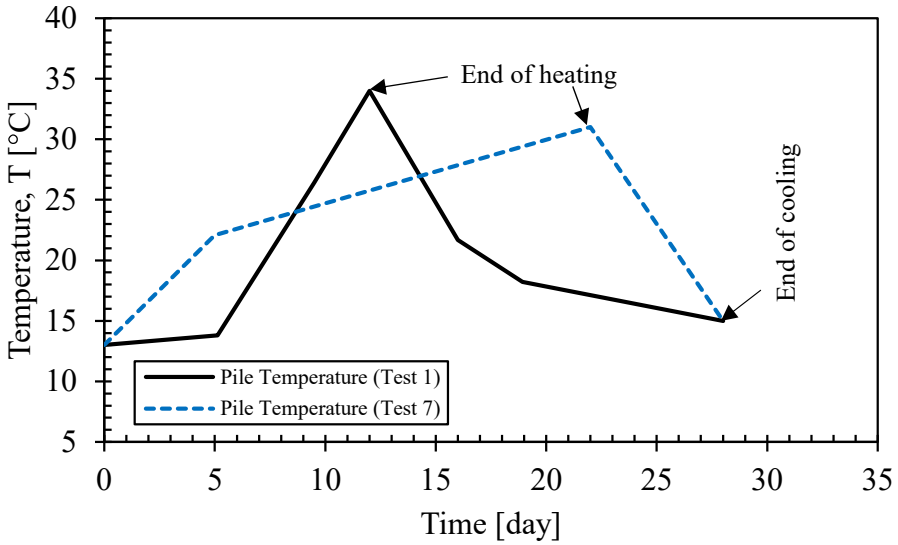

Figure 3.4. Thermal load imposed on the pile in terms of temperature variations with time for Lausanne energy pile Test 1 and Test 7

3.4. Results and Discussion of Base Case Analyses of Energy Pile Case Studies

In this section, results from the base case analyses using base case parameters of the energy piles in London and Lausanne were reported and discussed.

3.4.1. Temperature and Porewater Pressure Distributions

London energy pile:

As expected, during 31 days of cooling, the pile temperature reduced from an initial temperature of 19.5°C to just above zero at the end of cooling (EOC) and during 12 days of heating,

the pile temperature increased to 31°C at the end of heating (EOH). Note that, the temperature propagated in both vertical and radial directions through the pile and surrounding soils (Figure 3.5).

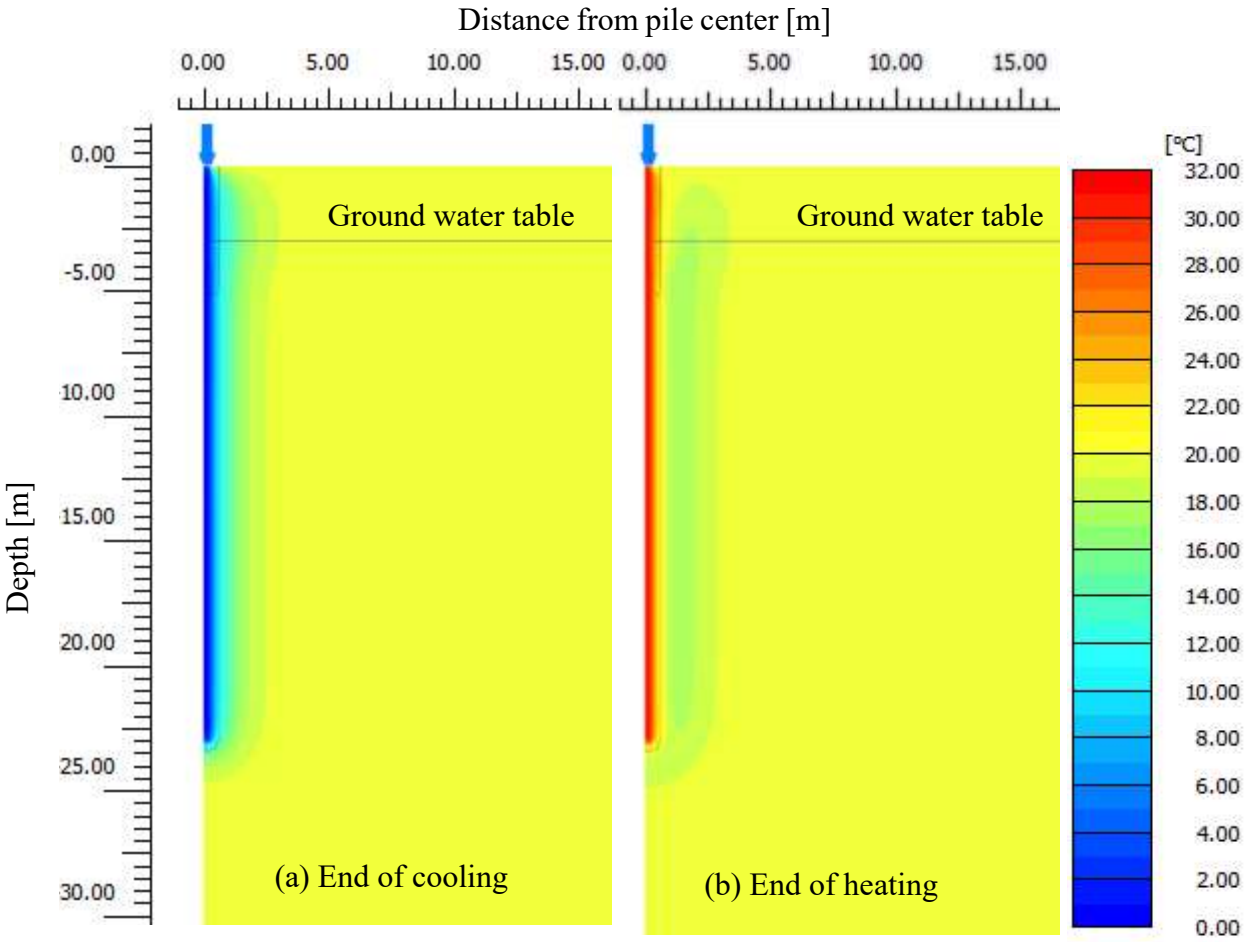

Figure 3.5. Temperature distributions in the pile and surrounding ground (a) at the end of cooling (EOC) (b) at the end of heating (EOH) for the London energy pile (base case)

Figure 3.6 displays the measured and simulated temperature changes with time during the cooling-heating cycle for the London energy pile. These values were taken at around the mid-length of the pile at locations of the observed borehole and the anchor pile at 0.5 m and 2.0 m away from the pile center, respectively. Even though at the EOC the pile temperature was about 0.88°C, the ground temperature at a distance of 0.5 m (≈ D) only reduced to 7.9°C from the initial ground

temperature of 19.5°C. Moreover, the pile cooling and heating, at least, for the test period of about 43 days did not affect the ground temperature at 2 m away (≈ 4D) from the pile. Since the groundwater flow is insignificant due to a very low hydraulic conductivity of the clay (in the order of $1x10^{-5}$ m/day), the heat transfer in the ground is mainly due to conduction. The measured temperature values using thermistors and optical fiber sensors, OFS (Bourne-Webb et al., 2009) and simulated temperature values agree well. The numerical model, therefore, was able to predict the temperature distribution in the surrounding ground accurately.

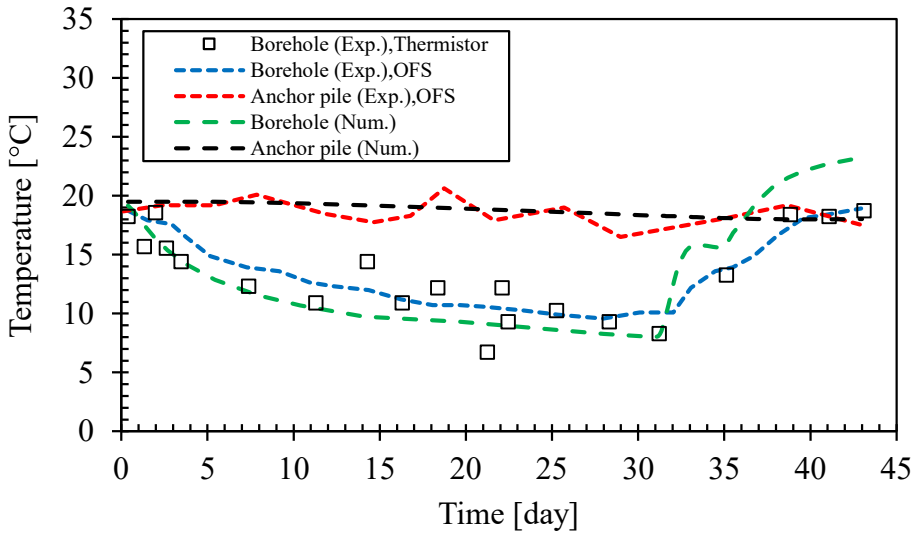

Figure 3.6. Temperature changes during a cooling-heating cycle at around the mid-depth of the pile at the borehole and the anchor pile locations: 0.5 m and 2 m distance from the pile center; respectively, for the London energy pile (base case)

As shown in Figure 3.7, the changes in the temperature of the surrounding soils caused by pile heating and cooling, led to the changes in the porewater pressures. This is because the London clay has a very low hydraulic conductivity. As a result, thermally induced excess porewater pressures (EPWPs) could not dissipate fast enough. The positive excess porewater pressures (tension) built up during cooling in the soil adjacent to the pile. A maximum value of 31 kPa was obtained at the end of cooling. This phenomenon is somewhat analogous to the excess porewater

pressures induced by unloading such as during deep excavations in saturated clays. During heating, the negative excess porewater pressures (compression) were induced with the maximum value of -34 kPa at the end of heating. The thermally induced excess porewater pressures during heating are similar to that of stress-induced cases by loading such as the construction of an embankment on saturated clays. The increase and decrease in porewater pressures during the cooling-heating cycle in the clay layer may be mainly due to low permeability of the clay and the large difference between a volumetric thermal expansion coefficient of porewater which is about 210×10^{-6} (1/ºC) at 20ºC and that of the soil skeleton (solid particles) with a typical value of about 15×10^{-6} (1/ºC). Therefore, the porewater is about 14 times more expansive than the soil skeleton. When the soil body was heated, its constituents (porewater and solid particles) tried to expand but not at the same rates. This, coupled with the low hydraulic conductivity coefficient of the clay, do not allow the expansion potential of porewater to occur. In other words, it was restricted or constrained (undrained condition) thereby causing the excess porewater pressures to build up in the soil body. The excess porewater responses in the soil adjacent to the energy pile observed from the numerical modeling agreed with the observations by Campanella & Mitchell (1968) in undrained triaxial tests on saturated illite specimens under thermal heating-cooling cycles (from 18.3 to 60ºC and then 4.4 to 60ºC for two compete cycles). They found that when temperatures increased, porewater pressures increased and vice versa. They also mentioned that the relationship between the porewater pressure and temperature was repeatable and created a closed hysteresis loop.

The excess porewater pressure profiles along the pile-soil interface are demonstrated in Figure 3.8(a). The excess porewater pressures (EPWPs) marginally increased with depth from the top of the London clay at -5 m to the maximum value just above the pile toe. The EPWPs then started to decrease sharply and reached almost zero at -29 m elevation (≈ 11D below the pile toe).

Note that there were no EPWPs generated in the sandy gravel layer below the groundwater table because of its high permeability. Figure 3.8(b) illustrates the EPWP profiles at the mid-depth of the pile at -11.5 m elevation from the pile center to 15 m sideways. As seen in the graph, the highest EPWPs occurred in the soil adjacent to the pile. The values dropped steeply and became nearly zero at a distance of about 8 m (≈ 15D) from the pile center.

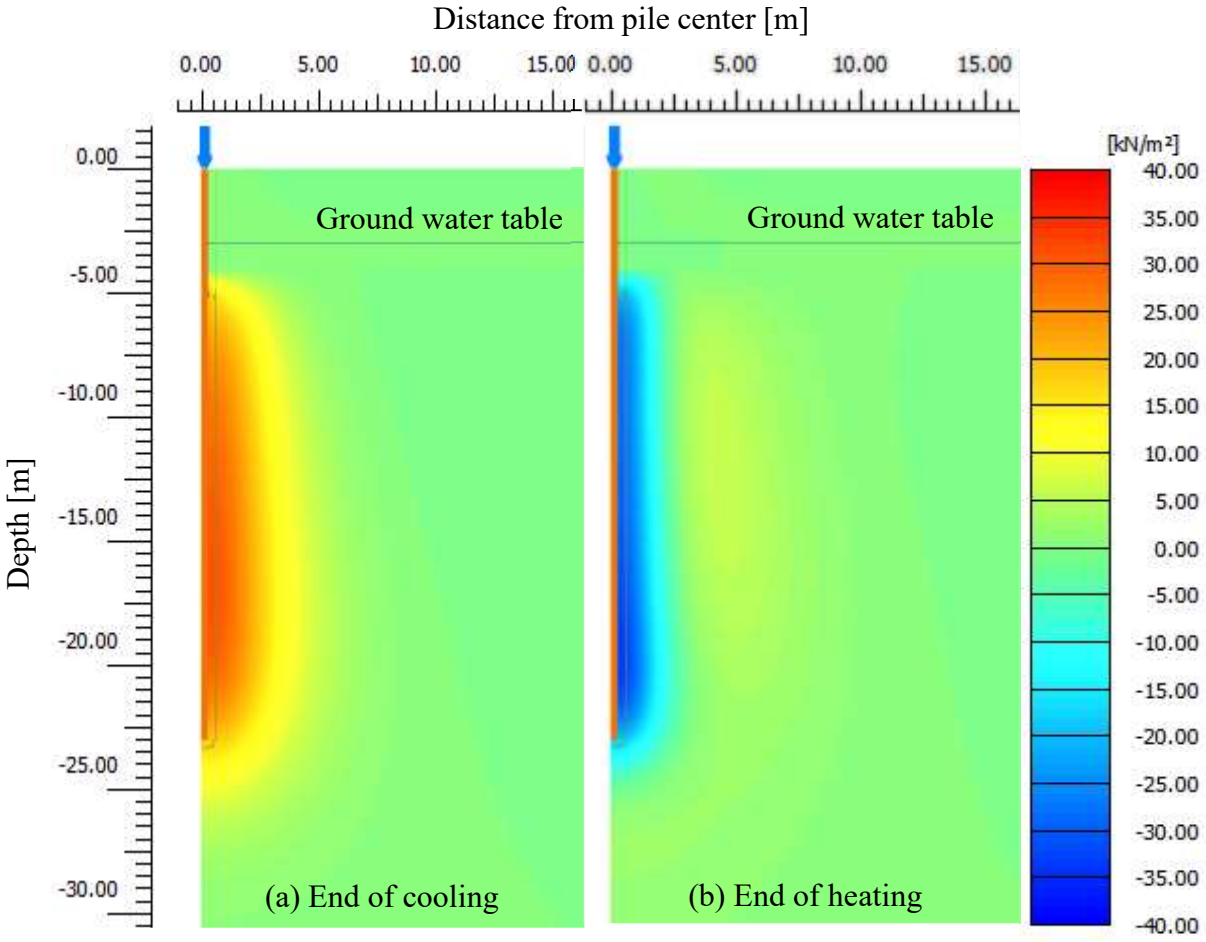

Figure 3.7. Thermally induced excess porewater pressures (EPWPs) in the ground (a) at the end of cooling (EOC) and (b) at the end of heating (EOH) for the London energy pile (base case)

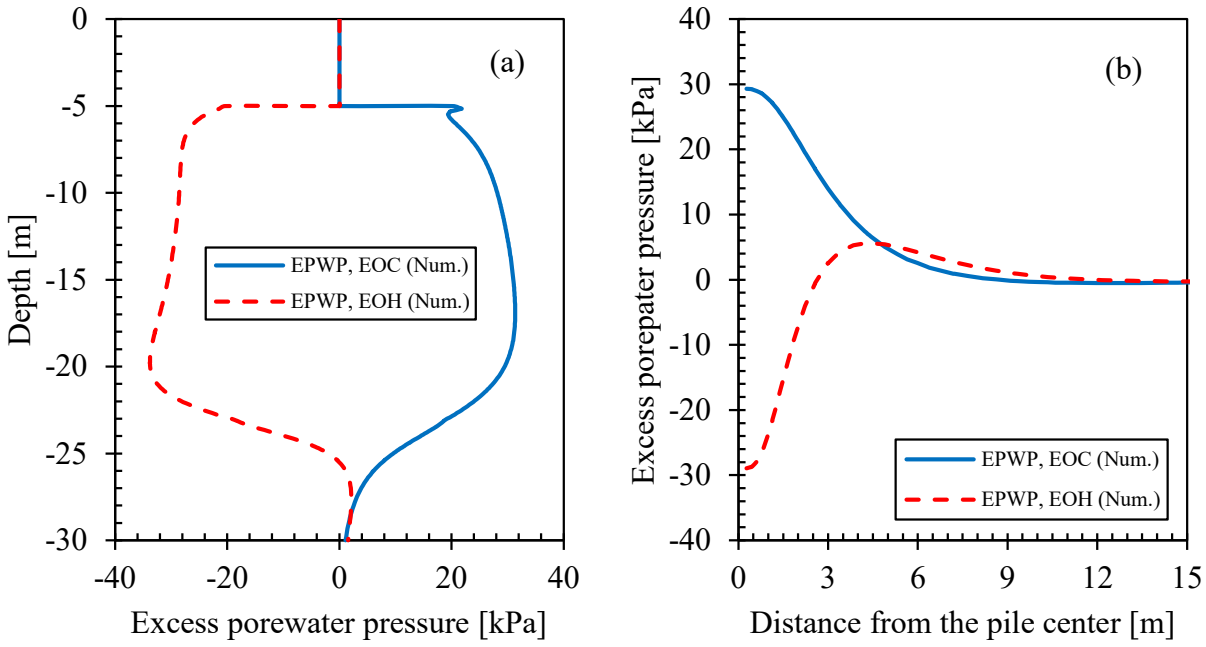

Figure 3.8. Thermally induced excess porewater pressures (EPWPs) (a) along the pile-soil interface to 13D below the pile toe (b) at the mid-depth of the pile from pile center to 15 m for the London energy pile (base case)

Lausanne energy pile:

The temperature distributions in the pile and surrounding ground in Test 1 and Test 7 are similar; therefore, only the temperature distributions of Test 7 are illustrated in Figure 3.9. As seen in the figure, the pile temperature at the EOH (22 days of heating) had reached the highest value of 31ºC. At the EOC (only six days of cooling), the pile temperature was reduced to about 15ºC. Note that, at EOC the pile temperature was still above the initial temperature of the ground (13ºC). The soil domain affected by the heating-cooling cycle was within a distance of 2.5 m (≈ 2.5D) from the pile center for the given test period.

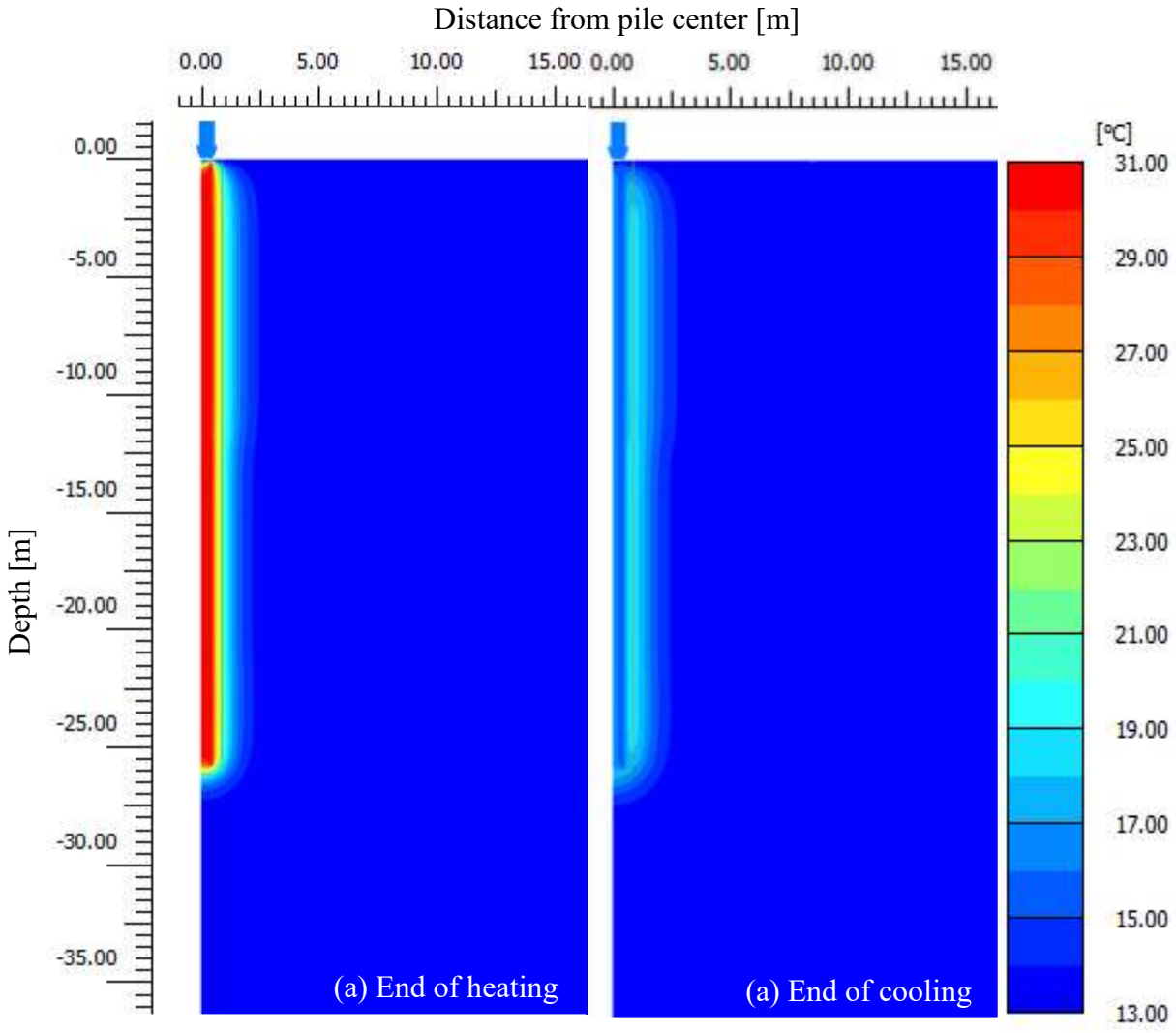

Figure 3.9. Temperature distributions in the pile and surrounding ground (a) at the end of heating (EOH) and (b) at the end of cooling (EOC) for the Lausanne energy pile: Test 7 (base case)

Regarding the excess porewater pressures generated due to the changes in temperature in the surrounding ground, there were no excess porewater pressures in the overburden soil layers because of their high permeability. In the sandstone bedrock with a very low hydraulic conductivity (1.7×10^{-5} m/day), the excess porewater pressures were generated. However, their magnitudes were small and negligible (-2 kPa and 6 kPa at the EOH and EOC, correspondingly) as shown in Figure 3.10.

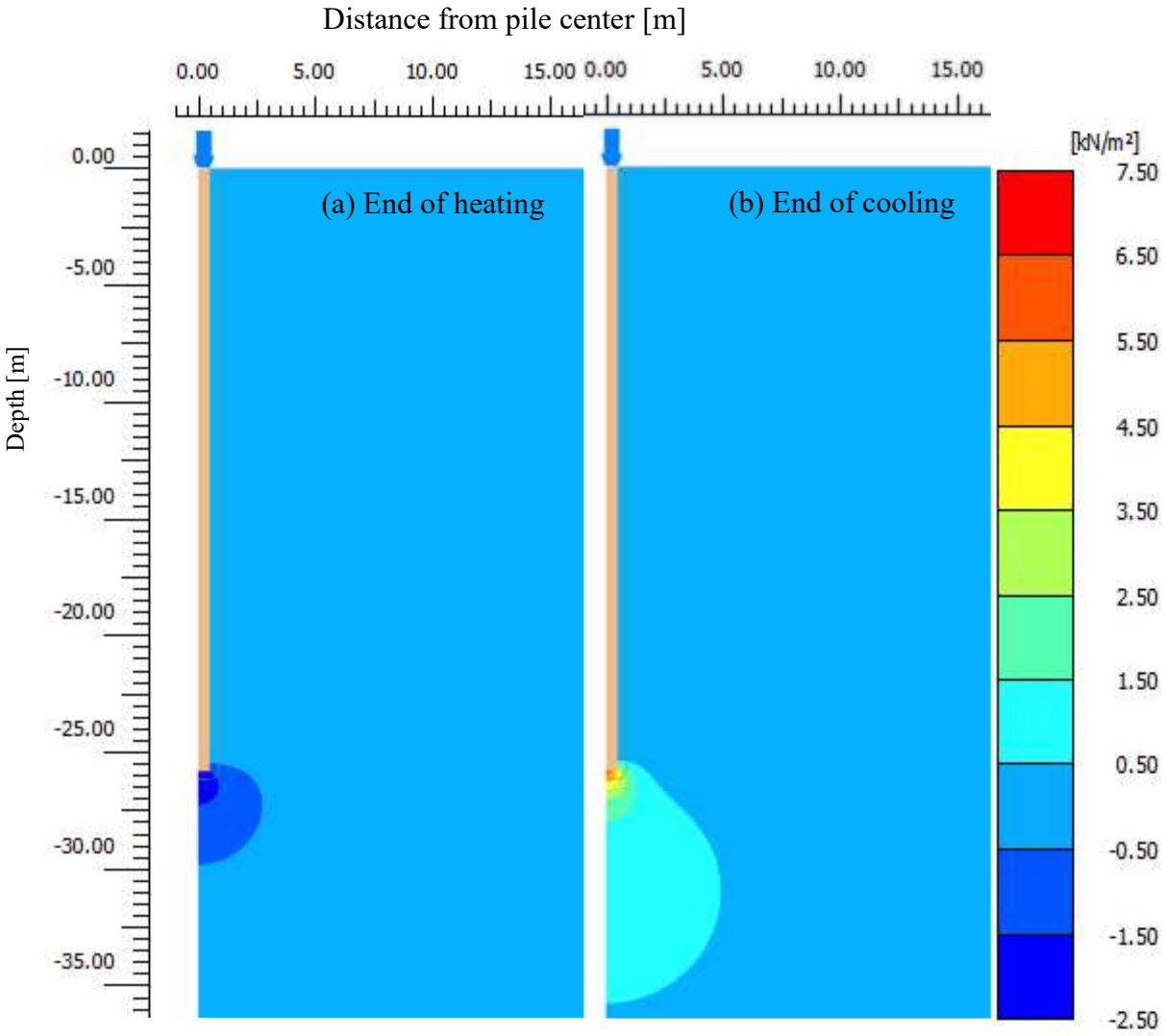

Figure 3.10. Thermally induced excess porewater pressures (PWP) in the ground (a) at the end of heating (EOH) and (b) at the end of cooling (EOC) for the Lausanne energy pile: Test 7 (base case)

3.4.2. Pile Vertical Displacement

London energy pile:

As a result of the cooling-heating cycle, the pile head moved up and down following the fall and rise of the temperature. As shown in Figure 3.11, under the thermo-mechanical load (M+T), the computed and measured pile head movements taken from Bourne-Webb et al. (2009)

agreed quite well, which means that the numerical simulations performed as desired. The maximum predicted movement of the pile head was -5.1 mm (-0.92% D, used D= 550 mm) at the end of cooling (EOC) in comparison with -4.8 mm (-0.88% D) from the experiment (a 0.3 mm difference). At the end of heating (EOH), the pile head movements were -2.3 mm (-0.42% D) and -3.1 mm (-0.56% D) for numerical and experimental results, respectively.

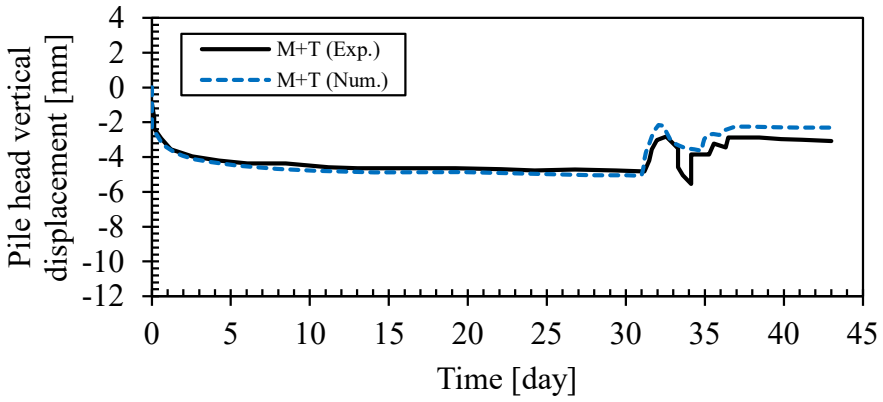

Figure 3.11. Pile head vertical displacements during the cooling-heating cycle for the London energy pile (base case)

Pile vertical displacements along the pile length for the London energy pile are shown in Figure 3.12. The mechanical load (M) caused the contraction in the entire pile, and downward displacements were induced with the maximum value of -2.3 mm (-0.41% D) at the pile head and the minimum value of -0.8 mm (-0.15% D) at the pile toe. Cooling caused the pile to contract even further, but unlike the contraction induced by the M, the thermally induced contraction occurred with respect to the location of the neutral plane (NP) where the pile did not move. During cooling, the portion above the NP moved down whereas the portion below it moved up. These resulted in further head displacement to -5.1 mm (-0.92% D) under the thermo-mechanical load (M+T) at the EOC (denoted by M+T, EOC) but reduced the toe displacement to -0.2 mm (-0.03% D). When the pile was heated, from the EOC position, about one-half of the pile moved up while other half

moved down. These happened because heating caused the pile to expand about the NP. Under the thermo-mechanical load (M+T) at the EOH (denoted by M+T, EOH), the pile head moved back up to -2.3 mm (-0.42% D). The pile toe moved down to -2.0 mm (-0.36% D).

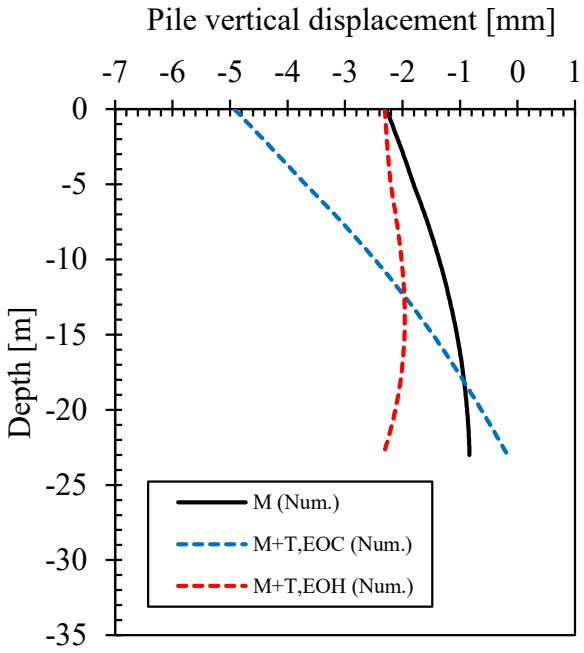

Figure 3.12. Pile vertical displacement profiles at the end of cooling (EOC) and at the end of heating (EOH) for the London energy pile (base case)

Lausanne energy pile:

Pile head displacements during the heating-cooling cycle of the pile in Test 1 are shown in Figure 3.13. The numerical results were plotted against the measured data using different monitoring instruments. The pile head movements produced by the numerical model fitted well within the array of the measured ones. The pile head moved up about 3.1 mm (0.31% D) due to the thermal load alone (T) at the EOH (denoted by T, EOH) and then moved back down during cooling, reaching 0.7 mm (0.07% D) at the end of cooling (T, EOC). In comparison, the pile head uplifts under the T alone measured using different monitoring instruments at the EOH for Test 1 varied from 3.4 mm (survey measurements - leveling), 3.7 mm (optical fibers data) to 4.4 mm

(extensometers). Whereas, the measured values at the end of cooling (T, EOC) were 0.8 mm (optical fibers data) and 0.6 mm as reported in Laloui et al. (2006).

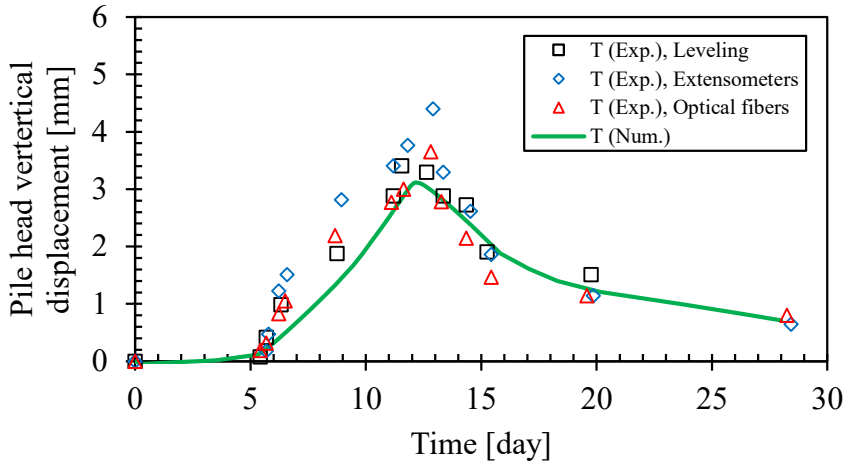

Figure 3.13. Pile head vertical displacements during the heating-cooling cycle for the Lausanne energy pile: Test 1 (base case)

Figure 3.14 shows the pile vertical displacements under the thermal load at the EOH and at the EOC for Test 1. Note that for a reference, the initial condition was also plotted in the figure. As expected, heating caused the pile to expand and mostly displace upwards. This is because the pile toe was socketed into the sandstone bedrock with very high stiffness. Similar phenomena happened in Test 7 as shown in Figure 3.15. In Test 7, the pile was mechanically loaded first (M), resulting in the pile head settlement of -0.8 mm (-0.08% D) and the pile toe of -0.03 mm (-0.003% D). Under the thermo-mechanical load at the end of heating (M+T, EOH), the pile head moved up to 1.5 mm (0.15% D) and the pile toe moved down to -0.4 mm (-0.04% D), respectively. Conversely, at the end of cooling (M+T, EOC), the pile head moved back down to -0.4 mm (-0.04% D) and the pile toe moved up to -0.1 mm (0.01% D).

A summary of the simulated pile head uplifts at the end of heating and settlements at the end of cooling due to a combination of thermal and mechanical loads for both London energy pile and Lausanne energy pile Test 7 are given in Table 3.7.

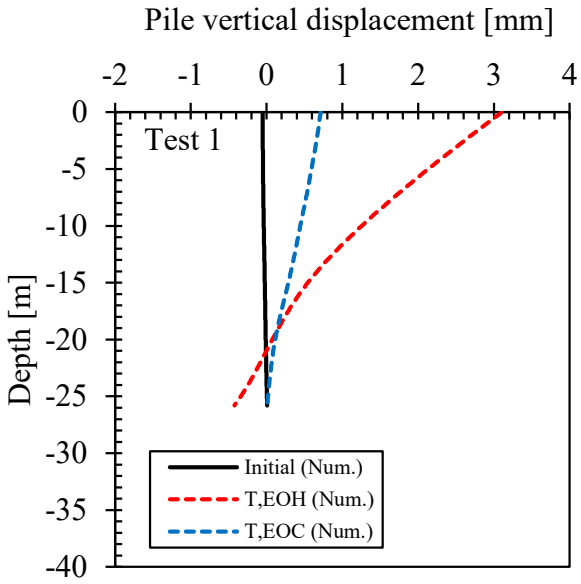

Figure 3.14. Pile vertical displacement profiles at the end of heating (EOH) and at the end of cooling (EOC) for the Lausanne energy pile: Test 1 (base case)

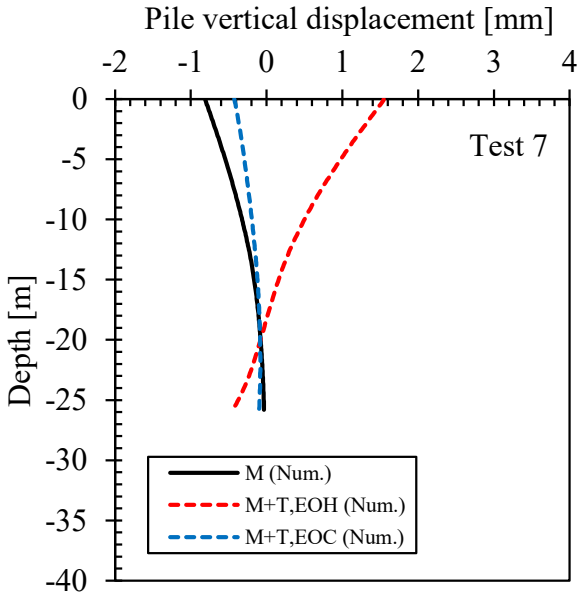

Figure 3.15. Pile vertical displacement profiles at the end of heating (EOH) and at the end of cooling (EOC) for the Lausanne energy pile: Test 7 (base case)

Table 3.7. Summary of simulated pile head uplifts and settlements due to thermo-mechanical load for energy pile case studies: London energy pile and Lausanne energy pile Test 7

Energy pile names	Applied mechanical load (M)	Initial temp.	Range of applied temperature	Temp. change from init. value	Pile head displacement due to thermo-mechanical loads (M+T)		Remark
	[kN]	[°C]	[°C]	[°C]	[mm]	[% D]	
London energy pile (D =0.55 m and L =23 m)							
At the EOC, settlement	-1200	19.5	0.88 to 30.5	-18.6	-5.06	-0.92	then 12-day heating
At the EOH, uplift	-1200	19.5	0.88 to 30.5	11	-2.31	-0.42	31-day cooling first,
Lausanne energy pile (Test 7) (D =1.0 m and L =25.8 m)							
At the EOH, uplift	-1300	13	15 to 31	18	1.54	0.15	22-day heating first,
At the EOC, settlement	-1300	13	15 to 31	2	0.43	0.04	then 6-day cooling

M = mechanical load, T = thermal load, M+T = thermo-mechanical load, D = pile diameter
EOH = end of heating, EOC = end of cooling

3.4.3. Pile Axial Strain Distribution

London energy pile:

Axial strain profiles of the pile in responses to mechanical (M) and thermo-mechanical loads (M+T) are illustrated in Figure 3.16 and Figure 3.17. Note that the axial strains caused by the M only were plotted in all figures for reference purposes. In Figure 3.16(a), the thermal cooling (T, EOC) induced contractive strains (negative) in the pile; and therefore, added to the contractive strains caused by the M and resulted in higher compressive strains in the pile. As a result, the strain profiles of a combined effect of mechanical and thermal loads at the end of cooling (M+T, EOC) shifted to the left-hand side as shown in Figure 3.16(b).

During heating in which the pile expanded, resulting in expansive strains (positive) in the pile (Figure 3.17(a)). This is opposite to the mechanically induced compressive strains. Therefore, lower contractive strains were obtained and the strain profiles induced by the thermo-mechanical load at the end of heating (M+T, EOH) shifted to the right-hand side, leading to expansive strains at the bottom half of the pile as shown in Figure 3.17(b). It can be seen that the mechanically induced expansive strains from numerical modeling were just slightly higher than the experimental data below -5 m. The deviations, however, were noticed in the upper 5 m of the pile. These deviations may be due to the fact that the numerical model used the unrestrained head condition for the pile and due to the abrupt change in the pile diameter at -5 m, from 0.55 m to 0.61 m. The strains caused by the thermo-mechanical load at the end of cooling (M+T, EOC) and heating (M+T, EOH) are also comparable. Even though they did not match, similar patterns were observed for both simulations and the experiment as reported in Amatya et al. (2012).

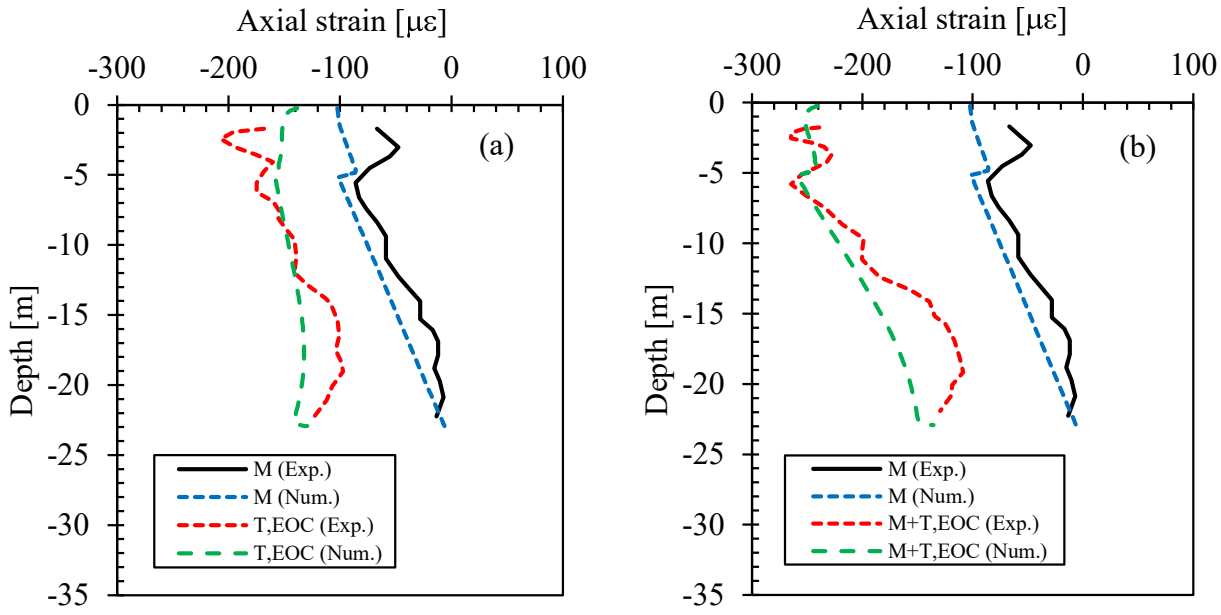

Figure 3.16. Axial strain profiles (a) thermal (T) and (b) thermo-mechanical (M+T) at the end of cooling (EOC) for the London energy pile (base case)

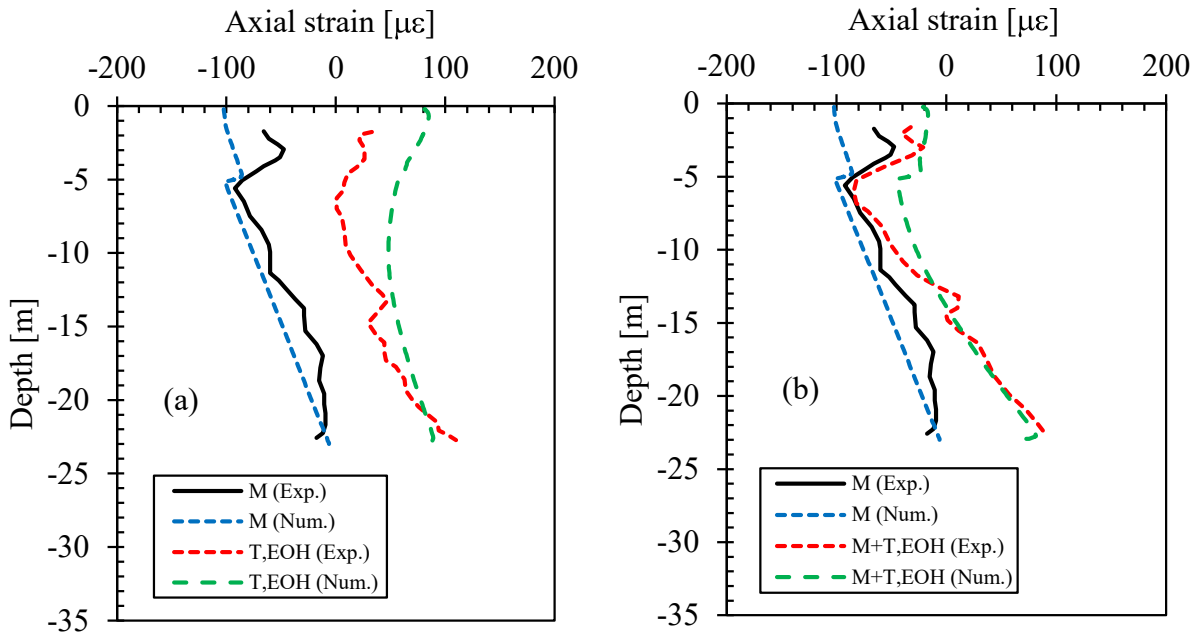

Figure 3.17. Axial strain profiles (a) thermal (T) and (b) thermo-mechanical (M+T) at the end of heating (EOH) for the London energy pile (base case)

Lausanne energy pile:

Figure 3.18 compares the expansive axial strains induced by the thermal load (T) between the numerical results and experiment data at the EOH and the EOC for Test 1. As can be seen, the strain profiles from the simulation and experiment were comparable, although the numerical model considerably under-predicted the strains at the lower part of the pile at the EOH. This may be due to the assumption that there was no stiffness reduction of the sandstone bedrock right underneath the pile toe in the model. In the field, however, this stiffness may be less because of the imperfection of borehole base cleaning before the concrete was poured.

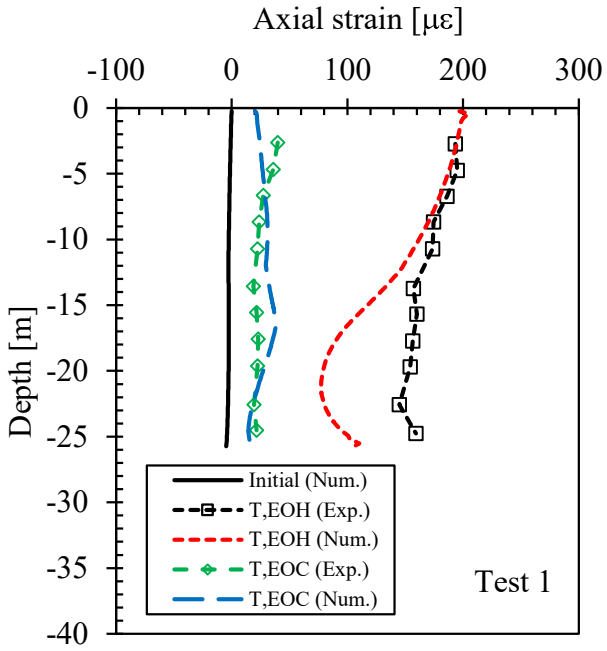

Figure 3.18. Axial strain profiles at the end of heating (EOH) and at the end of cooling (EOC) for the Lausanne energy pile: Test 1 (base case)

The axial strains induced by the M, the T and the M+T in Test 7 at the EOH and EOC are shown in Figure 3.19 and Figure 3.20. The experimental data at the EOH were taken from Amatya et al. (2012). The field data at the EOC were not available. It can be seen that the mechanically induced compressive strains were in good agreement with the measured data, especially at the lower half of the pile. When the pile was heated, applying the thermal heating load, expansive strains were induced; whereas, the M produced compressive strains as shown in Figure 3.19(a). As seen in Figure 3.19(b), the combined thermo-mechanical axial strains at the end of heating (M+T, EOH) from numerical and experimental results were also comparable. The numerical model gave slightly lower expansive strains for the lower half of the pile. This was because, as explained earlier for Test 1, no stiffness reduction due to a possible base cleaning problem of the drilled hole before casting concrete was considered in the model. On the other hand, the numerical model gave higher strain values for the upper half. This was due to the assumption of an

unrestrained head condition of the pile in the analysis. In reality, the pile head may be partially restrained by the superstructure. Different head restrained conditions of the pile would be subsequently discussed in the sensitivity analyses (see Section 3.5.6). At the end of cooling, as shown in Figure 3.20(b), the axial strain profiles moved back close to the original position before the beginning of heating.

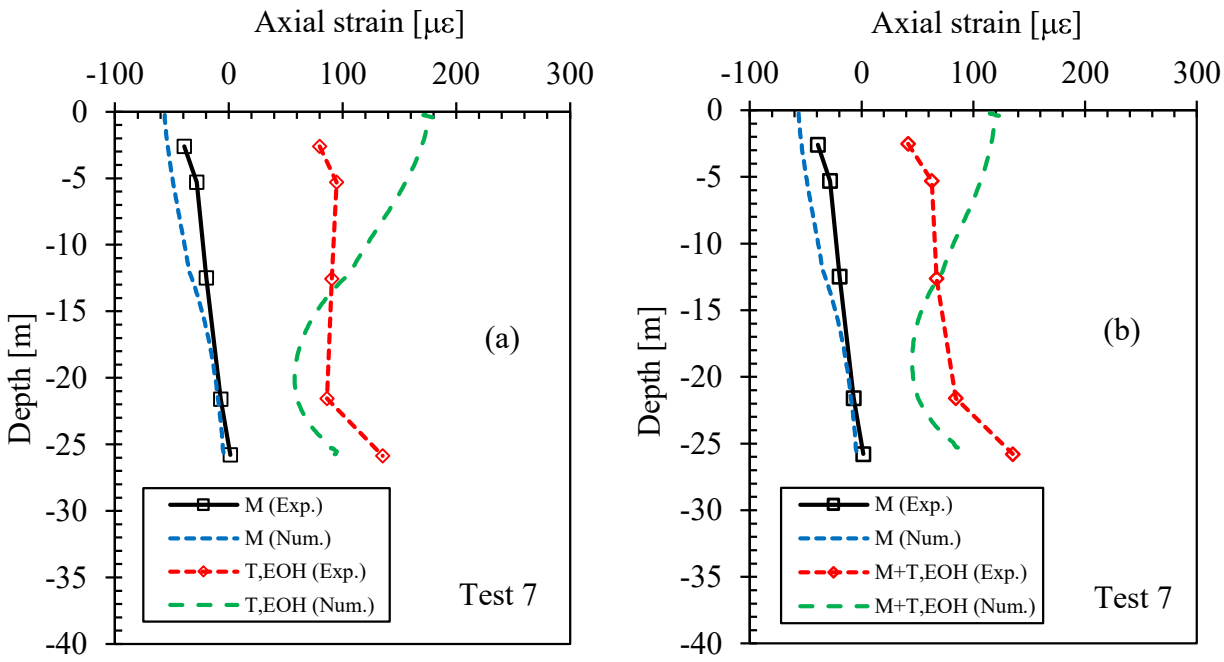

Figure 3.19. Axial strain profiles (a) thermal (T) and (b) thermo-mechanical (M+T) at the end of heating (EOH) for the Lausanne energy pile: Test 7 (base case)

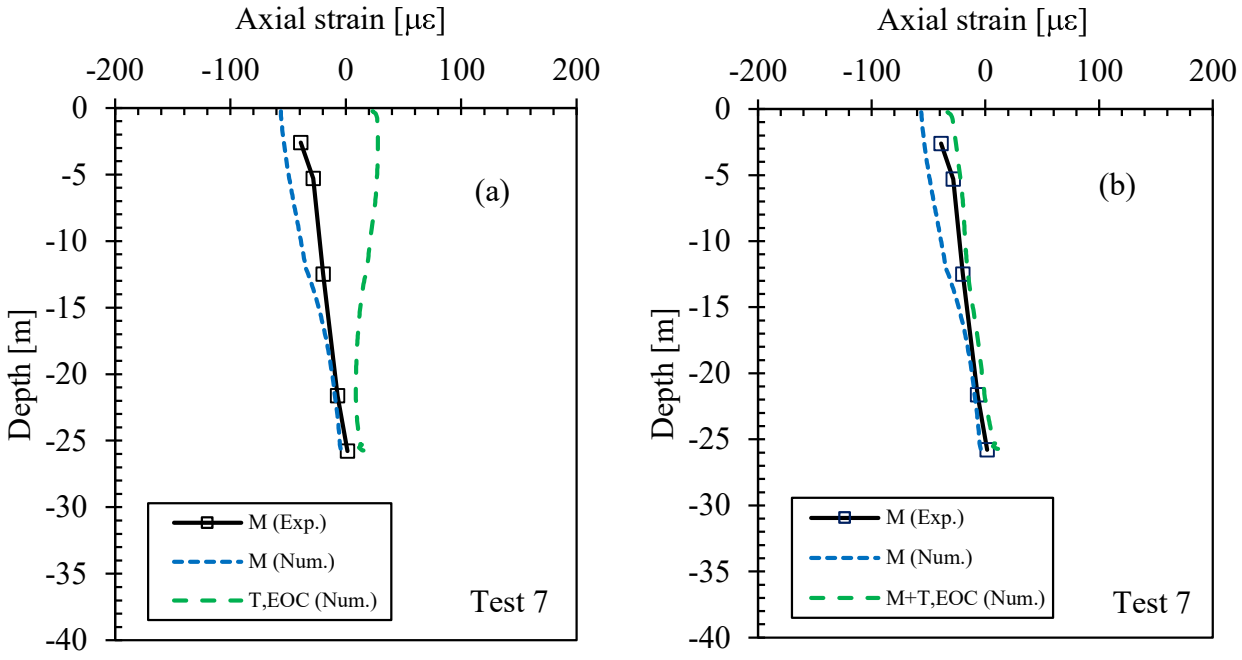

Figure 3.20. Axial strain profiles (a) thermal (T) and (b) thermo-mechanical (M+T) at the end of cooling (EOC) for the Lausanne energy pile: Test 7 (base case)

3.4.4. Pile Axial Load Distribution

London energy pile:

Axial load profiles induced by the mechanical (M), the thermal (T), and the thermo-mechanical (M+T) loads are shown in Figure 3.21 and Figure 3.22. The axial compressive stresses (negative) were induced in the pile when the M of -1200 kN was applied on the pile head. This load then transferred to the surrounding soils through the shaft friction and gradually decreasing, reaching -159 kN at the pile toe. The predicted load transfer profile due to the mechanical load closely resembled the field data reported in Bourne-Webb et al. (2009) from vibrating strain gauges (VWSG) and optical fiber sensors (OFS).

At the end of cooling (EOC), thermally induced tensile loads were generated along the pile as shown in Figure 3.21(a). The simulated tensile load profile and experimental tensile load profile

from vibrating strain gauges (VWSG) matched very well with the maximum values just below the mid-depth of the pile of 252 kN and 301 kN, correspondingly. Since cooling induced tensile loads in the pile in contrast to the mechanical load, the compressive loads in the pile reduced for the combined effects of the thermo-mechanical load at the end of cooling (M+T, EOC), as shown in Figure 3.21(b). Note that there were tensile loads near the pile toe at the end of cooling (M+T, EOC) with the maximum simulated value of 78 kN. This value from experimental data was about 122 kN using vibrating strain gauges (VWSG) and about 480 kN using optical fiber sensors (OFS) for ΔT≈-18.6°C (Bourne-Webb et al., 2009). It should be noted that there was a discrepancy in the axial load values in the pile obtained from the field using different measuring tools.

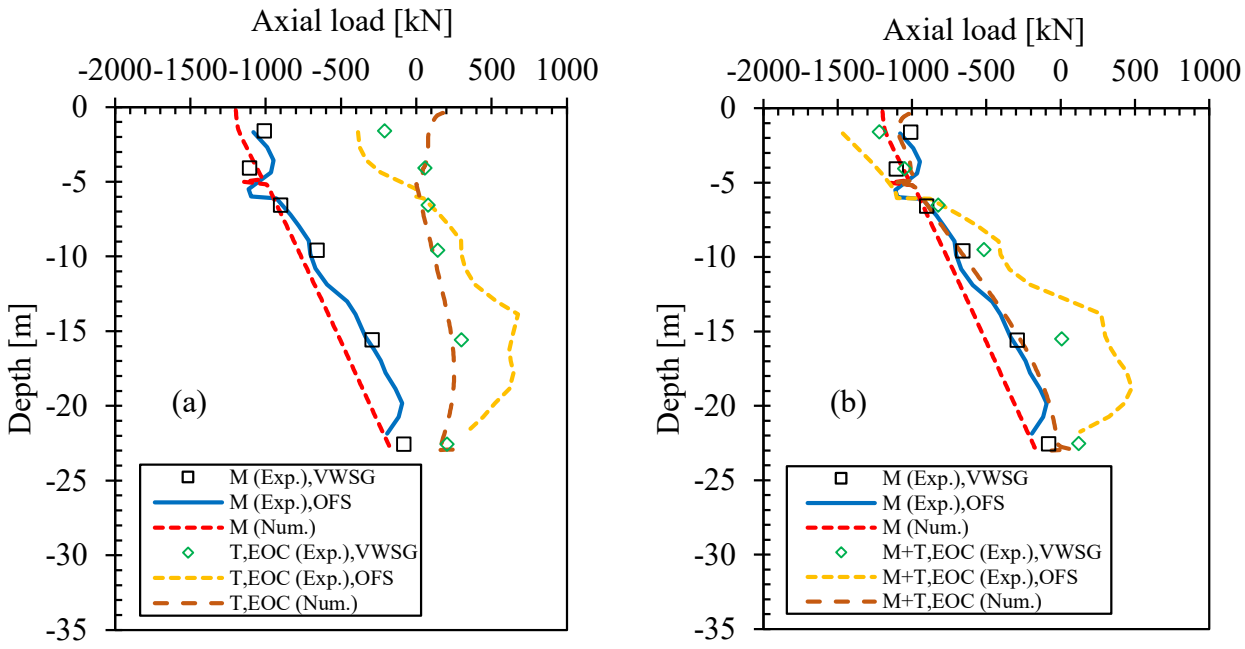

Figure 3.21. Axial load profiles (a) thermal (T) and (b) thermo-mechanical (M+T) at the end of cooling (EOC) for the London energy pile (base case)

During heating, the axial compressive loads were generated due to thermal load (T) in a similar way to the mechanical load, as shown in Figure 3.22(a). The maximum simulated value of -436 kN (about 36% of the applied M of -1200 kN), located at about the mid-depth of the pile, was

obtained at the end of heating (ΔT≈+11°C). From the field test data, the corresponding values were -930 kN using vibrating strain gauge (VWSG) and -853 kN optical fiber sensor (OFS), located at about -6 m. These values are twice greater than the simulated value and close to the theoretical value of the thermally induced load in case of the fully restrained body of -889 kN. In the author's opinion, the fully restrained condition at this location is unlikely to occur. Nonetheless, the spike in the axial loads in this location may be because of an abrupt change in the pile diameter from 0.61 m to 0.55 m at -5 m, leading to stress concentration and therefore higher loads. In the bottom half of the pile, however, the thermally induced load profile from the simulation closely followed the one from the field test. These thermally induced compressive loads due to the temperature increase were added to the mechanically induced ones (M+T, EOH) as shown in Figure 3.22(b) in which the maximum simulated value of -1567 kN located at -5 m was obtained. Comparing with this value with the maximum measured value of -1956 kN, the numerical model considerably under-predicted the combined thermo-mechanical load (by about 23%). The axial load profiles from both simulation and experiment agreed quite well along the bottom part of the pile.

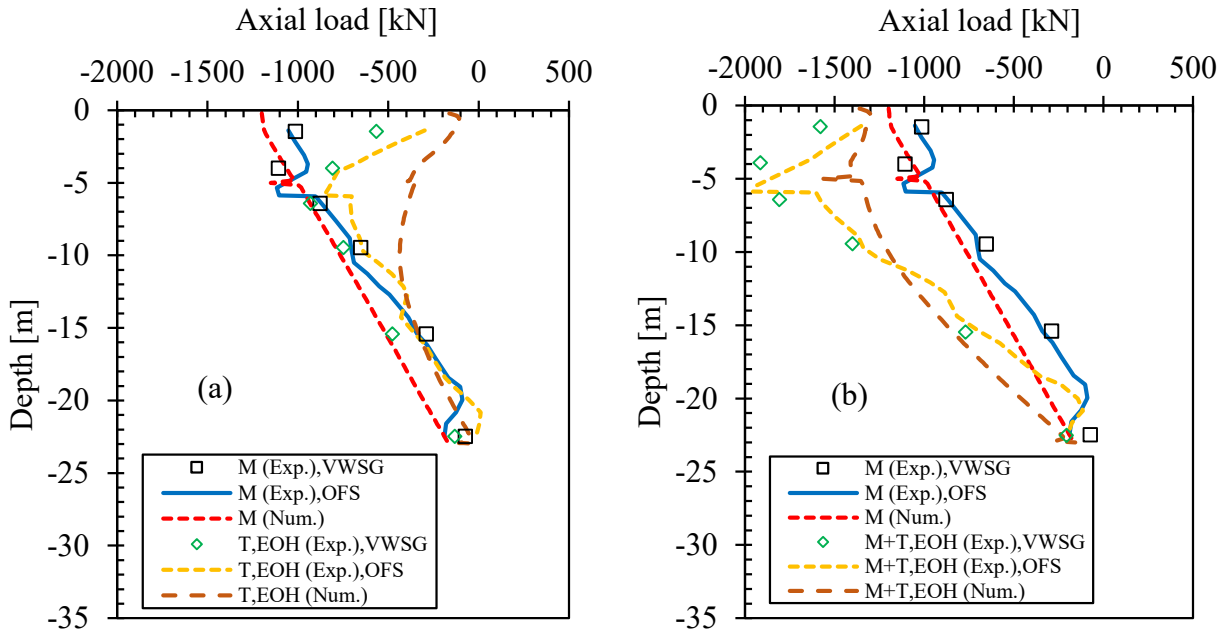

Figure 3.22. Axial load profiles (a) thermal (T) and (b) thermo-mechanical (M+T) at the end of heating (EOH) for the London energy pile (base case)

Lausanne energy pile:

The thermally induced axial load profiles for the Lausanne energy pile Test 1 are given in Figure 3.23. Along the upper half of the pile, the numerical results agreed well with the experimental data taken from Amatya et al. (2012) at the EOH (T, EOH). In the lower part, the model significantly over-predicted the axial loads. The maximum predicted thermally induced load was -3316 kN for ΔT=+21°C located at -22 m in comparison with the measured value of -2112 kN. As previously mentioned, this may be due to the assumption that there was no stiffness reduction of the sandstone bedrock right underneath the pile toe in the model. In the field, however, this stiffness may be less because of the imperfection of borehole base cleaning before the concrete was poured. At the end of cooling, the axial load profile moved back close to the initial position before the beginning of heating. Note that the axial load profile from the field test at the end of

cooling (EOC) was not provided in the literature. Therefore, only the simulated load profile at the EOC was shown in the figure.

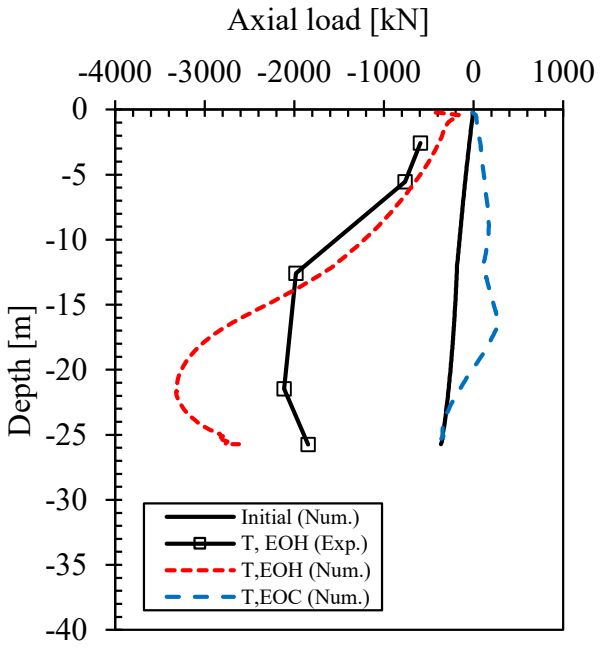

Figure 3.23. Axial load profiles at the end of heating (EOH) and at the end of cooling (EOC) for the Lausanne energy pile: Test 1 (base case)

In Test 7, the pile was subjected to a combination of the thermal and mechanical loads (M+T) as shown in Figure 3.24 and Figure 3.25. When the pile was heated, it tried to expand. The pile expansions, however, were restricted by the surrounding soils along the pile shaft and at the pile toe causing the increase in axial loads in the pile as shown in Figure 3.24(a). From the numerical analysis, a change in temperature in the pile (ΔT=+18ºC at the EOH) could generate the thermally induced compressive load up to -2842 kN (about 120% or 2.2 times of the applied M of -1300 kN). This thermally induced compression was then added to the mechanical load, resulting in the maximum thermo-mechanically induced axial load of -3376 kN as shown in Figure 3.24(b). This is slightly less than the measured value of -3594 kN (by 6.5 %). Since the unrestrained head condition was used for the pile in the base case analysis, there was little to none thermally induced

load at the pile head. This is the reason why the simulated load profile did not agree with the measured one along the upper part of the pile. In reality, however, the pile was underneath the structure which implies that the pile head was not free to move. In other words, the pile head was in a partially restrained condition. At the EOC, the pile was cooled down to almost the same temperature as the initial condition. Therefore, there was little change in the axial load of the pile as shown in Figure 3.25.

Table 3.8 provides a summary of the simulated thermally induced loads in the pile at the end of heating at the end of cooling for both London energy pile and Lausanne energy pile Test 7.

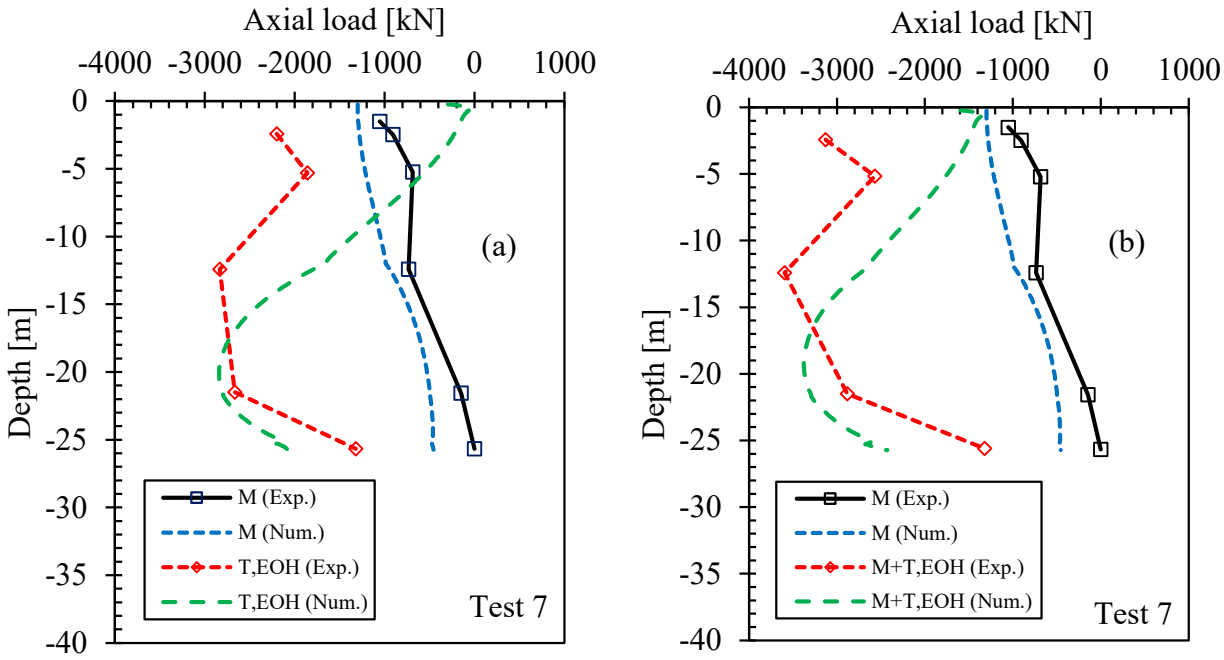

Figure 3.24. Axial load profiles (a) thermal (T) and (b) thermo-mechanical (M+T) at the end of heating (EOH) for the Lausanne energy pile: Test 7 (base case)

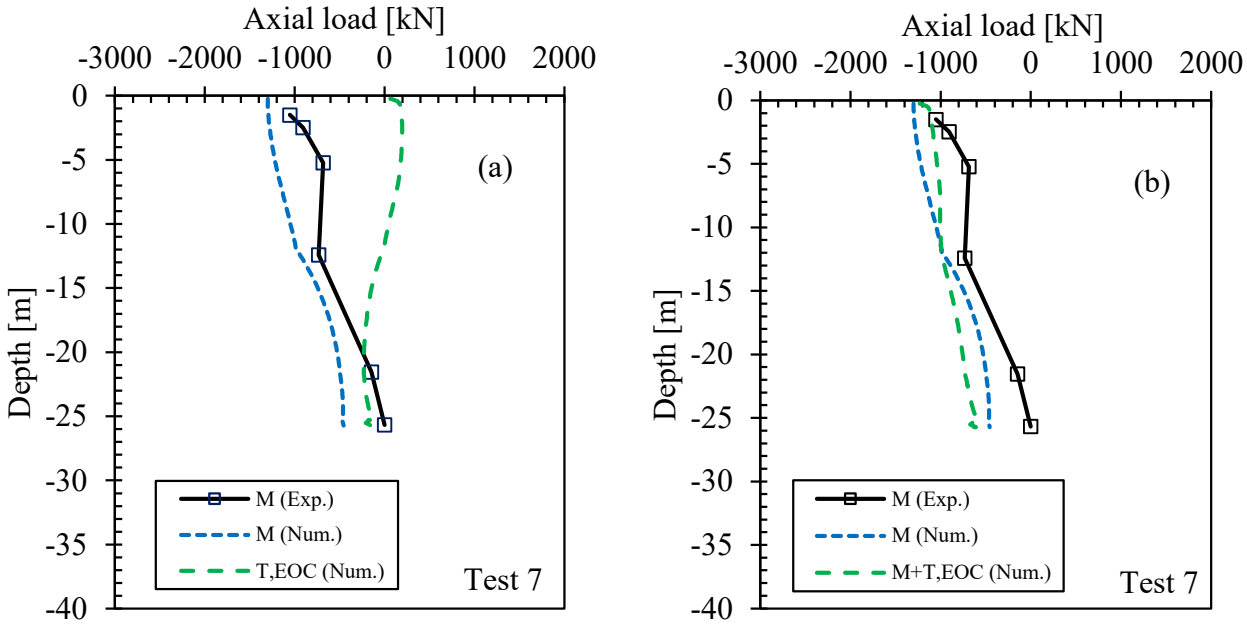

Figure 3.25. Axial load profiles (a) thermal (T) and (b) thermo-mechanical (M+T) at the end of cooling (EOC) for the Lausanne energy pile: Test 7 (base case)

Table 3.8. Summary of thermally and thermo-mechanically induced loads in the pile for energy pile case studies: London energy pile and Lausanne energy pile Test 7

Energy pile names	Applied mech. load (M)	Initial temp.	Range of applied temp.	Temp. change from init. value	Max. axial load in the pile due to thermal load (T)			Max. axial load in the pile due to thermo-mech. loads (M+T)		Remark
	[kN]	[ºC]	[ºC]	[ºC]	[kN]	[kN/ºC]	[% M]	[kN]	[% M]	
London energy pile (D=0.55 m and L=23 m)										
At the EOC	-1200	19.5	0.88 to 30.5	-18.6	251.63	13.53	20.97	-1130.26	-94.19	31-day cooling first, then 12-day heating
At the EOH	-1200	19.5	0.88 to 30.5	11	-435.85	-39.62	-36.32	-1566.97	-130.58	
Lausanne energy pile (Test 7) (D=1.0 m and L=25.8 m)										
At the EOH	-1300	13	15 to 31	18	-2841.81	-157.88	-218.60	-3375.54	-259.66	22-day heating first, then 6-day cooling
At the EOC	-1300	13	15 to 31	2	-232.37	-116.19	-17.87	-1233.17	-94.86	

M = mechanical load, T = thermal load, and M+T = thermo-mechanical load

EOH = end of heating, EOC = end of cooling

3.4.5. Mobilized Shaft Friction

London energy pile:

Energy piles cannot freely expand or contract when heated or cooled due in part to shaft friction developed along the pile-soil interface. Figure 3.26(a) and Figure 3.26(b) show the mobilized shaft friction induced by the M and the M+T at the EOC and the EOH for the London energy pile. The M generated all positive shaft friction (acting upwards) with the maximum value of 31 kPa. This value is comparable to the measured values of 50 kPa from vibrating wire strain gauge (VWSG) and 35 kPa from optical fiber sensors (OFS) given in (Bourne-Webb et al., 2009). At the EOC, the mobilized shaft friction increased in the upper two-third of the pile above the neutral plane (NP) at above -18 m. The maximum simulated value of 49 kPa comparing with the maximum experimental values of 61 kPa (VWSG) and 75 kPa (OFS). Below the NP, the shaft friction values reduced and may become negative. At the EOH, the mobilized shaft friction reduced in the top part (about the NP at -9 m), reaching -24 kPa (acting downwards) developing negative shaft friction. In about the bottom half below the NP, however, there was an increase in the mobilized shaft friction, reaching a maximum value of 52 kPa. Even though the numerically predicted values did not exactly match the measured values, the numerical models provided similar trends of the mobilized shaft friction. Note that the field mobilized shaft friction profiles at the EOC and at the EOH shown in the figures were obtained by extrapolation from the pile load tests (see Bourne-Webb et al., 2009 and Amatya et al., 2012).

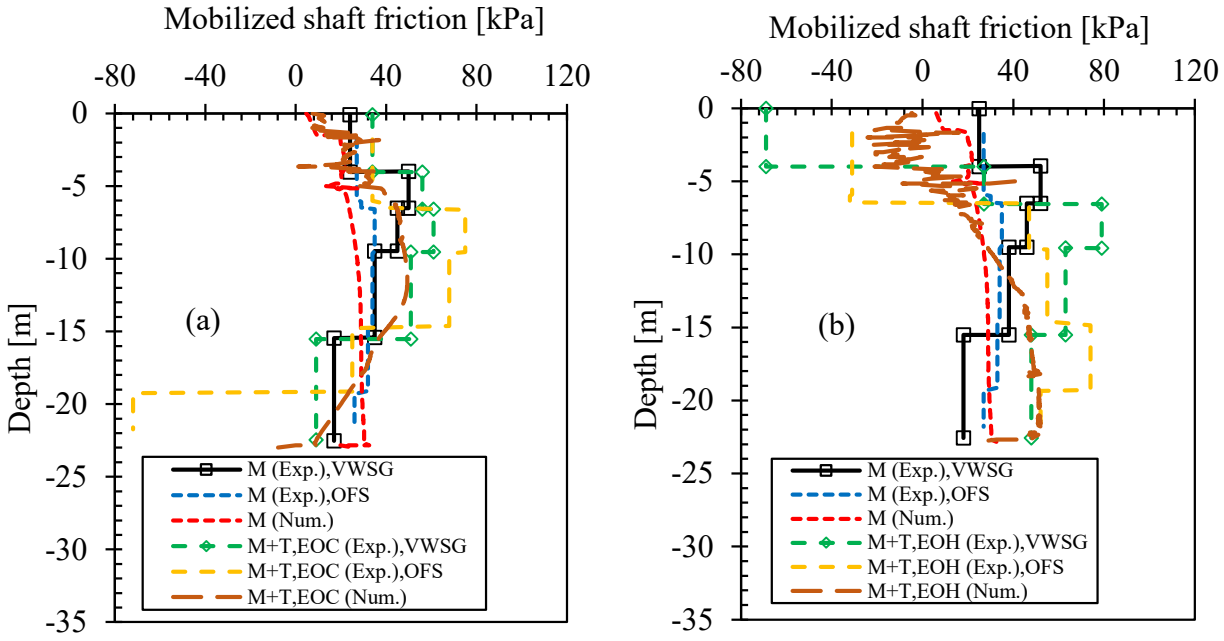

Figure 3.26. Mobilized shaft friction along the pile length (a) at the end of cooling (EOC) and (b) at the end of heating (EOH) for the London energy pile (base case)

Lausanne energy pile:

Figure 3.27 shows the mobilized shaft friction at the EOH and the EOC in Test 1. There was only the measured shaft friction at the EOH available in the literature (Amatya et al., 2012). As seen in the graph, the measured and simulated profiles at the EOH were comparable, and the maximum predicted negative shaft friction of -70 kPa was induced in the top part of the pile in comparison with -49 kPa from the field measurement. The opposite is true for the bottom part with the numerical shaft friction of up to 92 kPa in the soil layers and about 470 kPa in the sandstone layer. As can be seen in the graph, the shaft friction mobilized in the sandstone bedrock was much higher than in the overburden soils. Note that the measured shaft friction was only available in the soil layers with the value of 21 kPa at the EOH. At the EOC, the shaft friction profile moved back to about its initial position before the heating started.

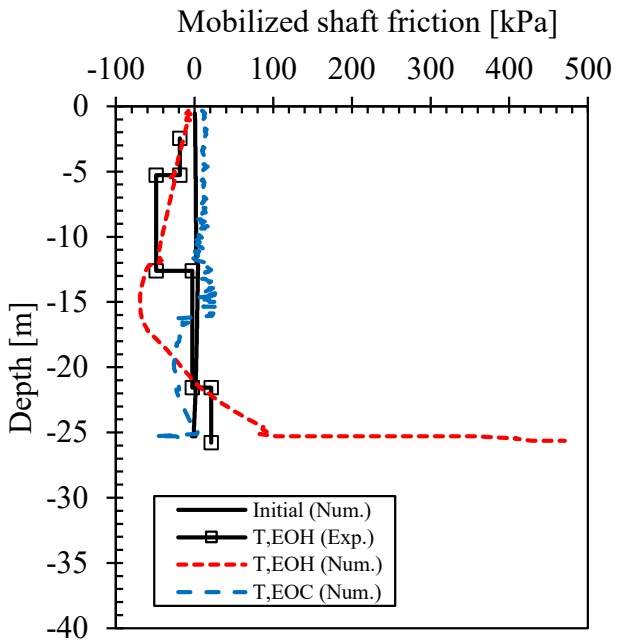

Figure 3.27. Mobilized shaft friction along the pile length at the end of heating (EOH) and at the end of cooling (EOC) for the Lausanne energy pile: Test 1 (base case)

Like in Test 1, only the measured data of shaft friction at the EOH was reported in the literature. As seen in Figure 3.28(a), under the mechanical loading (M) alone, the positive shaft friction was mobilized along the entire pile length with maximum values of 33 kPa in the soil layers and also about 33 kPa in the sandstone layer. At the EOH, the negative shaft friction developed in the upper part of the pile above the neutral plane (NP) at about -20 m (-51 kPa max.) and higher positive shaft friction developed in the lower part below the NP, especially near the pile toe with maximum values of 99 kPa in the soil and about 422 kPa in the sandstone layer. Again, as seen in the graph, the shaft friction mobilized along the pile-soil interface in the sandstone bedrock was much higher than in the overburden soils. Numerical and experimental values generally showed a good agreement. At the EOC, as shown in Figure 3.28(b), the shaft friction profile reduced back close to the position before heating began. This makes sense because the temperature change at the end of cooling was only 2ºC higher than the initial pile temperature.

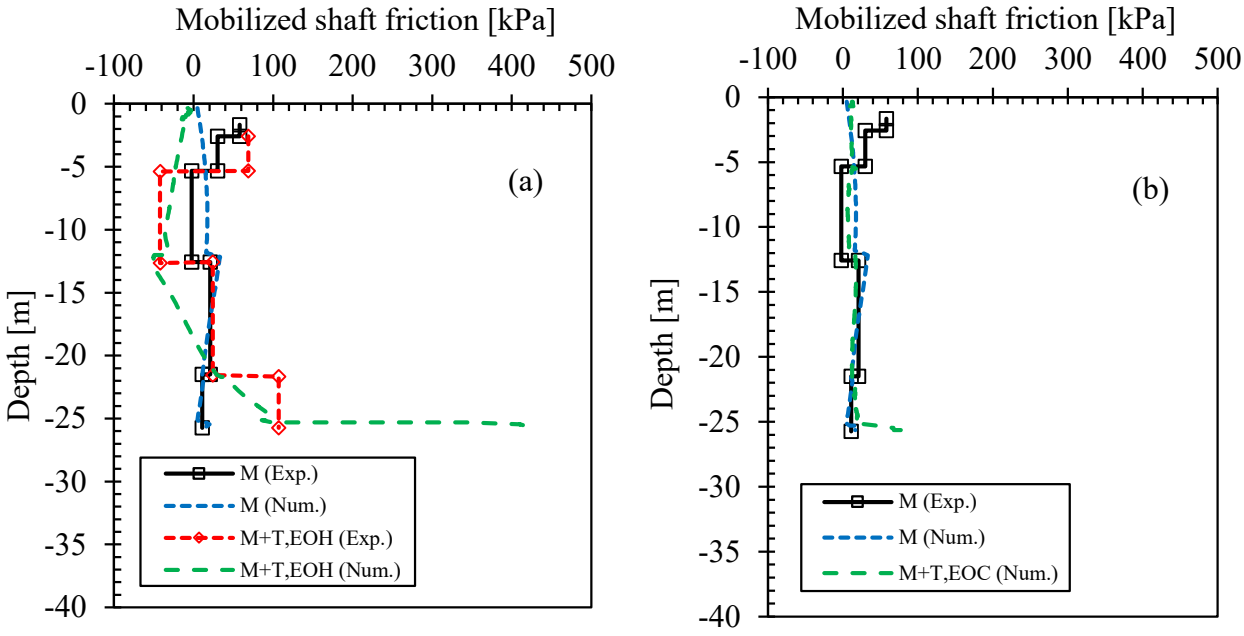

Figure 3.28. Mobilized shaft friction along the pile length (a) at the end of heating (EOH) and (b) at the end of cooling (EOC) for the Lausanne energy pile: Test 7 (base case)

3.4.6. Mobilized Effective Radial Stress

London energy pile:

Figure 3.29 shows the mobilized effective radial (normal) stresses along the pile length. In general, heating the pile increased the effective radial stresses at the pile-soil interface along the whole pile length. The higher increases in values were noticed above -5 m where no thermally induced excess pore pressures were generated. Cooling caused a reduction in effective radial stresses in the lower one-third of the pile from the pile toe, but surprisingly an increase in the upper two-third was prevalent which may be due to the stress redistributions to somewhat compensate the reduction in stresses at the lower part of the pile and at the pile toe at the end of cooling. The change in effective radial stresses could be caused by a change in a lateral soil pressure coefficient (K) due to relative thermal expansions or contractions of the pile and the surrounding soils. The K values generally

increased upon heating the pile-soil system and reduced upon cooling as reported in Gunawan, Ng, & Liu (2017). This makes sense because when the pile was heated it expanded and laterally pressed against the surrounding soils, producing K values and therefore higher radial effective stresses. The opposite happened during cooling. Another cause of the effective stress change was the generation of excess porewater pressures in the saturated clay during heating and cooling.

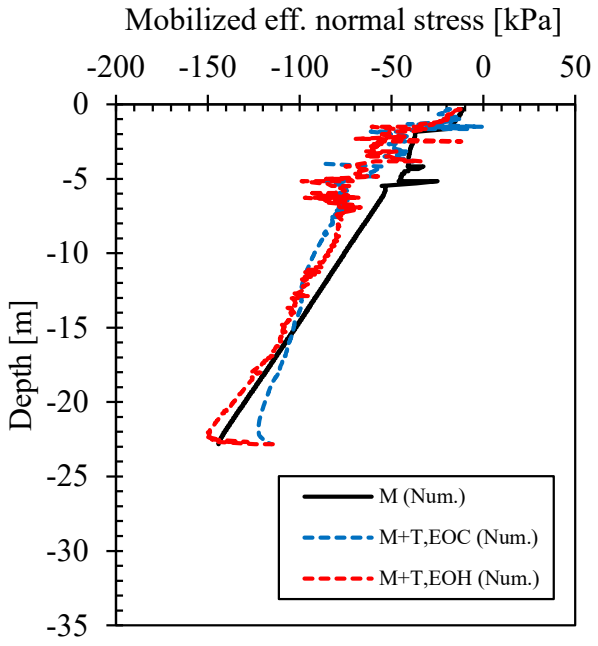

Figure 3.29. Mobilized effective radial (normal) stress at the pile-soil interface along the pile length at the end of cooling (EOC) and at the end of heating (EOH) for the London energy pile (base case)

Lausanne energy pile:

In Test 7, the radial stress profiles at the end of heating (EOH) and at the end of cooling (EOC) are provided in Figure 3.30. Like in the case of the London energy test pile, heating increased the effective radial stresses along the pile length. The increases in radial effective stresses in the sandstone layer near the pile toe were significant. This was because the sandstone has much higher stiffness value than the overlying soils and also a lower thermal expansion coefficient in

comparison with the concrete pile at this test site. When the system was cooled down back to about its initial temperature at the end of cooling, the effective radial stress profile also moved back to about its initial position.

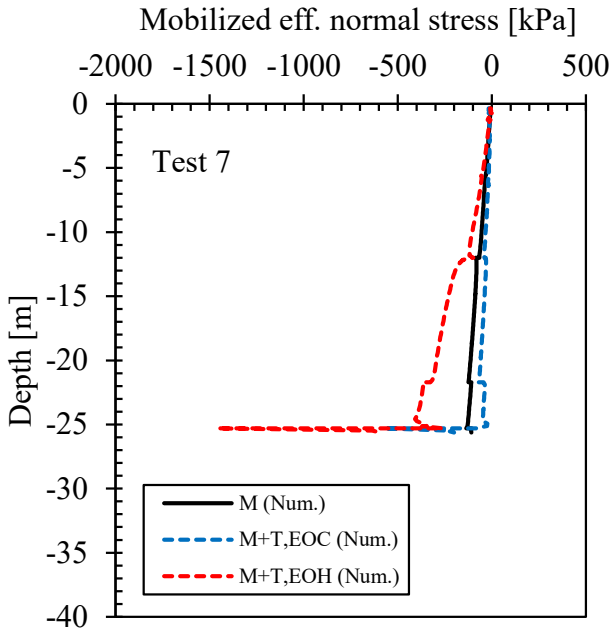

Figure 3.30. Mobilized effective radial (normal) stress at the pile-soil interface along the pile length at the end of heating (EOH) and at the end of cooling (EOC) for the Lausanne energy pile: Test 7 (base case)

3.5. Sensitivity Analyses for the Energy Case Studies

For the London energy pile, sensitivity analyses were carried out for the following five parameters: change in the coefficient of thermal expansion of concrete (CTEc), change in the coefficient of thermal expansion of soil (CTEs), change in the stiffness of soil (Es), change in the thermal conductivity of soil (TCs), and change in the specific heat capacity of soil (SHCs). Table 3.9 provides a summary of changes in model parameters in comparison with the base case parameters for the London energy pile.

Table 3.9. Summary of changes in model parameters for sensitivity analyses (London energy pile)

Model parameters	Decreased		Base case	Increased		Unit
1. Linear thermal expansion coefficient	-	-	CTEc	1.2 CTEc	1.4 CTEc	
of concrete (CTEc)	-	-	8.5	10	12	x10^{-6}[1/°C]
2. Linear thermal expan. coef. of soil (CTEs)	-	0.25 CTEs	CTEs	4 CTEs	-	
Made ground	-	1.25	5	20	-	x10^{-6}[1/°C]
Sandy gravel	-	1.25	5	20	-	x10^{-6}[1/°C]
London clay	-	1.25	5	20	-	x10^{-6}[1/°C]
3. Stiffness of soil (Es)	-	0.5 Es	Es	2 Es	-	
Made ground	-	9.9	19.8	39.6	-	[MPa]
Sandy gravel	-	38.5	77	154	-	[MPa]
London clay	-	19.25	38.5	77	-	[MPa]
4. Thermal conductivity of soil (TCs)	0.25 TCs	-	TCs	-	4 TCs	
Made ground	0.5	-	2	-	8	x10^{-3}[kW/m/°C]
Sandy gravel	0.5	-	2	-	8	x10^{-3}[kW/m/°C]
London clay	0.375	-	1.5	-	6	x10^{-3}[kW/m/°C]
5. Specific heat capacity of soil (SHCs)	0.25 SHCs	-	SHCs	2 SHCs	-	
Made ground	300	-	1200	2400	-	[kJ/t/°C]
Sandy gravel	300	-	1200	2400	-	[kJ/t/°C]
London clay	375	-	1500	3000	-	[kJ/t/°C]

For the Lausanne energy pile, Test 7, six parameters were considered: change in CTEc, change in CTEs, change in Es, change in TCs, change in SHCs, and change in head restrained

conditions of the pile (HRC). The head restrained conditions range from the unrestrained head (URH) which the pile head was free to move, the fixed or fully restrained head (FRH), and partially restrained heads (PRH). Table 3.10 gives a summary of changes in model parameters that were made for the sensitivity analyses for the Lausanne energy pile.

Table 3.10. Summary of changes in model parameters for sensitivity analyses (Lausanne energy pile)

Model parameters	Decreased	Base case	Increased			Unit
1. Linear thermal expansion coefficient	0.85 CTEc	CTEc	1.2 CTEc	-	-	
of concrete (CTEc)	8.5	10	12	-	-	x10^{-6}[1/°C]
2. Linear thermal expan. coef. of soil	0.25 CTEs	CTEs	6 CTEs	-	-	
Alluvial soil (A1)	0.83	3.33	19.98	-	-	x10^{-6}[1/°C]
Alluvial soil (A2)	0.83	3.33	19.98	-	-	x10^{-6}[1/°C]
Sandy-gravelly moraine (till)	0.83	3.33	19.98	-	-	x10^{-6}[1/°C]
Bottom moraine	0.83	3.33	19.98	-	-	x10^{-6}[1/°C]
Molasse (sandstone)	0.58	2.30	13.80	-	-	x10^{-6}[1/°C]
3. Stiffness of soil (Es)	0.5 Es	Es	2 Es	-	-	
Alluvial soil (A1)	71.5	143	286	-	-	[MPa]
Alluvial soil (A2)	71.5	143	286	-	-	[MPa]
Sandy-gravelly moraine (till)	123.75	247.5	495	-	-	[MPa]
Bottom moraine	173.25	346.5	693	-	-	[MPa]
Molasse (sandstone)	1500	3000	6000	-	-	[MPa]
4. Thermal conductivity of soil (TCs)	0.25 TCs	TCs	4 TCs	-	-	
Alluvial soil (A1)	0.45	1.8	7.2	-	-	x10^{-3}[kW/m/°C]
Alluvial soil (A2)	0.45	1.8	7.2	-	-	x10^{-3}[kW/m/°C]
Sandy-gravelly moraine (till)	0.45	1.8	7.2	-	-	x10^{-3}[kW/m/°C]
Bottom moraine	0.45	1.8	7.2	-	-	x10^{-3}[kW/m/°C]
Molasse (sandstone)	0.275	1.1	4.4	-	-	x10^{-3}[kW/m/°C]
5. Specific capacity of soil (SHCs)	0.5 SHCs	SHCs	2 SHCs	-	-	
Alluvial soil (A1)	600	1200	2400	-	-	[kJ/t/°C]
Alluvial soil (A2)	615.5	1231	2462	-	-	[kJ/t/°C]
Sandy-gravelly moraine (till)	600	1200	2400	-	-	[kJ/t/°C]
Bottom moraine	545.5	1091	2182	-	-	[kJ/t/°C]
Molasse (sandstone)	392	784	1568	-	-	[kJ/t/°C]
6. Head restrained condtions of the pile (HRC)		URH	PRH	PRH	FRH	
Axial stiffness (EA) of the spring		n/a	100	200	n/a	[MN]

As shown in Table 3.9 and Table 3.10, the model parameters were either increased or reduced from the base case values in order to investigate their sensitivity on the numerical results. Note that, in the sensitivity analyses for London and Lausanne energy piles, the model parameters were not increased and reduced in the same amounts or percentages from the base case values. These were done on purpose in order to cover the typical ranges (minimum to maximum values) of each material parameter generally reported in the literature (see Appendix I which provides the typical properties of geomaterials related to this thesis).

3.5.1. Change in Coefficient of Thermal Expansion of Concrete (CTEc)

London energy pile:

In the London energy pile case, the actual coefficient of thermal expansion of concrete (CTEc) reported in Bourne-Webb et al. (2009) is 8.5×10^{-6} (1/°C), 1.7 times higher than the coefficient of thermal expansion of soil (CTEs), which was used for the base case analysis. The value was increased by 18% and 41% to 10×10^{-6} (1/°C) and 12×10^{-6} (1/°C), twice and 2.4 times higher than the coefficient of thermal expansion of soil (CTEs), accordingly.

At the end of cooling, higher CTEc values induced marginally larger settlements (Figure 3.31(a)). There was about a 41% increase in a maximum thermally induced tensile (T, EOC) load when the CTEc rose by 41% (Figure 3.32 (a)). Even though a maximum thermo-mechanically induced (M+T, EOC) compressive load remained unchanged, there was a rise of tensile load by nearly 78% near the pile toe (Figure 3.32(b)). At the end of heating, a maximum tensile load due to the thermal load (T, EOH) only increased by 15% (Figure 3.33(a)). The compressive load due to the combined effects of thermal and mechanical loads (M+T, EOH) were unaffected (Figure 3.33(b)). Table 3.11 provides a summary of the numerical results in terms of settlements and uplifts of the pile head and axial loads in the pile. The results from analyses using other CTEc values were

compared with the results from the base case analysis. Other outputs such as shaft friction and effective radial stress profiles mobilized along the pile-soil interface at the end of cooling and heating can also be found in Appendix A.1.

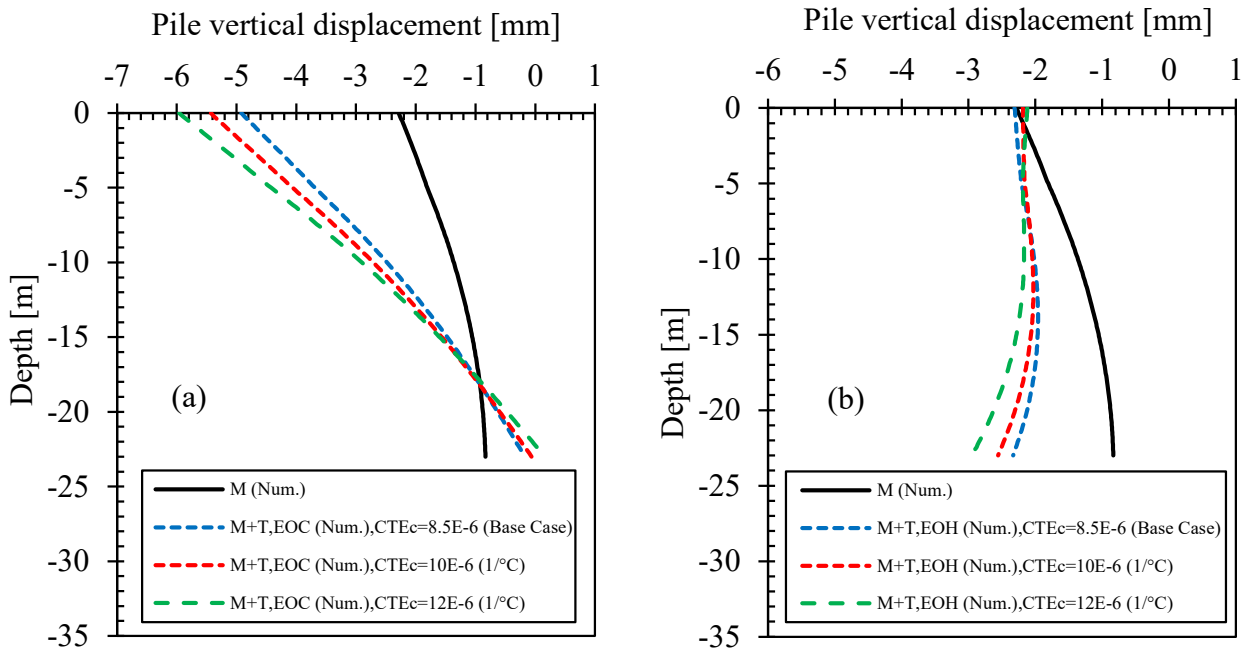

Figure 3.31. Pile vertical displacement profiles along its length (a) at the end of cooling (EOC) and (b) at the end of heating (EOH) for the London energy pile (change in CTEc)

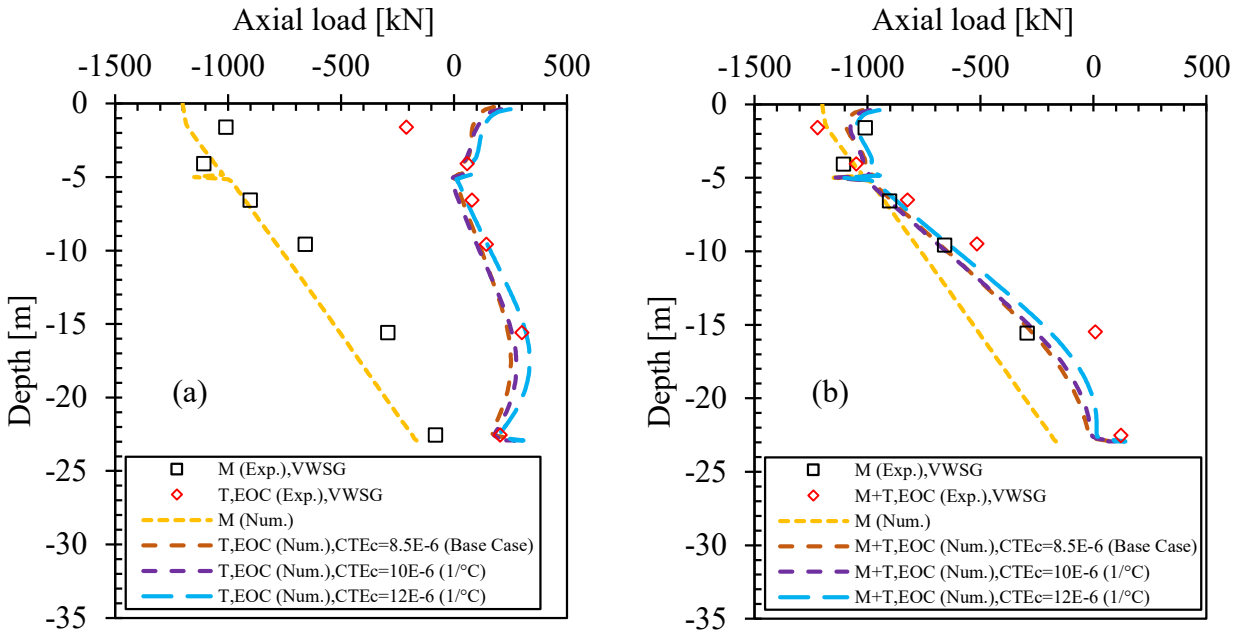

Figure 3.32. Axial load profiles (a) thermal (T) and (b) thermo-mechanical (M+T) at the end of heating (EOH) for the London energy pile (change in CTEc)

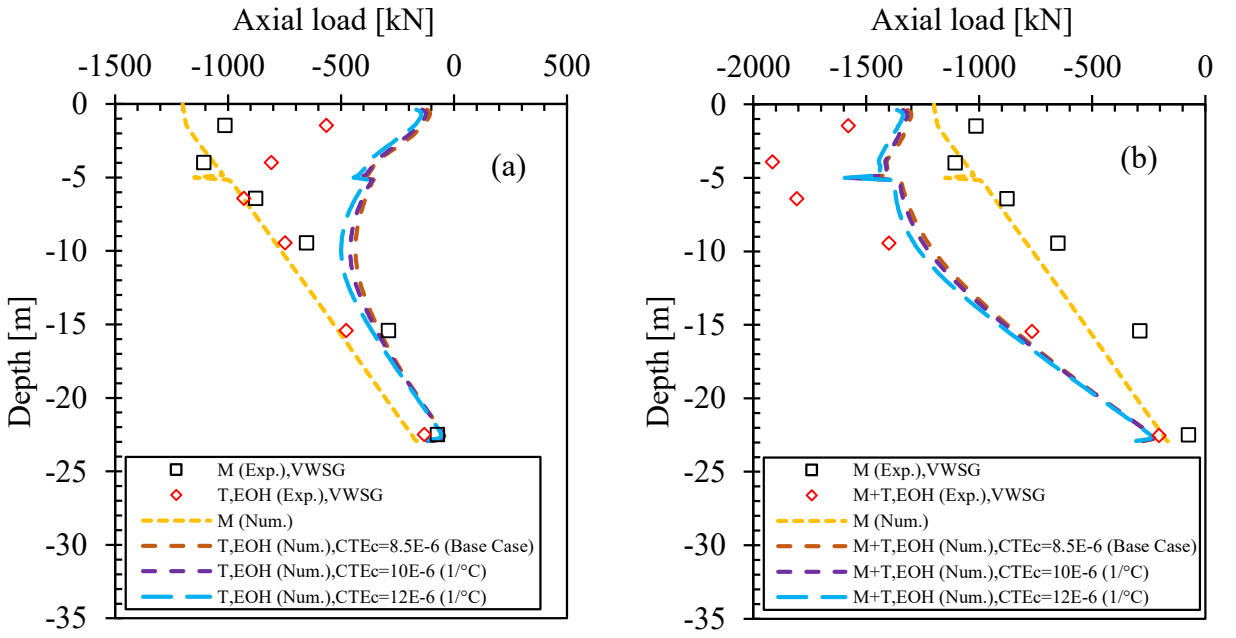

Figure 3.33. Axial load profiles (a) thermal (T) and (b) thermo-mechanical (M+T) at the end of heating (EOH) for the London energy pile (change in CTEc)

Table 3.11. Results from numerical analyses with varied CTEc values (London energy pile)

Description	Change in CTEc (Base case)			Unit	Remark
Linear thermal expansion coef.	8.5	10	12	$x10^{-6}$[1/°C]	
of concrete (CTEc)	= CTEc	=1.18 CTEc	=1.42 CTEc		
	-	18	41	[%]	Change from base case
M (max.)	-1200	-1200	-1200	[kN]	At the pile head
T, EOC					
Axial compressive load (max)		-18.43		[kN]	
	-			[%]	Change from base case
Axial tensile load (max)	251.63	276.21	355.01	[kN]	
	-	9.77	41.08	[%]	Change from base case
M+T, EOC					
Pile head settlement	-5.06	-5.45	-5.97	[mm]	
	-	7.71	17.98	[%]	Change from base case
Axial compressive load (max)	-1130.26	-1148.71	-1111.62	[kN]	
	-	1.63	-1.65	[%]	Change from base case
Axial tensile load (max)	8.37	22.90	47.17	[kN]	
	-	173.60	463.56	[%]	Change from base case
T, EOH					
Axial compressive load (max)	-435.85	-458.89	-499.17	[kN]	
	-	5.29	14.53	[%]	Change from base case
Axial tensile load (max)				[kN]	
				[%]	Change from base case
M+T, EOH					
Pile head uplift	-2.31	-2.18	-2.12	[mm]	
	-	5.63	8.23	[%]	Change from base case
Axial compressive load (max)	-1566.97	-1572.61	-1594.79	[kN]	
	-	0.36	1.78	[%]	Change from base case
Axial tensile load (max)				[kN]	
				[%]	Change from base case

M = mechanical load
T, EOC = thermally induced at the end of cooling
M+T, EOC = thermo-mechanically induced at end of cooling
T, EOH = thermally induced at the end of heating
M+T, EOH = thermo-mechanically induced at end of heating

Lausanne energy pile:

In Tests 7, the CTEc was changed from the base case value of $10x10^{-6}$ (1/°C) to $8.5x10^{-6}$ (1/°C) and $12x10^{-6}$ (1/°C), 15% decrease and 20% increase, accordingly. Similar to the observations in the London energy pile, higher CTEc produced marginally higher pile head uplifts at the EOH, increasing by 38% with the increase of 20% of CTEc value as shown in Figure 3.34. As shown in Figure 3.35(a) and Figure 3.35(b), the change in axial loads at the EOH occurred mostly in the bottom part of the pile. This was because the pile head was unrestrained. A 20% rise in a CTEc value led to an increase in thermally induced (T, EOH) compressive load of just about 18% and thermo-mechanically (M+T, EOH) induced compressive load of 15%. At the EOC, as summarized in Table 3.12, the axial load profiles mobilized during cooling with various CTEc values for the Lausanne energy pile Test 7 can be found in Appendix B.1.

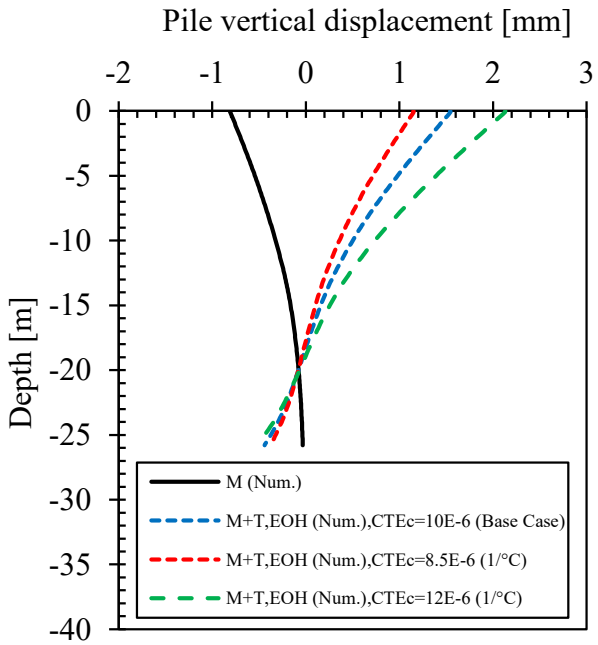

Figure 3.34. Pile vertical displacement profiles along its length at the end of heating (EOH) for the London energy pile (change in CTEc)

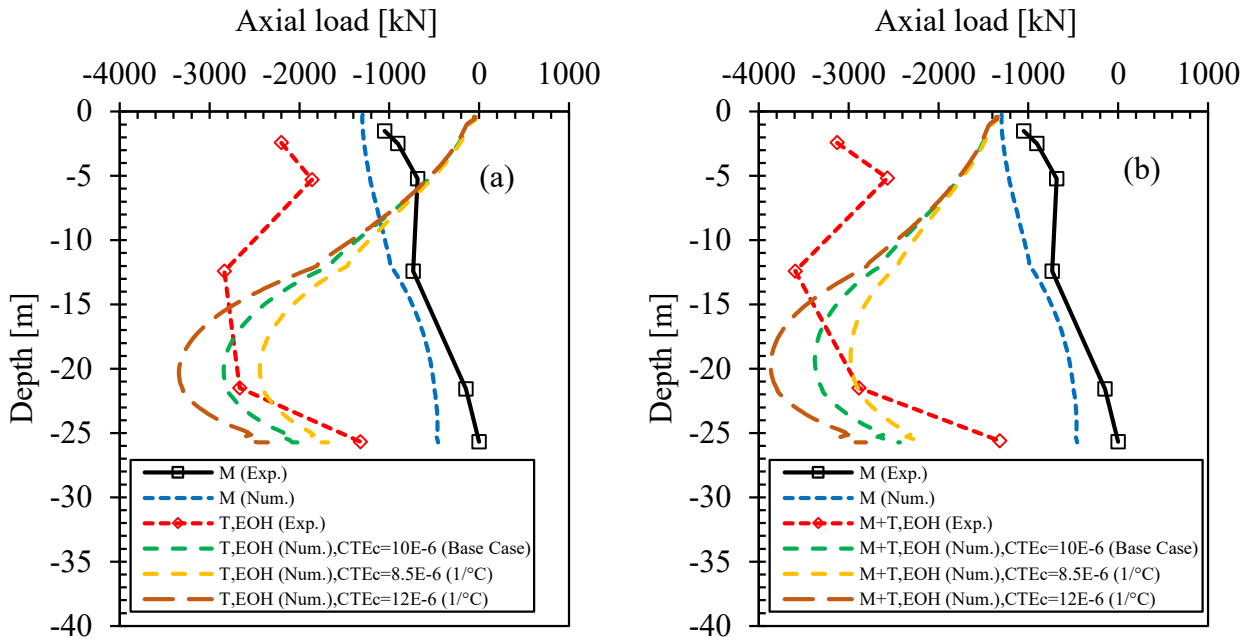

Figure 3.35. Axial load profiles (a) thermal (T) and (b) thermo-mechanical (M+T) at the end of heating (EOH) for the London energy pile (change in CTEc)

Table 3.12. Results from numerical analyses with varied CTEc values (Lausanne energy pile: Test 7)

Description	Change in CTEc	(Base case)		Unit	Remark
Linear thermal expansion coef.	8.5	10	12	$x10^{-6}$[1/°C]	
of concrete (CTEc)	= 0.85 CTEc	= CTEc	= 1.2 CTEc		
	-15	-	20	[%]	Change from base case
M (max.)	-1300	-1300	-1300	[kN]	At the pile head
T, EOH					
Axial compressive load (max)	-2439.91	-2841.81	-3340.77	[kN]	
	-14.14	-	17.56	[%]	Change from base case
Axial tensile load (max)				[kN]	
				[%]	Change from base case
M+T, EOH					
Pile head uplift	1.15	1.54	2.13	[mm]	
	-25.32	-	38.31	[%]	Change from base case
Axial compressive load (max)	-2978.48	-3375.54	-3867.19	[kN]	
	-11.76	-	14.57	[%]	Change from base case
Axial tensile load (max)				[kN]	
				[%]	Change from base case
T, EOC					
Axial compressive load (max)	-182.53	-232.37	-273.00	[kN]	
	-21.45	-	17.49	[%]	Change from base case
Axial tensile load (max)	146.21	195.03	243.97	[kN]	
	-25.03	-	25.09	[%]	Change from base case
M+T, EOC					
Pile head settlement	-0.32	-0.43	-0.48	[mm]	
	-25.58	-	11.63	[%]	Change from base case
Axial compressive load (max)	-1188.44	-1160.11	-1133.54	[kN]	
	2.44	-	-2.29	[%]	Change from base case
Axial tensile load (max)				[kN]	
				[%]	Change from base case

M = mechanical load
T, EOH = theramlly induced at the end of heating
M+T, EOH = thermo-mechanically induced at the end of heating
T, EOC = thermally induced at the end of cooling
M+T, EOC = thermo-mechanically induced at the end of cooling

3.5.2. Change in Coefficient of Thermal Expansion of Soil (CTEs)

London energy pile:

The coefficient of thermal expansion of soil (CTEs) of the base case was 5 x10^{-6} (1/°C). This value was reduced to 1.25 x10^{-6} (1/°C) and increased to 20x10^{-6} (1/°C), -75% and 300% changes from the base case value. These were about 0.15 to 2.35 times of thermal expansion of concrete (CTEc) which means that the soil skeleton was less and more expansive than concrete, respectively. As shown in Figure 3.36 and Figure 3.37, there were little changes in the maximum values of pile head settlements and also the maximum compressive axial loads in the pile during cooling. Table 3.13 gives a summary of important numerical results at the end of cooling and the end of heating. Other figures such as axial load profiles at the end of heating that are not given here can be found in Appendix A.2.

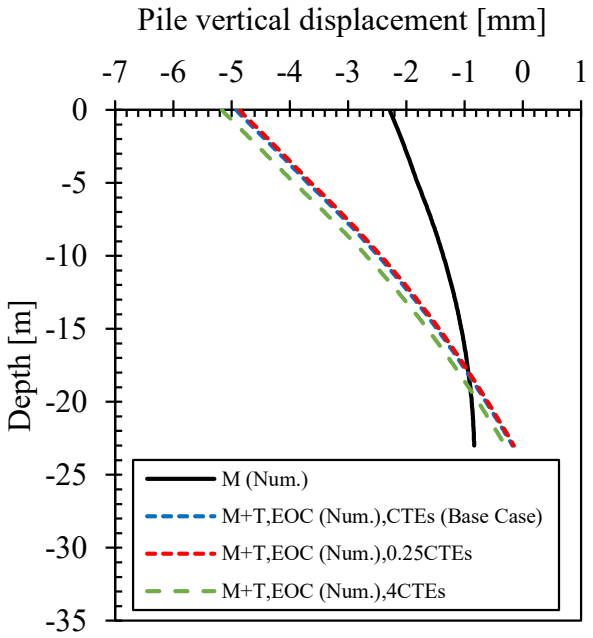

Figure 3.36. Pile vertical displacement profiles along its length at the end of cooling (EOC) for the London energy pile (change in CTEs)

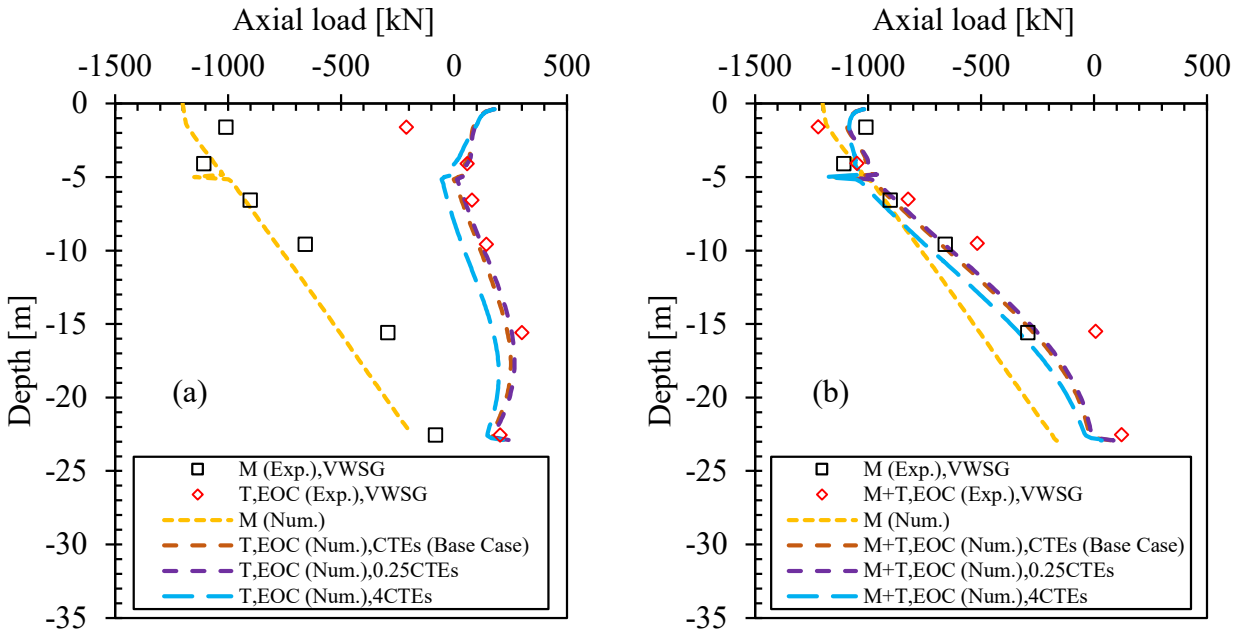

Figure 3.37. Axial load profiles (a) thermal (T) and (b) thermo-mechanical (M+T) at the end of heating (EOH) for the London energy pile (change in CTEs)

Table 3.13. Results from numerical analyses with varied CTEs values (London energy pile)

Description	Change in CTEs	(Base case)		Unit	Remark
Linear thermal expansion coef.	1.25	5	20	x10^{-6}[1/°C]	
of soil (CTEs)	= 0.25 CTEs	= CTEs	= 4 CTEs		
	-75	-	300	[%]	Change from base case
M (max.)	-1200	-1200	-1200	[kN]	At the pile head
T, EOC					
Axial compressive load (max)			-55.59	[kN]	
		-		[%]	
Axial tensile load (max)	267.99	251.63	230.17	[kN]	
	6.50	-	-8.53	[%]	Change from base case
M+T, EOC					
Pile head settlement	-4.87	-5.06	-5.08	[mm]	
	-3.75	-	0.40	[%]	Change from base case
Axial compressive load (max)	-1115.47	-1130.26	-1192.56	[kN]	
	-1.31	-	5.51	[%]	
Axial tensile load (max)	87.11	78.37	63.02	[kN]	
	11.15	-	-19.59	[%]	Change from base case
T, EOH					
Axial compressive load (max)	-432.61	-435.85	-358.91		
	-0.74	-	-17.65		
Axial tensile load (max)				[kN]	
				[%]	Change from base case
M+T, EOH					
Pile head uplift	-2.21	-2.31	-2.61	[mm]	
	4.33	-	-12.99	[%]	Change from base case
Axial compressive load (max)	-1576.35	-1566.97	-1509.03	[kN]	
	0.60	-	-3.70	[%]	
Axial tensile load (max)				[kN]	
				[%]	Change from base case

M = mechanical load
T, EOC = thermally induced at the end of cooling
M+T, EOC = thermo-mechanically induced at end of cooling
T, EOH = thermally induced at the end of heating
M+T, EOH = thermo-mechanically induced at end of heating

Lausanne energy pile:

In Test 7 of the Lausanne energy pile case, the thermal expansion coefficients of soils (CTEs) were reduced by 17% (-17%) and increased by 500% from the base case. The latter higher value was intentional in order to increase the CTEs to reach about the maximum value reported in the literature, and also to make the soil skeleton two times more expansive than the concrete. From the numerical results, as shown in Figure 3.38 and Figure 3.39, it can be said that the change in the CTEs values did not affect the pile responses during heating and cooling of the pile. Table 3.14 summarizes the numerical results with different values of the CTEs in terms of thermo-mechanically induced pile head displacements and axial loads. Other figures such as axial load profiles at the end of cooling and mobilized shaft friction profiles can be found in Appendix B.2.

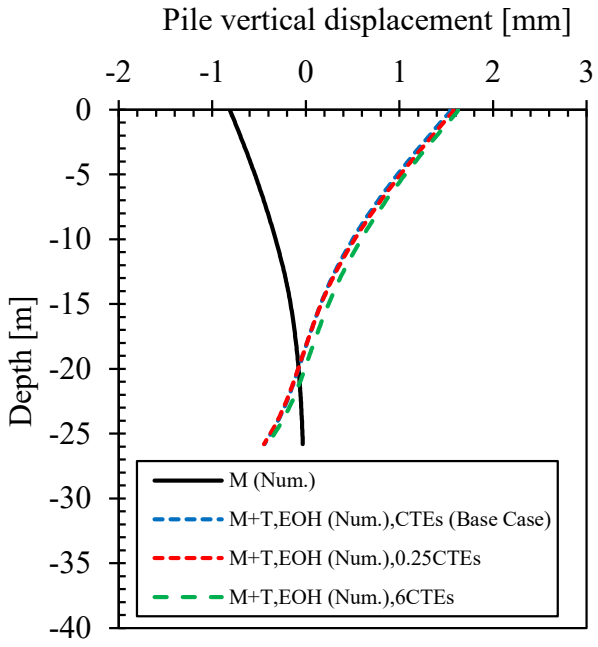

Figure 3.38. Pile vertical displacement profiles along its length at the end of heating (EOH) for the Lausanne energy pile (change in CTEs)

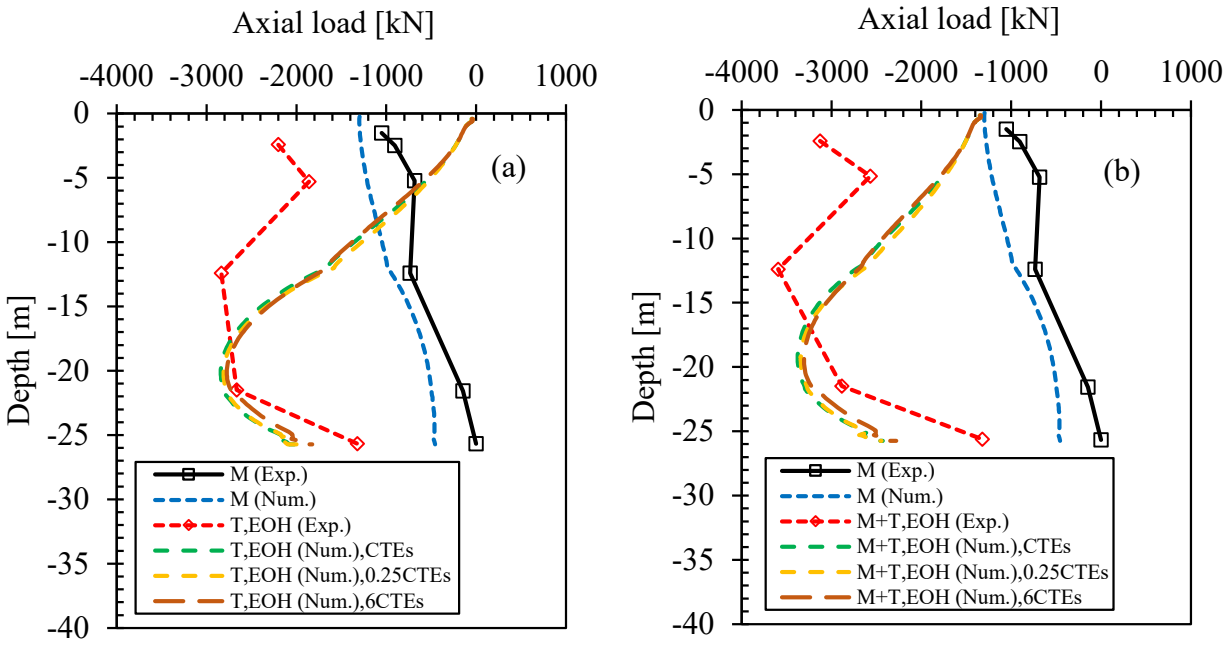

Figure 3.39. Axial load profiles (a) thermal (T) and (b) thermo-mechanical (M+T) at the end of heating (EOH) for the Lausanne energy pile (change in CTEs)

Table 3.14. Results from numerical analyses with varied CTEs values (Lausanne energy pile: Test 7)

Description	Change in CTEs	(Base case)		Unit	Remark
Linear thermal expansion coef. of concrete (CTEc)					
- Alluvial soil (A1)	0.83	3.33	19.98	x10^{-6}[1/°C]	
- Alluvial soil (A2)	0.83	3.33	19.98	x10^{-6}[1/°C]	
- Sandy-gravelly moraine	0.83	3.33	19.98	x10^{-6}[1/°C]	
- Bottom moraine	0.83	3.33	19.98	x10^{-6}[1/°C]	
- Sandstone (molasse)	0.58	2.33	13.8	x10^{-6}[1/°C]	
	= 0.25 CTEs	= CTEs	= 6 CTEs		
	-17	-	500	[%]	Change from base case
M (max.)	-1300	-1300	-1300	[kN]	At the pile head
T, EOH					
Axial compressive load (max)	-2810.71	-2841.81	-2774.70	[kN]	
	-1.09	-	-2.36	[%]	Change from base case
Axial tensile load (max)				[kN]	
				[%]	Change from base case
M+T, EOH					
Pile head uplift	1.58	1.54	1.62	[mm]	
	2.60	-	5.19	[%]	Change from base case
Axial comressive load (max)	-3342.69	-3375.54	-3306.63	[kN]	
	-0.97	-	-2.04	[%]	Change from base case
Axial tensile load (max)				[kN]	
				[%]	Change from base case
T, EOC					
Axial comressive load (max)	-238.73	-232.37	-177.52	[kN]	
	2.74		-23.60	[%]	Change from base case
Axial tensile load (max)	190.49	195.03	177.52	[kN]	
	-2.33	-	-8.98	[%]	Change from base case
M+T, EOC					
Pile head settlement	-0.43	-0.43	-0.39	[mm]	
	0.00	-	-9.30	[%]	Change from base case
Axial comressive load (max)	-1161.98	-1160.11	-1162.44	[kN]	
	0.16	-	0.20	[%]	Change from base case
Axial tensile load (max)				[kN]	
				[%]	Change from base case

M = mechanical load
T, EOH = theramlly induced at the end of heating
M+T, EOH = thermo-mechanically induced at the end of heating
T, EOC = thermally induced at the end of cooling
M+T, EOC = thermo-mechanically induced at the end of cooling

3.5.3. Change in Soil Stiffness (Es)

London energy pile:

To study the effects of soil stiffness on the pile responses, the values were reduced by 50% and increased by 100% from the base case values. Significant changes in numerical results were observed with changing soil stiffness values. As seen in Figure 3.40, lower soil stiffnesses produced larger pile head settlements under the mechanical load only (M) and also the thermo-mechanical load (M+T) during cooling. When the soil stiffnesses increased, the settlements reduced. Figure 3.41 shows the axial load profiles at the end of cooling with various values of soil stiffnesses. It shows that the thermally induced tensile load increased by 47% when the soil stiffness increased by 100% from the base value. Similarly, there was also a rise in the thermally induced compressive load of 45% at the end of heating as summarized in Table 3.15. These changes were more noticeable in the bottom half of the pile. Additional figures showing axial loads at the end of heating and mobilized shaft friction along the pile-soil interface were given in Appendix A.3.

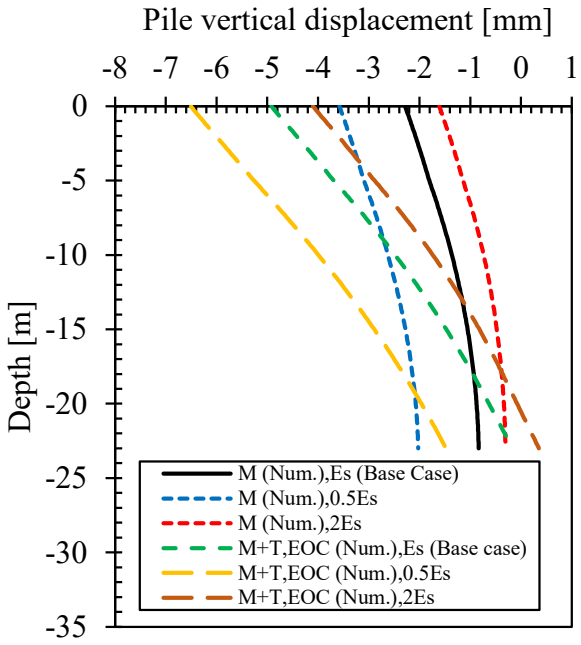

Figure 3.40. Pile vertical displacement profiles along its length at the end of cooling (EOC) for the London energy pile (change in Es)

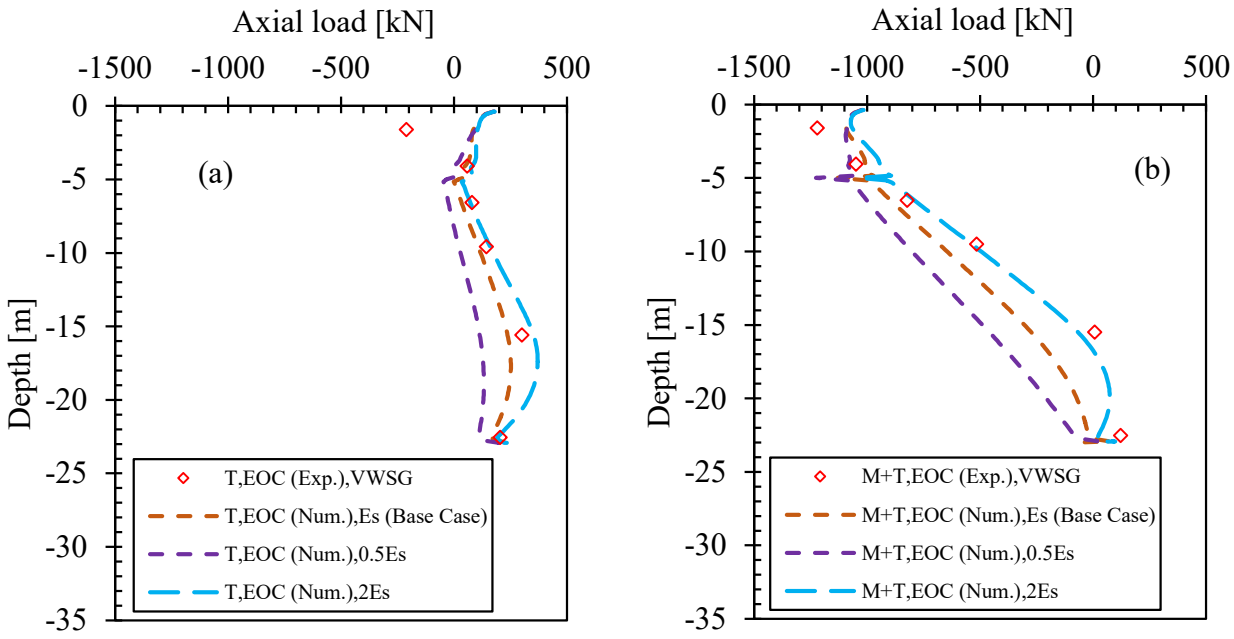

Figure 3.41. Axial load profiles (a) thermal (T) and (b) thermo-mechanical (M+T) at the end of cooling (EOC) for the London energy pile (change in Es)

Table 3.15. Results from numerical analyses with varied Es values (London energy pile)

Description	Change in Es	(Base case)		Unit	Remark
Soil stiffness (Es)					
- Made groound	9.9	19.8	39.6	[MPa]	
- Sandy gravel	38.5	77	154	[MPa]	
- London clay	19.25	38.5	77	[MPa]	
	= 0.5 Es	= Es	= 2 Es		
	-50	-	100	[%]	Change from base case
M (max.)	-1200	-1200	-1200	[kN]	At the pile head
T, EOC					
Axial compressive load (max)	-46.63			[kN]	
		-		[%]	Change from base case
Axial tensile load (max)	198.51	251.63	370.47	[kN]	
	-21.11	-	47.23	[%]	Change from base case
M+T, EOC					
Pile head settlement	-6.46	-5.06	-4.04	[mm]	
	27.67	-	-20.16	[%]	Change from base case
Axial compressive load (max)	-1225.95	-1130.26	-1072.33	[kN]	
	8.47	-	-5.13	[%]	Change from base case
Axial tensile load (max)	29.77	78.37	97.17	[kN]	
	-62.01	-	23.99	[%]	Change from base case
T, EOH					
Axial compressive load (max)	-340.85	-435.85	-633.78	[kN]	
	-21.80	-	45.41	[%]	Change from base case
Axial tensile load (max)				[kN]	
				[%]	Change from base case
M+T, EOH					
Pile head uplift	-3.61	-2.31	-1.61	[mm]	
	-56.28	-	30.30	[%]	Change from base case
Axial compressive load (max)	-1533.03	-1566.97	-1635.27	[kN]	
	-2.17	-	4.36	[%]	Change from base case
Axial tensile load (max)				[kN]	
				[%]	Change from base case

M = mechanical load
T, EOC = thermally induced at the end of cooling
M+T, EOC = thermo-mechanically induced at end of cooling
T, EOH = thermally induced at the end of heating
M+T, EOH = thermo-mechanically induced at end of heating

Lausanne energy pile:

In the case of Test 7 of the Lausanne energy pile, the soil stiffness values were reduced by 50% and increased by 100% from the base case values. Under the M only, using lower values of soil stiffnesses produced slightly higher settlements and higher uplifts at the end of heating (EOH) as illustrated in Figure 3.42. As can be seen in Figure 3.43, when the pile was heated after applying the M, in the case of 100% increase in soil stiffness, the thermally induced tensile load at the EOH climbed nearly 25%. This led to an increase in the thermo-mechanically compressive load by about 16%. Table 3.16 summarizes the important numerical results for the Lausanne energy pile, Test 7. Additional figures can also be found in Appendix B.3.

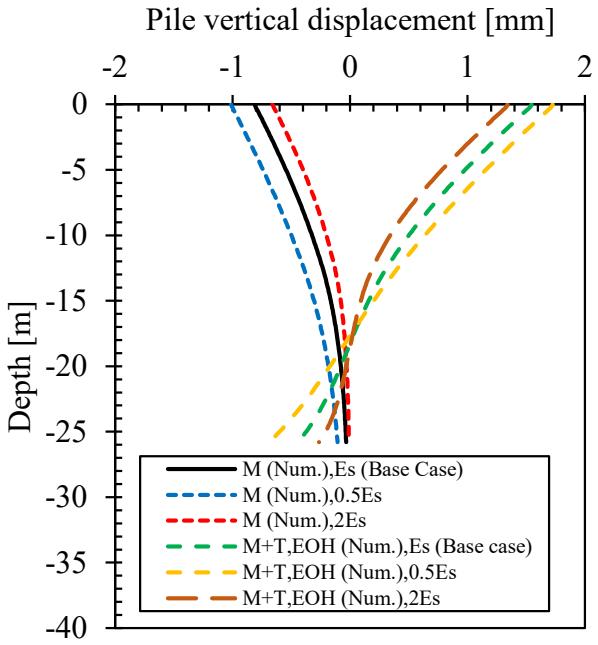

Figure 3.42. Pile vertical displacement profiles along its length at the end of heating (EOH) for the Lausanne energy pile (change in Es)

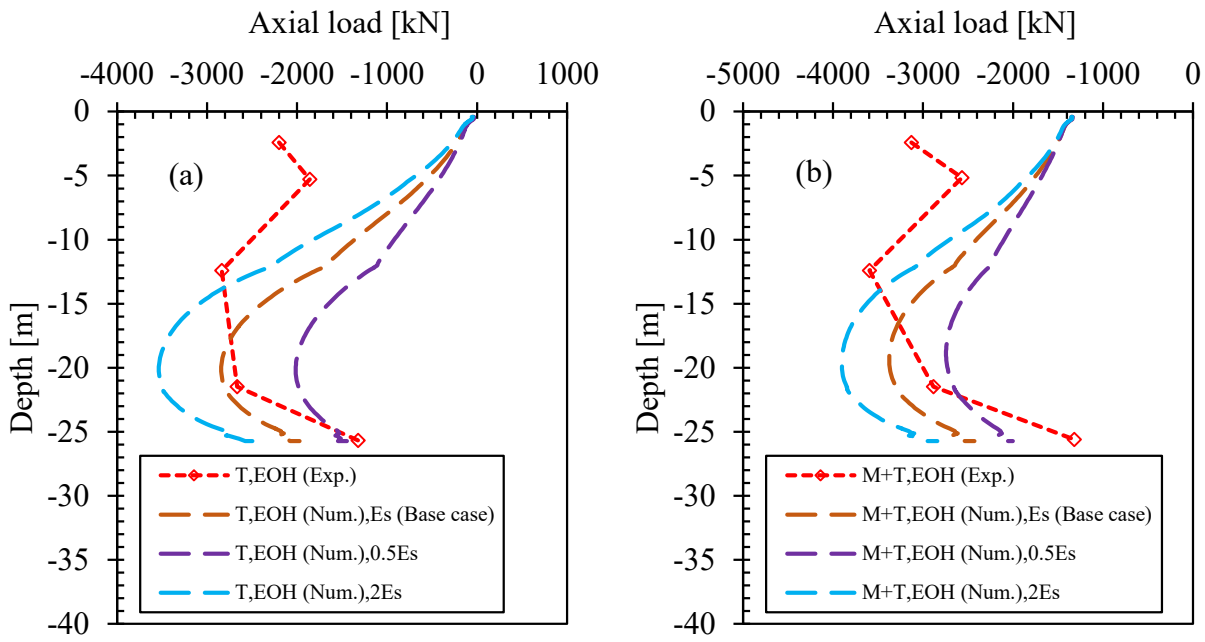

Figure 3.43. Axial load profiles (a) thermal (T) and (b) thermo-mechanical (M+T) at the end of heating (EOH) for the Lausanne energy pile (change in Es)

Table 3.16. Results from numerical analyses with varied Es values (Lausanne energy pile: Test 7)

Description	Change in Es	(Base case)		Unit	Remark
Soil stiffness (Es)					
- Alluvial soil (A1)	130	260	520	[MPa]	
- Alluvial soil (A2)	130	260	520	[MPa]	
- Sandy-gravelly moraine	225	450	900	[MPa]	
- Bottom moraine	315	630	1260	[MPa]	
- Sandstone (molasse)	1500	3000	6000	[MPa]	
	= 0.5 Es	= Es	= 2 Es		
	-50	-	100	[%]	Change from base case
M (Max.)	-1300	-1300	-1300	[kN]	At the pile head
T, EOH					
Axial compressive load (max)	-2014.03	-2841.81	-3535.19	[kN]	
	-29.13	-	24.40	[%]	Change from base case
Axial tensile load (max)				[kN]	
				[%]	Change from base case
M+T, EOH					
Pile head uplift	1.72	1.54	1.32	[mm]	
	11.69	-	-14.29	[%]	Change from base case
Axial compressive load (max)	-2744.01	-3375.54	-3901.73	[kN]	
	-18.71	-	15.59	[%]	Change from base case
Axial tensile load (max)				[kN]	
				[%]	Change from base case
T, EOC					
Axial compressive load (max)	-125.80	-232.37	-545.11	[kN]	
	-45.86	-	134.59	[%]	Change from base case
Axial tensile load (max)	123.76	195.03	168.18	[kN]	
	-36.54	-	-13.77	[%]	Change from base case
M+T, EOC					
Pile head settlement	-0.57	-0.43	-0.52	[mm]	
	32.56	-	20.93	[%]	Change from base case
Axial compressive load (max)	-1202.15	-1160.11	-1160.41	[kN]	
	3.62	-	0.03	[%]	Change from base case
Axial tensile load (max)				[kN]	
				[%]	Change from base case

M = mechanical load
T, EOH = theramlly induced at the end of heating
M+T, EOH = thermo-mechanically induced at the end of heating
T, EOC = thermally induced at the end of cooling
M+T, EOC = thermo-mechanically induced at the end of cooling

3.5.4. Change in Thermal Conductivity of Soil (TCs)

London energy pile:

The thermal conductivity of soils (TCs) ranging $0.5x10^{-3}$ to $8x10^{-3}$ kW/m/°C, -75% and 300% change from the base case value, were considered. As shown in Figure 3.44, the vertical displacements along the pile length were visually unchanged. Figure 3.45 shows the thermally and thermo-mechanically induced axial loads. It appears that changing the values of TCs had little effects on the pile responses, but the effect of the cooling itself was significant. Table 3.17 gives a summary of these numerical outputs. The temperature field in the surrounding ground also changed minimally when the TCs changed in which the temperature propagated further away from the pile center if the higher values of TCs was used. The excess porewater pressure also changed, but it was minimal (see Appendix A.4 for more details).

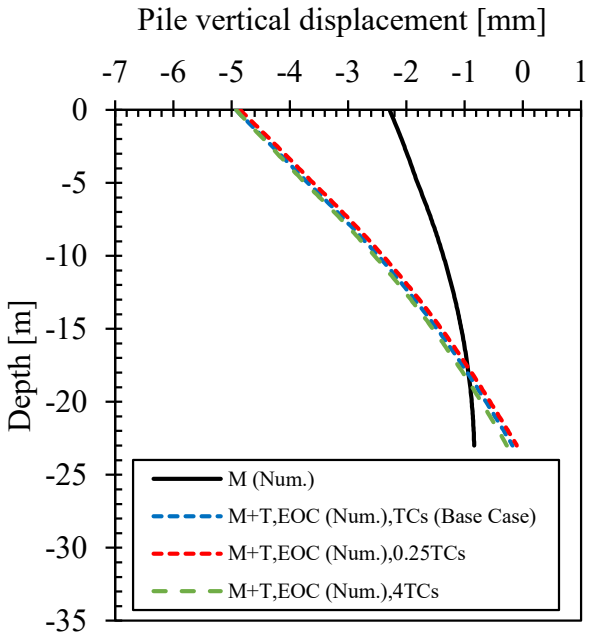

Figure 3.44. Pile vertical displacement profiles along its length at the end of cooling (EOC) for the London energy pile (change in TCs)

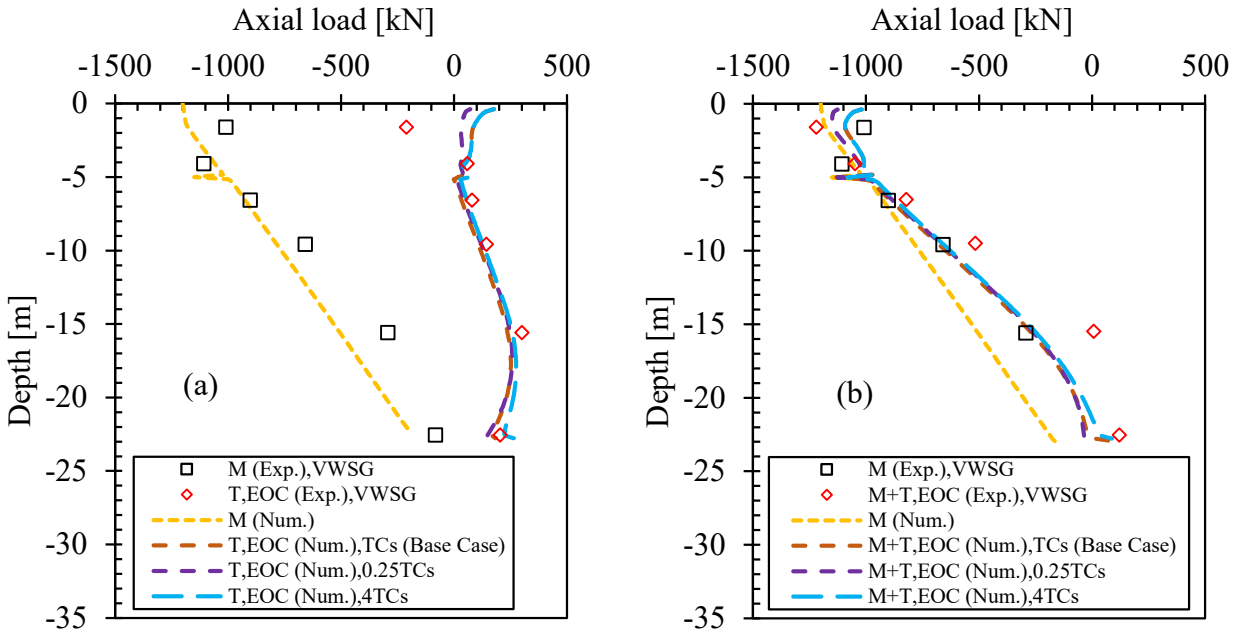

Figure 3.45. Axial load profiles (a) thermal (T) and (b) thermo-mechanical (M+T) at the end of cooling (EOC) for the London energy pile (change in TCs)

Table 3.17. Results from numerical analyses with varied TCs values (London energy pile)

Description	Change in TCs	(Base case)		Unit	Remark
Thermal conductivity of soil (TCs)					
- Made ground	0.5	2	8	$x10^{-3}$[kW/m/°C]	
- Sandy gravel	0.5	2	8	$x10^{-3}$[kW/m/°C]	
- London clay	0.375	1.5	6	$x10^{-3}$[kW/m/°C]	
	= 0.25 TCs	= TCs	= 4 TCs		
	-75	-	300	[%]	Change from base case
M (max.)	-1200	-1200	-1200	[kN]	At the pile head
T, EOC					
Axial tensile load (max)	257.61	251.63	274.83	[kN]	
	2.38		9.22	[%]	Change from base case
Axial compressive load (max)				[kN]	
				[%]	Change from base case
M+T, EOC					
Pile head settlement	-4.85	-5.06	-4.89	[mm]	
	-4.15	-	-3.36	[%]	Change from base case
Axial compressive load (max)	-1151.38	-1130.26	-1093.03	[kN]	
	1.87	-	-3.29	[%]	Change from base case
Axial tensile load (max)		78.37	88.10	[kN]	
		-	12.42	[%]	Change from base case
T, EOH					
Axial compressive load (max)	-395.13	-435.85	-467.71	[kN]	
	-9.34	-	7.31	[%]	Change from base case
Axial tensile load (max)				[kN]	
				[%]	Change from base case
M+T, EOH					
Pile head uplift	-2.11	-2.31	-2.39	[mm]	
	-8.66	-	3.46	[%]	Change from base case
Axial compressive load (max)	-1528.58	-1566.97	-1617.83	[kN]	
	-2.45	-	3.25	[%]	Change from base case
Axial tensile load (max)				[kN]	
				[%]	Change from base case

M = mechanical load
T, EOC = thermally induced at the end of cooling
M+T, EOC = thermo-mechanically induced at end of cooling
T, EOH = thermally induced at the end of heating
M+T, EOH = thermo-mechanically induced at end of heating

Lausanne energy pile:

In Test 7 of Lausanne energy pile, the thermal conductivity of soils was changed from the base case value of $1.8x10^{-3}$ kW/m/C by -55% and 300%. It was found that changing the TCs did not affect the numerical results as can be seen in Figure 3.46 and Figure 3.47. Table 3.18 gives a summary of the most important output values. Additional information also reported in Appendix B.4.

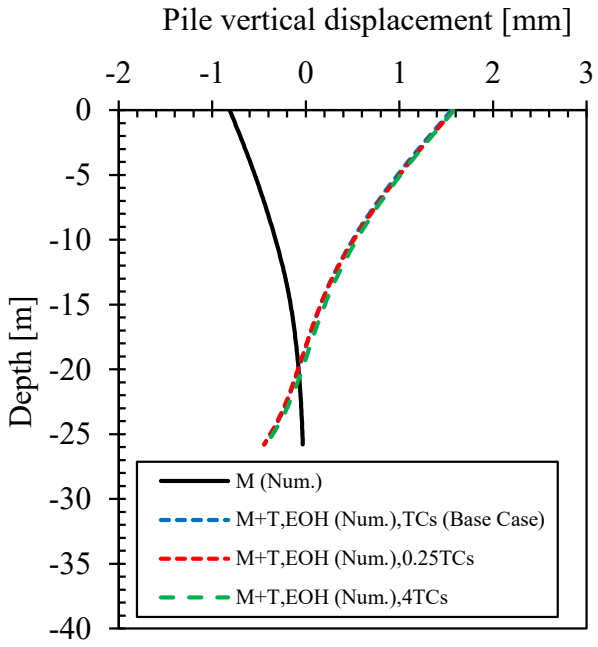

Figure 3.46. Pile vertical displacement profiles along its length at the end of heating (EOH) for the Lausanne energy pile (change in TCs)

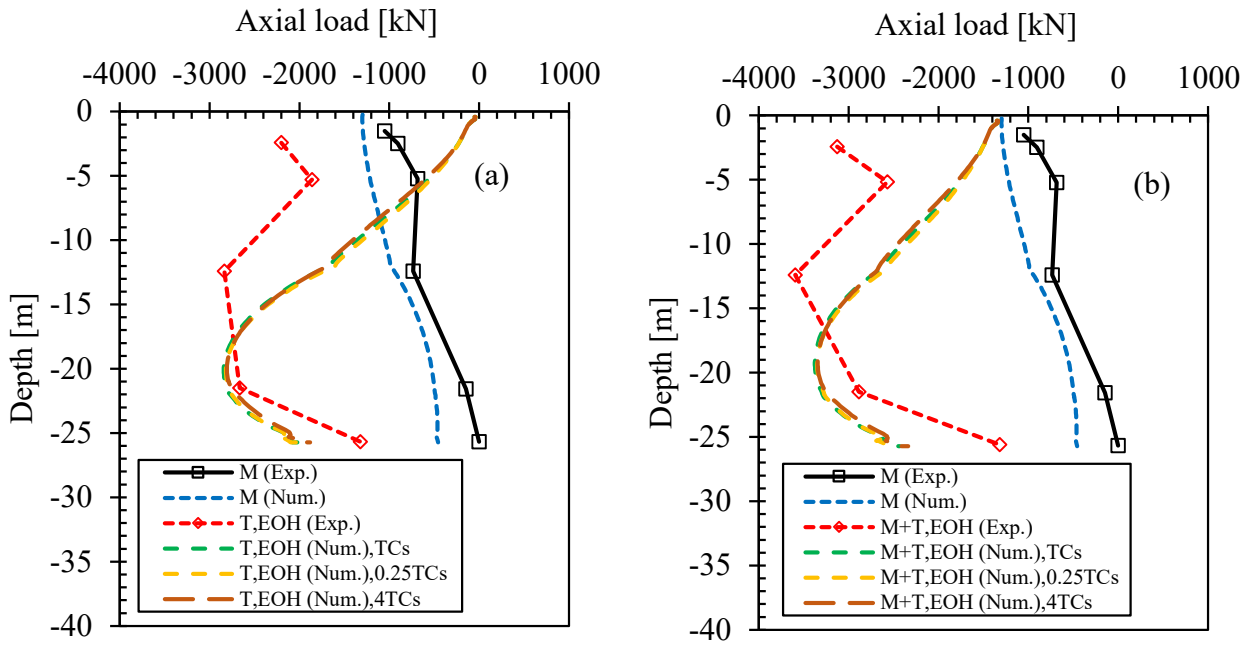

Figure 3.47. Axial load profiles (a) thermal (T) and (b) thermo-mechanical (M+T) at the end of heating (EOH) for the Lausanne energy pile (change in TCs)

Table 3.18. Results from numerical analyses with varied TCs values (Lausanne energy pile: Test 7)

Description	Change in TCs	(Base case)		Unit	Remark
Thermal conductivity of soil (TCs)					
- Alluvial soil (A1)	0.45	1.8	7.2	x10^{-3}[kW/m/°C]	
- Alluvial soil (A2)	0.45	1.8	7.2	x10^{-3}[kW/m/°C]	
- Sandy-gravelly moraine	0.45	1.8	7.2	x10^{-3}[kW/m/°C]	
- Bottom moraine	0.45	1.8	7.2	x10^{-3}[kW/m/°C]	
- Sandstone (molasse)	0.275	1.1	4.4	x10^{-3}[kW/m/°C]	
	= 0.25 TCs	= TCs	= 4 TCs		
	-55	-	300	[%]	Change from base case
M (max.)	-1300	-1300	-1300	[kN]	At the pile head
T, EOH					
Axial compressive load (max)	-2816.96	-2841.81	-2807.78	[kN]	
	-0.87	-	-1.20	[%]	Change from base case
Axial tensile load (max)				[kN]	
				[%]	Change from base case
M+T, EOH					
Pile head uplift	1.57	1.54	1.57	[mm]	
	1.95	-	1.95	[%]	Change from base case
Axial comressive load (max)	-3349.83	-3375.54	-3343.75	[kN]	
	-0.76	-	-0.94	[%]	Change from base case
Axial tensile load (max)				[kN]	
				[%]	Change from base case
T, EOC					
Axial comressive load (max)	-238.48	-232.37	-207.95	[kN]	
	2.63		-10.51	[%]	Change from base case
Axial tensile load (max)	191.54	195.03	182.62	[kN]	
	-1.79	-	-6.36	[%]	Change from base case
M+T, EOC					
Pile head settlement	-0.43	-0.43	-0.39	[mm]	
	0.00	-	-9.30	[%]	Change from base case
Axial comressive load (max)	-1159.29	-1160.11	-1161.08	[kN]	
	-0.07	-	0.08	[%]	Change from base case
Axial tensile load (max)				[kN]	
				[%]	Change from base case

M = mechanical load
T, EOH = theramlly induced at the end of heating
M+T, EOH = thermo-mechanically induced at the end of heating
T, EOC = thermally induced at the end of cooling
M+T, EOC = thermo-mechanically induced at the end of cooling

3.5.5. Change in Specific Heat Capacity of Soil (SHCs)

London energy pile:

The values of the specific heat capacities of soils (SHCs) were reduced and increased by 75% and 100% from the base case values. As seen in Figure 3.48, the settlements of the pile head at the end of cooling were almost unchanged, reducing by only about 6% when the values of SHCs were increased by 100%. The uplifts of the pile head also remained almost the same at the end of heating.

In terms of temperature distributions in the ground around the pile, increasing the SHCs value reduced the distance of temperature propagation through the ground while reducing the SHCs increased these distance. These are expected because the specific heat capacity is the ability of the material to hold heat. The higher the SHCs, the more heat the material can hold. In consequence, the temperature or heat cannot propagate far away from the source. During the cooling and heating cycle of 43 days, the temperature transfer from the pile only affected the ground temperature within 3.5 m (6.4D) from the pile center in the lowest case of the SHCs. The porewater pressure also influenced by the change in SHCs. However, this was small and negligible (details of temperature and excess porewater pressure distributions in the soils around the pile can be found in Appendix A.5). Changing the values of the SHCs affected the pile responses minimally at the EOC, as can be seen in Figure 3.49. The same was true at the end of heating. The numerical results using various SHCs values are summarized in Table 3.19.

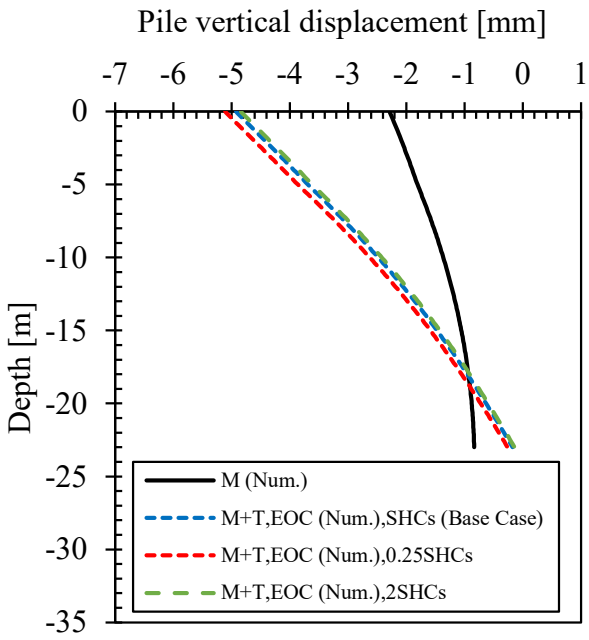

Figure 3.48. Pile vertical displacement profiles along its length at the end of cooling (EOC) for the London energy pile (change in SHCs)

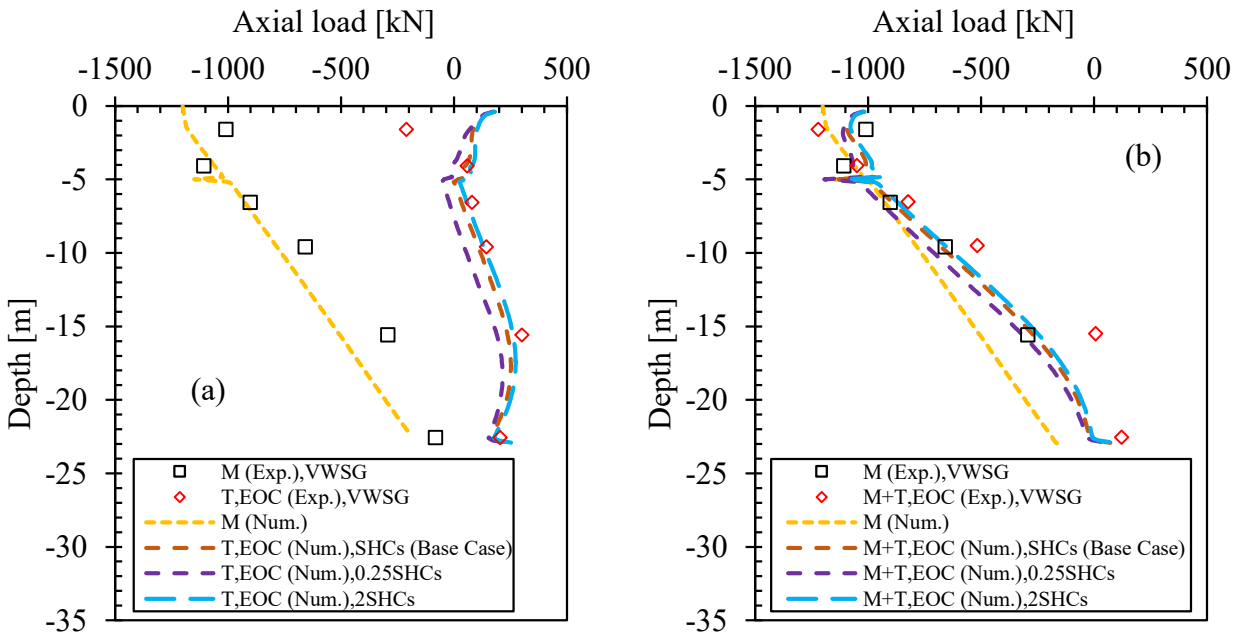

Figure 3.49. Axial load profiles (a) thermal (T) and (b) thermo-mechanical (M+T) at the end of cooling (EOC) for the London energy pile (change in SHCs)

Table 3.19. Results from numerical analyses with varied SHCs values (London energy pile)

Description	Change in SHCs	(Base case)		Unit	Remark
Specific heat capacity of soil (SHCs)					
- Made ground	300	1200	2400	[kJ/t/°C]	
- Sandy gravel	300	1200	2400	[kJ/t/°C]	
- London clay	375	1500	3000	[kJ/t/°C]	
	= 0.25 SHCs	= SHCs	= 2 SHCs		
	-75	-	100	[%]	Change from base case
M (max.)	-1200	-1200	-1200	[kN]	At the pile head
T, EOC					
Axial compressive load (max.)	-53.14			[kN]	
		-		[%]	Change from base case
Axial tensile load (max)	229.74	251.63	272.77	[kN]	
	-8.70	-	8.40	[%]	Change from base case
M+T, EOC					
Pile head settlement	-4.97	-5.06	-4.78	[mm]	
	-1.78	-	-5.53	[%]	Change from base case
Axial compressive load (max.)	-1193.20	-1130.26	-1101.02	[kN]	
	5.57	-	-2.59	[%]	Change from base case
Axial tensile load (max)	62.59	78.37	94.31	[kN]	
	-20.14	-	20.34	[%]	Change from base case
T, EOH					
Axial compression load (max)	-401.23	-435.85	-417.80	[kN]	
	-7.94	-	-4.14	[%]	Change from base case
Axial tensile load (max)				[kN]	
				[%]	Change from base case
M+T, EOH					
Pile head uplift	-2.33	-2.31	-2.15	[mm]	
	0.87	-	-6.93	[%]	Change from base case
Axial compressive load (max.)	-1549.76	-1566.97	-1567.28	[kN]	
	-1.10	-	0.02	[%]	Change from base case
Axial tensile load (max)				[kN]	
				[%]	Change from base case

M = mechanical load
T, EOC = thermally induced at the end of cooling
M+T, EOC = thermo-mechanically induced at end of cooling
T, EOH = thermally induced at the end of heating
M+T, EOH = thermo-mechanically induced at end of heating

Lausanne energy pile:

Figure 3.50 and Figure 3.51 show the vertical displacements and axial loads along the pile length at the end of heating, accordingly. The numerical results were practically the same for all changes in the SHCs values. This means that there were no effects of the values of SHCs on the pile responses in the case of Lausanne energy pile. A summary of important outcomes from the simulations is provided in Table 3.20. Additional figures of pile responses at the end of cooling can be found in Appendix B.5.

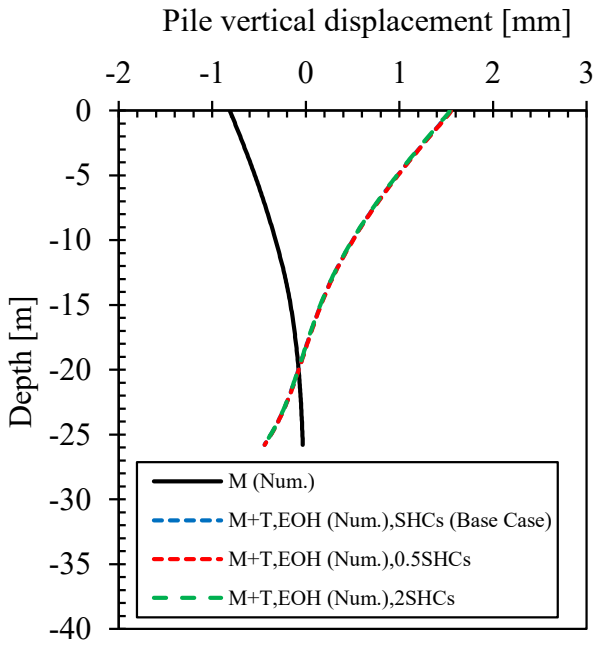

Figure 3.50. Pile vertical displacement profiles along its length at the end of heating (EOH) for the Lausanne energy pile (change in SHCs)

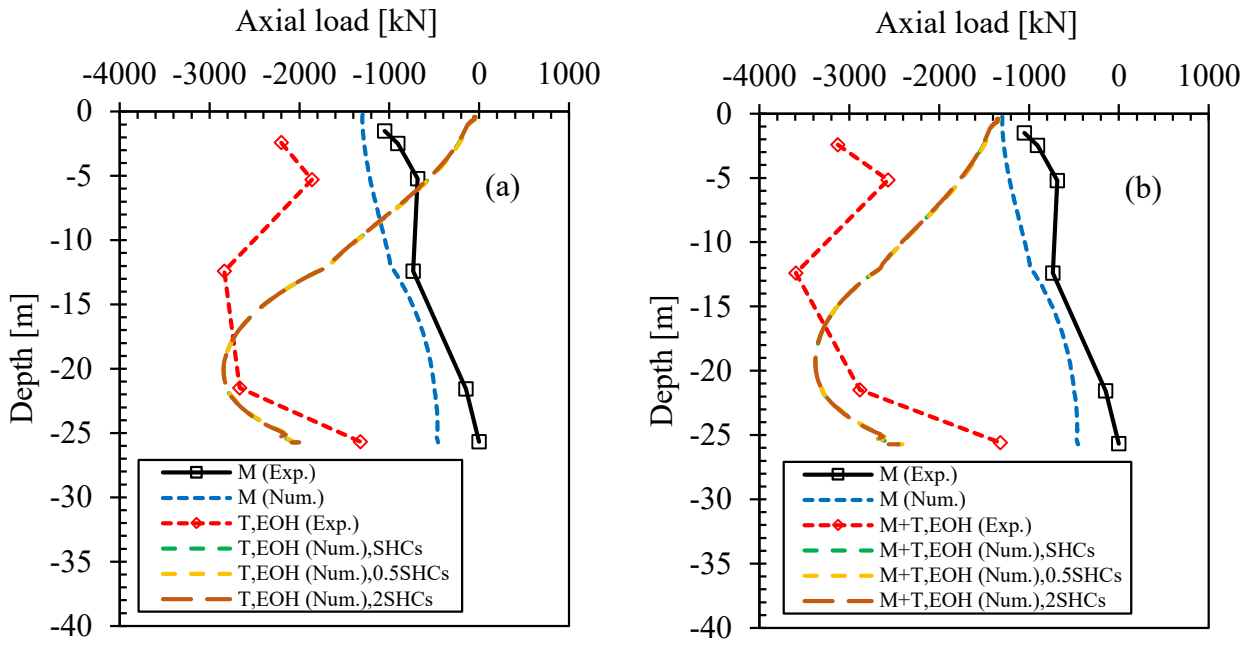

Figure 3.51. Axial load profiles (a) thermal (T) and (b) thermo-mechanical (M+T) at the end of heating (EOH) for the Lausanne energy pile (change in SHCs)

Table 3.20. Results from numerical analyses with varied SHCs values (Lausanne energy pile: Test 7)

Description	Change in SHCs	(Base case)		Unit	Remark
Specific capacity of soil (SHCs)					
- Alluvial soil (A1)	600	1200	2400	[kJ/t/°C]	
- Alluvial soil (A2)	615.5	1231	2462	[kJ/t/°C]	
- Sandy-gravelly moraine	600	1200	2400	[kJ/t/°C]	
- Bottom moraine	545.5	1091	2182	[kJ/t/°C]	
- Sandstone (molasse)	392	784	1568	[kJ/t/°C]	
	= 0.5 SHCs	= SHCs	= 2 SHCs		
	-50	-	100	[%]	Change from base case
M (max.)	-1300	-1300	-1300	[kN]	At the pile head
T, EOH					
Axial compressive load (max)	-2841.37	-2841.81	-2843.48	[kN]	
	-0.02	-	0.06	[%]	Change from base case
Axial tensile load (max)				[kN]	
				[%]	Change from base case
M+T, EOH					
Pile head uplift	1.55	1.54	1.53	[mm]	
	0.65	-	-0.65	[%]	Change from base case
Axial comressive load (max)	-3375.47	-3375.54	-3376.92	[kN]	
	0.00	-	0.04	[%]	Change from base case
Axial tensile load (max)				[kN]	
				[%]	Change from base case
T, EOC					
Axial comressive load (max)	-216.31	-232.37	-234.32	[kN]	
	-6.91		0.84	[%]	Change from base case
Axial tensile load (max)	202.81	195.03	183.09	[kN]	
	3.99	-	-6.12	[%]	Change from base case
M+T, EOC					
Pile head settlement	-0.44	-0.43	-0.40	[mm]	
	2.33	-	-6.98	[%]	Change from base case
Axial comressive load (max)	-1154.39	-1160.11	-1167.84	[kN]	
	-0.49	-	0.67	[%]	Change from base case
Axial tensile load (max)				[kN]	
				[%]	Change from base case

M = mechanical load
T, EOH = theramlly induced at the end of heating
M+T, EOH = thermo-mechanically induced at the end of heating
T, EOC = thermally induced at the end of cooling
M+T, EOC = thermo-mechanically induced at the end of cooling

3.5.6. Change in Head Restrained Conditions of the Pile (HRC)

Lausanne energy pile:

Heating-cooling of the Lausanne energy pile Test 7 was carried out after the completion of the superstructure. Changing the restrained conditions (HRC) of the pile head in the models was a way to study the effects of the superstructure on the pile responses. Note that in the base case analysis, the unrestrained head condition (URH) was used which means that the pile head could move freely during heating and cooling. For the sensitivity analyses, the pile head restrained conditions were assumed to be fully restrained or fixed head (FRH) and partially restrained head (PRH) with different assigned axial spring stiffnesses denoted by EA. These EA values applied on the pile head represented the stiffness of the superstructure. Note that, without the details of the structural elements of the building, it was difficult to estimate the appropriate EA values. Therefore, the EA values used in the models were assumed.

As shown in Figure 3.52, changing the pile head restrained conditions altered the pile head uplifts significantly at the end of heating. As expected, the uplift values of the partial restrained head (PRH) were located in between the unrestrained head (URH) and fully restrained head (FRH). Higher values of spring stiffnesses (EA) applied on the pile head produced smaller uplifts of the pile head. The axial load profiles of the pile at the end of heating (EOH) are demonstrated in Figure 3.53. It can be seen that the FRH produced the highest axial loads in the pile in contrast with the URH which gave the lowest axial loads. It is important to note that the head restrained conditions affected strongly the responses of the pile in the upper part near the pile head and lesser effects in the lower part near the part toe. The axial loads produced by using partially restrained head conditions (PRH) were within those induced by the URH and FRH. Note that the model results using the PRH with EA=100 MN seems to fit well with the measured axial load profile, with the

maximum axial load of -3492 kN under the M+T at the EOH in comparison with -3640 kN from the field experiment (Amatya et al., 2012). Outcomes from the numerical simulations in terms of pile head displacements and axial loads at the end of heating and the end of cooling are summarised in Table 3.21. Additional figures that are not shown here such as axial load profiles at the end of cooling and developments of shaft friction along the pile-soil interface can be found in Appendix B.6.

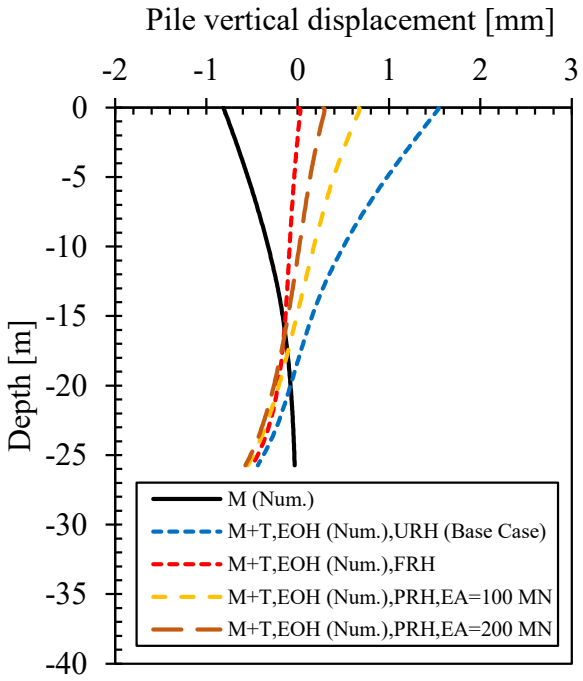

Figure 3.52. Pile vertical displacement profiles along its length at the end of heating (EOH) for the Lausanne energy pile (change in HRC)

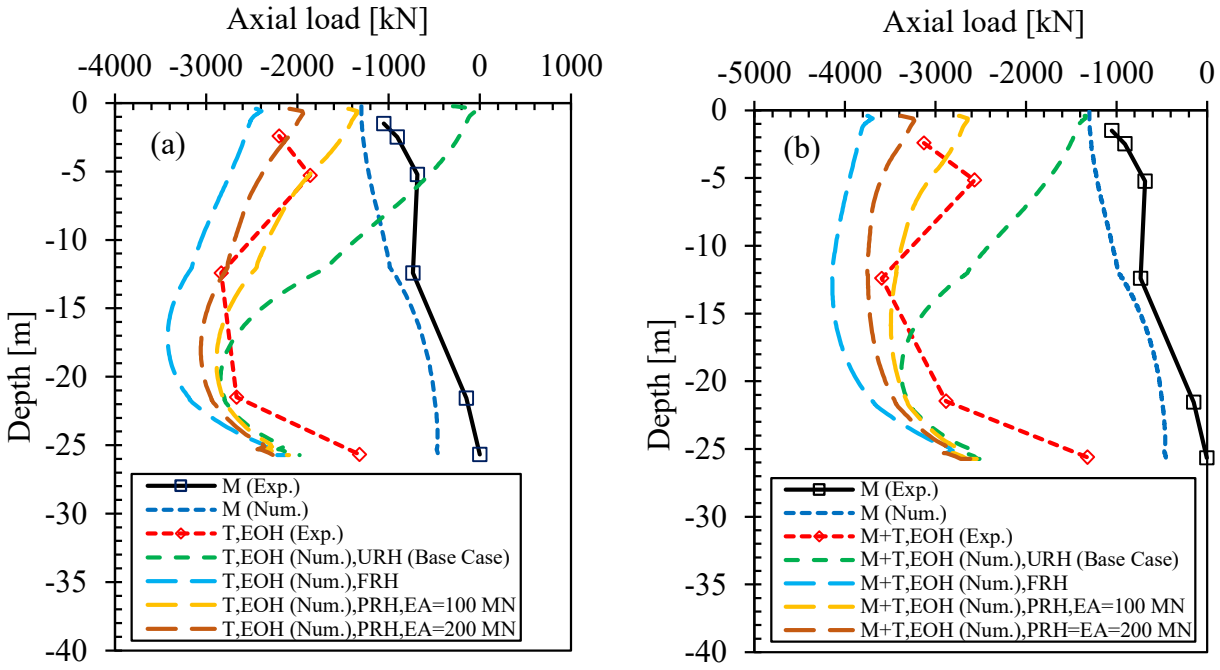

Figure 3.53. Axial load profiles (a) thermal (T) and (b) thermo-mechanical (M+T) at the end of heating (EOH) for the Lausanne energy pile (change in HRC)

Table 3.21. Results from numerical analyses with different HRC (Lausanne energy pile: Test 7)

Description	Change in HRC (Base case)				Unit	Remark
Head restrained condition (HRC)	URH	PRH	PRH	FRH		
Spring axial stiffness (EA)	n/a	100	200	n/a	[MN]	
M (max.)	-1300	-1300	-1300	-1300	[kN]	At the pile head
T, EOH						
Axial compressive load (max)	-2841.81	-2886.2	-3057.9	-3420.9	[kN]	
	-	1.56	7.61	20.38	[%]	Change from base case
Axial tensile load (max)					[kN]	
					[%]	Change from base case
M+T, EOH						
Pile head uplift	1.54	0.67	0.28	0	[mm]	
	-	-56.49	-81.82	-100.00	[%]	Change from base case
Axial compressive load (max)	-3375.54	-3492.34	-3754.00	-4143.99	[kN]	
	-	3.46	11.21	22.77	[%]	Change from base case
Axial tensile load (max)					[kN]	
					[%]	Change from base case
T, EOC						
Axial compressive load (max)	-232.37	-289.20	-315.15	-170.00	[kN]	
	-	24.46	35.62	-26.84	[%]	Change from base case
Axial tensile load (max)	195.03			1048.61	[kN]	
	-			437.67	[%]	Change from base case
M+T, EOC						
Pile head settlement	-0.43	-0.57	-0.64	0	[mm]	
	-	32.56	48.84		[%]	Change from base case
Axial compressive load (max)	-1160.11	-1393.62	-1489.73	-671.84	[kN]	
	-	20.13	28.41	-42.09	[%]	Change from base case
Axial tensile load (max)					[kN]	
					[%]	Change from base case

M = mechanical load
T, EOH = theramlly induced at the end of heating
M+T, EOH = thermo-mechanically induced at the end of heating
T, EOC = thermally induced at the end of cooling
M+T, EOC = thermo-mechanically induced at the end of cooling
URH = unrestrained head; PRH = partial restrained head; FRH = fully restrained or fixed head

Chapter 4: THM Modeling of Geothermal Energy Piles in Winnipeg

4.1. Winnipeg Strata

The City of Winnipeg is located on the ground deposited in the area of Proglacial Lake Agassiz. In this area, till was deposited directly on top of karstic carbonate bedrock and was followed by deposition of glaciolacustrine clay with occasionally interbedded silt layers. Details of these stratigraphic units and some of their geotechnical properties are provided below which was mostly based on information reported by Baracos, Shields, & Kjartanson (1983).

4.1.1. Glaciolacustrine Clay

A brief description of the glaciolacustrine clay given by Baracos et al. (1983) is given here. Throughout most of the Winnipeg area, the glaciolacustrine clay deposit lies on top of the till deposit. The top 3 m below the ground level (bgl), consisting of interbedded layers of silty clay and silt with varying amounts of organic matter, is known locally in Winnipeg as the Upper Complex Zone. This Upper Complex Zone is heavily fissured and has a nuggety structure because of intense physical weathering. It is usually not recommended to place building foundations within this zone.

The thickness of the glaciolacustrine silty clay underneath the Upper Complex Zone is typically about 9 to 12 m. The upper 1.5 to 4.5 m is brown or mottled grey-brown, highly plastic with a laminated structure and stiff consistency. The lower part is grey, medium to highly plastic with firm to stiff consistency. Moisture contents of the clay increase with depth, ranging from 40 to 60 %. As a result, undrained shear strengths decrease with depth. Near the top of the till the

values are typically in the order of 40 kPa but occasionally as low as 25 kPa in some locations (Skaftfeld, 2014). Baracos et al. (1983) reported the typical values of shear strengths of the Winnipeg lacustrine clay of about 35 to 85 kPa. Skaftfeld (2014) provided lower values, ranging from 40 to 60 kPa. As reported in Baracos & Graham (1981), the effective shear strength parameters of Winnipeg clay are about 3 kPa and 23°. The groundwater table is generally located within the lacustrine clay deposit, varying from about 3 m to 6 m bgl. However, exceptional cases may exist, in the form of upward (artesian) hydraulic gradients. Regarding permeability, the upper brown clay is more permeable with the hydraulic conductivity varying from $5x10^{-10}$ to $3x10^{-9}$ m/s. For the lower grey clay, the values are from $1x10^{-10}$ to $1x10^{-13}$ m/s. Hairline cracks are usually found in the clay and therefore cause an increase in the hydraulic conductivity values of the clay which may range from $3x10^{-10}$ to $1x10^{-9}$ m/s. The clay is active chemically and is known as a "swelling clay". A summary of typical properties of the Winnipeg lacustrine clay is given in Table G.1 in Appendix G.

4.1.2. Till Deposit

Underlying the lacustrine clay is the till deposit which is a heterogeneous mixture of usually well-graded clay to boulder size sediments. The typical thickness ranges from about 3 to 6 m, but sometimes the till can be as thick as 9 m in some locations. The till usually contains 40 to 60 % of fines (silt and clay sizes) in the matrix with frequently predominant silt sizes. Therefore, they often locally referred to as the silt till. The moisture content of the till is a very useful indicator in terms of its strength. The loose upper part of the till, sometimes referred to as an ablation till (Skaftfeld, 2014), often has a water content of about 10 to 15%. Water contents in the dense till, locally referred to as basal till or "hardpan" (Skaftfeld, 2014) can be 7 to 10%. In some locations, water

contents can be as low as 4 to 6%, which is usually classified as the very dense till. Belbas (2013) reported the moisture contents ranging from 3.5 to 8%.

In Winnipeg, it is very uncommon to obtain undisturbed core samples of the till. Instead, the strength of the till is frequently evaluated using the Standard Penetration Test (SPT) method (Belbas, 2013). The SPT-N value in the very dense till is typically greater than 75 blows per 300 mm (Skaftfeld, 2014). Whereas, Belbas (2013) reported 50 blows per 300 mm or greater as a typical value for the same till. The internal friction angle of 40° is commonly assumed for the very dense till. The value as high as 42° has been used for numerical analyses of the riverbank slope stability in Winnipeg. (Thiessen, 2010; Thiessen, Alfaro, & Blatz, 2011). Cao, Peaker, & Ahmad (2015) conducted 81 triaxial tests on cohesive till samples: silty clay till and clayey silt till found in Toronto, Ontario. These Toronto tills have similar properties to that of Winnipeg tills. They found that the effective friction angle ranges from 31º to 41º and cohesion range from 0 to 50 kPa. Likewise, the cohesionless glacial till was found to have ϕ' = 31° to 45° (Manzari, Devininkas, Olshansky, & Galaa, 2014). Cao et al. (2015) also provided a correlation between the friction angle and SPT-N value for the tills as ϕ'=32.5+0.09N ±2. To the author's knowledge, there is no available correlation between the ϕ' and SPT-N value for the Winnipeg till. Using the correlation by Cao et al. (2015) would give the upper bound values of ϕ' about 39 to 41º for SPT-N values of 50 and 75 blow per 300 mm, respectively.

As reported in Baracos et al. (1983), pressuremeter tests conducted in the till unit in Winnipeg provided Young's modulus values as high as 170 to 240 MPa. Dry and moist unit weights were found to be about 18.8 to 22 kN/m^3 and 21.2 to 24.3 kN/m^3, respectively. Hydraulic conductivity of the till in the eastern area of Winnipeg varies from 2.5x10^{-10} to 6.4x10^{-7} m/s.

4.1.3. Carbonate Bedrock

Underlying the till deposit is the carbonate bedrock consisting primarily of dolomite and dolomitic limestone (Belbas, 2013; Skaftfeld, 2014). The depth to the bedrock from the ground surface varies generally ranges from about 15 m to 21 m. It is usually found that the top 0.3 to 0.9 m of the bedrock is highly fractured with infilled sands and gravels. The deep foundations supporting high-rise buildings or heavy structures located in the city center of Winnipeg are often placed on the Lower Fort Garry member of the Red River Formation (Skaftfeld, 2014).

As described in Baracos et al. (1983), the bedrock in the Winnipeg area is classified into three groups based on their unconfined compressive strengths. The first group is high strength rocks having unconfined compressive strengths greater than 60 MPa. This group includes the Lower Fort Garry member of the Red River Formation and Gunton member of the Stony Mountain Formation. The second group is medium strength rocks that include the Selkirk and Williams members of the Red River and Stony Mountain Formations. Their unconfined compressive strengths range from 34 to 37 MPa. The third group is the weakest rocks with unconfined compressive strengths of about 29 MPa. This includes the Penitentiary and Gunn members of the Stony Mountain Formation.

Elastic (Young's) moduli of the rocks can be about 9.7×10^3 to 12.4×10^3 MPa for high strength rocks while for the low strength rocks the values can be as low as 4×10^3 MPa. Porosities of the carbonate bedrock found in the Winnipeg area typically range from about 4 to 12% (Baracos et al., 1983).

4.2. Use of Cast-in-Place Concrete Piles in Winnipeg

It is important to note that energy piles are structural piles equipped with heat exchange pipes used to support buildings. In this sense, the same layout and dimensions required by the structural and geotechnical provisions are usually adopted in the design of such foundations, and their energy capacities would be estimated based on their layout and dimensions but not usually the other way around. Therefore, it is vital to know the general practice of pile foundations in the Winnipeg area.

In Winnipeg, pile foundations are used widely to support medium to heavy structures such as an apartment, commercial and industrial buildings. However, to avoid potential damage and maintenance cost that may be brought about by large differential settlements and heaving associated with the footings founded in the shallow ground within 3 m below ground surface, homeowners and engineers prefer to use piles for even light structures (Baracos et al., 1983). Cast-in-place friction piles with a minimum length of 6 m and a diameter of 0.4 m are widely used nowadays to support new single-detached houses built in the City of Winnipeg (Blatz & Mroz, 2017). The pile diameter, however, could vary from 0.35 to 0.9 m (Baracos et al., 1983). The allowable adhesion (unit shaft resistance) of about 11 to 20 kPa is typically used for the geotechnical design of the friction piles installed in the Winnipeg clay (Baracos et al., 1983). Likewise, Skaftfeld (2014) used the value of 15 kPa. Similarly, Blatz & Mroz (2017) mentioned that 14.5 kPa is traditionally adopted in local practice.

Cast-in-place end-bearing piles with pile toes embedded in the till layer have been used frequently to support medium to heavy buildings in the Winnipeg area. For cast-in-place piles installed in the undisturbed dense till, the design bearing resistance up to 720 kPa has been used. Values as high as 1450 kPa have been used for the very dense or very hard till (Baracos et al., 1983).

Rock-socketed cast-in-place piles or caissons have also been used to support very heavy structures or high-rise buildings. The Manitoba Legislative Building and the 34-story Richardson Building were the first structures in Winnipeg to use rock-socketed caissons (Skaftfeld, 2014). Typically, these rock-socketed caissons with their toes buried in limestone bedrock could be about 16 to 22 m long and diameters in the order of 1.2 to 1.8 m (Harms, Skaftfeld, & Belbas, 2017). Baracos et al. (1983) reported that caissons socketed into sound bedrock were typically designed using an allowable unit shaft resistance of 1.0 MPa and unit end-bearing of 2.9 MPa. For soft or fractured rocks, this allowable unit end-bearing should be reduced to 1.0 MPa. Surprisingly, these design values are still being used in local practice nowadays as reported in Harms et al. (2017). The allowable unit shaft resistance of 1.0 MPa and unit end-bearing of 3 MPa are suggested for caissons socketed into sound bedrock. For caissons socketed into fractured bedrock, these values were estimated to be around 0.7 MPa and 1.0 MPa, respectively. Moreover, Harms et al. (2017) stated that the rock-socketed caisson is sometimes designed using the shaft resistance alone. This is especially in the case where the rock quality at the base of the caisson is uncertain or base cleaning is not guaranteed.

4.3. Numerical Modeling of Energy Piles in Winnipeg

Axisymmetric thermo-hydro-mechanical (THM) finite element analyses using PLAXIS 2D software were carried out for energy piles in Winnipeg. Currently, there are no actual energy piles installed in Winnipeg. For numerical simulation purposes, friction and end-bearing piles were used as generic energy piles. They were subjected to local ground and thermal conditions in Winnipeg. Figure 4.1 shows a schematic of generic energy piles.

The friction energy pile was assumed to have a diameter of 0.4 m, a minimum diameter normally adopted in Winnipeg. This pile was 12 m long and installed entirely in the Winnipeg clay. The pile derives its capacity from the shaft friction. Similarly, the end-bearing energy pile was assumed to have a diameter of 0.8 m and a length of 20 m. Its toe was embedded 5 m into the very dense till layer with much higher strength and stiffness in comparison with those of the overlying clay layer.

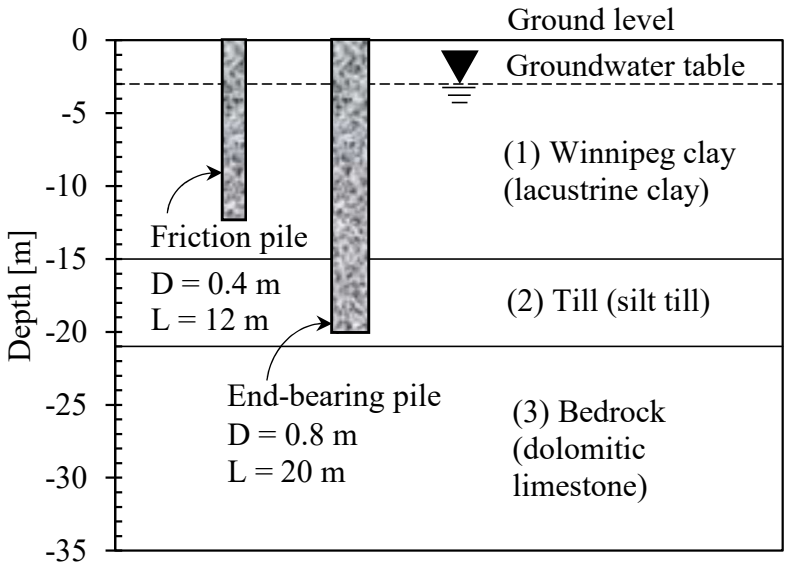

Figure 4.1. Typical soil profile and generic energy piles in Winnipeg

4.3.1. Material Characteristics

Soil stratigraphy in the Winnipeg area where pile foundations are installed is assumed uniform. For numerical modeling, the soil profile was generalized and consists of three main layers, disregarding the Upper Complex Zone. The first layer is the Winnipeg clay (lacustrine clay), from the ground surface to about 15 m below ground level (bgl), which is underlain by the silt till (glacial till), from about 15 m to 21 m bgl. Below this till layer is the dolomitic limestone bedrock, extending to a great depth (Figure 4.1). The groundwater table at 3 m bgl was used in the

models. Table 4.1 shows the material parameters used for the base case analyses, including the adopted constitutive material models. The concrete pile was modeled non-porous (solid) elastic material using the linear elastic constitutive model (LEM). The hardening soil with small strain stiffness (HSSM) was used for the Winnipeg clay layer and silt till. The LEM was also used for the dolomitic limestone bedrock layer. The interface elements were represented by the Mohr-Coulomb model (MCM). The interface properties were calculated automatically by PLAXIS software using the soil properties in the associated data set and the interface strength reduction factors (R_{inter}). Note that the material parameters for numerical modeling were taken or assumed based on the same types of materials reported in the literature (more information can be found in Table G.1 to Table G.5 in Appendix G).

Table 4.1. Material parameters for the base case analyses for energy piles in Winnipeg

Parameter	Symbol	Winnipeg clay	Silt till	Dolomitic limestone	Concrete pile	Unit
Material model	-	HSSM	HSSM	LEM	LEM	-
Analysis type	-	Fully coupled	Fully coupled	Fully coupled	Non-porous	-
Unit weight (above GWL)	γ_{unsat}	17	21	23	25	[kN/m^3]
Unit weight (below GWL)	γ_{sat}	18	23	24	-	[kN/m^3]
Initial void ratio	e_{init}	1.3	0.25	0.087	-	[-]
Young's modulus	E'	-	-	11000x10^3	40000x10^3	[kPa]
Poisson's ratio	ν'	-	-	0.2	0.15	[-]
Ref. secant stiffness (in standard dr. tri. test)	E_{50}^{ref}	21x10^3	110x10^3	-	-	[kPa]
Ref. tangent stiffness (for primary oed. loading)	E_{eod}^{ref}	21x10^3	110x10^3	-	-	[kPa]
Ref. un/reloading stiffness	E_{ur}^{ref}	63x10^3	330x10^3	-	-	[kPa]
Un/reloading Poisson's ratio	ν_{ur}	0.2	0.2	-	-	[-]
Exponential power	m	1	0.5	-	-	[-]
Failure ratio	R_f	0.9	0.9	-	-	[-]
Shear stiffness (at very small strain)	G_0^{ref}	84x10^3	440x10^3	-	-	[kPa]
Threshold shear strain	$\gamma_{0.7}$	0.0002	0.0002	-	-	[-]
Cohesion	c'	3	3	-	-	[kPa]
Friction angle	φ'	23	40	-	-	[°]
Dilatancy angle	ψ	0	0	-	-	[°]
Interface strength reduction factor	R_{inter}	1	1	1	-	[-]
Hydraulic conduc. (hor.)	k_x	6.70E-05	0.028	8.64	-	[m/day]
Hydraulic conduc. (vert.)	k_y	6.70E-05	0.028	8.64	-	[m/day]
Specific heat capacity	c_s	830	720	1300	800	[kJ/t/°C]
Thermal conductivity	λ_s	1.20E-03	1.50E-03	2.30E-03	1.80E-03	[kW/m/°C]
Density	ρ_s	1.83	2.34	2.45	2.55	[t/m^3]
Linear thermal exp. coef.	$\alpha_{sL(x,y,z)}$	5.00E-06	5.00E-06	5.00E-06	1.00E-05	[1/°C]

LEM = Linear Elastic Model; HSSM = Hardening Soil with Small strain stiffness Model

4.3.2. Geometry and Boundary Conditions

For both friction and end-bearing piles, it was assumed that the piles were located underneath the center of the building which is 30 m wide and without any basements. With these

assumptions, the axisymmetric finite element models were used for numerical analyses. The model domains were set at a distance of 50 m (> 2L) and 75 m (> 3L) for the side and bottom boundaries, respectively as illustrated in Figure 4.2. These distances were considered to minimize the potential effects of the assumed boundary conditions. The model domain was divided into zones for discretization in which a very fine mesh was used for the pile body, along the pile-soil interface, and around the pile toe in order to ensure that there were enough elements to capture the correct pile behavior. Coarser mesh sizes were used for the zones further away from the pile.

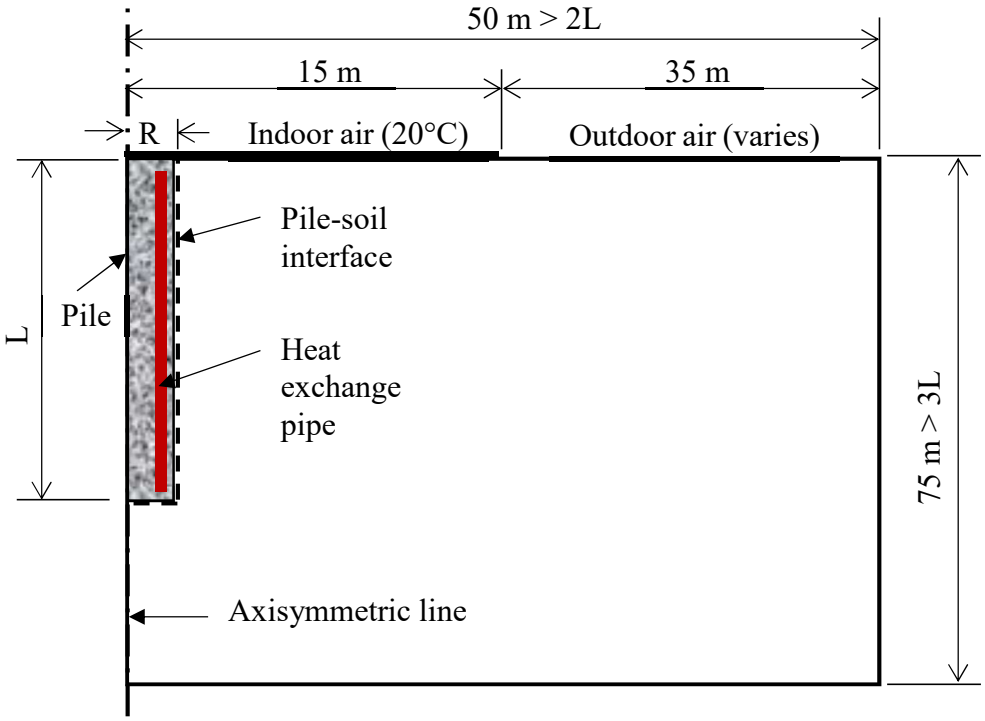

Figure 4.2. The axisymmetric geometry of the models for the energy piles in Winnipeg (not to scale)

For displacement boundary conditions, free displacements were allowed at the top boundary. On the other hand, both vertical and horizontal displacements were restrained at the bottom boundary (i.e., pinned boundary). Only vertical displacements were allowed at the left-

hand side and right-hand side boundaries which mean that, in the horizontal direction, horizontal displacements were prevented for both sides (i.e., roller boundaries).

For hydraulic boundary conditions, the drainage was allowed at the top and right-hand side boundaries. A closed flow boundary was assigned along the axisymmetric line (left-hand side boundary) and the bottom boundary.

For thermal boundary conditions, the heat flow was closed (adiabatic boundary condition) at the right-hand side boundary as well as at the left-hand side boundary. The latter was due to the axisymmetric condition. At the top boundary, the indoor air temperature was used as a boundary condition inside the building while the outdoor air temperature was used as a boundary outside the building. A constant ground temperature of 7°C was assigned at the bottom boundary. The initial ground temperature for the entire model domain was also set at 7°C which was approximately the undisturbed average ground temperature in the Winnipeg area (Ferguson & Woodbury, 2004; Mitalas, 1987). Table 4.2 summarizes the boundary conditions used for the base case analyses of both the friction and the end-bearing energy piles.

Table 4.2. Boundary conditions used for the energy piles in Winnipeg

Boundary conditions	Top	Bottom	Left-hand side	Right-hand side
Displacement				
Vertical	Allowed	Not allowed	Allowed	Allowed
Horizontal	Allowed	Not allowed	Not allowed	Not allowed
Hydraulic	Open	Closed	Closed	Open
Thermal	Constant temperature of 20°C (indoor) Varied temperature (seasonal outdoor air temperature)	Constant temperature of 7°C	Closed	Closed

Note: Initial ground temperature was set at 7°C for the entire model domain

4.3.2.1. *Indoor Air Temperature*

In the base case analyses, the indoor air temperature was set at a constant value of 20°C, corresponding to the commonly controlled air temperature inside the buildings. The concrete slab (slab-on-ground) was not placed in the models. However, its effect was represented using the thermal boundary (convective boundary condition) with the assumed overall thermal transmittance value (U-value) of 0.2×10^{-3} kW/m^2/ºC. This value was assumed based on Thomas & Rees (1999) who reported the measured U-values of 0.26 and 0.20×10^{-3} kW/m^2/C for the insulated concrete slab on grade using normal weight concrete and light-weight concrete, accordingly.

4.3.2.2. *Outdoor Air Temperature*

Winnipeg has extreme seasonal temperatures. Winter in Winnipeg, which is defined as a time when the daily mean air temperature remains below 0°C, generally lasts for about five months starting from the first week of November until the first week of April. The coldest month of the year is January with a mean daily air temperature of -16.4°C. A frost depth during winter, which varies significantly based on surface conditions, could reach about -1.8 m (Baracos et al., 1983). CBCNews (2014) reported that the frost line in some places in Winnipeg has reached as deep as -2.5 m in recent years. Spring begins in about mid-April and lasts for only a few weeks. The fall season is also very short. Both of the spring and fall seasons are defined as a period when the mean daily air temperature stays between 0 to 6°C. Summer has the mean daily air temperature that can be as high as 19.7°C in July, which is the hottest month of the year.

Figure 4.3 shows the observed seasonal variation of the mean daily air temperature data for 30 years (from 1981 – 2010) at the Winnipeg Richardson International Airport, which were recorded and maintained by the Environment and Climate Change Canada (ECCC, 2016). The

figure also includes the fitted sine function to the climate data. Note that the 30-year daily average air temperature cycle was then simply projected for 6 years (6 cycles) for the numerical simulations. The sine function as given in the following equation (PLAXIS 2D, 2018) was fitted in this daily average air temperature for the numerical simulations.

$$y(t) = Asin(\omega_0 t + \phi_0) + y_o \; ; \; \omega_0 = 2\pi/B \qquad \text{[Equation 4.1]}$$

where A is the amplitude (18.045°C), B is the wave period (0.0172 rad.), t is time increment (0 to 2160 days), ϕ_0 is initial phase angle (4.172 rad.), and y_0 is a center of harmonic variation (1.645°C).

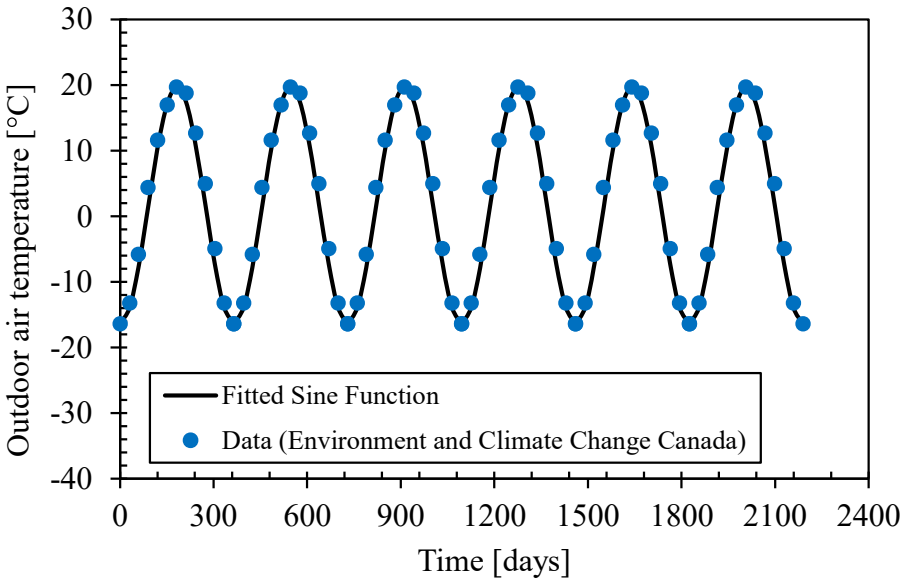

Figure 4.3. Daily average of the outdoor air temperature at the Winnipeg Richardson International Airport (daily average of data from 1981-2010: 30 years)

The convective boundary condition was assigned with assumed overall thermal transmittance value (U-value) of the ground surface of 15×10^{-3} kW/m^2/ºC. This U-value was used because it provided the simulated frost depth of about 2.0 m below the ground surface, which is close to the frost depth of -1.8 m reported in Winnipeg (Baracos et al., 1983). The author is aware

that the frost depth may vary from place to place, depending on the local conditions such as the ground surface cover materials and vegetation.

4.3.3. Modeling Procedures

Modeling procedure used for the Winnipeg energy piles was largely the same as that of the London energy pile case study (see Section 3.2.3). Structural or mechanical loads applied on the pile heads before heating-cooling cycles were assumed to be equal to working loads of the piles. These working loads were estimated using the semi-empirical static method and based on the geotechnical properties of the ground typically found in Winnipeg. From the estimations, the working load of the friction pile with a diameter of 0.4 m and a length 12 m long installed entirely in the Winnipeg lacustrine clay was -235 kN (compression), corresponding to the stress on the pile head of -1870 kPa in the models. Similarly, for the end-bearing pile with a diameter of 0.8 m and a length of 20 m with pile toe embedded in the till, the working load was estimated to be about -1300 kN (compression), corresponding to the stress on the pile head of -2586 kPa. Note that these working loads on the pile heads were calculated from the ultimate pile capacities using partial factors of safety of 2.5 and 3.0 for the shaft resistance and toe resistance, respectively. The detailed geotechnical pile capacity estimations can be found in Appendix H.

In addition to the structural loads, energy piles are also subjected to thermal loads due to heating and cooling by the circulating heat-carrying fluid in the pipes installed inside the piles. In typical operations, the temperature in the piles ranges from 4 to 30°C (Knellwolf et al., 2011). Whereas, Laloui & Di Donna (2011) stated that the value could be from 0 to 50°C. Brandl (2006) reported the highest temperature in the operational thermal-active geostructures was 30°C and the lowest was -0.6°C. In this study, a change of temperature of the fluid in the pipe inside the pile as a function of time from 0 to 40°C was used for the base case analyses as shown Figure 4.4. Note

that the temperatures in the energy pile should not be less than zero degree Celsius to avoid frozen ground occurring around the pile as recommended by GSHPA (2012). The convective boundary condition (line-based internal thermal boundary which implies a circular shell in the axisymmetric models) at 70 mm from the pile shaft was used to represent the heat exchange pipe. This convective boundary condition was used with a thermal transmittance value (U-value) of 1.0 kW/m^2/ºC. Temperature ranges from 0 to 30°C and 0 to 50°C, as shown in Figure 4.5, were also considered in the sensitivity analysis, as discussed in Section 4.5.1.

It was assumed that the changing pattern of the temperature in the pile with time generally follows the rising and falling pattern of the seasonal air temperature. The assumption was made based on the field observation by Brandl (2006) on the operational energy geostructures. The energy piles were subjected to six heating-cooling cycles, corresponding to six years of heating and cooling of the building. Here, the term at the end of heating (EOH) means the pile was heated to the maximum temperature (the peak). Likewise, the term at the end of cooling (EOC) means the pile was cooled to the minimum temperature (the trough) in the particular year. The numerical simulations were carried out in a time series as summarized in Table 4.3. For instance, the simulations at the end of heating and the end of cooling in the first year (denoted by EOH, 1st Yr and EOC, 1st Yr) would have the simulation times of 181 days and 365 days, respectively.

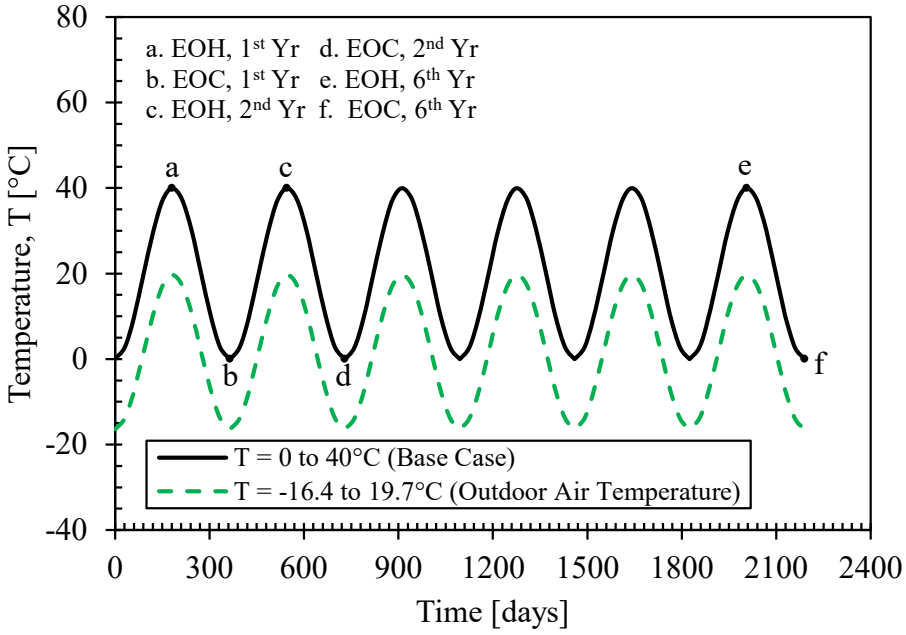

Figure 4.4. Thermal loads in the pile in terms of temperature changes with time starting from the 1st of January

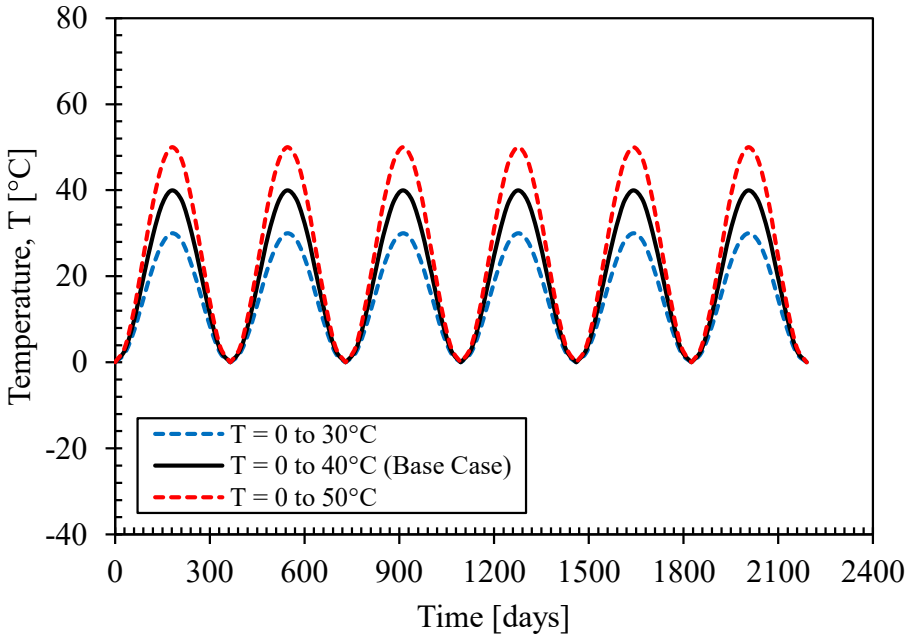

Figure 4.5. Various thermal load ranges in the pile in terms of temperature changes with time starting from the 1st of January

Table 4.3. Simulation series considered for the Winnipeg energy piles

Simulation series for the Winnipeg energy piles		Simulation time [days]
a. At the end of heating in the first year	EOH, 1st Yr	181
b. At the end of cooling in the first year	EOC, 1st Yr	365
c. At the end of heating in the second year	EOH, 2nd Yr	546
d. At the end of cooling in the second year	EOC, 2nd Yr	730
e. At the end of heating in the sixth year	EOH, 6th Yr	2006
f. At the end of coolinng in the sixth year	EOC, 6th Yr	2190

4.4. Results and Discussion of Base Case Analyses of Winnipeg Energy Piles

In this section, the numerical results from the base case analyses using the base case model parameters of the generic or hypothetical friction and end-bearing energy piles in Winnipeg were reported and discussed.

4.4.1. Temperature and Porewater Pressure Distributions

Friction energy pile:

Simulated ground temperature profiles outside the building located at 15 m away from the edge of the building are shown in Figure 4.6. As seen in the figure, the ground temperature fluctuated significantly throughout the years from the ground surface to about -3 m due to the seasonal change in the ambient air temperature. However, at the depth from about -5 m to -15 m, the ground temperature variation was very minimal. Below -15 m, the ground temperature stayed constant throughout the years. Note that the estimated frost depth, where the ground temperature was equal to zero in the winter, was about -2.0 m in comparison with the reported value of -1.8 m in Winnipeg area (Baracos et al., 1983).

Temperature profiles along the pile-soil interface at the end of heating (EOH) and end of cooling (EOC) are provided in Figure 4.7. The temperatures were relatively constant with depths, except reductions (roll-offs) near the pile head and pile toe due to mechanisms of heat transfer at this pile ends. The temperatures slightly increased with the increase in the simulation times. At the mid-depth of the pile (-6 m), the temperature was 37.1ºC at the EOH in the 1st year, comparing with 37.6ºC in the 6th year. This gave an increase in temperature of 1.3%. Even though this difference is insignificant, it shows that temperatures along the pile-soil interface trend to increase with time. This was due to the influence of heat loss through the ground floor slab that accumulated in the ground underneath the building with time and the imbalance in thermal loads during heating and cooling periods in relation to the initial ground temperature (more details of these temperature distributions can be found in Appendix C.1).

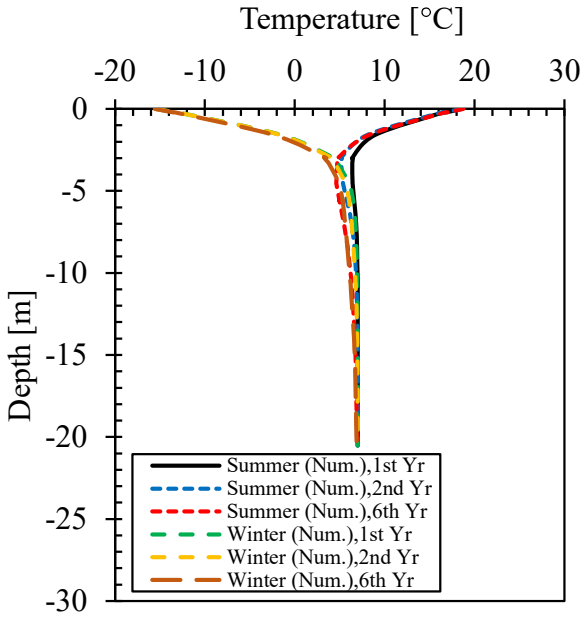

Figure 4.6. Ground temperature profiles outside the building (20 m away from the building edge) for the friction energy pile (base case)

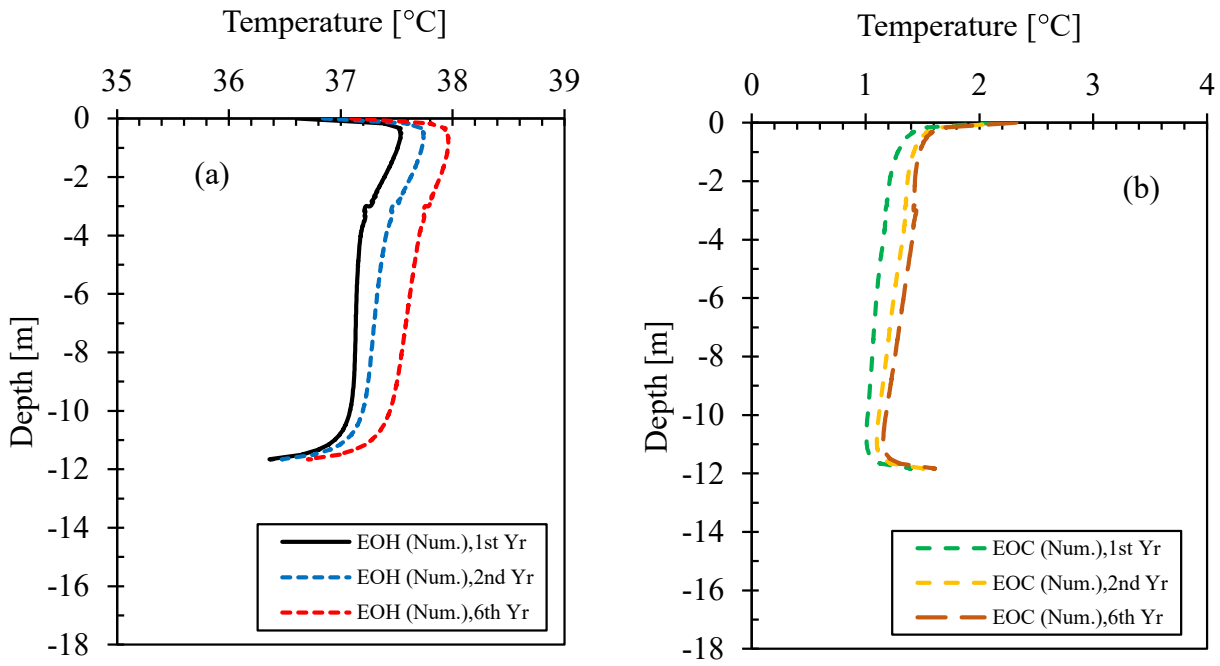

Figure 4.7. Temperature profiles along the pile-soil interface (a) at the end of heating (EOH) and (b) at the end of cooling (EOC) in the 1st, 2nd, and 6th year for the friction energy pile (base case)

The radial temperature profiles through a horizontal cross-section at the mid-depth of the pile to 15 m away from the pile center are illustrated in Figure 4.8. At the end of heating, it can be seen that the temperatures dropped sharply from the pile center to 2 m away. Outside this distance, the changes in temperatures were small. Likewise, at the end of cooling, the temperatures increase steeply from the center of the pile to a distance of about 2 m. There were minimal changes beyond this point. Note that there was the overall temperature increase over time in the soil domain due to the heat transfer from the ground floor slab and the imbalance in thermal loads during heating and cooling periods in relation to the initial ground temperature.

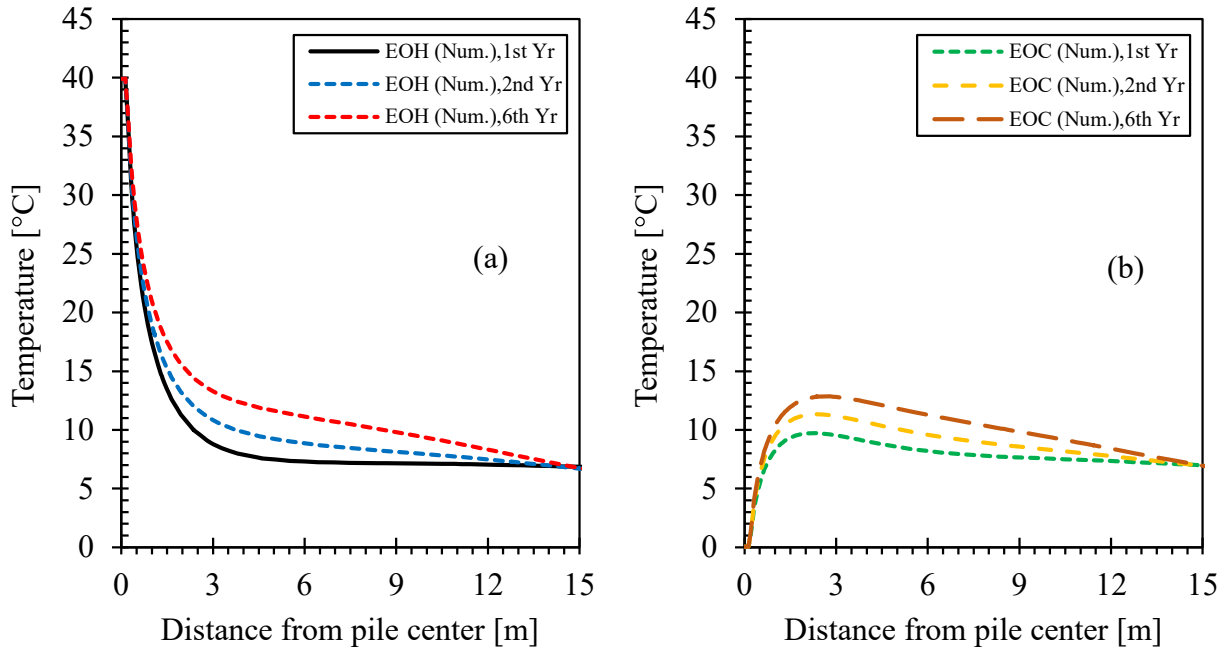

Figure 4.8. Temperature profiles at mid-depth of the pile from the pile center to 15 m (a) at the end of heating (EOH) and (b) at the end of cooling (EOC) in the 1st, 2nd, and 6th year for the friction energy pile (base case)

The thermally induced excess porewater pressure profiles in the surrounding ground at the end of heating and cooling in the first, second, and sixth year for the base case analyses are shown in Figure 4.9. As seen in Figure 4.9(a), the excess porewater pressures (EPWPs) were induced in the clay layer with low permeability. Heating produced positive EPWPs with the maximum values of -6.7, -6.4, and -5.1 kPa at the EOH in the 1st, 2nd, and 6th year, accordingly. Similarly, the maximum value of EPWP of -4 kPa was obtained from a heating test on normally consolidated kaolin clay with a change in temperature of 20ºC (Britto et al. as cited in Ng et al. (2014)). From the energy pile centrifuge tests in clays (Ng et al., 2014), it was also found that the EPWPs reduced from -34 kPa in the first thermal cycle to -24 kPa in the fifth cycle. As the numerical results showed, the EPWPs at the EOH in the Winnipeg clay adjacent to the energy pile slightly reduced with time (about 23.9% reduction from 1st year to 6th year). This reduction in EPWPs may be partially due to the consolidation. Another reason may result from the lesser temperature difference

between the pile and surrounding ground at the end of heating due to overall ground warming. The opposite occurred during cooling in which the negative EPWPs were generated with the maximum values of 3.7, 4.2, and 4.5 kPa at the EOC in the 1st, 2nd, and 6th year. Therefore, the negative EPWPs somewhat increased with time by 17.8% from the 1st to 6th year, resulting from the larger temperature difference between the pile and surrounding ground at the end of cooling due to overall ground warming. Figure 4.9(b) shows the EPWP profiles through a horizontal cross-section at mid-depth of the pile from the pile-soil interface to 15 m away. The porewater pressure change occurred within a distance of 8 m (20D) from the pile-soil interface with maximum values adjacent to the pile.

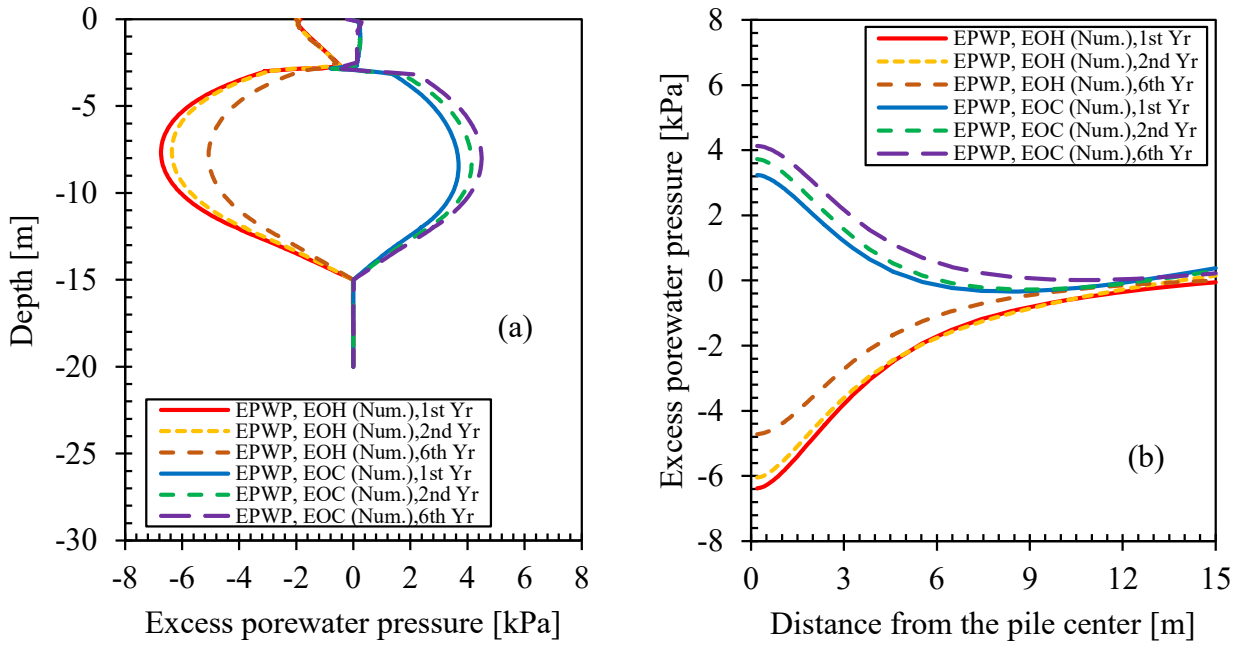

Figure 4.9. Thermally induced excess porewater pressures (EPWPs) (a) along the pile-soil interface to 20D below the pile toe (b) at mid-depth of the pile from pile center to 15 m in the 1st, 2nd, and 6th year for the friction energy pile (base case)

End-bearing energy pile:

As shown in Figure 4.10, the temperature profiles along the pile-soil interface were relatively constant in the clay layer. The small reductions in the till layer were observed that may be due to lower specific heat capacity and higher thermal conductivity of the till. The roll-offs of temperature profiles were again observed near the pile ends. There were little changes (increased from 38.5 to 38.7ºC and from 7.9 to 8.9ºC) in the maximum temperature values at the EOH and the EOC from the first to sixth year, respectively. Nonetheless, the ground temperatures seem to increase marginally with time. Figure 4.11 shows the horizontal temperature profiles at the mid-depth of the pile from the center of the pile to 15 m away at the EOH and the EOC. As seen in the figures, large changes in the ground temperatures only occurred within a distance of about 2 m from the pile center.

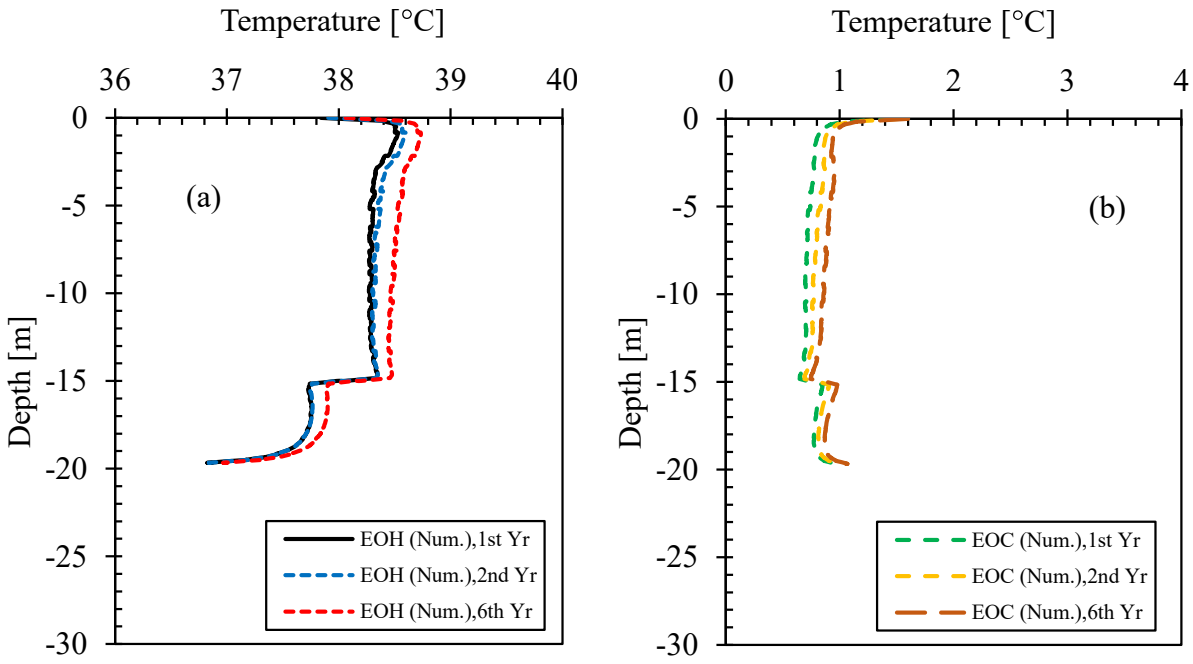

Figure 4.10. Temperature profiles along the pile-soil interface (a) at the end of heating (EOH) and (b) at the end of cooling (EOC) in the 1st, 2nd, and 6th year for the end-bearing energy pile (base case)

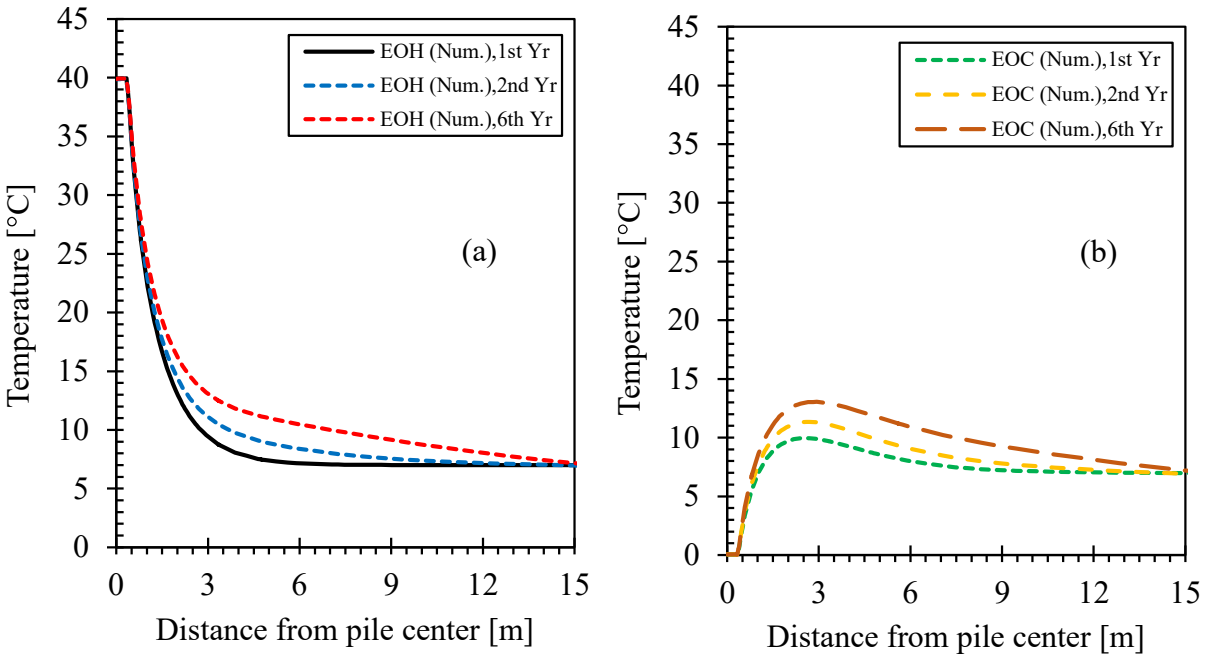

Figure 4.11. Temperature at mid-depth of the pile from the pile center to 15 m (a) at the end of heating (EOH) and (b) at the end of cooling (EOC) in the 1st, 2nd, and 6th year for the end-bearing pile (base case)

The thermally induced excess porewater pressure (EPWP) profiles in the surrounding ground at the end of heating and cooling in the first, second, and sixth year for the end-bearing energy pile are shown in Figure 4.12. Similar EPWP distributions in the clay layer to those of the friction energy pile were observed in which heating induced negative EPWPs and cooling produced positive EPWPs. Note that there were no EPWPs induced in the till layer located below -15 m because of its high hydraulic conductivity. As shown in Figure 4.12(a), the maximum value of EPWPs at the EOH was in the 1st year (-9.1 kPa) and at the EOC in the 6th year (6.6 kPa). The porewater pressure changes occurred within a distance of about 9 m (11D) from the pile-soil interface where the maximum values were generated as shown in Figure 4.12(b).

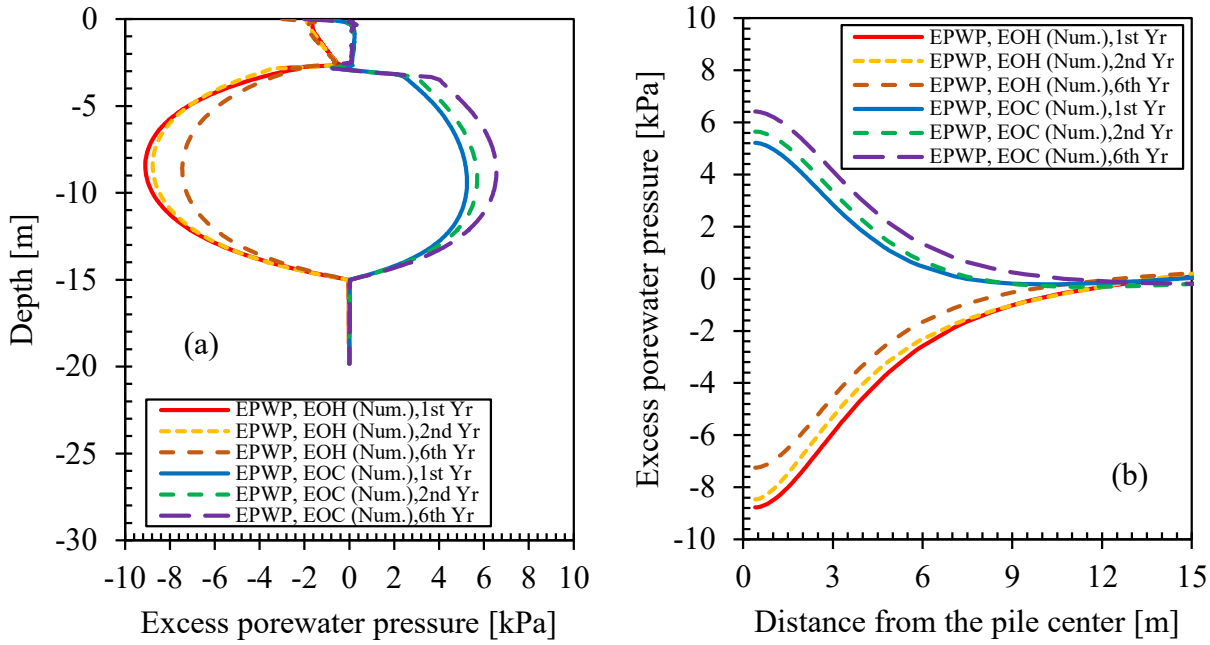

Figure 4.12. Thermally induced excess porewater pressures (EPWPs) (a) along the pile-soil interface (b) at mid-depth of the pile from pile center to 15 m in the 1st, 2nd, and 6th year for the end-bearing energy pile (base case)

4.4.2. Pile Vertical Displacement

Friction energy pile:

The simulated vertical pile head displacements during six-year heating and cooling cycles for the friction energy pile are shown in Figure 4.13. The mechanical load (M) caused a pile head settlement of -2.01 mm (-0.50% D). When the pile heated, with the applied mechanical maintained on the pile head, upward movements or uplifts were induced. In contrast, when the pile cooled, downward movements or settlements occurred. The uplift-settlement trend moved downwards gradually when the number of thermal cycles increased. This downward trend (also known as ratcheting settlements) of the pile head during thermal cycles. This settlement phenomenon was also observed in the centrifuge tests of energy piles in clays subjected to five thermal cycles (Ng et al., 2014). The ratcheting settlements were probably due to the accumulated plastic strains occurred in soils surrounding the pile which in turn were caused by thermal cyclic loading. As also mentioned in GSHPA (2012) applying thermal cycles repeatedly on the energy pile would result in accumulated settlements. The dissipations of excess porewater pressures in the clay layer may also contribute to the continuing settlements. The pile head uplifts due to thermo-mechanical loads at the end of heating (EOH) in the 1st and 6th year were 0.28 mm (0.07% D) and 0.04 mm (0.01% D), correspondingly. This gave a reduction in the pile head uplift of 85.71%. At the end of cooling (EOC) in the 1st and 6th year, the pile head settlements were -0.85 mm (0.21% D) and -0.96 mm (0.24% D), leading to an increase in the settlement of 12.94%. Figure 4.14 shows the pile vertical displacements along the pile length at the EOH and the EOC in the first, second, and sixth year. The displacement profiles observed were slightly different in terms of their positions.

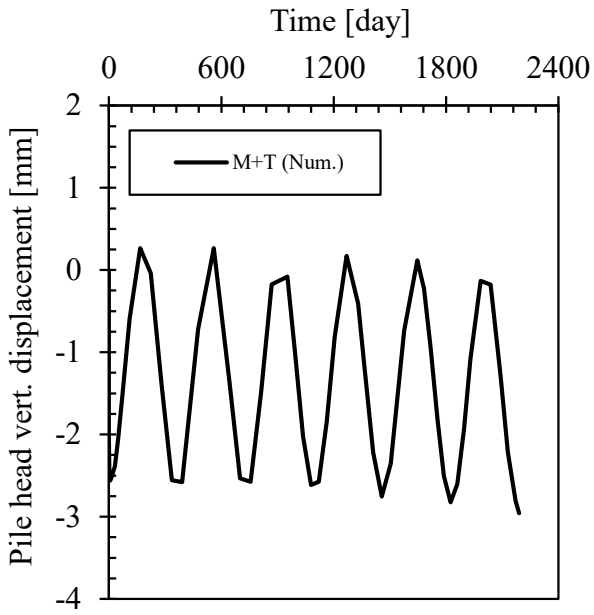

Figure 4.13. Pile head vertical displacements during cooling-heating cycles for the friction energy pile (base case)

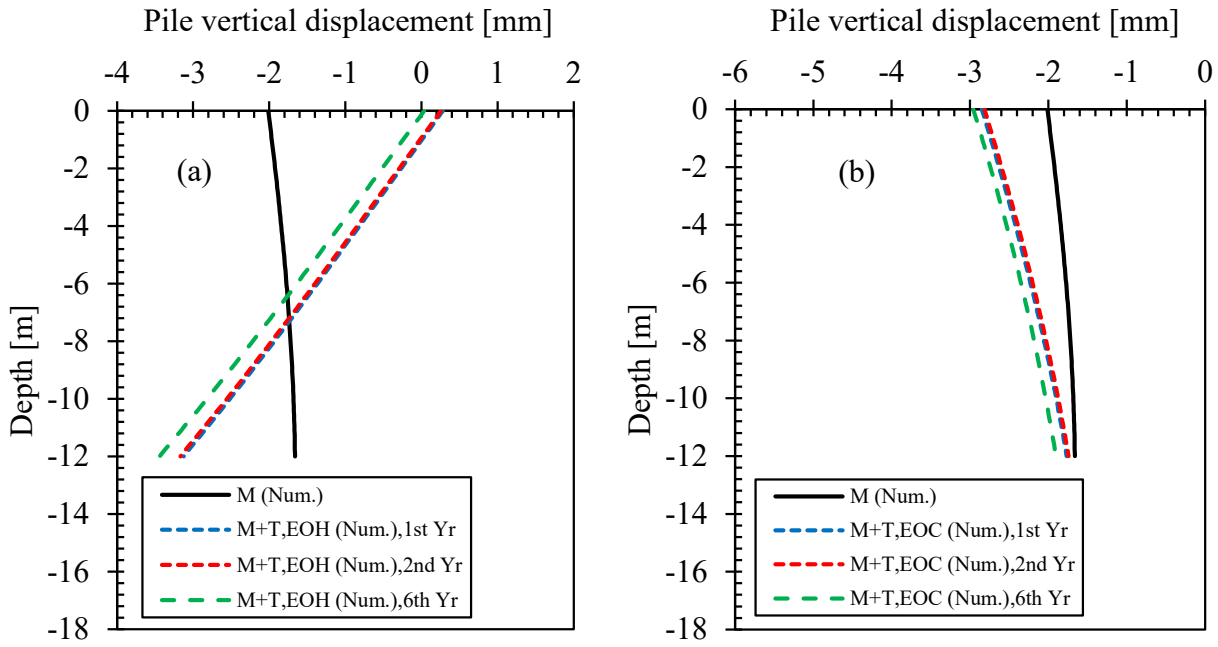

Figure 4.14. Pile vertical displacement profiles (a) at the end of heating (EOH) and (b) at the end of cooling (EOC) in the 1st, 2nd, and 6th year for the friction energy pile (base case)

End-bearing energy pile:

Figure 4.15 shows the simulated vertical pile head displacements (settlements and uplifts) for six-year heating and cooling for the end-bearing energy pile. The mechanical load (M) caused a pile head settlement of -1.89 mm (-0.24% D). The thermal cycles caused to pile head displacements to move downwards gradually (a phenomenon of ratcheting settlements). As mentioned previously, this was because of the cyclic accumulated plastic strains in the surrounding soils as well as the dissipations of excess porewater pressures in the clay layer. At the end of heating (EOH) in the 1st and 6th year, the uplifts of the pile head of 2.78 mm (0.35% D) and 0.52 mm (0.07% D) were obtained, a drop of 81.29%. On the other hand, the settlements at the end of cooling (EOC) in the 1st and 6th year were -4.18 mm (-0.52% D) and -5.91 mm (-0.74% D), increasing by 41.39%. Figure 4.16 shows the vertical pile displacement profiles along the pile length at different simulated times. As can be seen, the displacement profiles changed from the 1st to 6th year of heating and cooling. Table 4.4 gives a summary of pile head displacements (uplifts and settlements) induced by the combination of thermal and mechanical loads for both friction and end-bearing energy piles.

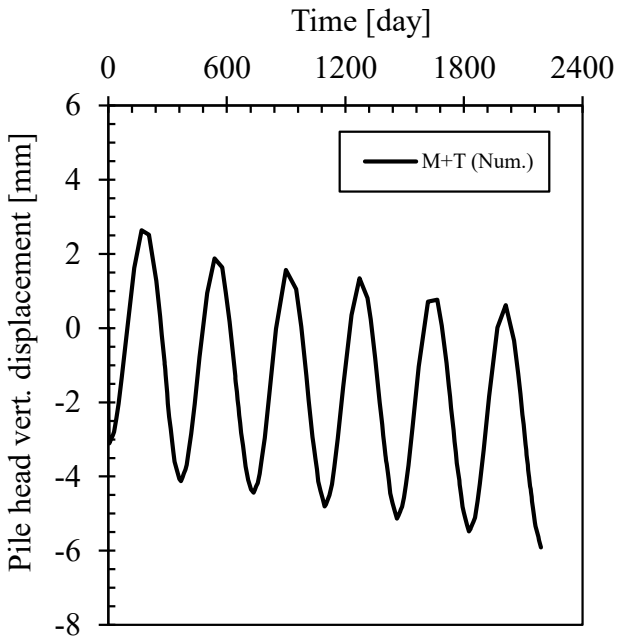

Figure 4.15. Pile head vertical displacements during cooling-heating cycles for the end-bearing energy pile (base case)

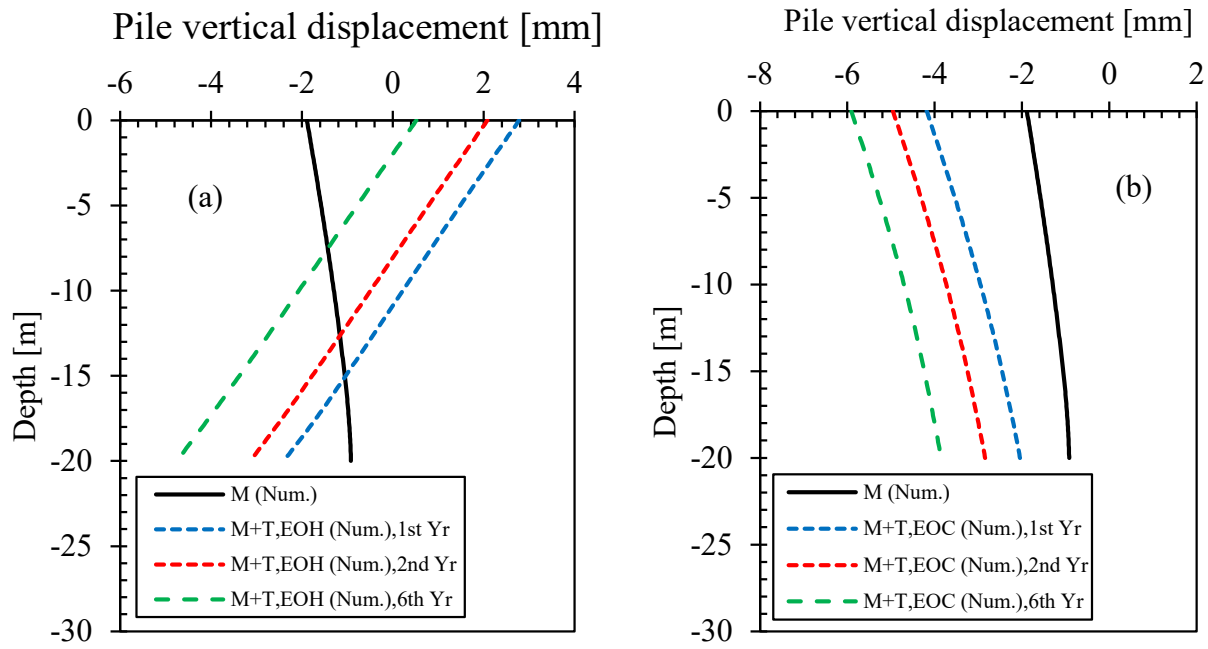

Figure 4.16. Pile vertical displacement profiles (a) at the end of heating (EOH) and (b) at the end of cooling (EOC) in the 1st, 2nd, and 6th year for the end-bearing energy pile (base case)

Table 4.4. Summary of simulated uplifts and settlements due to thermo-mechanical loads for Winnipeg energy piles

Energy pile names	Applied mechanical load (M) [kN]	Initial temp. [ºC]	Range of applied temp. [ºC]	Temp. change from init. value [ºC]	Pile head displacement due to thermo-mechanical loads M+T) [mm]	[% D]	Remark
Winnipeg friction energy pile (D =0.4 m and L =12 m)							
At the EOH, uplift	-235	7	0 to 40	33	0.28	0.07	At the EOH (1st year)
At the EOC, settlement	-235	7	0 to 40	-7	-0.96	-0.24	At the EOC (6th year)
Winnipeg end-bearing energy pile (D =0.8 m and L =20 m)							
At the EOH, uplift	-1300	7	0 to 40	33	2.78	0.35	At the EOH (1st year)
At the EOC, settlement	-1300	7	0 to 40	-7	-5.91	-0.74	At the EOC (6th year)

M = mechanical load, T = thermal load, M+T = thermo-mechanical load
EOH = end of heating, EOC = end of cooling

4.4.3. Pile Axial Strain Distribution

Friction energy pile:

The mechanical load (M) produced contractive strains (negative) in the entire pile length as shown in Figure 4.17. Expansive strains (positive) were induced due to the thermal heating in contradiction with the mechanical load as shown in Figure 4.18. At the end of heating, slightly lower strains were observed with lower simulated times, 1st, 2nd, and 6th year, accordingly. The thermally induced expansive strain at the EOH in the 1st year was 309.48 με and in the 6th year was 316.39 με (2.23% increase). Cooling the pile generated contractive strains, as shown in Figure 4.19, with lower contractive strains at the EOC in the 6th year.

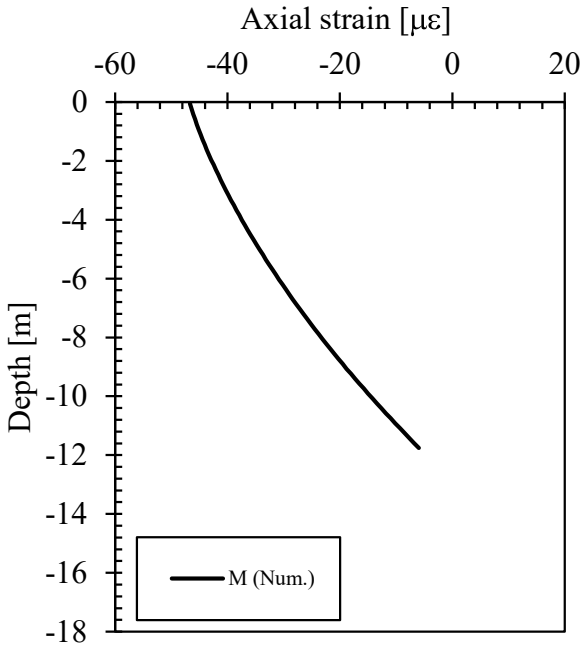

Figure 4.17. Axial strain profile due to the mechanical load (M) only for the friction energy pile (base case)

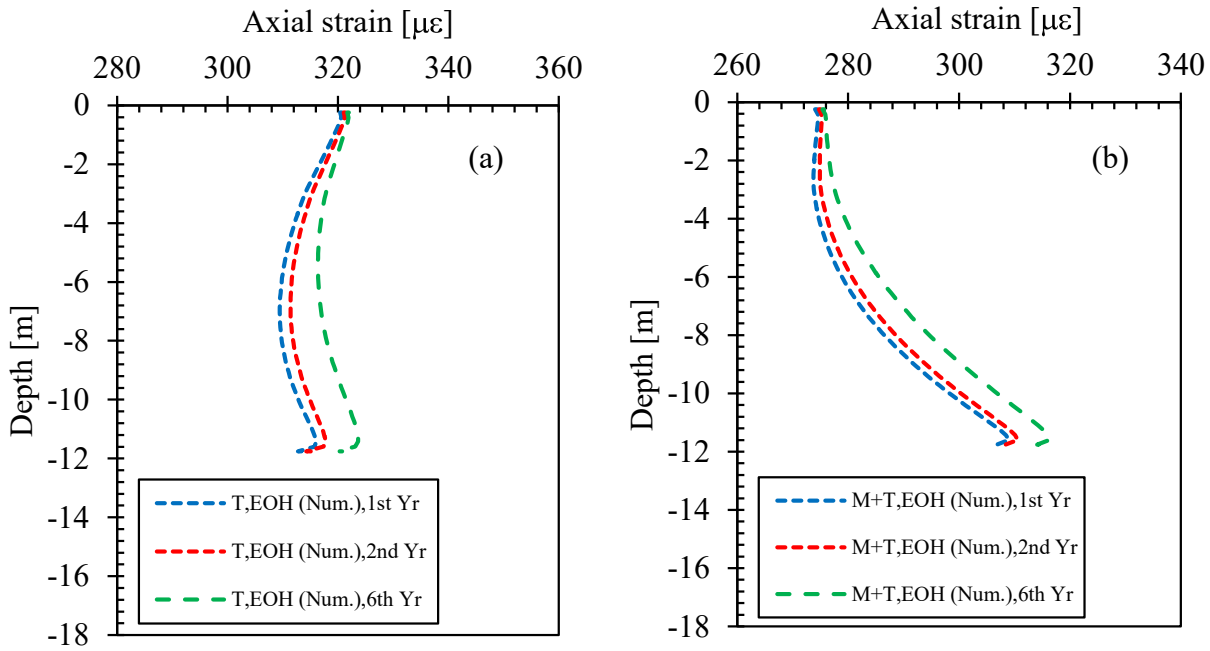

Figure 4.18. Axial strain profiles (a) thermal (T) and (b) thermo-mechanical (M+T) at the end of heating (EOH) in the 1st, 2nd, and 6th year for the friction energy pile (base case)

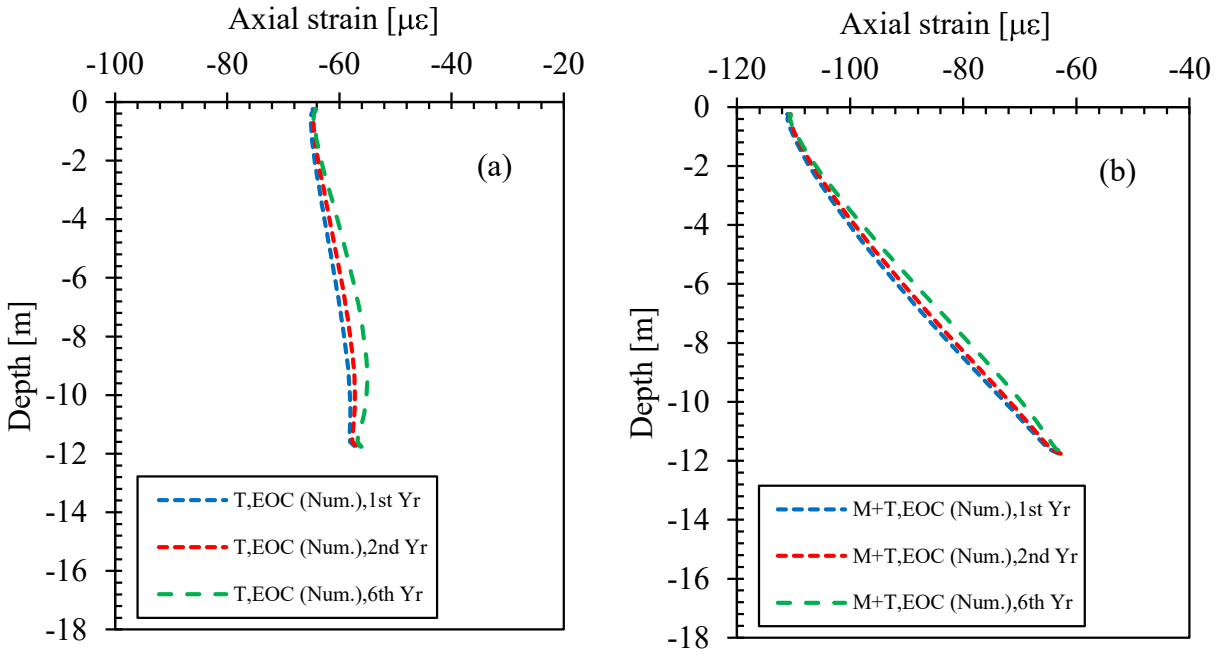

Figure 4.19. Axial strain profiles (a) thermal (T) and (b) thermo-mechanical (M+T) at the end of cooling (EOC) in the 1st, 2nd, and 6th year for the friction energy pile (base case)

End-bearing energy pile:

Similar phenomena occurred for the end-bearing energy pile during the heating-cooling cycles. Figure 4.20 shows the contractive strain profile due to the mechanical load. Figure 4.21(a) shows expansive strain profiles induced by heating alone. The strains at the EOH in the 6th year were generally higher than in the 1st year. The strains induced by a combination of thermal and mechanical loads were plotted in Figure 4.21(b) which also gave higher strains at the end of the 6th year of heating. Figure 4.22(a) shows the contractive strains caused by cooling in which lower strains were observed in the pile at the EOC for the higher simulated times. The resulted thermo-mechanically induced strain profiles are given in Figure 4.22(b).

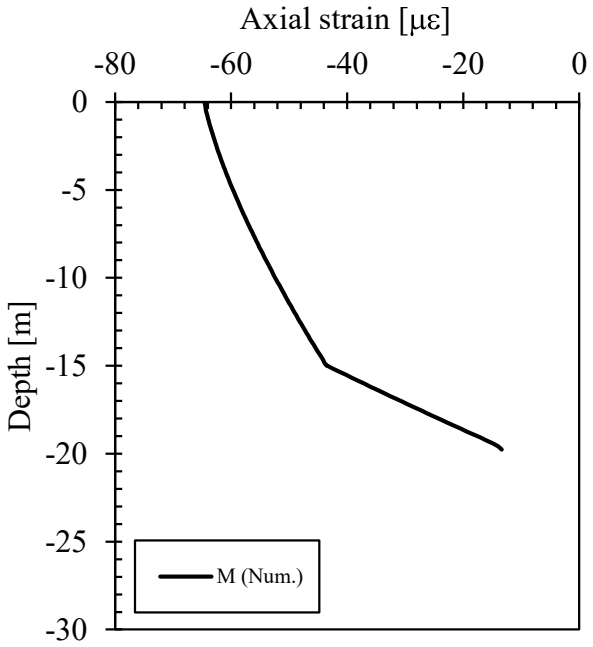

Figure 4.20. Axial strain profile due to the mechanical load (M) for the end-bearing energy pile (base case)

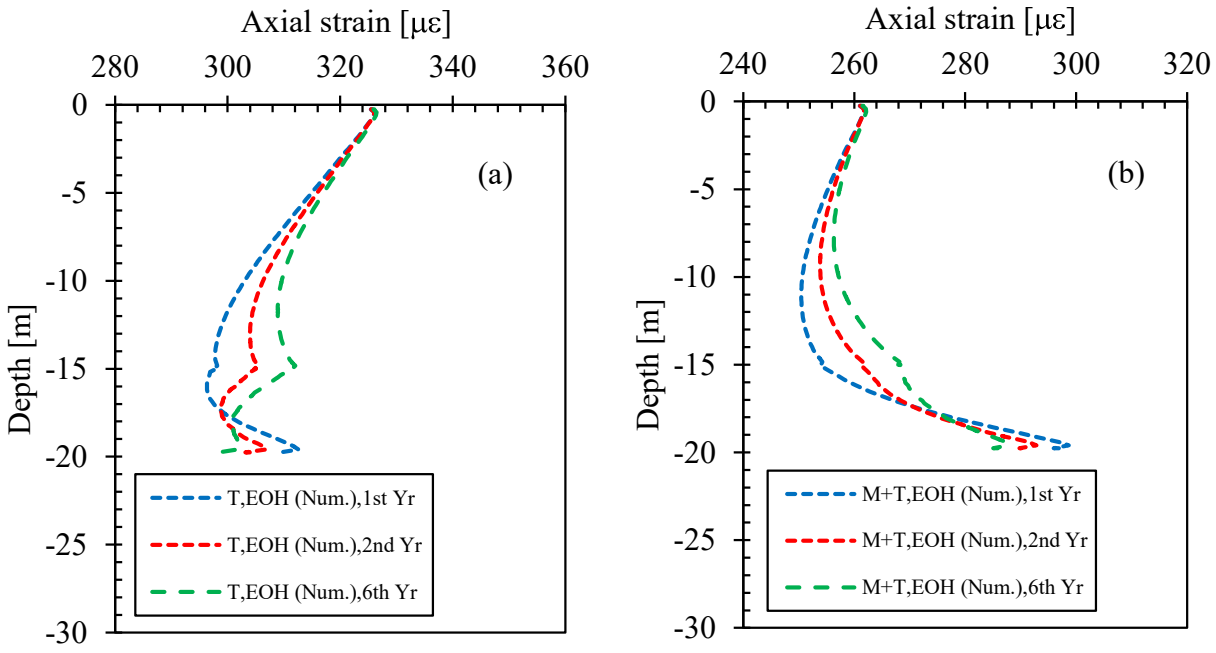

Figure 4.21. Axial strain profiles (a) thermal (T) and (b) thermo-mechanical (M+T) at the end of heating (EOH) in the 1st, 2nd, and 6th year for the end-bearing energy pile (base case)

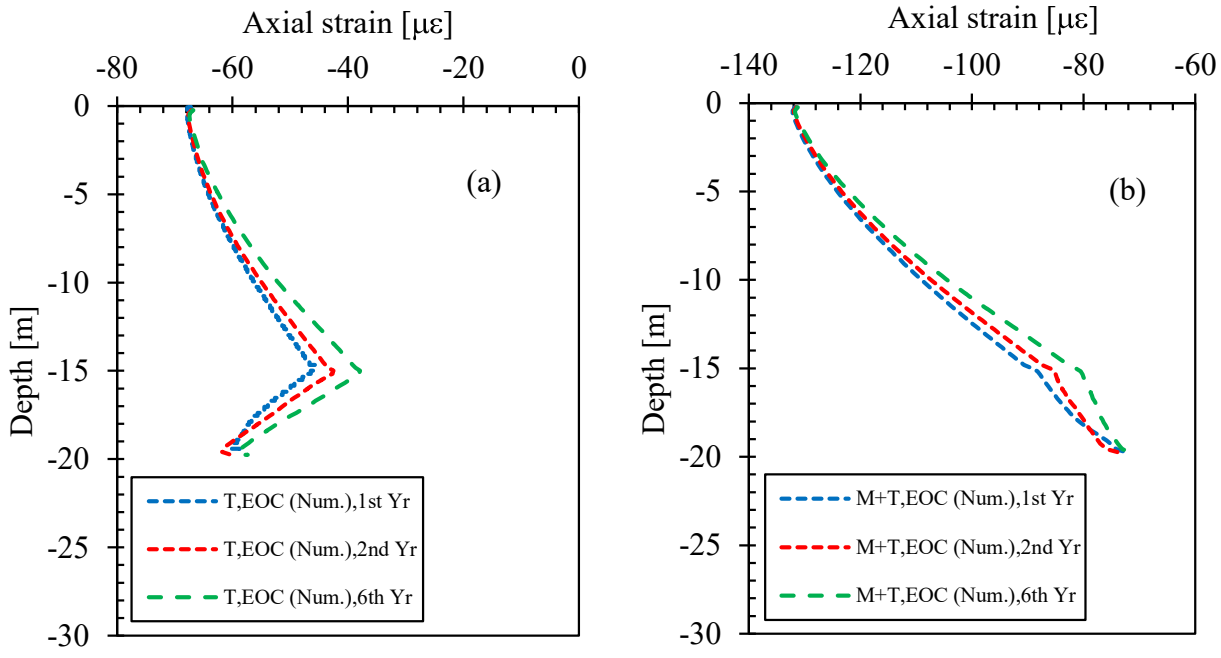

Figure 4.22. Axial strain profiles (a) thermal (T) and (b) thermo-mechanical (M+T) at the end of cooling (EOC) in the 1st, 2nd, and 6th year for the end-bearing energy pile (base case)

4.4.4. Pile Axial Load Distribution

Friction energy pile:

Figure 4.23 shows the axial load profiles generated in the friction energy pile. It can be seen that the mechanical load of -235 kN applied on the pile head transferred to the surrounding ground, reducing with the depth almost linearly. As seen in Figure 4.23(a), the thermally induced compressive loads due to heating along the pile were lower with longer simulated times. This was due to the smaller temperature difference in the pile and the surrounding ground caused by the overall warming of the model domain. This overall ground warming was caused by the heat loss through the ground floor slab and also the thermal heating-cooling imbalance of the pile. The maximum values at the EOH in the 1st, 2nd, and 6th year were -109, -96 and -71 kN, accordingly. This gave a fall of 35% from the 1st to 6th year. The thermo-mechanically induced compressive

load profiles are shown in Figure 4.23(b) with the highest compressive (M+T, EOH) obtained in the 1st year of heating (-293 kN). The load values then reduced with simulated times, reaching –278 kN at the EOH in the 6th year. This led to a decrease in the maximum combined compressive load of 5.4%.

In contrast to the heating, the cooling induced tensile loads (positive) in the pile as shown in Figure 4.24(a). Therefore, for the thermo-mechanical loads at the EOC, the compressive loads in the pile were reduced, especially in the lower part of the pile near the pile toe as shown in Figure 4.24(b). At the EOC in the 6th year, slightly higher tensile loads (T, EOC) were produced (79 kN max.) in comparison with the values in the 1st year (67 kN max.) and 2nd year (69 kN max.), increasing by 16% from the 1st to the 6th year. The combined effects of thermal and mechanical loads (M+T, EOC) also created small tensile loads near the pile toe with the maximum values of 9 kN, 11 kN, and 15 kN in the 1st, 2nd, and 6th year, accordingly.

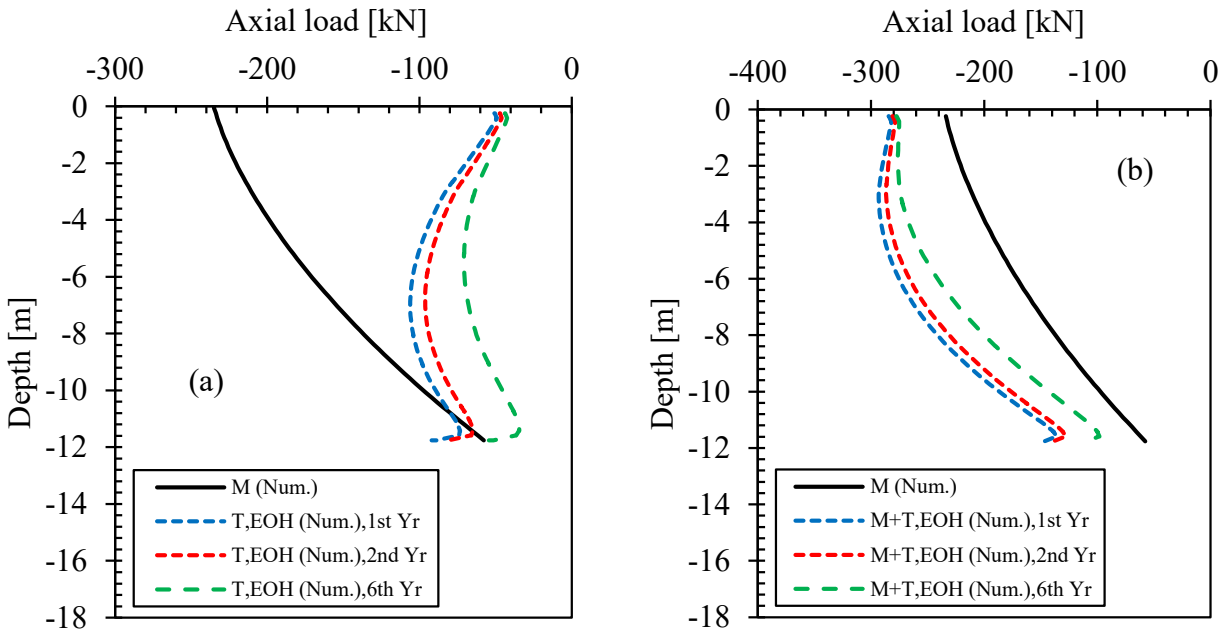

Figure 4.23. Axial load profiles (a) thermal (T) and (b) thermo-mechanical (M+T) at the end of heating (EOH) in the 1st, 2nd, and 6th year for the friction energy pile (base case)

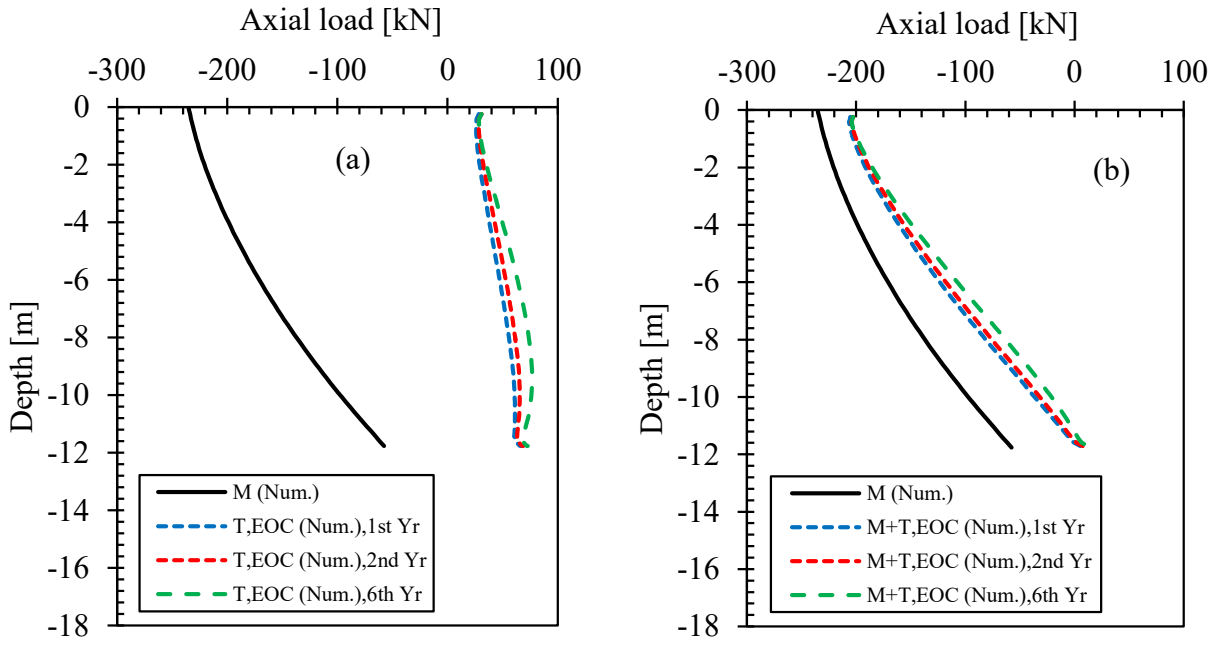

Figure 4.24. Axial load profiles (a) thermal (T) and (b) thermo-mechanical (M+T) at the end of cooling (EOC) in the 1st, 2nd, and 6th year for the friction energy pile (base case)

End-bearing energy pile:

For the end-bearing energy pile, the mechanical load of -1300 kN was applied on the pile head. The mechanical load profile was plotted in all figures for reference as shown in Figure 4.25 and Figure 4.26. As seen in the figures, the mechanical load transferred mostly into the till layer, located below -15 m, beneath the Winnipeg clay (lacustrine clay). Thermally induced compressive loads, Figure 4.25(a), were -699 kN at the EOH in the 1st year. This value reduced to -654 kN in the 6th year (a fall of 6.4%). As shown in Figure 4.25(b), at the EOH, the axial compressive loads increased in the pile as a result of thermo-mechanical loads. This was because heating induced additional compressive loads in the pile. The maximum value of -699 kN (≈ 54% of M) occurred in the 1st year. The values reduced marginally for the later years, reaching -651 kN in the 6th year (6.9% decrease).

The thermally induced tensile load profiles at the EOC are plotted in Figure 4.26(a). Considerable tensile loads were generated in the pile during cooling. The maximum values located at about -15 m were 494 kN (at the EOC, 1st year), 555 kN (at the EOC, 2nd year), and 649 kN (at the EOC, 6th year). This shows an increase in the thermally induced tensile load of 31.3% from the 1st to 6th year. As shown in Figure 4.26(b), even though there were large reductions of the mechanical loads due to pile cooling, especially at -15 m elevation which is the interface between the clay and till, no tensile loads were induced for the thermo-mechanical effects.

Table 4.5 provides a summary of thermally induced loads in the pile at the end of heating and at the end of cooling for both friction and end-bearing energy piles.

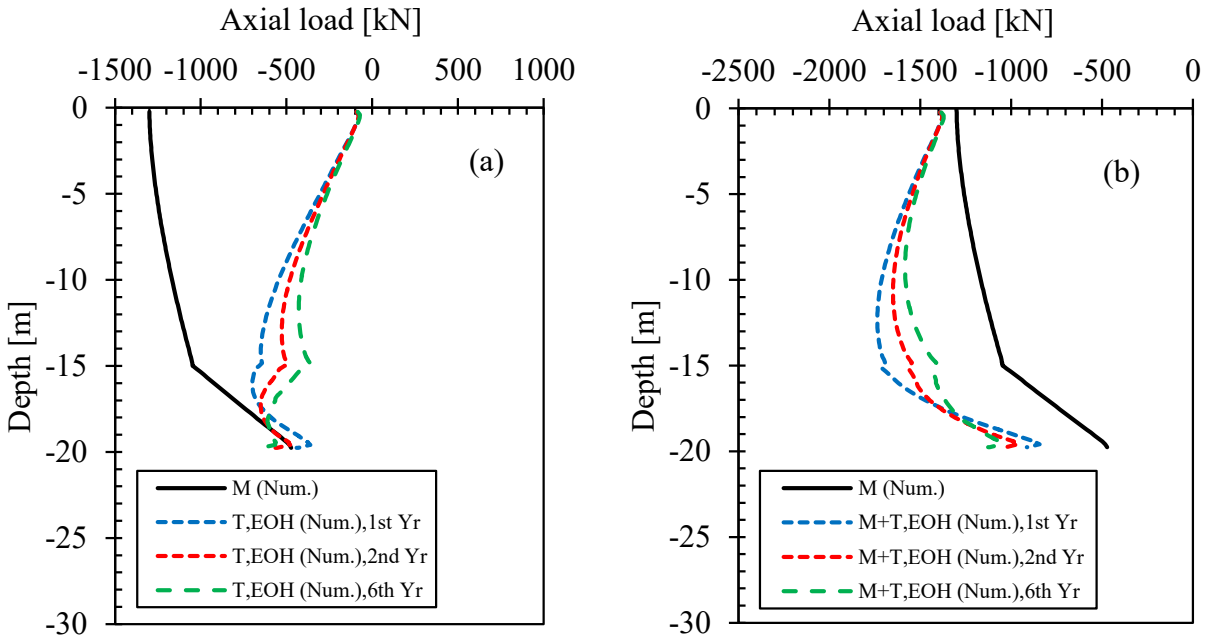

Figure 4.25. Axial load profiles (a) thermal (T) and (b) thermo-mechanical (M+T) at the end of heating (EOH) in the 1st, 2nd, and 6th year for the end-bearing energy pile (base case)

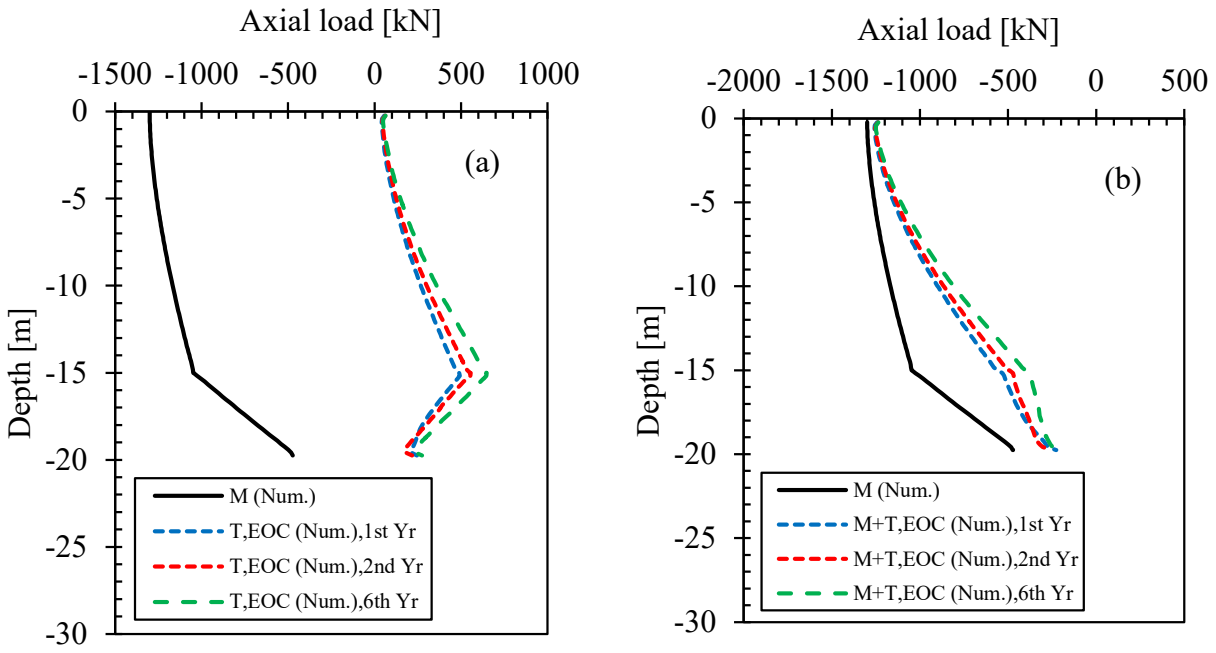

Figure 4.26. Axial load profiles (a) thermal (T) and (b) thermo-mechanical (M+T) at the end of cooling (EOC) in the 1st, 2nd, and 6th year for the end-bearing energy pile (base case)

Table 4.5. Summary of thermally and thermo-mechanically induced loads in the pile for Winnipeg energy piles

Energy pile names	Applied mech. load (M)	Initial temp.	Range of applied temp.	Temp. change from init. value	Max. axial load in the pile due to thermal load (T)			Max. axial load in the pile due to thermo-mech. loads (M+T)		Remark
	[kN]	[ºC]	[ºC]	[ºC]	[kN]	[kN/ ºC]	[%M]	[kN]	[% M]	
Winnipeg friction energy pile (D=0.4 m and L=12 m)										
At the EOH	-235	7	0 to 40	33	-109.09	-3.31	-46.42	-293.26	-124.79	At the EOH (1st year)
At the EOC	-235	7	0 to 40	-7	78.67	11.24	33.48	-204.28	-86.93	At the EOC (6th year)
Winnipeg end-bearing energy pile (D=0.8 m and L=20 m)										
At the EOH	-1300	7	0 to 40	33	-699.26	-21.19	-53.79	-1735.73	-133.52	At the EOH (1st year)
At the EOC	-1300	7	0 to 40	-7	648.46	92.64	49.88	-1250.23	-96.17	At the EOC (6th year)

M = mechanical load, T = thermal load, and M+T = thermo-mechanical load
EOH = end of heating, EOC = end of cooling

4.4.5. Mobilized Shaft Friction

Friction energy pile:

Figure 4.27(a) and Figure 4.27(b) shows the mobilized shaft friction along the pile-soil interface at the EOH and at the EOC in the 1st, 2nd, and 6th year. As seen in these figures, the positive skin friction was mobilized along the entire pile length due to the mechanical load (M). During heating, the upper half of the pile moved up relative to the surrounding soils, caused the shaft friction to decrease and created a small amount of negative skin friction. In the lower half, however, the pile moved down and induced higher shaft friction. During cooling, shaft friction was increased along the pile, except near the pile toe where the shaft friction was reduced. This was because the pile contracted more in relation to the surrounding soils as the pile was cooled. There were minimal changes in the shaft friction profiles with different simulated times.

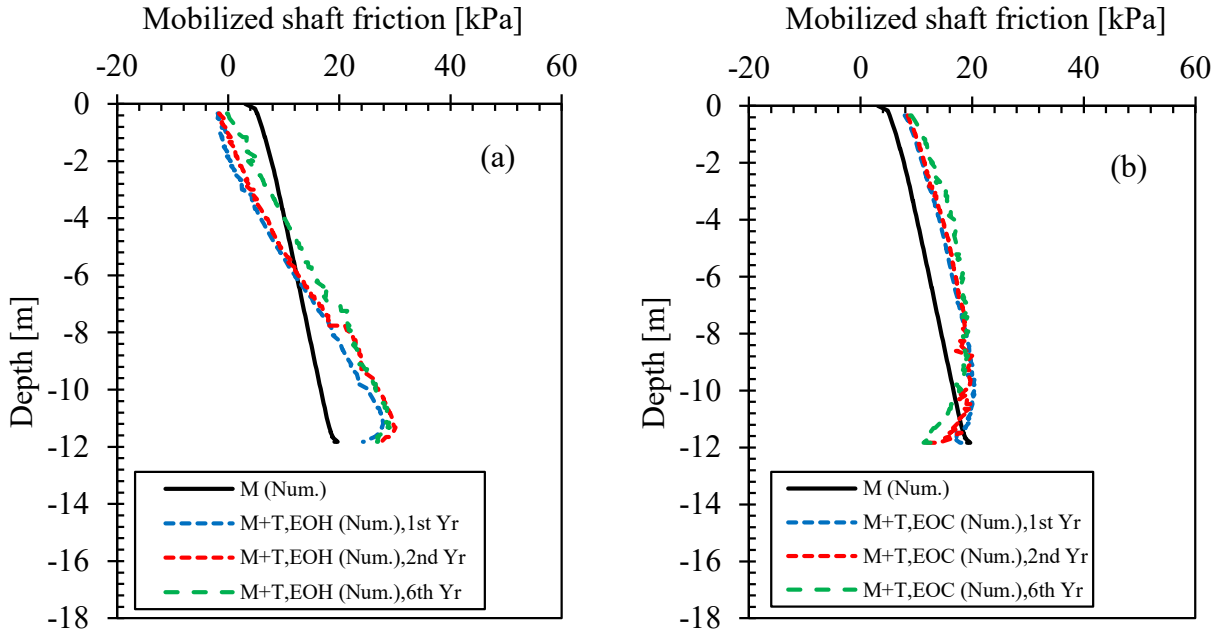

Figure 4.27. Mobilized shaft friction along the pile-soil interface (a) at the end of heating (EOH) and (b) at the end of cooling (EOC) in the 1st, 2nd, and 6th year for the friction energy pile (base case)

End-bearing energy pile:

Figure 4.28 shows the mobilized shaft friction along the pile-soil interface at the EOH and at the EOC in the 1st, 2nd, and 6th year. Again, it was observed that the mechanical load induced positive skin friction along the whole pile length. Larger values (51 kPa max.) were mobilized in the till layer below -15 m depth than in the overlying clay layer (25 kPa max.) because the till has much higher stiffness and strength. At the end of heating (EOH), the shaft friction in the upper two-third of the pile reduced and resulted in negative values. In the lower one-third; however, the shaft friction increased considerably. Conversely, at the end of cooling (EOC), the shaft friction increased in the upper two-third portion, but it reduced in the lower one-third part where the pile was installed through the till layer. Some irregularities in shaft friction in the till were observed as shown in the graph. This may be due to a sudden change in the soil stiffness from a very low value in the clay to a very high value in the till and also high permeability of the till which somehow caused oscillations in the THM computations.

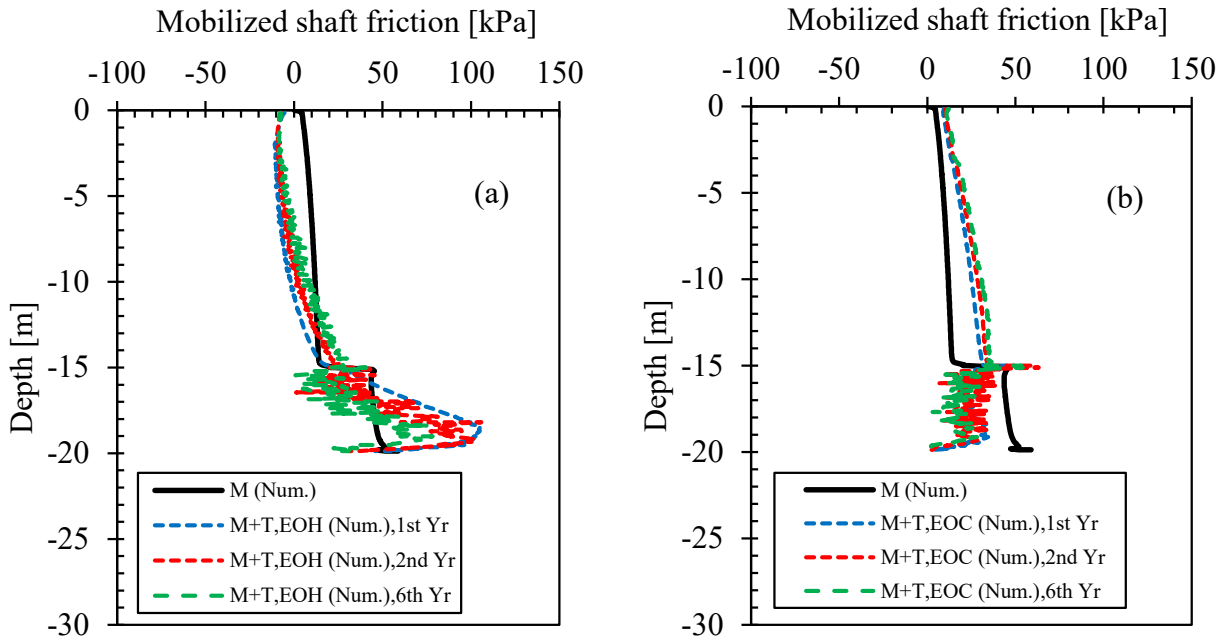

Figure 4.28. Mobilized shaft friction along the pile-soil interface (a) at the end of heating (EOH) and (b) at the end of cooling (EOC) in the 1st, 2nd, and 6th year for the end-bearing energy pile (base case)

4.4.6. Mobilized Effective Radial Stress

Friction energy pile:

As seen in Figure 4.29(a), the radial effective stresses along the entire pile-soil interface increased due to heating. At the EOC, this effective stresses reduced in the lower part of the pile but seemed to stay the same and marginally increase in the upper part as shown in Figure 4.29(b). The reasons for these phenomena were previously explained in Section 3.4.6. Note that, there were slight differences among the results obtained from the selected simulation times.

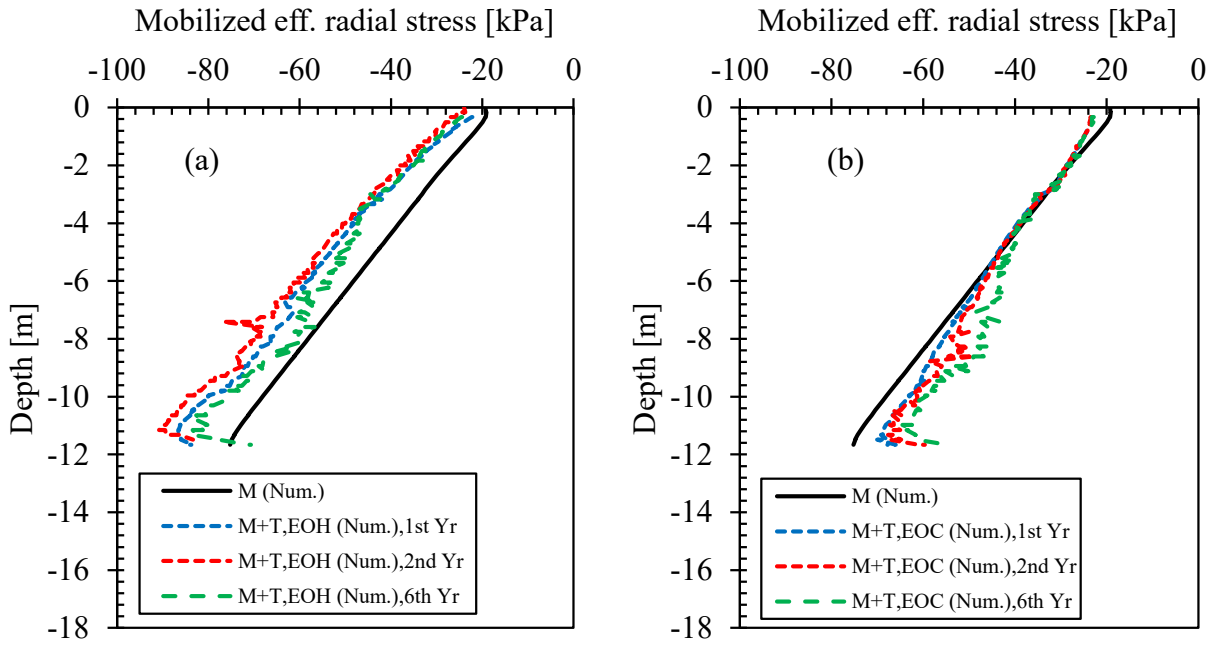

Figure 4.29. Mobilized effective radial (normal) stress along the pile-soil interface (a) at the end of heating (EOH) and (b) at the end of cooling (EOC) in the 1st, 2nd, and 6th year for the friction energy pile (base case)

End-bearing energy pile:

Figure 4.30 shows the mobilized radial effective stress profiles at the EOH and at the EOC. As can be seen, heating generally caused the radial effective stresses to increase along the entire pile length. Also, there were marked rises in the radial effective stress values along the pile-soil interface in the till layer. This may be due to the sudden change in the soil stiffness from very low to very high for the clay and the till, respectively, and also due to the high permeability of the till which somehow caused oscillations in the THM computations and therefore outputs. Cooling did the opposite to the heating in which the radial effective stresses reduced in the lower two-third of the pile in the till layer but slightly increased in the upper two-third. This later stress increase was due to the stress redistribution as explained earlier in Section 3.4.6.

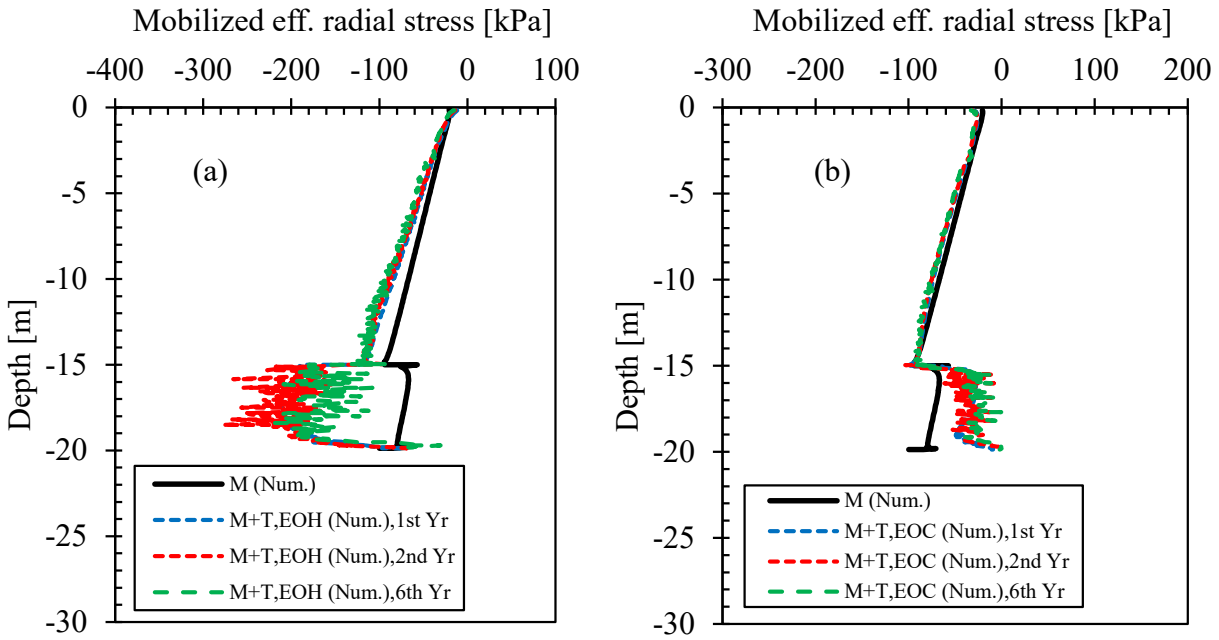

Figure 4.30. Mobilized effective radial (normal) stress along the pile-soil interface (a) at the end of heating (EOH) and (b) at the end of cooling (EOC) in the 1st, 2nd, and 6th year for the end-bearing energy pile (base case)

4.5. Sensitivity analysis for Winnipeg Energy Piles

4.5.1. Change in Thermal Load Ranges on the Pile (T)

In the base case analyses, the thermal load in terms of temperature variation with time ranging from the lowest of 0°C at the EOC to the highest of 40°C at the EOH was used. The temperature ranges of 0 to 30°C and 0 to 50°C were also considered as discussed here.

Friction energy pile:

Pile head displacements from numerical modeling results using three temperature ranges: 0 to 30°C, 0 to 40°C (base case), and 0 to 50°C are shown Figure 4.31. As expected, the higher temperatures at the EOH caused the larger upward movements of the pile head. At the EOH, the uplifts of the pile head were 0.3 mm and 1 mm (233% increase) in the 1st year for 40°C and 50°C. The corresponding values at the EOH in the 6th year were 0.04 mm and 0.43 mm, accordingly. There were small changes in the settlements of the pile head at the end of cooling (EOC) in comparison with the uplifts. These settlement values at the EOC in the 6th year for 40°C and 50°C were -3 mm and -3.1 mm (≈ 3% increase). The vertical displacements at the EOH along the pile length for all temperature ranges can be seen in Figure 4.32.

As can be seen Figure 4.33(a), the maximum thermally induced compressive loads in the pile at the EOH were -47 kN, -71 kN, and -98 kN (42% M of -235 kN) for 30°C, 40°C (base case), and 50°C, respectively. It can be seen that the thermally induced loads increased when the temperature values increased. The percentage increases were 51% from 30 to 40°C and 39% from 40 to 50°C. For the thermo-mechanically induced loads, as shown in Figure 4.33(b), the combined compressive loads at the EOH were -261 kN, -278 kN, and -297 kN for 30°C, 40°C and 50°C,

accordingly. The corresponding increases were 6% from 30 to 40°C and 7% from 40 to 50°C. It can be seen that when the temperatures increased the axial loads in the pile increased. Table 4.6 gives a summary of important results for friction energy pile using various temperature ranges. Other information can be found in Appendix C.2.

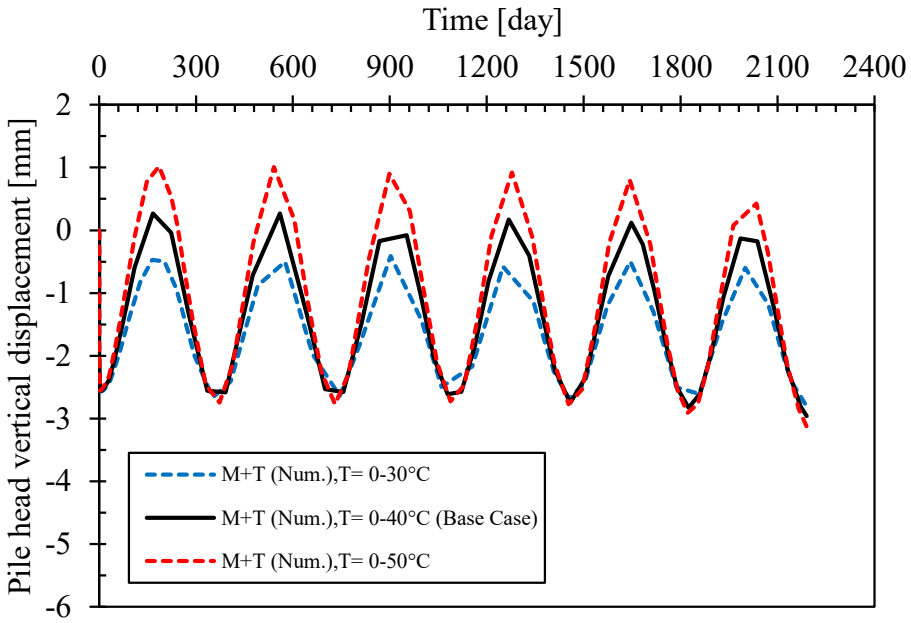

Figure 4.31. Pile head vertical displacements during six-year heating and cooling cycles for the friction energy pile (change in thermal load ranges)

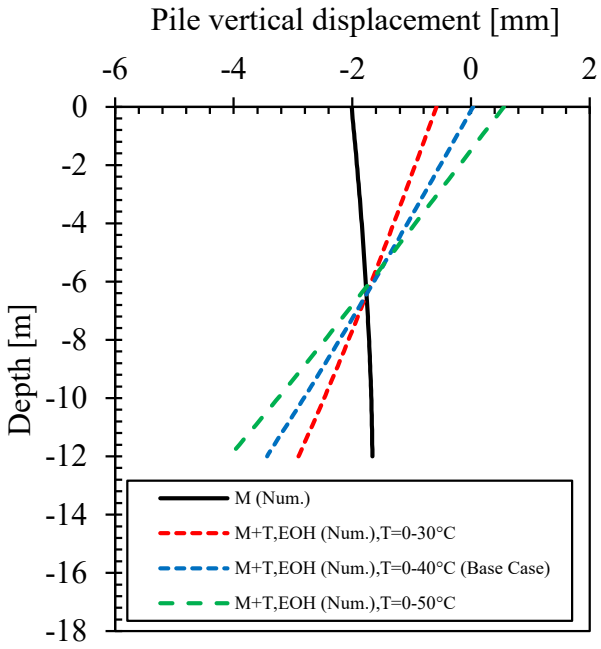

Figure 4.32. Pile vertical displacement profiles at the end of heating (EOH) in the 1st, 2nd, and 6th year for the friction energy pile (change in thermal load ranges)

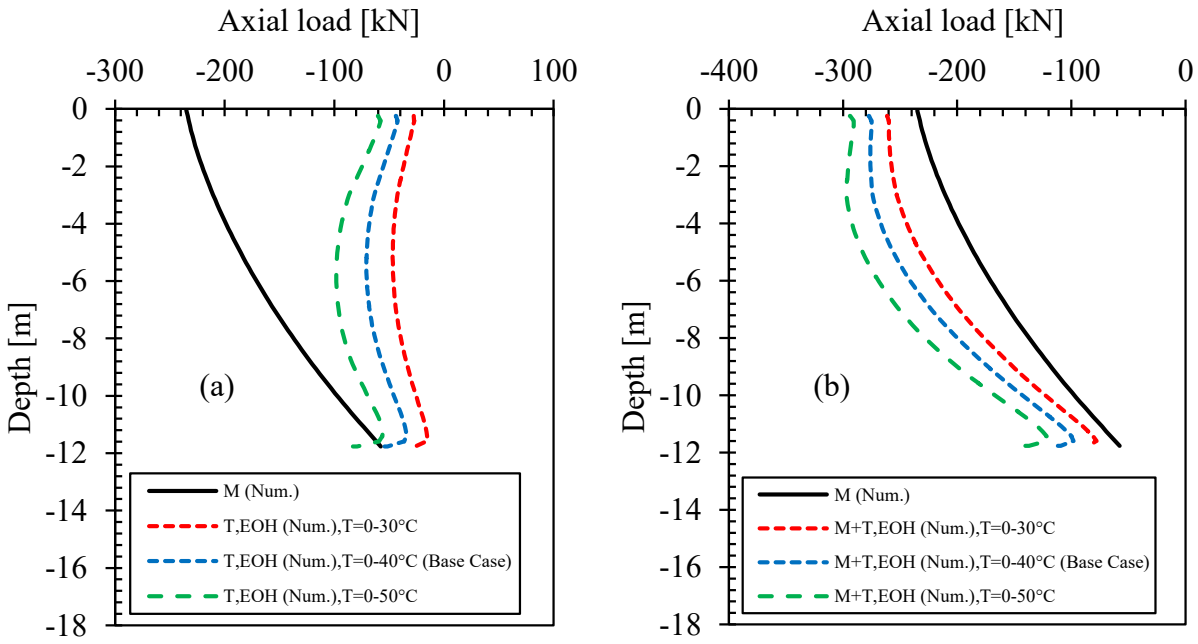

Figure 4.33. Axial load profiles (a) thermal (T) and (b) thermo-mechanical (M+T) at the end of heating (EOH) in the 1st, 2nd, and 6th year for the friction energy pile (change in thermal load ranges)

Table 4.6. Results from numerical analyses at the end of heating and cooling in the 6th year with different temperature ranges (friction energy pile)

Description	Change in temperature ranges (Base case)			Unit	Remark
Temperature ranges	0 to 30	0 to 40	0 to 50	[°C]	
M (max)	-235	-235	-235	[kN]	At the pile head
T, EOH					
Axial compressive load (max)	-46.75	-70.74	-98.27	[kN]	
	-33.91	-	38.92	[%]	Change from base case
Axial tensile load (max)				[kN]	
				[%]	Change from base case
M+T, EOH					
Pile head uplift	-0.13	0.04	0.43	[mm]	
	-425.00	-	975.00	[%]	Change from base case
Axial compressive load (max)	-261.47	-277.57	-297.22	[kN]	
	-5.80	-	7.08	[%]	Change from base case
Axial tensile load (max)				[kN]	
				[%]	Change from base case
T, EOC					
Axial compressive load (max)				[kN]	
				[%]	Change from base case
Axial tensile load (max)	275.73	307.48	335.12	[kN]	
	-10.33	-	8.99	[%]	Change from base case
M+T, EOC					
Pile head settlement	-2.81	-2.96	-3.13	[mm]	
	-5.07	-	5.74	[%]	Change from base case
Axial compressive load (max)	-205.78	-204.28	-201.98	[kN]	
	0.73	-	-1.13	[%]	Change from base case
Axial tensile load (max)	11.30	15.56	19.78	[kN]	
	-27.38	-	27.12	[%]	Change from base case

M = mechanical load
T, EOH = thermally induced at the end of heating
M+T, EOH = thermo-mechanically induced at the end of heating
T, EOC = thermally induced at the end of cooling
M+T, EOC = thermo-mechanically induced at the end of cooling

End-bearing energy pile:

The results from numerical models using different temperature ranges are shown in Figure 4.34. As seen in the figure, the higher temperatures the larger pile head uplifts were obtained. A similar trend was also observed for the pile head settlements. The thermal expansions along the pile length were more pronounced for the higher temperatures as shown in Figure 4.35. Higher temperatures also induced higher loads in the pile as illustrated in Figure 4.36(a). The maximum thermally induced compressive loads at the EOH were -517 kN, -654 kN, and -866 kN (67% M of -1300 kN) for 30ºC, 40ºC, and 50ºC, respectively. The corresponding values for the thermo-mechanically compressive loads at the EOH were -1459 kN, -1584 kN, and -1721 kN, as shown in Figure 4.36(b). Other numerical outputs are summarized in Table 4.7 and more information can also be found in Appendix D.2.

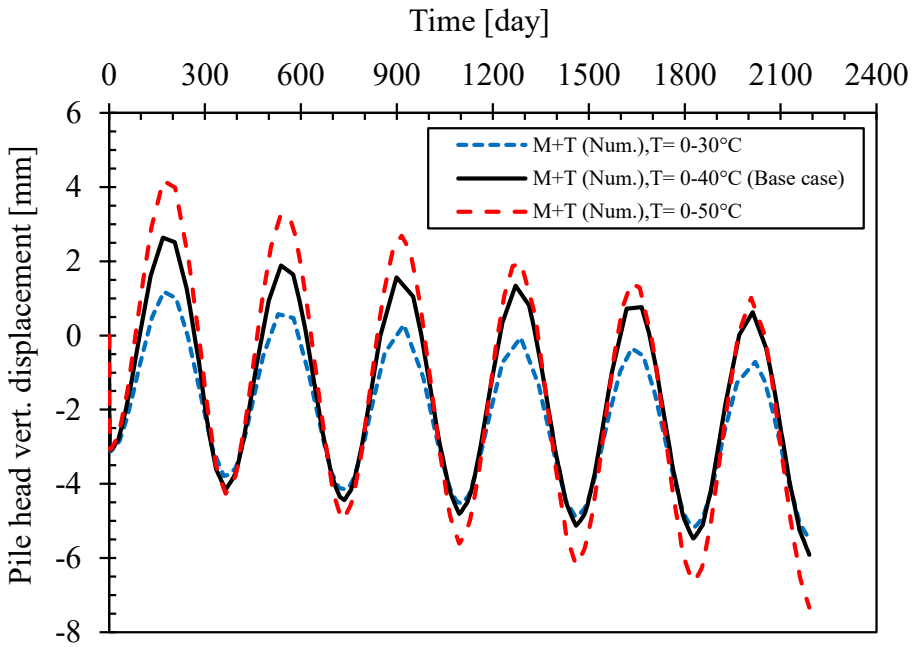

Figure 4.34. Pile head vertical displacements during six-year heating and cooling cycles for the end-bearing energy pile (change in thermal load ranges)

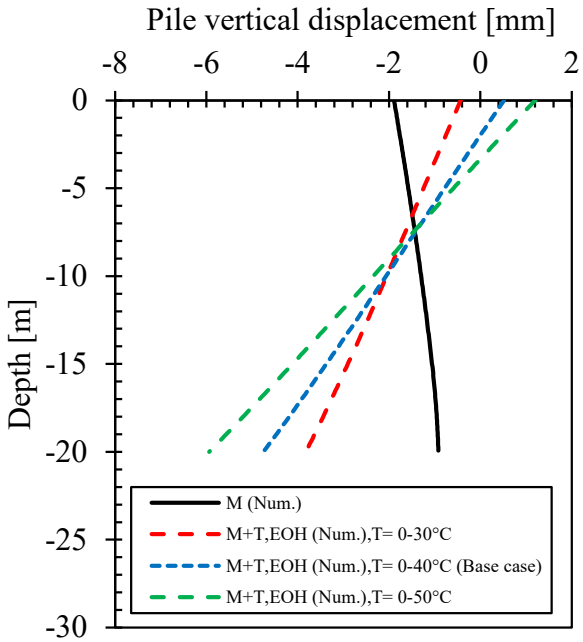

Figure 4.35. Pile vertical displacement profiles at the end of heating (EOH) in the 1st, 2nd, and 6th year for the friction energy pile (change in thermal load ranges)

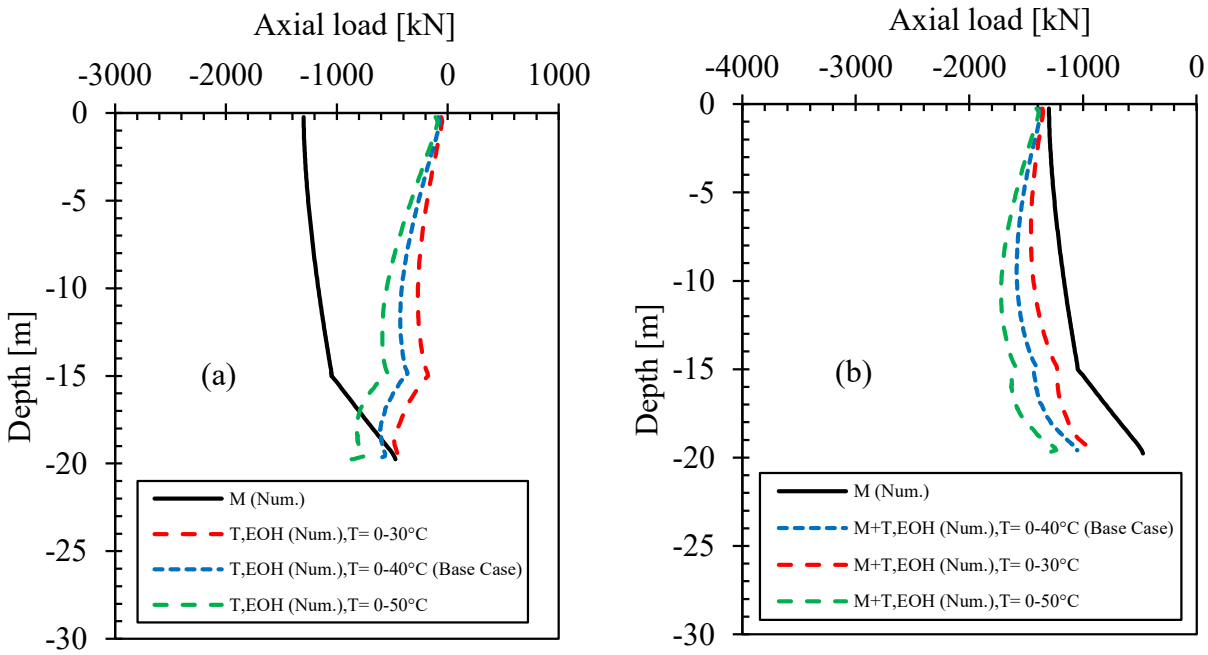

Figure 4.36. Axial load profiles (a) thermal (T) and (b) thermo-mechanical (M+T) at the end of heating (EOH) in the 1st, 2nd, and 6th year for the end-bearing energy pile (change in thermal load ranges)

Table 4.7. Results from numerical analyses at the end of heating and cooling in the 6th year with different temperature ranges (end-bearing energy pile)

Description	Change in temperature ranges (Base case)			Unit	Remark
Temperature ranges	0 to 30	0 to 40	0 to 50	[°C]	
M (max)	-1300	-1300	-1300	[kN]	At the pile head
T, EOH					
Axial compressive load (max)	-516.97	-654.31	-865.93	[kN]	
	-20.99	-	32.34	[%]	Change from base case
Axial tensile load (max)				[kN]	
				[%]	Change from base case
M+T, EOH					
Pile head uplift	-0.43	0.52	1.2	[mm]	
	-182.69	-	130.77	[%]	Change from base case
Axial compressive load (max)	-1458.93	-1583.57	-1721.27	[kN]	
	-7.87	-	8.70	[%]	Change from base case
Axial tensile load (max)				[kN]	
				[%]	Change from base case
T, EOC					
Axial compressive load (max)				[kN]	
				[%]	Change from base case
Axial tensile load (max)	649.06	648.46	667.94	[kN]	
	0.09	-	3.00	[%]	Change from base case
M+T, EOC					
Pile head settlement	-5.49	-5.91	-7.34	[mm]	
	-7.11	-	24.20	[%]	Change from base case
Axial compressive load (max)	-1257.59	-1250.23	-1239.89	[kN]	
	0.59	-	-0.83	[%]	Change from base case
Axial tensile load (max)				[kN]	
				[%]	Change from base case

M = mechanical load
T, EOH = thermally induced at the end of heating
M+T, EOH = thermo-mechanically induced at the end of heating
T, EOC = thermally induced at the end of cooling
M+T, EOC = thermo-mechanically induced at the end of cooling

4.6. Numerical Simulations of Energy Pile Load Tests

In this section, the effects of temperature changes on the ultimate geotechnical capacities of energy piles were investigated. The axisymmetric models were utilized for the energy pile load test simulations for the same generic friction and end-bearing energy piles as described in Section 4.3. The reported geotechnical ultimate pile capacities were derived from simulated load-settlement curves using the 10% D failure criterion in which D is the pile toe or base diameter in accordance with the Eurocode 7 (EN 1997-1, 2004). In this 10% D criterion, the so-called "failure load" or "ultimate pile capacity" was simply the load corresponding to the settlement of 10% pile diameter whether or not the pile really reached the "failure". There are many other criteria in the literature used to determine the "failure loads" or "ultimate pile capacities" from the static pile load tests; for example, the Davison Offset Limit method, the Chin-Kondner Extrapolation method, and the Decourt Extrapolation method. These methods, which have their own strengths and weaknesses, were not considered in this thesis.

4.6.1. Simulating the Pile Load Test Results without the Effect of Temperature Change

The pile load tests were modeled without considering the effect of temperature change for the friction pile installed in the Winnipeg clay. This pile has a diameter of 0.4 m and 6 m long. The purpose of doing this is to compare the simulated geotechnical pile capacities with the available data from full-scale field tests of the same pile size and length performed in Winnipeg by Blatz & Mroz (2017).

Numerical results of pile load tests, plotted in terms of axial loads against pile head settlements, are shown in Figure 4.37. The simulations were performed using different stiffness values for the clay layer. The first simulation was carried out with the base case stiffness values,

here denoted as Es (as given earlier in Table 4.1 - material parameters for the base case analyses for energy piles in Winnipeg). The two other simulations were done with a reduction of stiffness values by 50% (0.5 Es) and an increase of 100% (2 Es) from the base case values. As can be seen in Figure 4.37, the larger stiffness values gave stiffer load-settlement curves. Increasing soil provided the stiffer load-settlement curves and slightly higher failure loads. Figure 4.38 shows the simulated load-settlement curves plotted over the field load-settlement curves from the static load tests. Five static load tests were carried out for five different piles at the same site. More details for these pile load tests can be found in Blatz & Mroz (2017). It can be seen that the ultimate geotechnical pile capacities from the field were somewhat varied even though they were tested at the same site, only a few meters away from each other. It seemed that simulated geotechnical pile capacities fall within the range of the tested ones; and therefore, the numerical models gave reasonably accurate results. Table 4.8 provides a summary of the ultimate pile capacities for both field and simulated data.

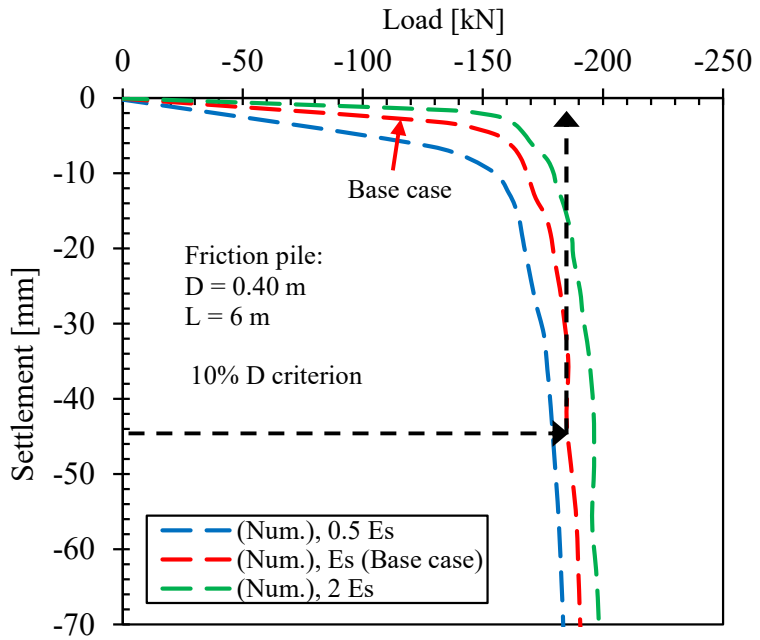

Figure 4.37. Predicted load-settlement curves simulated with different soil stiffness for the friction pile without the effect of temperature change

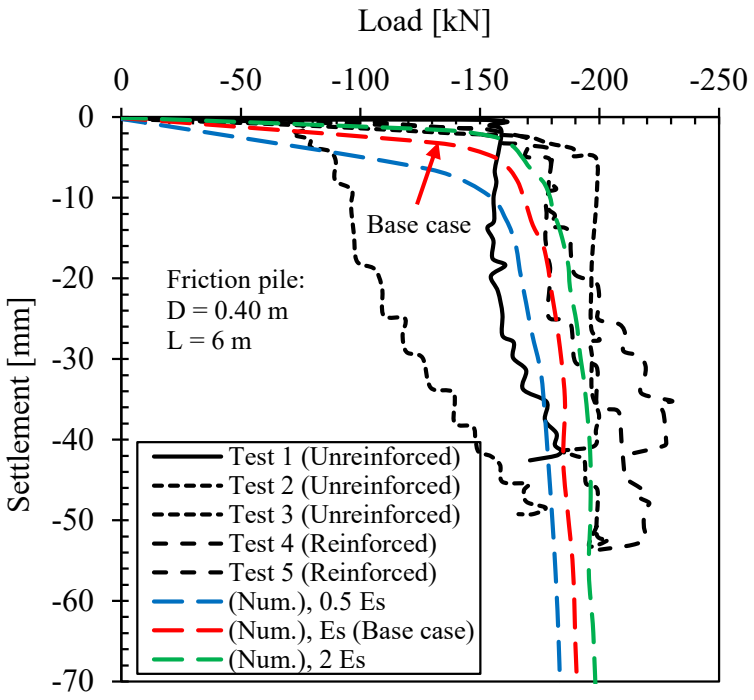

Figure 4.38. Load-settlement curves: full-scale static load tests versus numerical simulations for the friction pile without the effect of temperature change

Table 4.8. Ultimate geotechnical capacities: full-scale static load tests versus numerical simulations for the friction pile in Winnipeg

Pile type	Diameter [m]	Length [m]	Test No.	Static pile load tests Blatz & Mroz (2017) Values as reported [kN]	Used 10% D criterion* [kN]	Numerical results with 0.5 E_s Used 10% D criterion [kN]	E_s (Base case) [kN]	2 E_s [kN]
Cast-in-place friction pile	0.4	6	Test 1 (unreinforced)	187.0	150	177.92	185.10	195.69
			Test 2 (unreinforced)	179.8	180			
			Test 3 (unreinforced)	204.1	200			
			Test 4 (reinforced)	221.4	210			
			Test 5 (reinforced)	229.4	275			
			Average:	204.3	203			

* This critirion was given in EN 1997-1: 2004 and D is the pile diameter

4.6.2. Simulating the Pile Load Test Results with the Effect of Temperature Change

The effects of temperature on the ultimate geotechnical capacities of energy piles were investigated for both friction and end-bearing energy piles. For both energy piles, the pile load tests were done at the EOH and at the EOC in the 6th year. That means that the energy piles went through six heating-cooling cycles before their capacities were determined with the temperature ranging from 0 to 40°C, the temperature range used in the base case analyses.

Friction energy pile:

The simulated load-settlement curves determined at the EOH and at the EOC in the 6th year are shown in Figure 4.39, together with the initial test in which temperature effect was not considered. The summary of the ultimate geotechnical capacities is given in Table 4.9. It can be seen that higher temperatures generally produced larger pile resistances. This was mainly due to an increase in radial effective stresses during heating. At the EOH, even though the ultimate pile capacity determined by a 10% D criterion only increased by about 2%, higher increases were noticed in a very low settlement range, less than 10 mm. In contrast, at the end of cooling, the pile capacity considerably reduced (-19%).

Table 4.9. Ultimate geotechnical capacities from numerical simulations for the friction energy pile in Winnipeg

Pile type	Diameter [m]	Length [m]	Pile load tests at different time	Numerical results [kN]	[%]	Remark
Cast-in-place friction energy pile	0.4	12	Initial	504	-	
			End of heating, in the 6th year	511	2	Increased
			End of cooling, in the 6th year	407	-19	Decreased

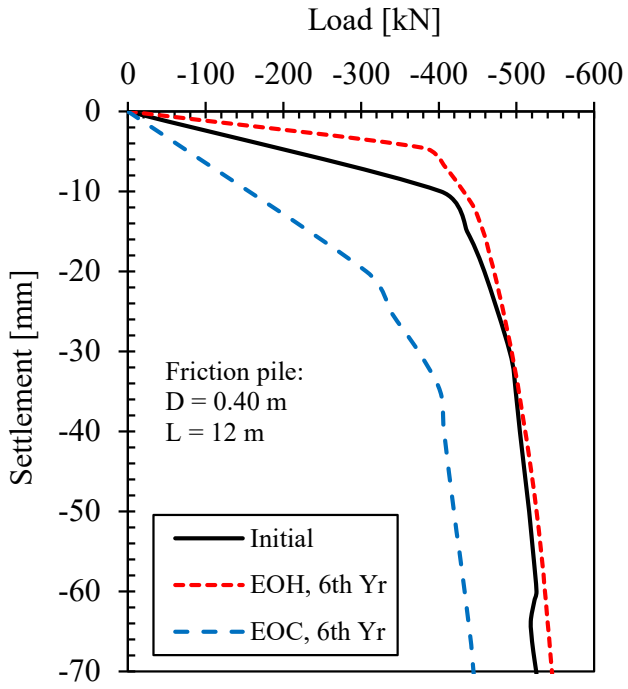

Figure 4.39. Load-settlement curves of simulated at the initial stage, at the end of heating (EOH) and at the end of cooling (EOC) in the 6th year for the friction pile

End-bearing energy pile:

For the end-bearing energy pile as shown in Figure 4.40, the ultimate geotechnical pile capacity increased at the EOH by 12%. The reduction of 9% was observed at the EOC. Table 4.10 summarizes the ultimate geotechnical capacities from numerical simulations for the end-bearing energy pile. The reason why there was an increase in ultimate geotechnical capacities of the piles may be due to the increase in radial stresses along the pile as a result of heating. As it is known, when the pile is heated, it will try to expand vertically and radially. The radial expansion, in this case, could not fully mobilize because of the restriction of the surrounding soils. Consequently, higher radial stresses were developed along the pile-soil interface, leading to an increase of the ultimate geotechnical capacity of the pile. The opposite reason seemed to be valid when the pile was cooled. In addition, because of the contraction (moving upwards) of the pile toe during

cooling, there was a reduction of the end-bearing stress which could also contribute to a decrease in the ultimate geotechnical capacity of the pile at the end of cooling.

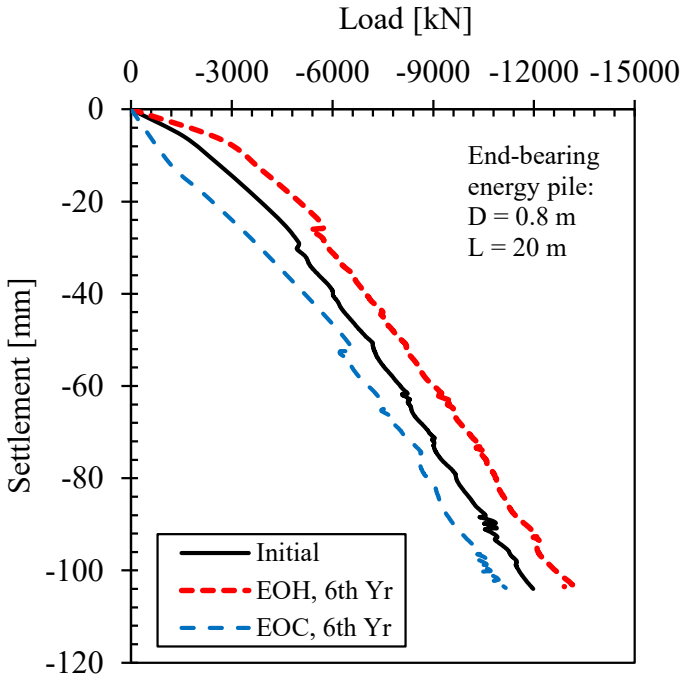

Figure 4.40. Load-settlement curves simulated at the initial stage, at the end of heating (EOH) and at the end of cooling (EOC) in the 6th year for the end-bearing pile

Table 4.10. Ultimate geotechnical capacities from numerical simulations for the end-bearing energy pile in Winnipeg

Pile type	Diameter [m]	Length [m]	Pile load tests at different time	Numerical results [kN]	[%]	Remark
Cast-in-place end-bearing energy pile	0.8	20	Initial	9683	-	
			End of heating, in the 6th year	10865	12	Increased
			End of cooling, in the 6th year	8840	-9	Decreased

The outcomes from the numerical simulations of the energy pile load tests carried out in this thesis are in reasonable agreements with the previous studies by other researchers using centrifuge model tests. For instance, McCartney (2011) tested energy piles installed in dry compacted silt at 24 g. At this g-level, the centrifuge piles represented the real (prototype) piles with a diameter of 1.8 m and 9.1 m long. It was found that the ultimate geotechnical capacities of the piles increased by about 60% when the temperature in the pile increased from 15ºC to 50ºC (a change of 35ºC). However, no changes in the ultimate pile capacities were observed from centrifuge tests (24g) of a concrete pile (63.5 mm dia. and 342.9 mm long) in dry Nevada sand with temperature differences of 7ºC, 12ºC, and 18ºC (Goode, Zhang, & McCartney, 2014). From a small-scale laboratory test (1g) of the concrete pile (0.1 m dia. and 1.22 m long) in dry Ottawa sand with a change of temperature of 20ºC, only a marginal increase in pile capacity was observed (Kramer & Basu, 2014). Similarly, Ng et al. (2015) reported that the ultimate geotechnical capacities, using the 10% D failure criterion, increased by 19% and 42% with the increase in temperature of 15ºC and 30ºC, respectively. These results were obtained from centrifuge model tests carried out at 40 g in saturated Toyoura sand. No excess porewater pressures were generated during the tests. The equivalent prototype piles, which were installed entirely in saturated sand, had a diameter of 0.88 m and a length of 24 m. Full-scale load tests of an energy pile were performed at Monash University in Australia (Wang et al., 2015). The piles have a diameter of 0.6 m and about 15 m long installed in clayey sand. They stated that the shaft resistance increased (14%) with the short-term heating with $\Delta T \approx 20$ºC and returned to the initial value when the pile was cooled down naturally back to the initial ground temperature of (17 to 18ºC). The cooling effects on the pile capacity of the floating pile in the sand with 0.88 m in diameter and 24 m in length in prototype scale using the centrifuge model test at 40 g was also studied by Gunawan et

al. (2017). In their study, before the pile load test started, the pile was cooled down from the initial temperature of 25 to 11.5ºC. They found that the pile capacity increased by 12%, which is surprising. Heating, in general, increases the pile capacity mainly due to the increase in the radial stress. Then cooling, in contrast, should result in the opposite phenomena, as the numerical results have shown. In fact, small-scale laboratory model tests on concrete piles in Nanjing sand conducted by Liu et al. (2018) showed a decrease of the pile capacity by 4.6% when the temperature reduced by 7ºC and increase by 10.3% when heated by 23ºC. It is important to note; however, that the energy pile load tests in the literature, as given above, were carried out in either dry soils or saturated sands with no excess pore pressures built up during the tests. The response might be different for energy piles in clays because of the generation of excess porewater pressures. Field data on the effects of pile capacities are extremely limited, especially at lower temperatures close to zero degree Celsius. Further full-scale field tests to study temperature effects on geotechnical pile capacities are needed.

Chapter 5: Conclusions and Recommendations

5.1. Conclusions

Using structural piles as ground heat exchangers for the ground source heat pump (GSHP) systems can be beneficial for the building owners and property developers in terms of energy saving on heating and cooling.

The behavior of energy piles subjected to thermal and thermo-mechanical loadings have been examined numerically in this research through the use of fully coupled THM finite element models. The simulations were able to capture the general responses of energy piles quite well in comparison with the experimental data observed for the two case studies conducted in the U.K and Switzerland. Based on these findings, it was presumed that the THM finite element models could also capture the energy pile behavior in Winnipeg under local climatic and geological conditions. Even though, there were no field data to be compared with the numerical results.

Based on the numerical results, it can be said that temperature changes in the piles had significant effects on their displacements, strains, stresses, and loads. In general, heating caused the piles to expand. The portion of the pile above the neutral plane (NP) moved upwards, but the part below the NP displaced downwards. These expansions resulted in expansive strains in the pile. If the piles cannot expand freely due to the shaft friction and end restraints, thermal compressive stresses would be generated in addition to the mechanically induced stresses. Therefore, for the thermal and mechanical combined effects, the compressive loads in the pile would be higher during heating which may cause over-stressing of the pile if it is not designed accordingly. From the numerical analyses, additional compressive loads in the pile due to heating

were significant. The values for the base cases of all energy piles were -436 kN (36% M) for London energy pile, -2842 kN (219% M) for Lausanne energy pile, -109 kN (46% M) for Winnipeg friction pile, and -699 kN (54% M) for Winnipeg end-bearing pile. Lausanne energy pile produced a very high compressive load because it was a rock-socketed pile.

Cooling caused reverse effects in which the pile contracted. The part of the pile above the NP moved downwards while the part below it moved upwards. In consequence, compressive strains were generated and led to the tensile stresses build up in the pile. The tensile stresses usually occurred near the pile toe, where the mechanically induced stresses are low, for the thermo-mechanical combined effects. These tensile stresses need special attention because it may cause cracking in the concrete pile. Thermally induced tensile loads at the end of cooling for base case analyses of all energy piles were: 252 kN (21% M), 79 kN (34% M), and 649 kN (50% M) for London energy pile, Winnipeg friction energy pile, and Winnipeg end-bearing pile, accordingly.

In terms of pile head displacements, heating produced uplifts of the pile head while cooling caused settlements. These should be considered in the energy pile design as well. It is important to note that the settlement values kept on increasing with longer simulation times (ratcheting settlement phenomena). For Winnipeg friction energy pile, at the end of cooling in the 1st year, the simulated settlement was -0.85 mm (0.21% D) and in the 6th year was -0.96 mm (0.24% D), leading to an increase in the settlement of 13%. The corresponding values for the end-bearing energy pile were -4.2 mm (-0.5% D) and -5.9 mm (-0.74% D), increasing by 41.4%. From the settlement values given here, it can be said that the settlements of the pile head within the considered time (6 years) are still small and well within the tolerable limit. The tolerable settlement limit is usually depending on the type of structures. The most stringent settlement limit specified in the design criteria is typically 25 mm. Note that, in this research, the pile head settlements were

only evaluated for only 6 years, and as it was observed from the numerical results, the settlements kept on increasing gradually with time. It is interesting to find out what is going to happen in the long-term. Therefore, more research still needs to be carried out to evaluate the settlements for a longer period of time (up to 50 years for instance).

The heating-cooling cycles of the pile also affected the surrounding ground temperatures to some distances which were depending on the simulation times. Excess porewater pressures were generated in the soils with low hydraulic conductivities. The mobilized shaft friction and the radial stresses along the pile length were also affected by the temperature changes to some extent.

In the sensitivity analyses carried out for the energy pile case studies, the changes in the following parameters were carried out: the coefficient of thermal expansions of both concrete and soils, soil stiffnesses, thermal conductivities of soils, specific heat capacities of soils, and pile head restrained conditions. The numerical results showed that the effects of the thermal conductivity, specific heat capacity, and thermal expansion coefficient of soils on the thermo-mechanical pile responses were minimal. In contrast, there were considerable effects of the thermal expansion of concrete and soil stiffness on the thermo-mechanical pile responses. This dictates the importance of proper selections of the coefficient of thermal expansion of concrete and soil stiffness for numerical modeling. The pile head restrained conditions also affected the behavior of energy piles in which stronger effects were noticed in the upper part of the pile near the pile head and lesser effects near the pile toe. Therefore, it is essential to consider an appropriate head restrained condition in the models to capture the appropriate pile responses along the pile entire length.

Simulated ultimate geotechnical capacities for the non-energy friction pile agreed well with the data from full-scale field tests in Winnipeg clay. Numerical results from the energy pile load tests performed for the Winnipeg energy friction and end-bearing piles showed that the ultimate

geotechnical pile capacities increased at the end of the heating period but decreased at the end of cooling. For the friction pile, there was an increase of only about 2% at the end of heating, but a reduction of 19% at the end of cooling. For end-bearing pile, these values were 12% and 9%, respectively. From this information, it can be said that when designing the Winnipeg energy piles in terms of geotechnical capacities, the factor of safety applied to the ultimate geotechnical capacities need to be increased by up to at least 19% if the conventional working stress design (WSD) is used. For the ultimate limit state (ULS) design, the reduction factor on the geotechnical pile capacities should be reduced by at least 19%.

5.2. Recommendations for Future Research

In future research on energy piles in Winnipeg, 3D analyses could be used to study the behavior of a group of energy piles or energy piled raft foundations under the whole buildings. Moreover, this thesis only investigated the thermo-mechanical behavior of energy piles, but not their energy performance in which their heating and cooling capacities are evaluated, i.e., the amount of thermal energy that can be extracted from or injected into the piles. Therefore, this may be a useful topic to explore in the future for energy piles in Winnipeg. Also, only a relatively short period of time (6 years) was considered in this thesis. It is interesting to know what will happen, especially in terms of pile head settlements, in a longer period of time; for example, 50 years of heating and cooling. Therefore, the long-term performance of energy piles should be investigated in the future.

Finally, it is important to note that whatever software packages used to analyze or predict the behavior of the energy piles, their numerical outputs should be validated against full-scale measurements. In the future, it would be very valuable to carry out the full-scale energy pile tests in Winnipeg's geological and climatic conditions.

References

Abuel-Naga, H., Raouf, A. M. I., Raouf, M. I. N., & Nasser, A. G. (2015). Energy Piles: Current State of Knowledge and Design Challenges. *Environmental Geotechnics*, *2*(EG4), 195–210. https://doi.org/10.1680/envgeo.13.00019

Adinolfi, M., Mauro, A., Maiorano, R., Massarotti, N., & Aversa, S. (2016). Thermo-Mechanical Behaviour of Energy Pile in Underground Railway Construction Site. In Wuttke, Bauer, & Sanchez (Eds.), *Energy Geotechnics* (pp. 83–88). London: Taylor & Francis Group.

Al-Khoury, R. (2012). *Computational Modeling of Shallow Geothermal Systems*. Boca Raton. FL: CRC Press.

Allani, M., Van Lysebetten, G., & Huybrechts, N. (2017). Experimental and Numerical Study of the Thermo-Mechanical Behaviour of Energy Piles for Belgian Practice. In A. Ferrari & L. Laloui (Eds.), *Advances in Laboratory Testing and Modelling of Soils and Shales (ATMSS)* (pp. 405–412). Springer International Publishing. https://doi.org/10.1007/978-3-319-52773-4_48

Amatya, B. L., Soga, K., Bourne-Webb, P. J., Amis, T., & Laloui, L. (2012). Thermo-Mechanical Behaviour of Energy Piles. *Géotechnique*, *62*(6), 503–519. https://doi.org/10.1680/geot.10.P.116

Amis, T., Bourne-Webb, P., Davidson, C., Amatya, B., & Soga, K. (2008). The Effects of Heating and Cooling Energy Piles under Working Load at Lambeth College, UK. In *Proceedings of the 33rd Annual and 11th International Conference on Deep Foundations*.

Amis, T., & Loveridge, F. (2014). Energy Piles and Other Thermal Foundations for GSHP – Developments in UK Practice and Research. *REHVA Journal*, (January), 32–35.

Banks, D. (2012). *An Introduction to Thermogeology: Ground Source Heating and Cooling* (2nd ed.). Oxford, UK: Wiley-Blackwell. https://doi.org/10.1002/9781118447512

Baracos, A., & Graham, J. (1981). Landslide Problems in Winnipeg. *Canadian Geotechnical Journal*, *18*(3), 390–401. https://doi.org/10.1139/t81-045

Baracos, A., Shields, D. H., & Kjartanson, B. (1983). *Geological Engineering Report for Urban Development of Winnipeg*. Department of Geological Engineering, University of Manitoba.

Barry-Macaulay, D., Bouazza, A., Singh, R. M., Wang, B., & Ranjith, P. G. (2013). Thermal Conductivity of Soils and Rocks from the Melbourne (Australia) Region. *Engineering Geology*, *164*, 131–138. https://doi.org/10.1016/j.enggeo.2013.06.014

Batini, N., Rotta Loria, A. F., Conti, P., Testi, D., Grassi, W., & Laloui, L. (2015). Energy and Geotechnical Behaviour of Energy Piles for Different Design Solutions. *Applied Thermal Engineering*, *86*, 199–213. https://doi.org/10.1016/j.applthermaleng.2015.04.050

Belbas, R. (2013). *The Capacity of Driven Steel H-Piles in Lacustrine Clay, Till, and Karst Bedrock: A Winnipeg Case Study*. M.Sc. Thesis, University of Manitoba, Canada.

Bererton, J. (2010). WestJet Calgary Campus. Retrieved October 8, 2018, from https://www.canadianconsultingengineer.com/features/westjet-calgary-campus/

Blatz, J., & Mroz, D. (2017). Static Load-Test Performance of Cast-in-Place Concrete Piles in the City of Winnipeg. In *The 70th Canadian Geotechnical Conference and the 12th Joint CGS/IAH-CNC Groundwater Conference*. GeoOttawa 2017, Ottawa, Canada.

Bodas Freitas, T. M., Cruz Silva, F., & Bourne-Webb, P. J. (2013). The Response of Energy Foundations under Thermo-Mechanical Loading. In *18th Intl Conf Soil Mechanics and Geotechnical Engineering* (pp. 3347–3350).

Bot, D. (2017). *Numerical Modelling of an Experimental Energy Pile*. M.Sc. Thesis, Delft

University of Technology, The Netherlands.

Bouazza, A., Singh, R. M., Wang, B., Barry-Macaulay, D., Haberfield, C., Chapman, G., … Carden, Y. (2011). Harnessing on Site Renewable Energy through Pile Foundations. *Australian Geomechanics Journal*, *46*(4), 79–89.

Bourne-Webb, P. J., Amatya, B., & Soga, K. (2013). A Framework for Understanding Energy Pile Behaviour. *Proceedings of the Institution of Civil Engineers - Geotechnical Engineering*, *166*(2), 170–177. https://doi.org/10.1680/geng.10.00098

Bourne-Webb, P. J., Amatya, B., Soga, K., Amis, T., Davidson, C., & Payne, P. (2009). Energy Pile Test at Lambeth College, London: Geotechnical and Thermodynamic Aspects of Pile Response to Heat Cycles. *Géotechnique*, *59*(3), 237–248. https://doi.org/10.1680/geot.2009.59.3.237

Bourne-Webb, P. J., Burlon, S., Javed, S., Kürten, S., & Loveridge, F. (2016). Analysis and Design Methods for Energy Geostructures. *Renewable and Sustainable Energy Reviews*, *65*, 402–419. https://doi.org/10.1016/j.rser.2016.06.046

Bowles, J. E. (1996). *Foundation Analysis and Design* (5th ed.). Singapore: McGraw-Hill.

Brandl, H. (2006). Energy Foundations and Other Thermo-Active Ground Structures. *Géotechnique*, *56*(2), 81–122. https://doi.org/10.1680/geot.2006.56.2.81

Budhu, M. (2011). *Soil Mechanics and Foundations* (3rd ed.). John Wiley & Sons, Inc.

Campanella, R. G., & Mitchell, J. K. (1968). Influence of Temperature Variations on Soil Behaviour. *Journal of Soil Mechanics and Foundations Division. ASCE.*, *94*(SM3), 709–734.

Cao, L., Peaker, S., & Ahmad, S. (2015). Engineering Characteristic of Glacial Tills in GTA. In *The 68th Canadian Geotechnical Conference and 7th Canadian Permafrost Conference*. GEOQuebec2015, Quebec, Canada.

Cashman, P. M., & Preene, M. (2013). *Groundwater Lowering in Construction - A Practical Guide to Dewatering* (2nd ed.). Boca Raton. FL: CRC Press.

CBCNews. (2014, March 19). Frost Keeps Pushing Deeper into Winnipeg's Frozen Terrain. Manitoba. Retrieved from https://www.cbc.ca/news/canada/calgary/frozen-water-pipes-mains-services-surge-calls-1.5046713

Cekerevac, C., & Laloui, L. (2004). Experimental Study of Thermal Effects on the Mechanical Behaviour of a Clay. *International Journal for Numerical and Analytical Methods in Geomechanics*, *28*(3), 209–228. https://doi.org/10.1002/nag.332

CFEM. (2006). *Canadian Foundation Engineering Manual* (4th ed.). Canadian Geotechnical Society.

CGC. (2009). *A Buyer's Guide for Residential Ground Source Heat Pump Systems*. Canadian GeoExchange Coalition.

Das, B. M., & Sobhan, K. (2014). *Principles of Geotechnical Engineering* (8, SI ed.). Cengage Learning.

De Santos, C., Ledesma, A., & Gens, A. (2012). Back-analysis of Measured Movements in Ageing Tunnels. In Viggiani (Ed.), *Geotechnical Aspects of Underground Construction in Soft Ground* (pp. 223–229). London: Taylor & Francis Group.

Di Donna, A. (2014). *Thermo-Mechanical Aspects of Energy Piles*. Ph.D. Thesis, Swiss Institute of Technology in Lausanne, Switzerland.

Di Donna, A., & Laloui, L. (2015). Numerical Analysis of the Geotechnical Behaviour of Energy Piles. *International Journal for Numerical and Analytical Methods in Geomechanics*, *39*(8), 861–888. https://doi.org/10.1002/nag.2341

Di Donna, A., Rotta Loria, A. F., & Laloui, L. (2016). Numerical Study of the Response of a Group

of Energy Piles under Different Combinations of Thermo-Mechanical Loads. *Computers and Geotechnics*, *72*, 126–142. https://doi.org/10.1016/j.compgeo.2015.11.010

Domenico and Schartz. (1998). *Physical and Chemical Hydrogeology* (2nd ed.). John Wiley & Sons, Inc.

ECCC. (2016). The Environment and Climate Change Canada (ECCC), Canadian Climate Normals 1981-2010 Station Data. Retrieved August 8, 2016, from http://climate.weather.gc.ca/climate_normals/results_1981_2010_e.html?searchType=stnProv&lstProvince=MB&txtCentralLatMin=0&txtCentralLatSec=0&txtCentralLongMin=0&txtCentralLongSec=0&stnID=3698&dispBack=0

EN 1997-1. (2004). *Eurocode 7 Geotechnical Design, Part 1_General Rules*. European Committee for Standardization.

Farouki, O. T. (1981). *Thermal Properties of Soils*. U.S. Army Cold Regions Research and Engineering Laboratory, Hanover, New Hampshire.

Ferguson, G., & Woodbury, A. D. (2004). Subsurface Heat Flow in an Urban Environment. *Journal of Geophysical Research: Solid Earth*, *109*(B2), 1–9. https://doi.org/10.1029/2003JB002715

Fetter, C. W. (2011). *Applied Hydrogeology* (4th ed.). Prentice-Hall.

Flynn, D., Kurz, D., Alfaro, M., Graham, J., & Arenson, L. U. (2016). Forecasting Ground Temperatures under a Highway Embankment on Degrading Permafrost. *Journal of Cold Regions Engineering*, *30*(4), 04016002. https://doi.org/10.1061/(ASCE)CR.1943-5495.0000106

Gao, J., Zhang, X., Liu, J., Li, K. S., & Yang, J. (2008). Thermal Performance and Ground Temperature of Vertical Pile-Foundation Heat Exchangers: A Case Study. *Applied Thermal*

Engineering, *28*(17–18), 2295–2304. https://doi.org/10.1016/j.applthermaleng.2008.01.013

Gawecka, K. A., Potts, D. M., Taborda, D. M. G., Cui, W., & Zdravkovi, L. (2016). Effects of Transient Phenomena on the Behaviour of Thermo-Active Piles. In Wuttke, Bauer, & Sanchez (Eds.), *Energy Geotechnics* (pp. 71–78). London: Taylor & Francis Group.

Gawecka, K. A., Taborda, D. M. G., Potts, D. M., Cui, W., Zdravković, L., & Haji Kasri, M. S. (2017). Numerical Modelling of Thermo-Active Piles in London Clay. *Proceedings of the Institution of Civil Engineers - Geotechnical Engineering*, *170*(3), 201–219. https://doi.org/10.1680/jgeen.16.00096

Gibb, F. G. F. (1999). High-Temperature, Very Deep, Geological Disposal: A Safer Alternative for High-Level Radioactive Waste? *Waste Management*, 207–211. https://doi.org/10.1016/S0956-053X(99)00050-1

Goode, J. C. I., Zhang, M., & McCartney, J. S. (2014). Centrifuge Modelling of Energy Foundations in Sand. In Gaudin & White (Eds.), *Physical Modelling in Geotechnics* (pp. 729–735). London: Taylor & Francis Group.

Graham, J., Tanaka, N., Crilly, T., & Alfaro, M. (2001). Modified Cam-Clay Modelling of Temperature Effects in Clays. *Canadian Geotechnical Journal*, *38*, 608–621. https://doi.org/10.1139/t00-125

GSHPA. (2012). *Thermal Pile Design, Installation and Materials Standards*. Ground Source Heat Pump Association, National Energy Centre, The United Kingdom.

Gunawan, A., Ng, C. W. W., & Liu, H. (2017). Effects of Cooling on the Ultimate Capacity of Energy Pile. In *The 19th International Conference on Soil Mechanics and Geotechnical Engineering* (pp. 3439–3442). Seoul, South Korea. Retrieved from http://linkinghub.elsevier.com/retrieve/pii/S0962184996800059

Hamada, Y., Saitoh, H., Nakamura, M., Kubota, H., & Ochifuji, K. (2007). Field Performance of an Energy Pile System for Space Heating. *Energy and Buildings*, *39*(5), 517–524. https://doi.org/10.1016/j.enbuild.2006.09.006

Harms, S. M., Skaftfeld, K. M., & Belbas, R. (2017). Design and Construction of Rock-Socketed Caissons in Dolomitic Limestone : A Winnipeg Perspective. In *The 70th Canadian Geotechnical Conference and the 12th Joint CGS/IAH-CNC Groundwater Conference*. GeoOttawa 2017, Ottawa, Canada.

Harvey, R. D. (1967). *Thermal Expansion of Certain Illinois Limestones and Dolomites*. Illinois State Geological Survey, Urbana, U.S.A.

Head, K. H. (1994). *Manual of Soil Laboratory Testing, Permeability, Shear Strength and Compressibility Tests* (2nd ed.). John Wiley & Sons, Inc.

Hight, D. W., McMillan, F., Powell, J. J. M., Jardine, R. J., & Allenou, C. P. (2003). Some Characteristics of London Clay. In T. S. Tan, K. K. Phoon, D. W. Hight, & S. Leroueil (Eds.), *Characterisation and Engineering Properties of Natural Soils* (Vol. 2, pp. 851–907). Swets & Zeitlinger, Lisse.

Hueckel, T., & Baldi, G. (1990). Thermoplasticity of Saturated Clays: Experimental Constitutive Study. *Journal of Geotechnical Engineering*, *116*(12), 1778–1796. https://doi.org/10.1061/(ASCE)0733-9410(1990)116

Huotari, T., & Kukkonen, I. (2004). *Thermal Expansion Properties of Rocks: Literature Survey and Estimation of Thermal Expansion Coefficient for Olkiluoto Mica Gneiss*. Geological Survey of Finland, Espoo, Finland.

Karamouz, M., Ahmadi, A., & Akhbari, M. (2011). *Groundwater Hydrology - Engineering, Planning, and Management*. CRC Press.

Khosravi, A., Moradshahi, A., McCartney, J. S., & Kabiri, M. (2016). Numerical Analysis of Energy Piles under Different Boundary Conditions and Thermal Loading Cycles. In *E3S Web of Conferences* (pp. 1–6). https://doi.org/10.1051/e3sconf/20160905005

Kirk, S. S., & Williamson, D. M. (2012). Structure and Thermal Properties of Porous Geological Materials. In *AIP Conference, American Institute of Physics* (pp. 867–870). American Institute of Physics. https://doi.org/10.1063/1.3686415

Knellwolf, C., Peron, H., & Laloui, L. (2011). Geotechnical Analysis of Heat Exchanger Piles. *Journal of Geotechnical and Geoenvironmental Engineering*, *137*(October), 890–902. https://doi.org/10.1061/(ASCE)GT.1943-5606.0000513.

Kramer, C. ., & Basu, P. (2014). Performance of a Model Geothermal Pile in Sand. In Gaudin & White (Eds.), *Physical Modelling in Geotechnics* (pp. 771–777). London: Taylor & Francis Group.

Kuwabara, B., Auer, T., Gouldsborough, T., Akerstream, T., & Klym, G. (2009). Manitoba Hydro Place - Integrated Design Process Exemplar. In *PLEA2009 - 26th Conference on Passive and Low Energy Architecture*. Quebec City, Canada.

Laloui, L., & Di Donna, A. (2011). Understanding the Behaviour of Energy Geo-Structures. *Proceedings of the Institution of Civil Engineers - Civil Engineering*, *164*(4), 184–191. https://doi.org/10.1680/cien.2011.164.4.184

Laloui, L., & Nuth, M. (2009). Investigations on the Mechanical Behaviour of a Heat Exchanger Pile. In W. F. Van Impe & P. Van Impe (Eds.), *Deep Foundations on Bored and Auger Piles* (pp. 343–347). London: Taylor & Francis Group.

Laloui, L., Nuth, M., & Vulliet, L. (2006). Experimental and Numerical Investigations of the Behaviour of a Heat Exchanger Pile. *International Journal for Numerical and Analytical*

Methods in Geomechanics, *30*(8), 763–781. https://doi.org/10.1002/nag.499

Liu, H., Wang, C., Kong, G., & Bouazza, A. (2018). Ultimate bearing capacity of energy piles in dry and saturated sand. *Acta Geotechnica*, *6*. https://doi.org/10.1007/s11440-018-0661-6

Loveridge, F. (2012). *The Thermal Performance of Foundation Piles used as Heat Exchangers in Ground Energy Systems*. The *University of Southampton*. Ph.D. Thesis, University of Southampton, The United Kingdom.

Loveridge, F., Powrie, W., & Smith, P. (2013). A Review of the Design and Construction Aspects for Bored Thermal Piles. *Ground Engineering*, 28–31.

Manitoba Hydro. (2018). Geothermal Heat Pump Systems. Retrieved August 8, 2018, from https://www.hydro.mb.ca/your_home/geothermal_heat_pumps/index.shtml

Manzari, M., Devininkas, A., Olshansky, D., & Galaa, A. (2014). Behavioural Modelling of Toronto Glacial Soils and Implementation in Numerical Modelling. In *The 67th Canadian Geotechnical Conference*. GeoRegina 2014, Regina, Canada.

McCartney, J. S. (2011). Engineering Performance of Energy Foundations. In *2011 PanAm CGS Geotechnical Conference*. Toronto, Canada.

Mitalas, G. P. (1987). Calculation of Below-Grade Residential Heat Loss - Low-Rise Residential Building. *ASHRAE Transactions*, *93*, 743–783.

Moon, C. E., & Choi, J. M. (2015). Heating Performance Characteristics of the Ground Source Heat Pump System with Energy-Piles and Energy-Slabs. *Energy*, *81*, 27–32. https://doi.org/10.1016/j.energy.2014.10.063

Murphy, K. D., & McCartney, J. S. (2015). Seasonal Response of Energy Foundations During Building Operation. *Geotechnical and Geological Engineering*, *33*, 343–356. https://doi.org/10.1007/s10706-014-9802-3

Murphy, K. D., McCartney, J. S., & Henry, K. S. (2015). Evaluation of Thermo-Mechanical and Thermal Behavior of Full-Scale Energy Foundations. *Acta Geotechnica*, *10*, 179–195. https://doi.org/10.1007/s11440-013-0298-4

Ng, C. W. W., Shi, C., Gunawan, A., & Laloui, L. (2014). Centrifuge modelling of energy piles subjected to heating and cooling cycles in clay. *Geotechnique Letters*, *4*, 310–316. https://doi.org/10.1680/geolett.14.00063

Ng, C. W. W., Shi, C., Gunawan, A., Laloui, L., & Liu, H. L. (2015). Centrifuge Modelling of Heating Effects on Energy Pile Performance in Saturated Sand. *Canadian Geotechnical Journal*, *52*(8), 1045–1057. https://doi.org/10.1139/cgj-2014-0301

Oke, T. R. (1987). *Boundary Layer Climates* (2nd ed.). Routledge. https://doi.org/10.1016/0012-8252(90)90005-G

Olgun, C. G., Ozudogru, T. Y., & Arson, C. F. (2014). Thermo-Mechanical Radial Expansion of Heat Exchanger Piles and Possible Effects on Contact Pressures at Pile–Soil Interface. *Géotechnique Letters*, 1–9. https://doi.org/10.1680/geolett.14.00018

Ouyang, Y., Soga, K., & Leung, Y. F. (2011). Numerical Back-analysis of Energy Pile Test at Lambeth College, London. In *Geo-Frontiers 2011 © ASCE 2011* (pp. 440–449).

Pahud, D., & Hubbuch, M. (2007). Measured Thermal Performances of the Energy Pile System of the Dock Midfield at Zürich Airport. In *Proceeding European Geothermal Congress 2007* (pp. 1–7). Unterhaching, Germany.

Pascquale, V., Verdoya, M., & Chiozzi, P. (2014). *Geothermics - Heat Flow in the Lithosphere*. Springer.

PLAXIS. (2015). *Thermal and Coupled THM Analysis*. Delft, The Netherlands: PLAXIS. Retrieved from https://www.plaxis.com/

PLAXIS 2D. (2018). *PLAXIS User's Manuals*. Delft, The Netherlands: PLAXIS. Retrieved from https://www.plaxis.com/

Poulos, H. G., & Davis, E. H. (1980). *Pile Foundation Analysis and Design*. Rainbow-Bridge Book Co.

Randolph, M. F., Dolwin, J., & Beck, R. (1994). Design of Driven Piles in Sand. *Géotechnique*, *44*(3), 427–448. https://doi.org/10.1680/geot.1994.44.3.427

Rigby-Jones, J., & Milne, C. (2010). PLAXIS Analysis of a Basement Excavation in Central London. *PLAXIS Bulletin, Autumn Issue 2010*, 14–17. Retrieved from www.plaxis.nl

Rotta Loria, A. F., & Laloui, L. (2017). Thermally Induced Group Effects among Energy Piles. *Géotechnique*, *67*(5), 374–393. https://doi.org/10.1680/jgeot.16.P.039

Singh, R. M., Bouazza, A., & Wang, B. (2015). Near-Field Ground Thermal Response to Heating of a Geothermal Energy Pile: Observations from a Field Test. *Soils and Foundations*, *55*(6), 1412–1426. https://doi.org/10.1016/j.sandf.2015.10.007

Skaftfeld, K. (2014). *Experience as a Guide to Geotechnical Practice In Winnipeg*. M.Sc.Thesis, University of Manitoba, Canada.

Suckling, T., & Cannon, R. (2004). Energy piles for Pallant House, Chichester, UK. *Ground Engineering*, 27–29.

Sutman, M., Brettmann, T., & Olgun, C. G. (2018). Full-Scale In-Situ Tests on Energy Piles: Head and Base-Restraining Effects on the Structural Behaviour of Three Energy Piles. *Geomechanics for Energy and the Environment*, 1–13. https://doi.org/10.1016/j.gete.2018.08.002

Terzaghi, K., Peck, R. B., & Mesri, G. (1996). *Soil Mechanics in Engineering Practice* (3rd ed.). John Wiley & Sons, Inc.

Thiessen, K. (2010). *Stabilization of Natural Clay Riverbanks with Rockfill Columns: A Full-Scale Field Test and Numerical Verification*. Ph.D. Thesis, University of Manitoba, Canada.

Thiessen, K., Alfaro, M. C., & Blatz, J. A. (2011). Measuring the load-deformation response of rockfill columns by a full-scale field test on a natural riverbank. *Canadian Geotechnical Journal*, *48*(7), 1032–1043. https://doi.org/10.1139/t11-019

Thomas, H. R., & Rees, S. W. (1999). The Thermal Performance of Ground Floor Slabs - A Full-scale In-situ Experiment. *Building and Environment*, *34*, 139–164.

Thomas, H. R., & Rees, S. W. (2009). Measured and Simulated Heat Transfer to Foundation Soils. *Géotechnique*, *59*(4), 365–375. https://doi.org/10.1680/geot.2008.59.4.365

Wai, S. C., & Lo, K. Y. (1982). Temperature Effects on Strength and Deformation Behaviour of Rocks in Southern Ontario, *19*, 307–319.

Wang, B., Bouazza, A., Singh, R. M., Haberfield, C., Barry-Macaulay, D., & Baycan, S. (2015). Posttemperature Effects on Shaft Capacity of a Full-Scale Geothermal Energy Pile. *Journal of Geotechnical and Geoenvironmental Engineering*, *141*(4), 04014125-1-04014125-12. https://doi.org/10.1061/(ASCE)GT.1943-5606.0001266.

Weber, J., Ganz, B., Schellschmidt, R., Burkhard, S., & Schulz, R. (2015). Geothermal Energy Use in Germany. In *World Geothermal Congress*. Melbourne, Australia.

Yavari, N., Tang, A. M., Pereira, J. M., & Hassen, G. (2014). A Simple Method for Numerical Modelling of Mechanical Behaviour of an Energy Pile. *Géotechnique Letters*, *4*, 119–124. https://doi.org/10.1680/geolett.13.00053

Appendix A : Additional Numerical Results for the London Energy Pile (Case Study 1)

A.1. London Energy Pile: Change in the coefficient of thermal expansion of concrete (CTEc)

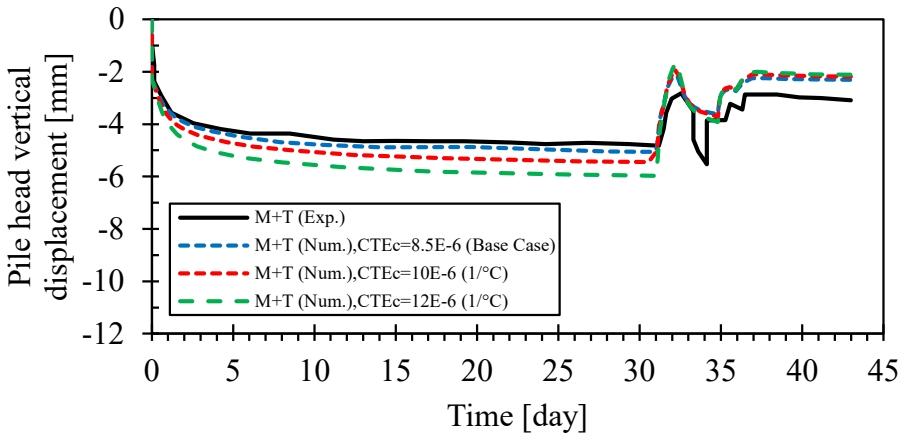

Figure A.1. Pile head vertical displacements during a cooling-heating cycle for the London energy pile (change in CTEc)

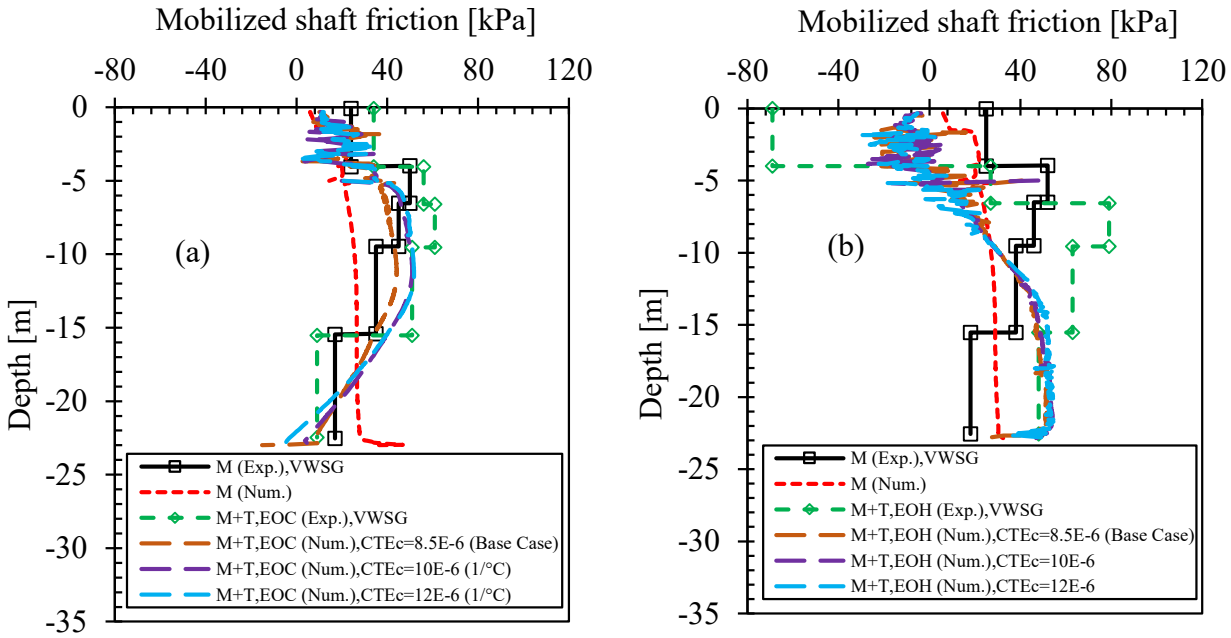

Figure A.2. Mobilized shaft friction along the pile-soil interface (a) at the end of cooling (EOC) and (b) at the end of heating (EOH) for the London energy pile (change in CTEc)

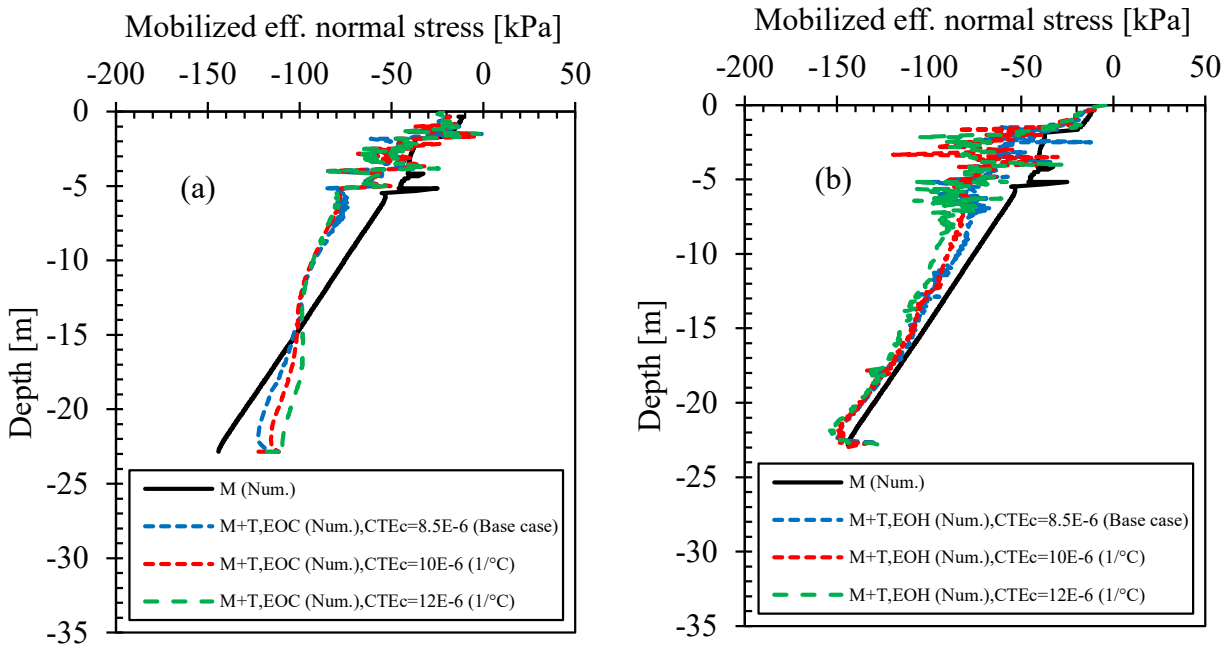

Figure A.3. Mobilized effective radial (normal) stress at the pile-soil interface along the pile length (a) at the end of cooling (EOC) and (b) at the end of heating (EOH) for the London energy pile (Change in CTEc)

A.2. London Energy Pile: Change in the coefficient of thermal expansion of soils (CTEs)

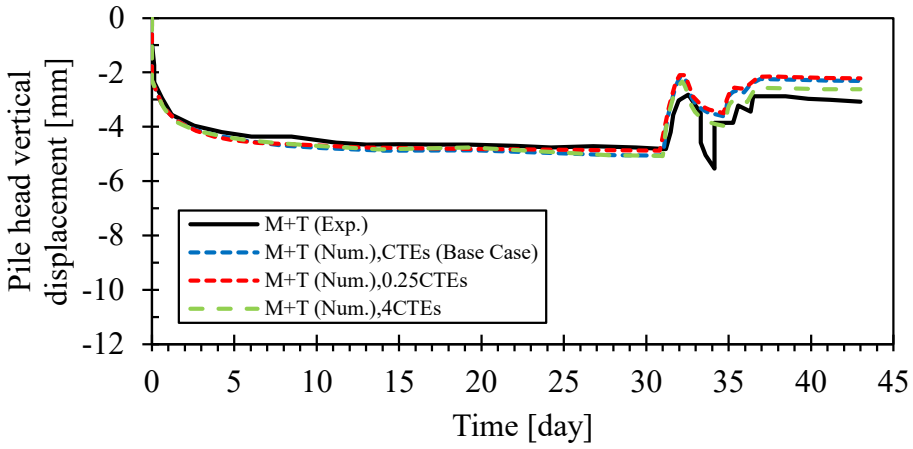

Figure A.4. Pile head vertical displacement during a cooling-heating cycle for the London energy pile (change in CTEs)

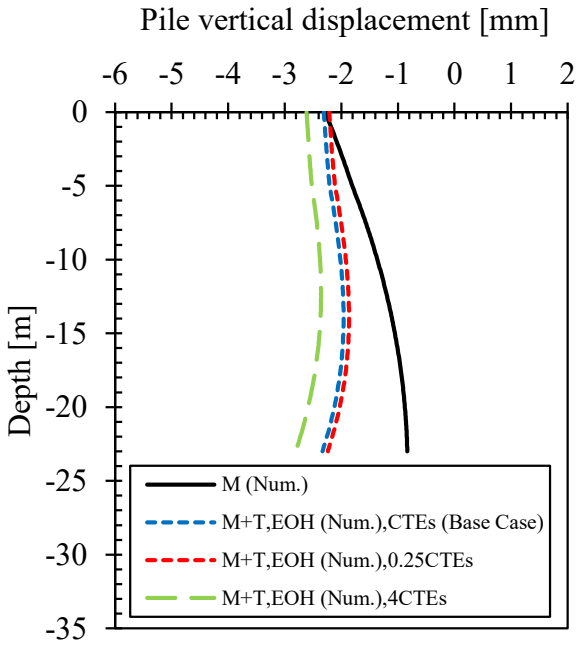

Figure A.5. Pile vertical displacement profiles along its length at the end of heating (EOH) for the London energy pile (change in CTEs)

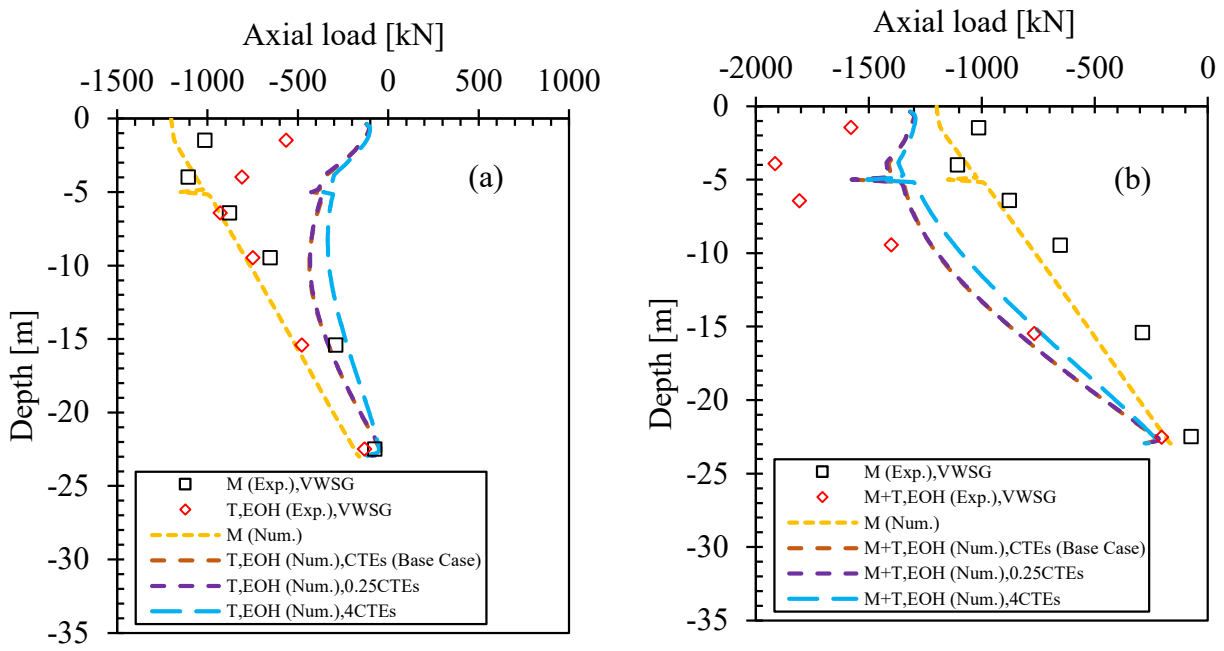

Figure A.6. Axial load profiles (a) thermal (T) and (b) thermo-mechanical (M+T) at the end of heating (EOH) for the London energy pile (change in CTEs)

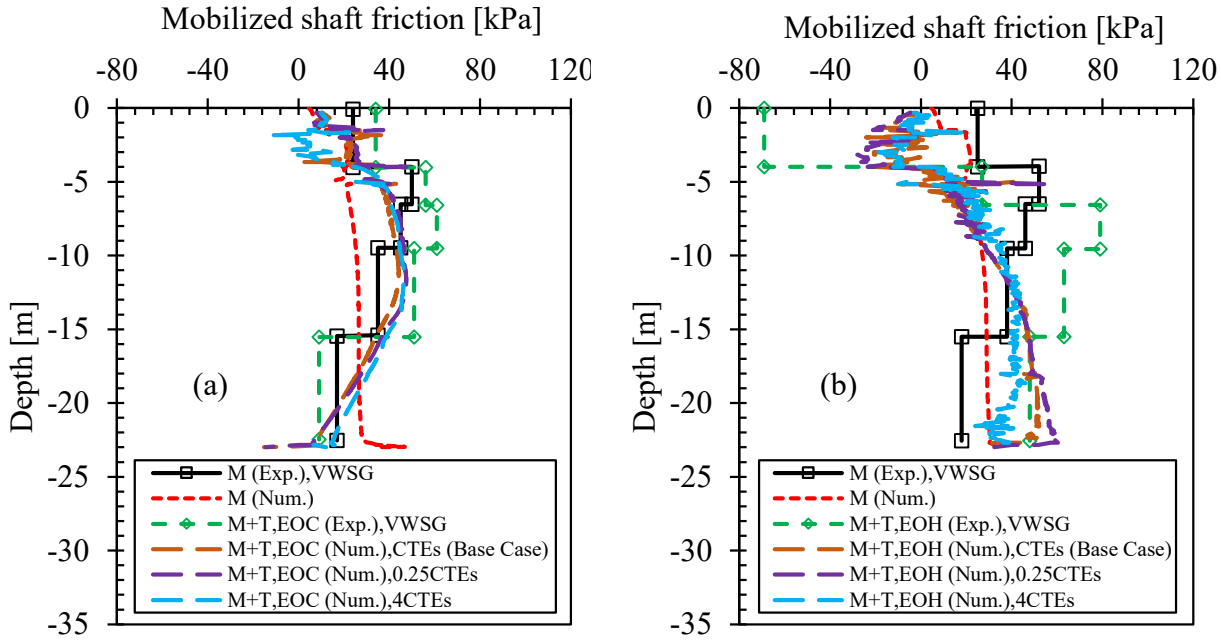

Figure A.7. Mobilized shaft friction along the pile-soil interface (a) at the end of cooling (EOC) and (b) at the end of heating (EOH) for the London energy pile (change in CTEs)

A.3. London Energy Pile: Change in soil stiffness (Es)

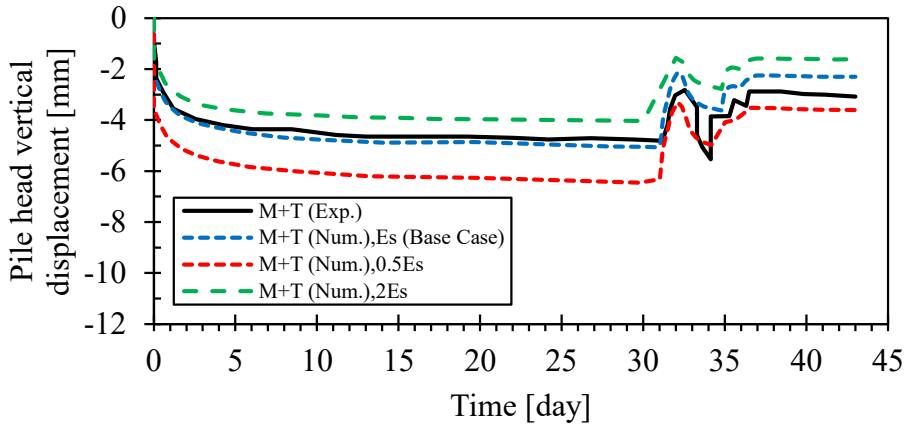

Figure A.8. Pile head vertical displacements during a cooling-heating cycle for the London energy pile (change in Es)

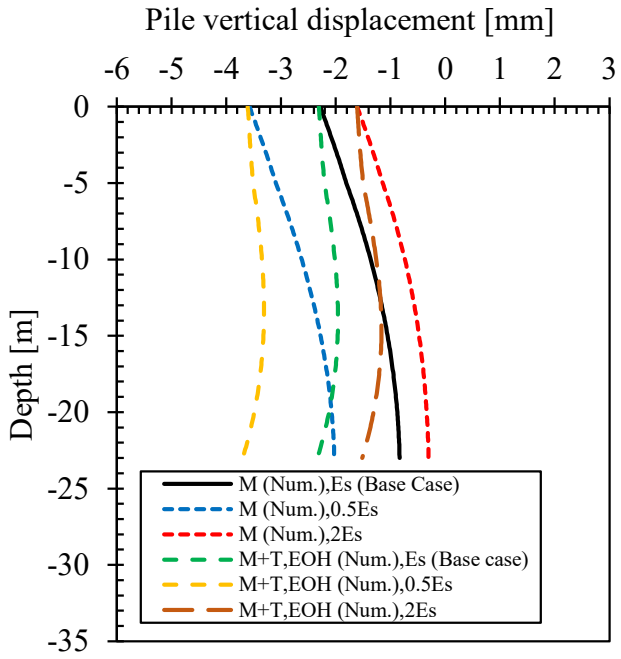

Figure A.9. Pile vertical displacement profiles along its length at the end of heating (EOH) for the London energy pile (change in Es)

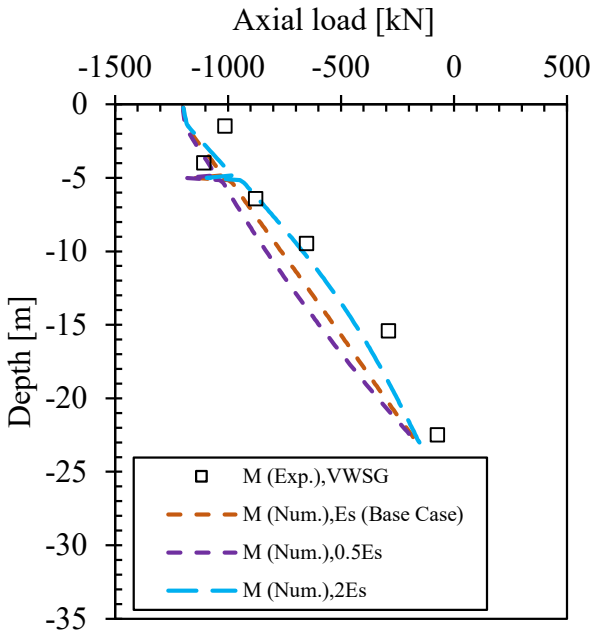

Figure A.10. Axial load profiles due to the mechanical (M) load only for the London energy pile (change in Es)

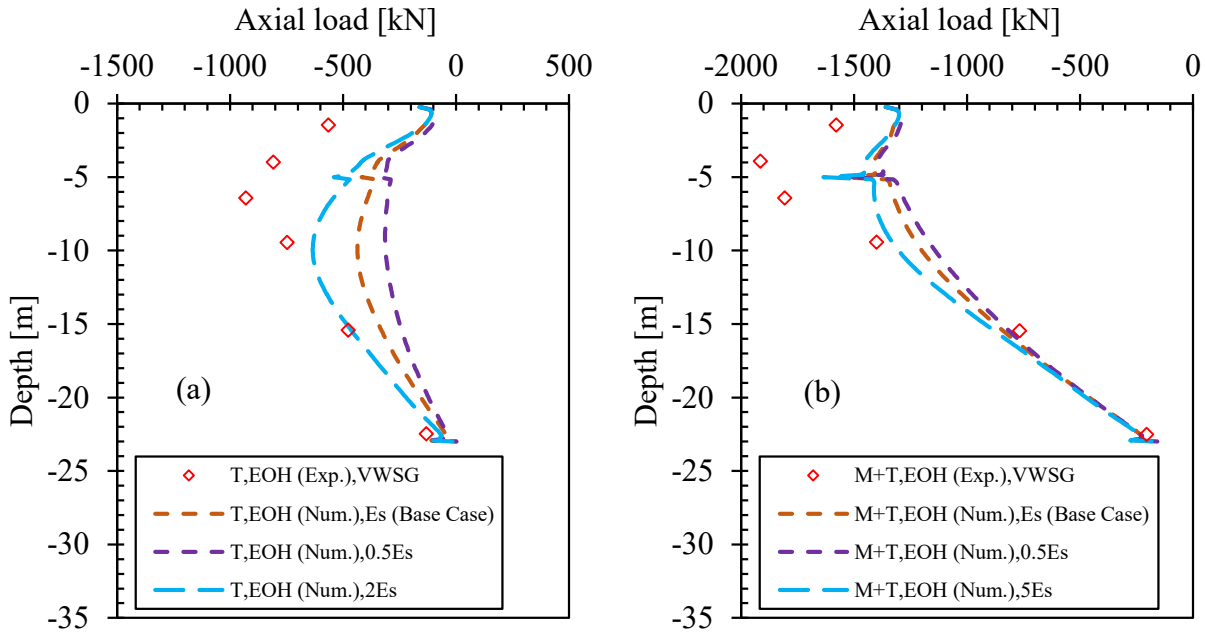

Figure A.11. Axial load profiles (a) thermal (T) and (b) thermo-mechanical (M+T) at the end of heating (EOH) for the London energy pile (change in Es)

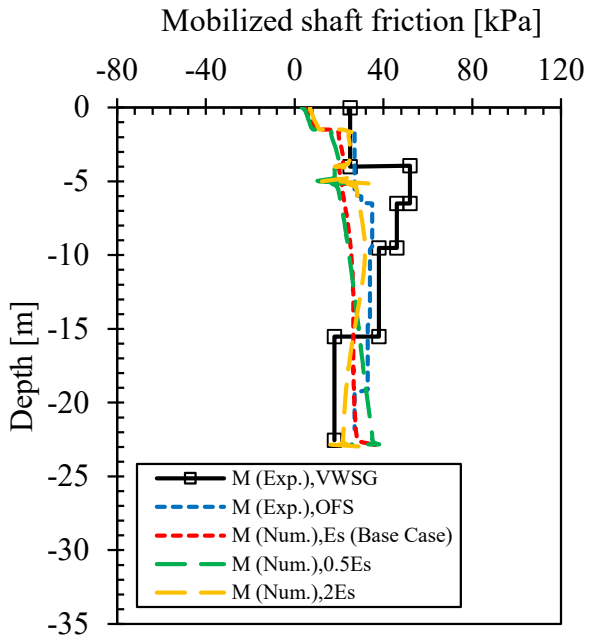

Figure A.12. Mobilized shaft friction along the pile-soil interface due to the mechanical load only (M) for the London energy pile (change in Es)

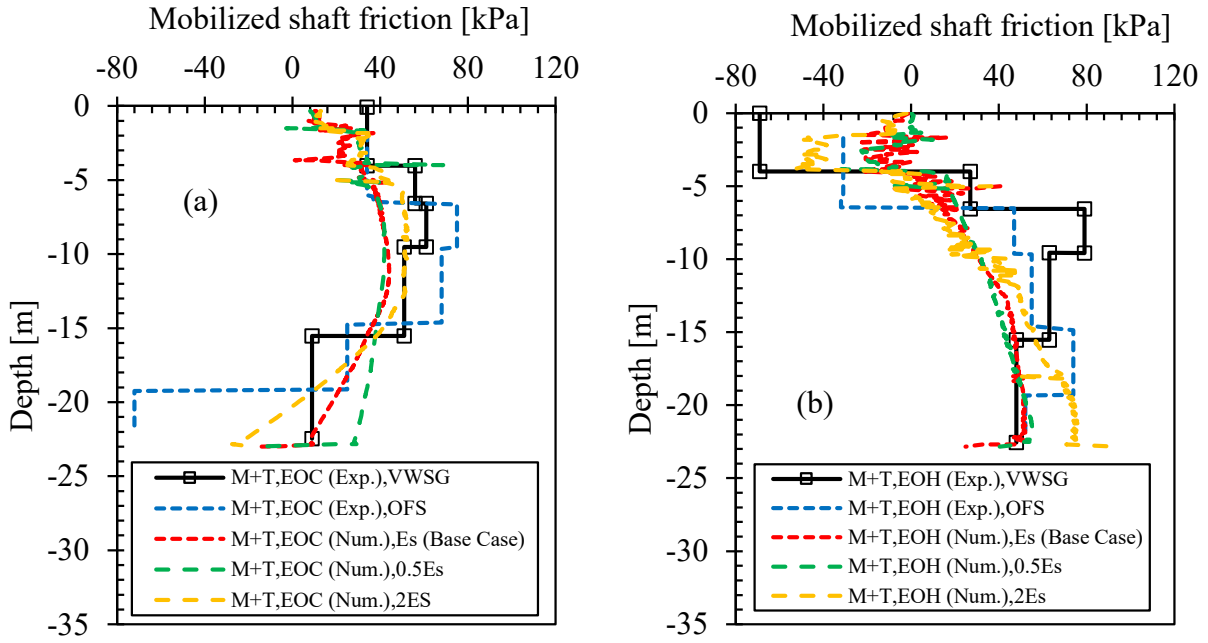

Figure A.13. Mobilized shaft friction along the pile-soil interface (a) at the end of cooling (EOC) and (b) at the end of heating (EOH) for the London energy pile (change in Es)

A.4. London Energy Pile: Change in thermal conductivity of soils (TCs)

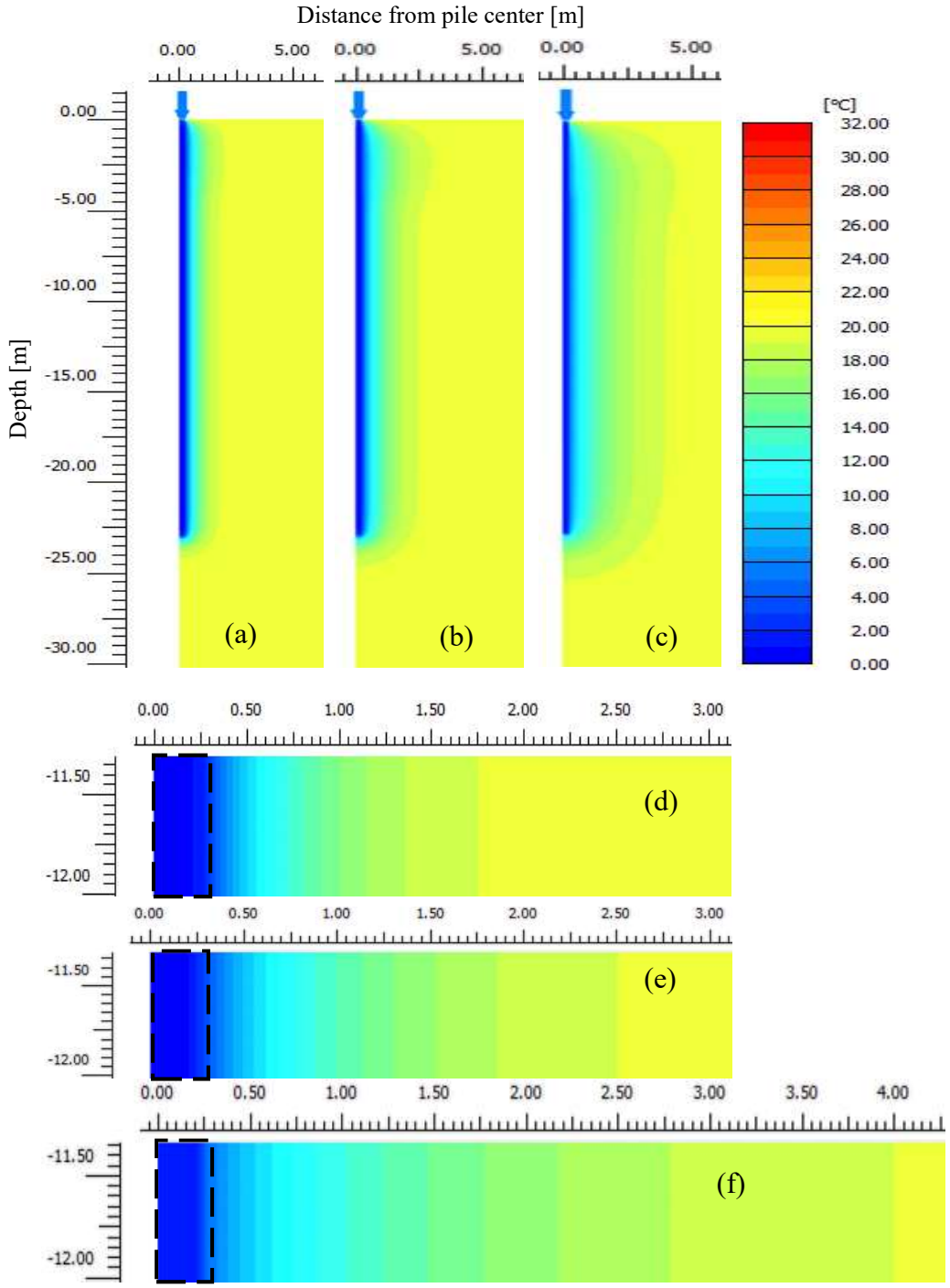

Figure A.14. Temperature distributions in the pile and surrounding ground (a) 0.25TCs (b) TCs-base case (c) 4TCs at the end of cooling (EOC) and (d), (e), and (f) enlarged views around the mid-depth of the pile; respectively, for the London energy pile (change in TCs)

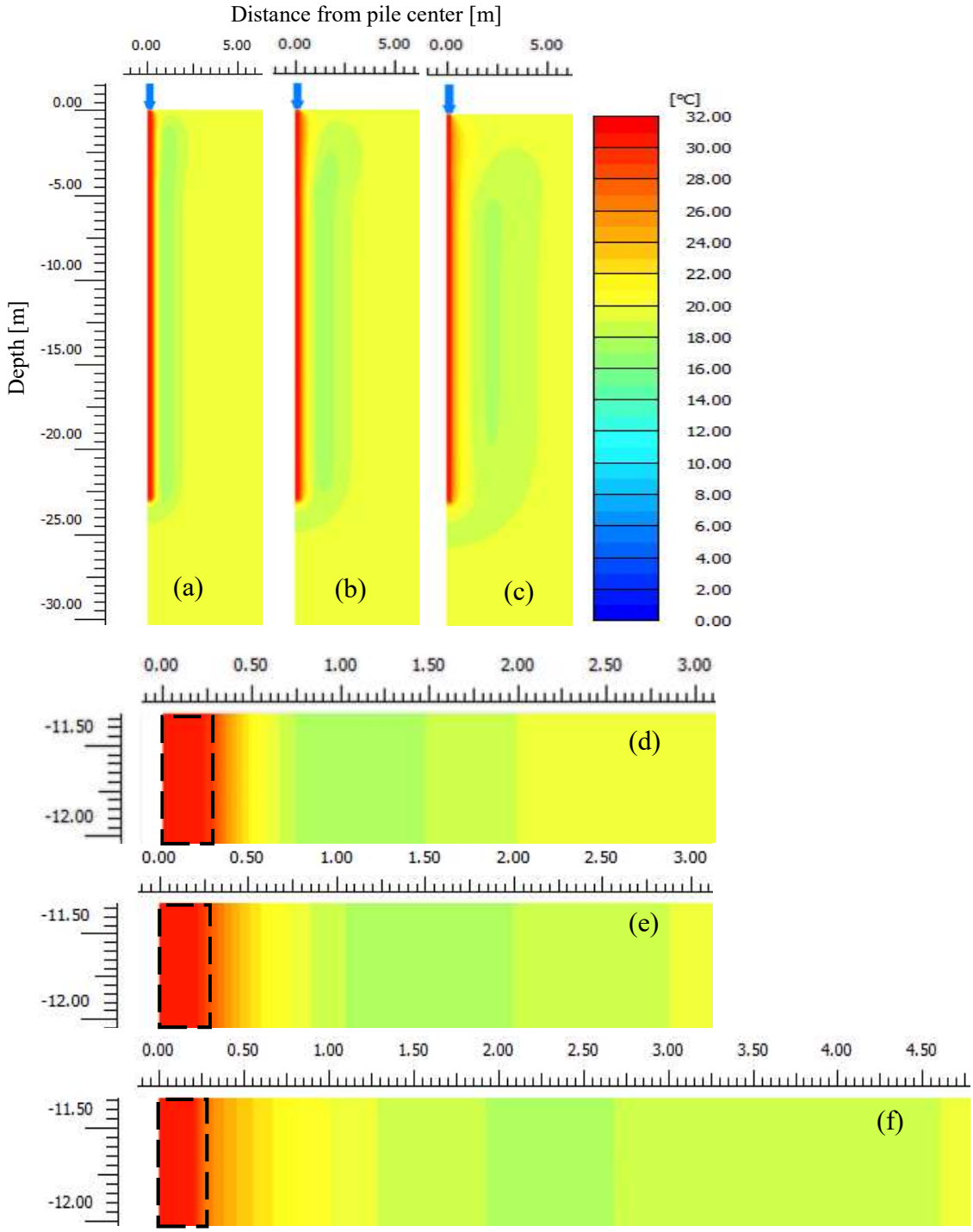

Figure A.15. Temperature distributions in the pile and surrounding ground (a) 0.25TCs (b) TCs-base case (c) 4TCs at the end of heating (EOH) and (d), (e), and (f) enlarged views of (a), (b) and (c) around the mid-depth of the pile; respectively, for the London energy pile (change in TCs)

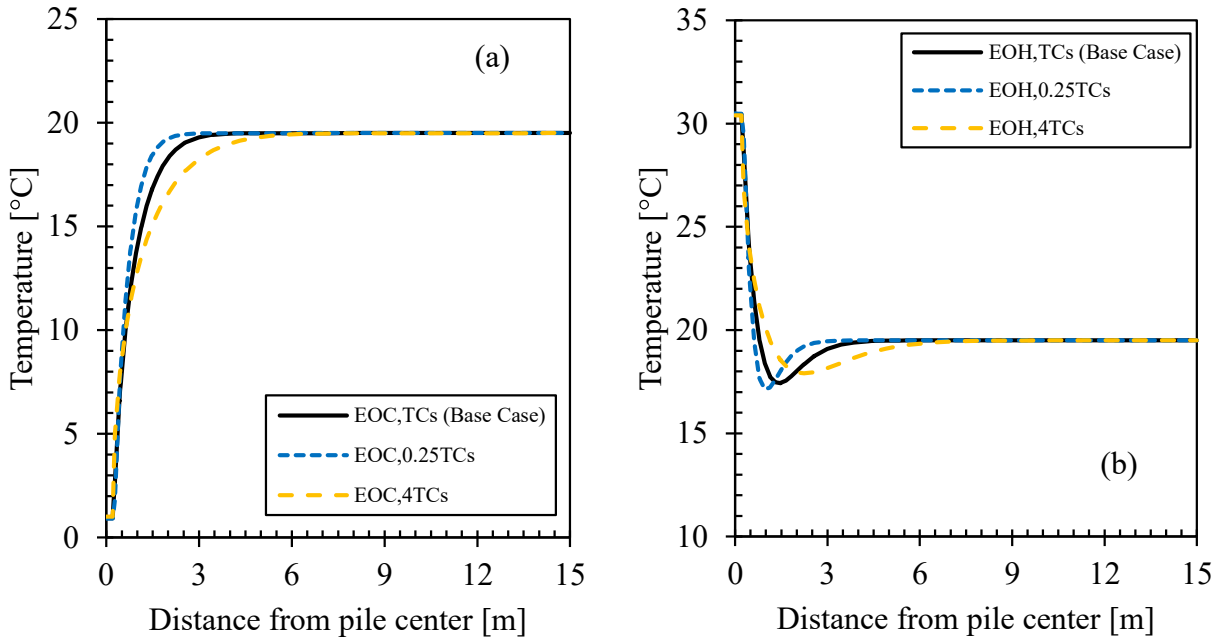

Figure A.16. Temperature distributions in the pile and surrounding ground at mid-depth of the pile (a) at the end of cooling (EOC) and (b) at the end of heating (EOH) for the London energy pile (change in TCs)

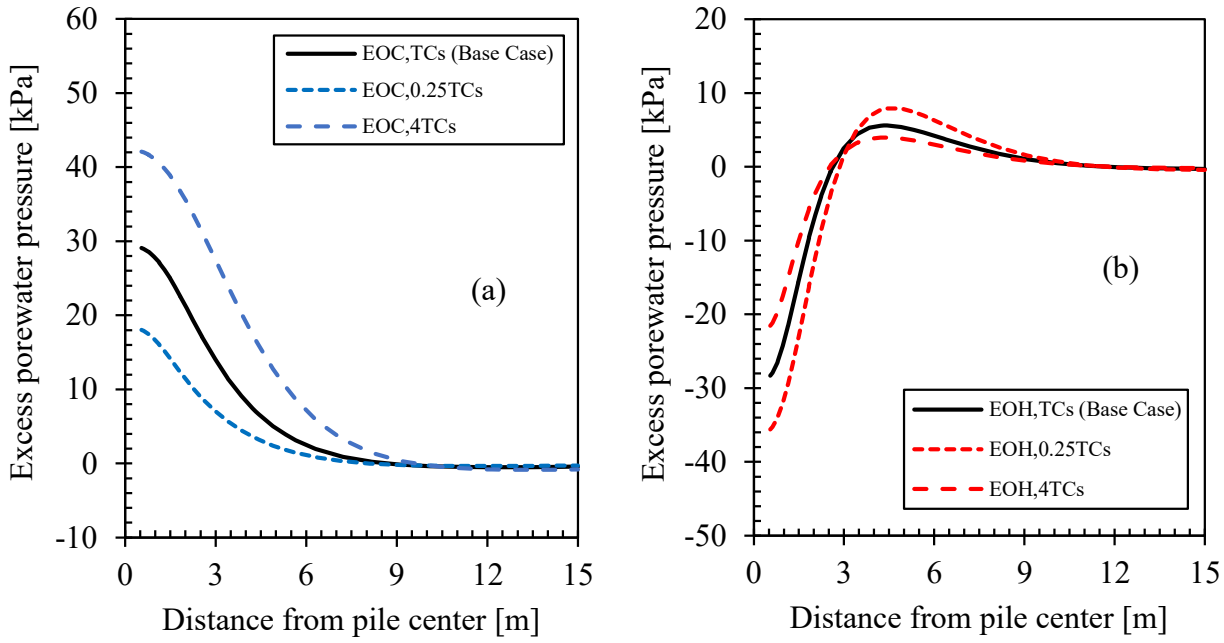

Figure A.17. Excess porewater pressure distributions in surrounding ground at mid-depth of the pile (a) at the end of cooling (EOC) and (b) at the end of heating (EOH) for the London energy pile (change in TCs)

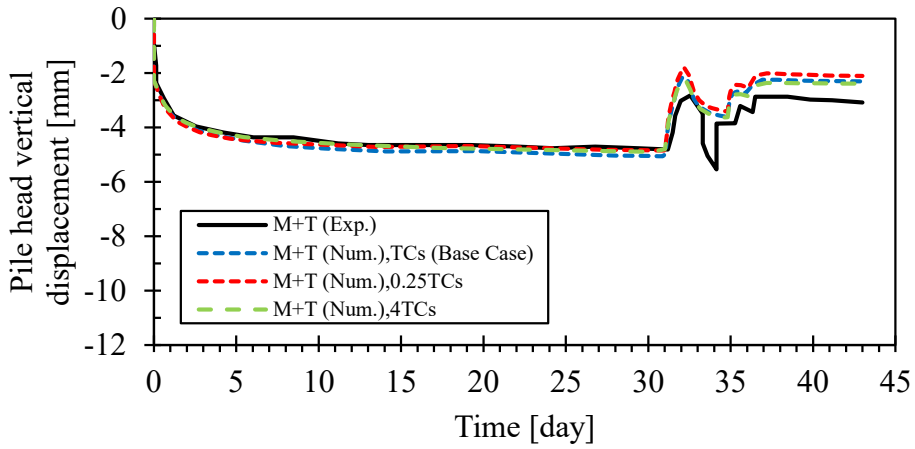

Figure A.18. Pile head vertical displacements during a cooling-heating cycle (change in TCs)

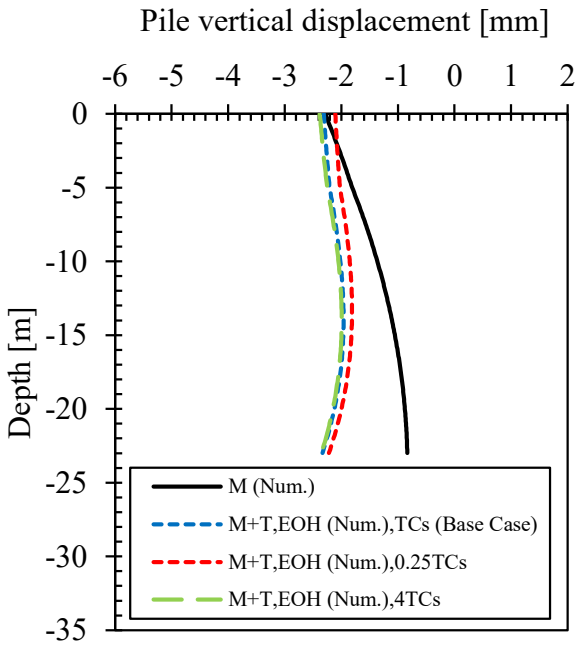

Figure A.19. Pile vertical displacement profiles along its length at the end of heating (EOH) for the London energy pile (change in TCs)

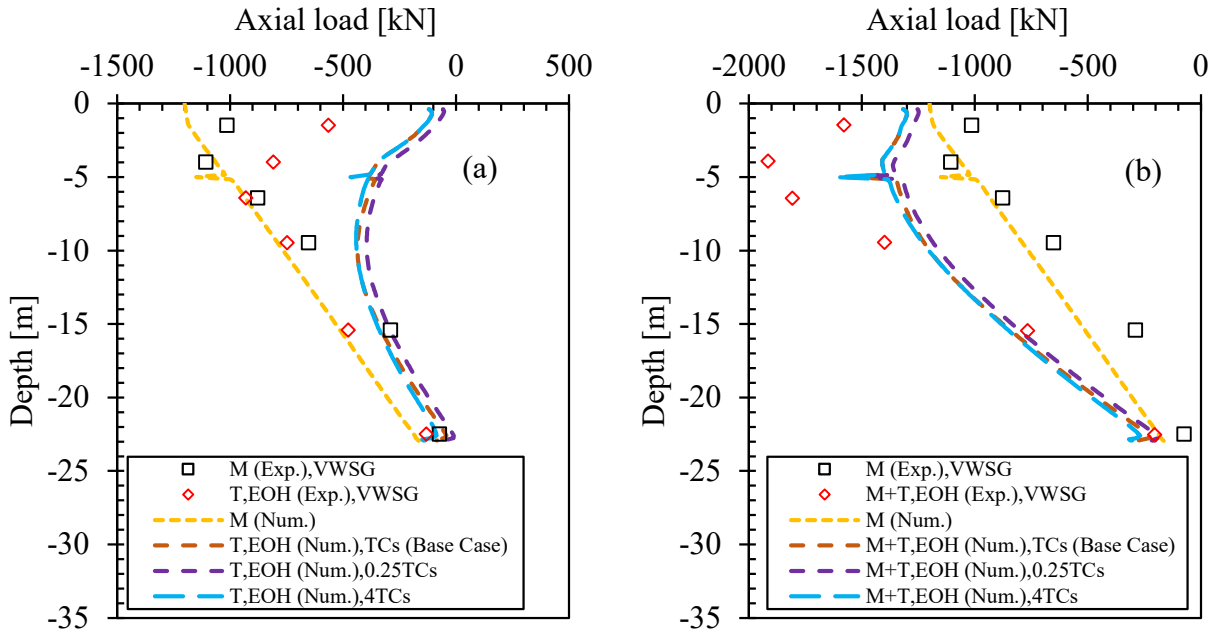

Figure A.20. Axial load profiles (a) thermal (T) and (b) thermo-mechanical (M+T) at the end of heating (EOH) for the London energy pile (change in TCs)

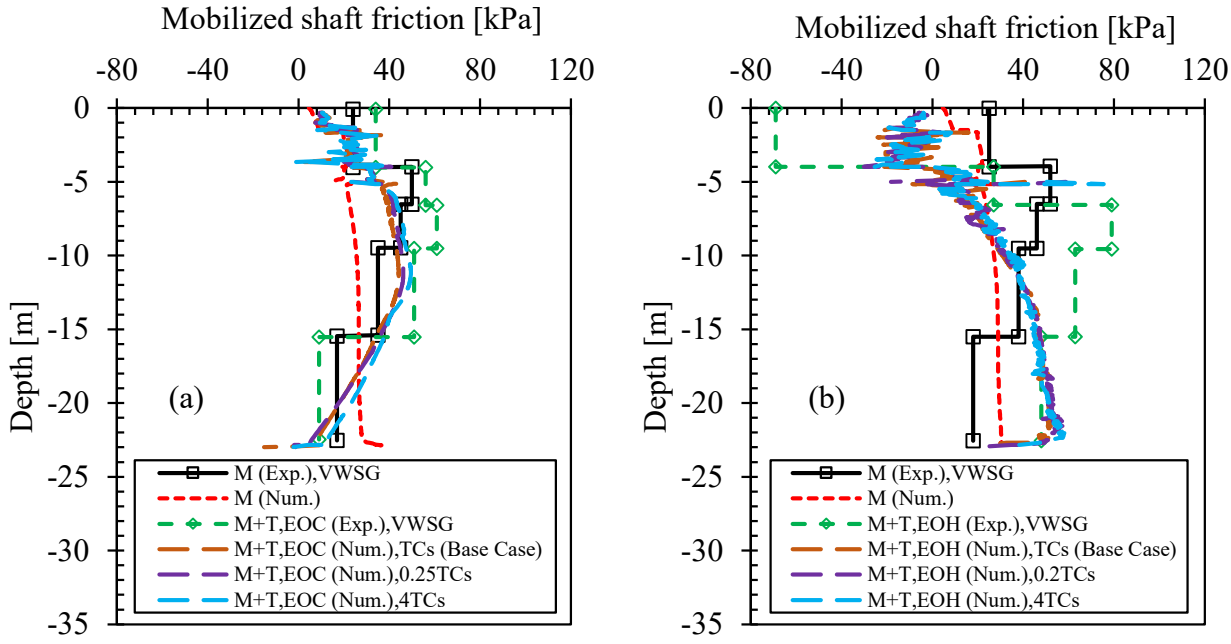

Figure A.21. Mobilized shaft friction along the pile-soil interface (a) at the end of cooling (EOC) and (b) at the end of heating (EOH) for the London energy pile (change in TCs)

A.5. London Energy Pile: Change in specific heat capacity of soils (SHCs)

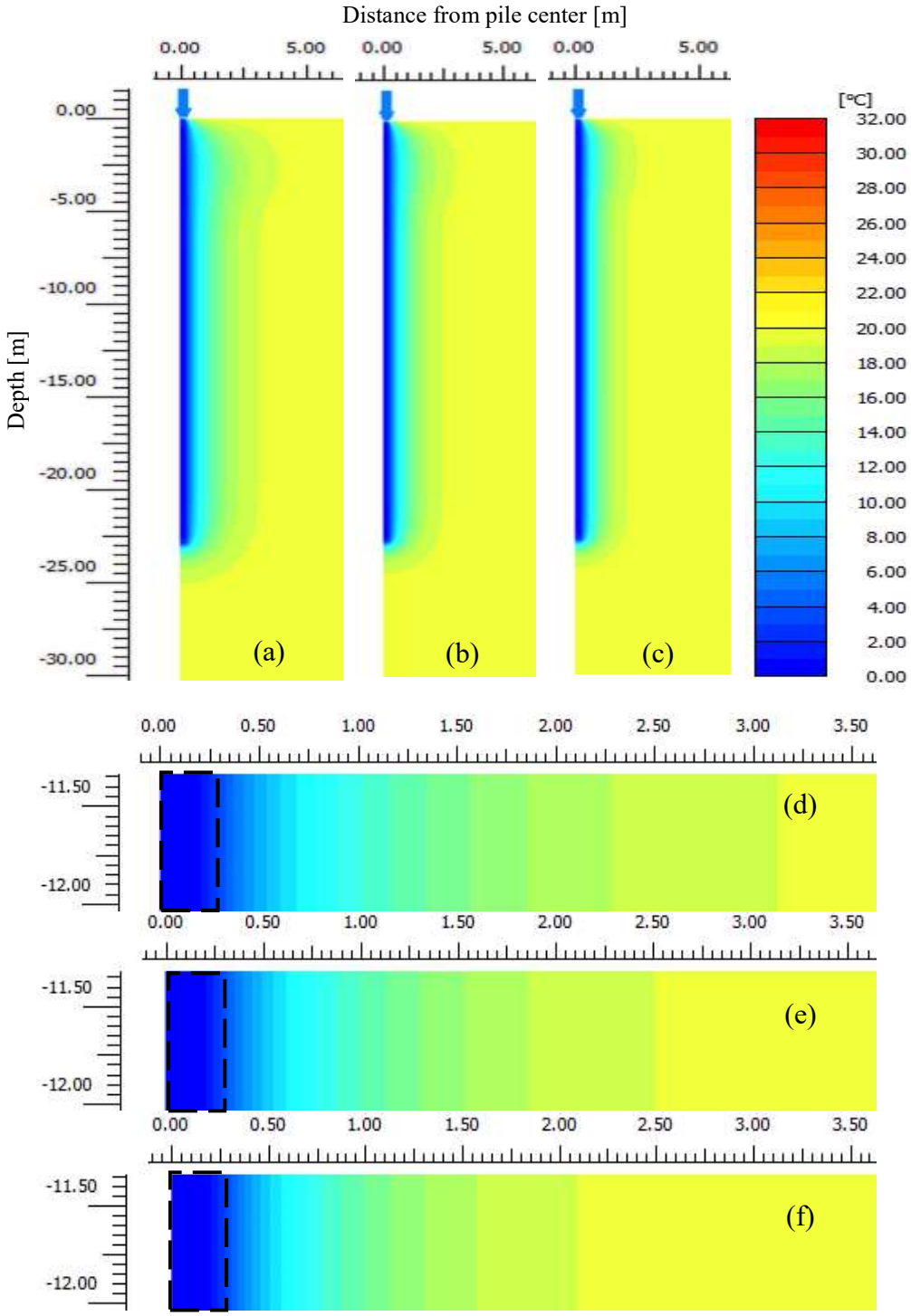

Figure A.22. Temperature distributions in the pile and surrounding ground (a) 0.25SHCs (b) SHCs-base case (c) 2SHCs at the end of cooling (EOC) and (d), (e), and (f) enlarged views of (a), (b) and (c) around the mid-depth of the pile; respectively, for the London energy pile (change in SHCs)

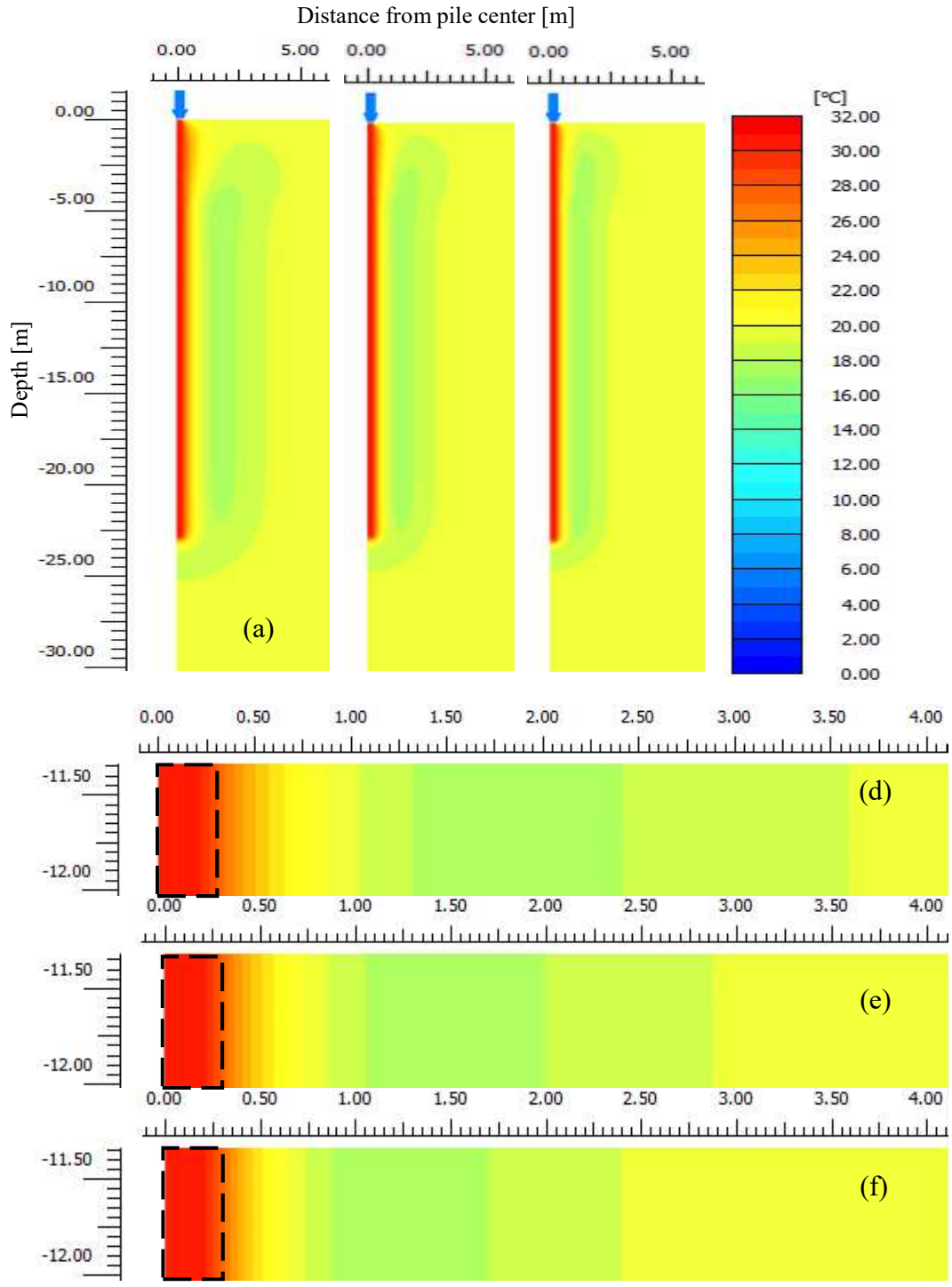

Figure A.23. Temperature distributions in the pile and surrounding ground (a) 0.25SHCs (b) SHCs-base case (c) 2SHCs at the end of heating (EOH) and (d), (e), and (f) enlarged views around the mid-depth of the pile; respectively, for the London energy pile (change in SHCs)

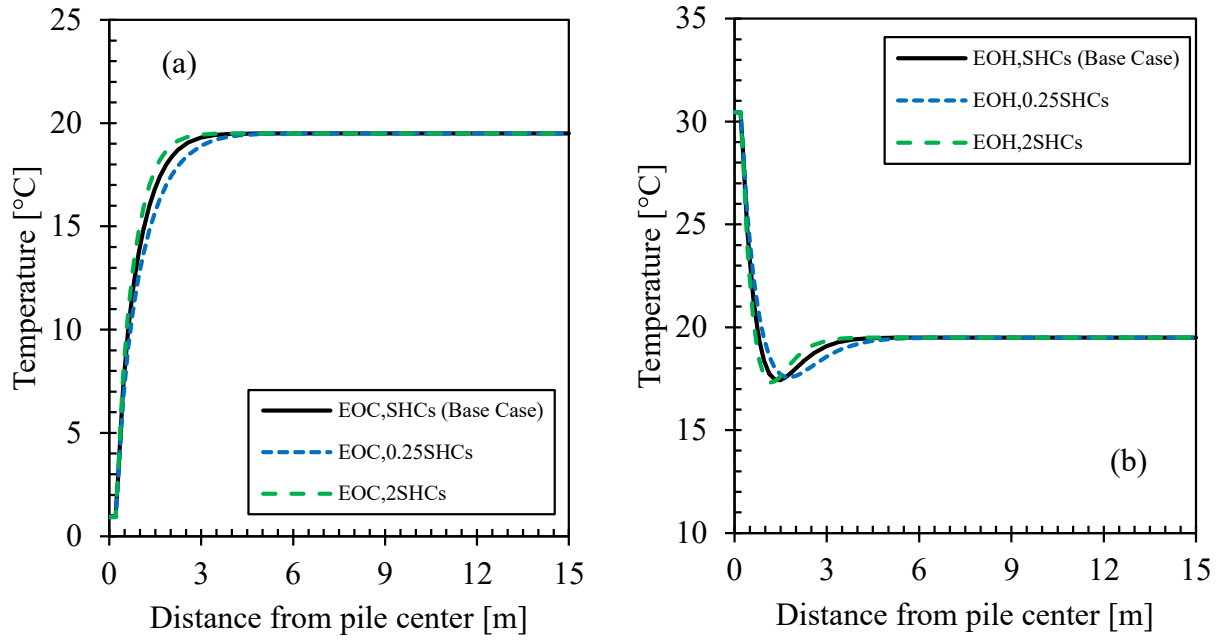

Figure A.24. Temperature profiles in the pile and surrounding ground at the mid-depth of the pile from the pile center (a) at the end of cooling (EOC) and (b) at the end of heating (EOH) for the London energy pile (change in SHCs)

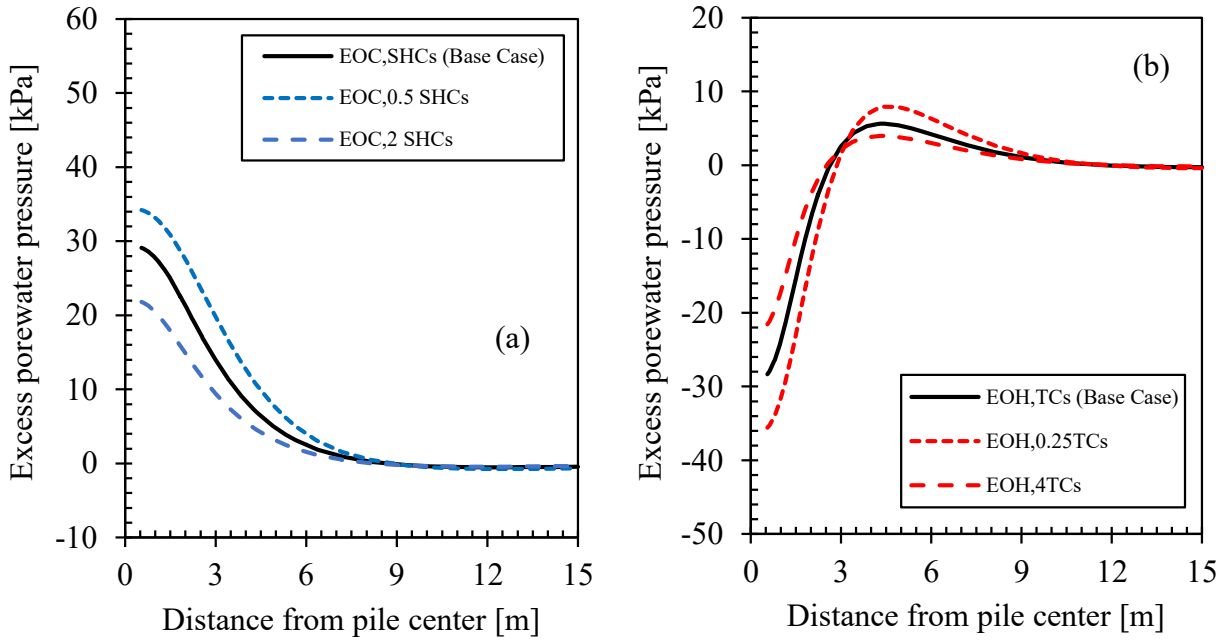

Figure A.25. Excess porewater pressure (EPWP) distributions in the surrounding ground at the mid-depth of the pile from the pile center (a) at the end of cooling (EOC) and (b) at end of heating (EOH) for the London energy pile (change in SHCs)

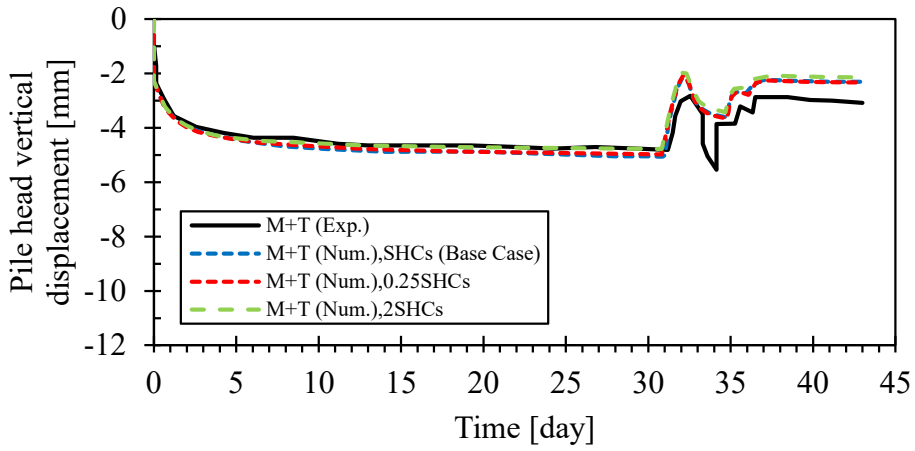

Figure A.26. Pile head vertical displacements during a cooling-heating cycle (change in SHCs)

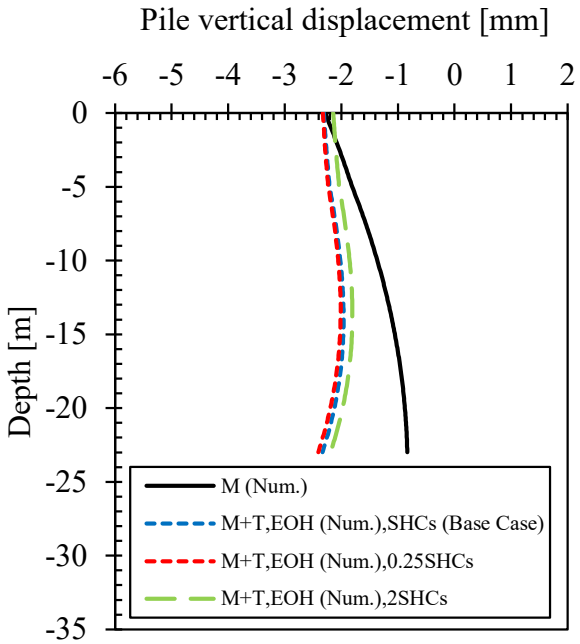

Figure A.27. Pile vertical displacement profiles along its length at the end of heating (EOH) for the London energy pile (change in SHCs)

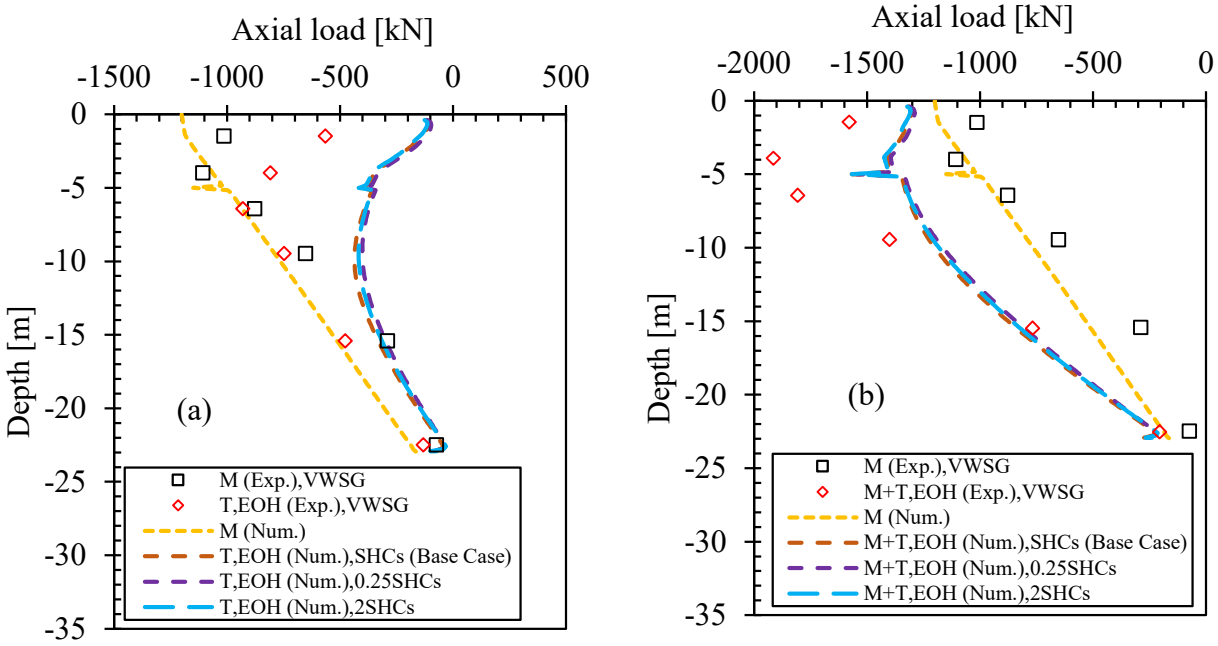

Figure A.28. Axial load profiles (a) thermal (T) and (b) thermo-mechanical (M+T) at the end of heating (EOH) for the London energy pile (change in SHCs)

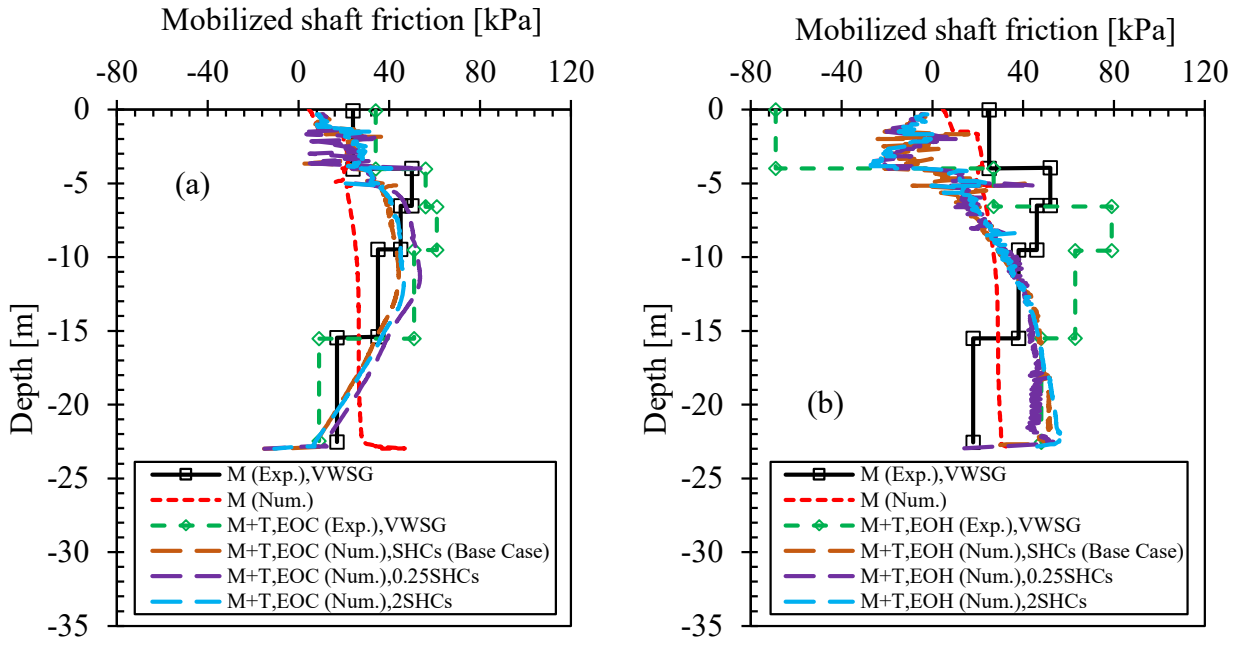

Figure A.29. Mobilized shaft friction along the pile-soil interface (a) at the end of cooling (EOC) and (b) at the end of heating (EOH) for the London energy pile (change in SHCs)

Appendix B : Additional Numerical Results for the Lausanne Energy Pile (Case Study 2)

B.1. Lausanne Energy Pile: Test 7 with changes in coefficient of thermal expansion of concrete (CTEc)

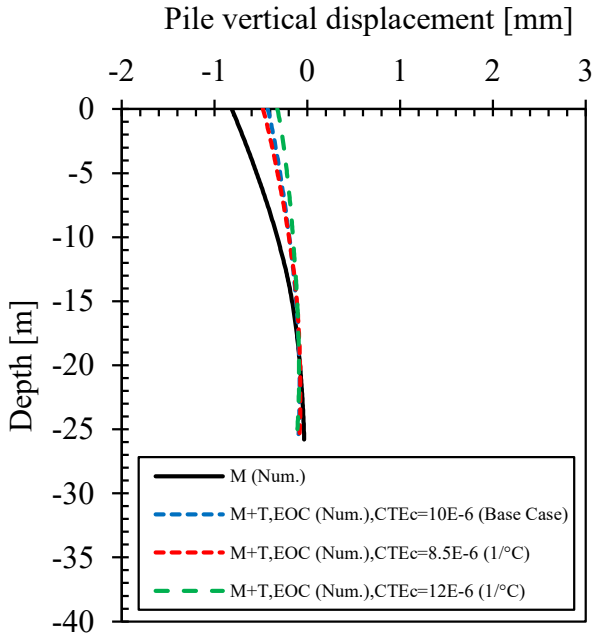

Figure B.1. Pile vertical displacement profiles at the end of cooling (EOC) for the Lausanne energy pile: Test 7 (change in CTEc)

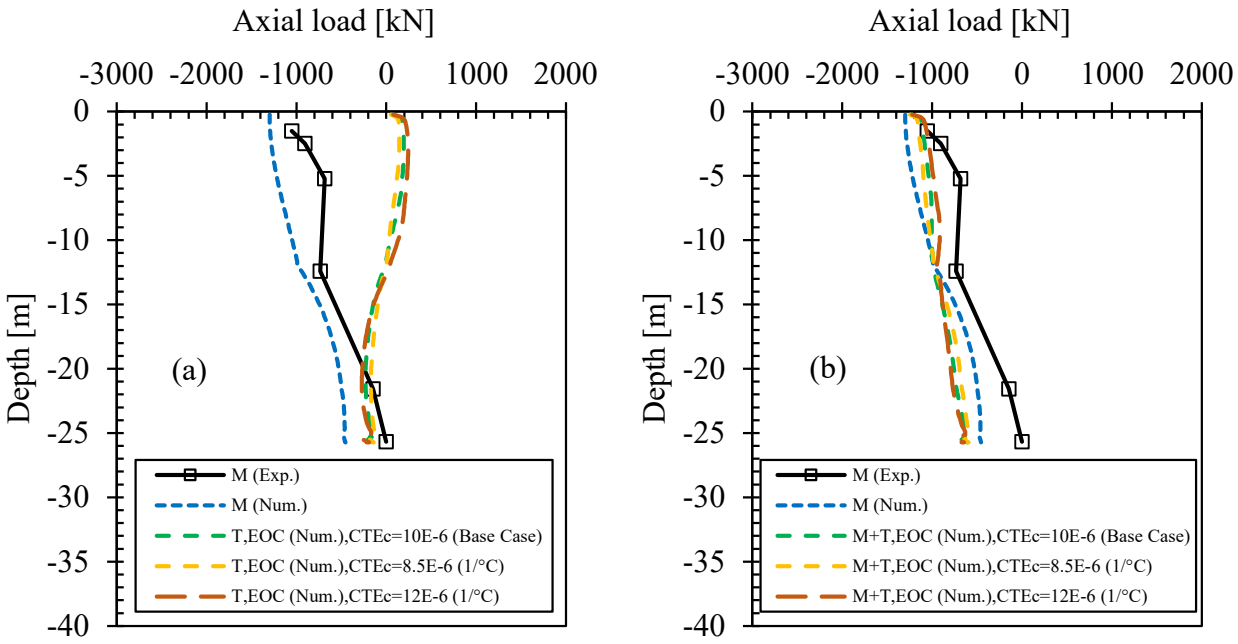

Figure B.2. Axial load profiles (a) thermal (T) and (b) thermo-mechanical (M+T) at the end of cooling (EOC) for the Lausanne energy pile: Test 7 (change in CTEc)

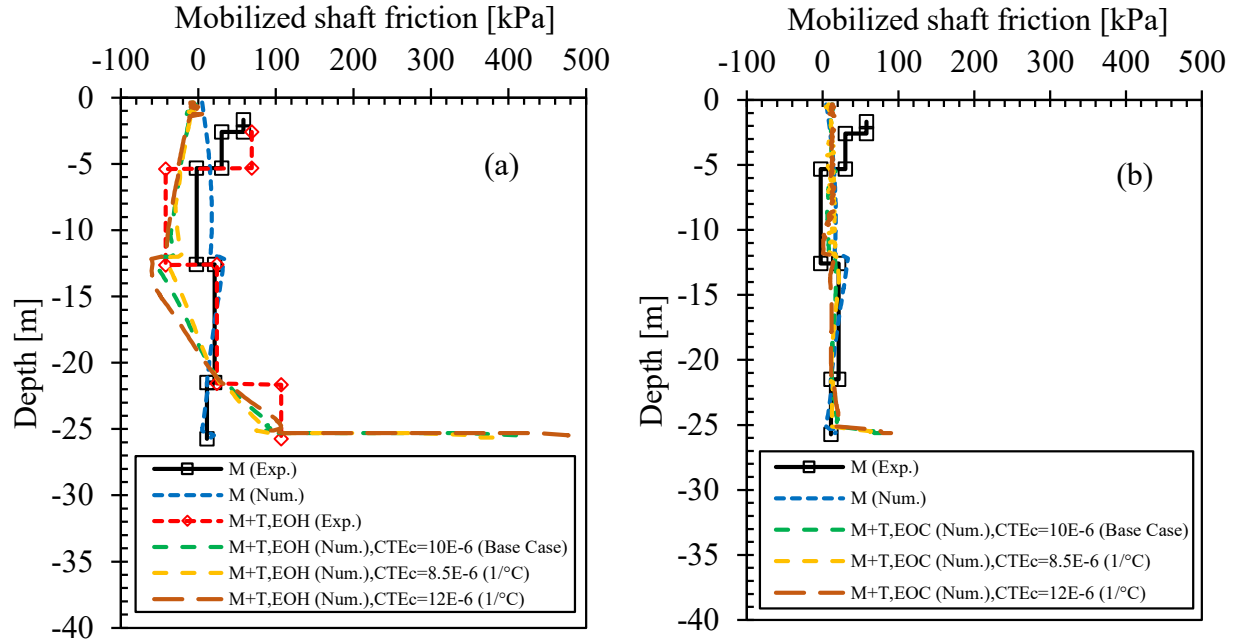

Figure B.3. Mobilized shaft friction along the pile length (a) at the end of heating (EOH) and (b) at the end of cooling (EOC) for the Lausanne energy pile: Test 7 (change in CTEc)

B.2. Lausanne Energy Pile: Test 7 with changes in the coefficient of thermal expansion of soils (CTEs)

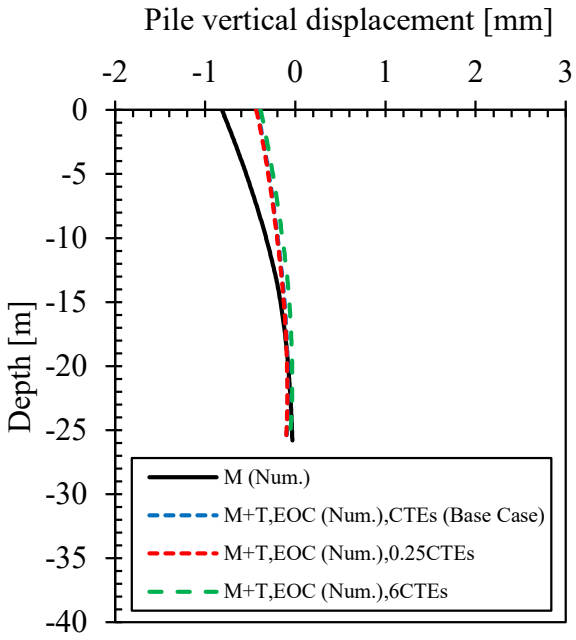

Figure B.4. Pile vertical displacement profiles at the end of cooling (EOC) for the Lausanne energy pile: Test 7 (change in CTEs)

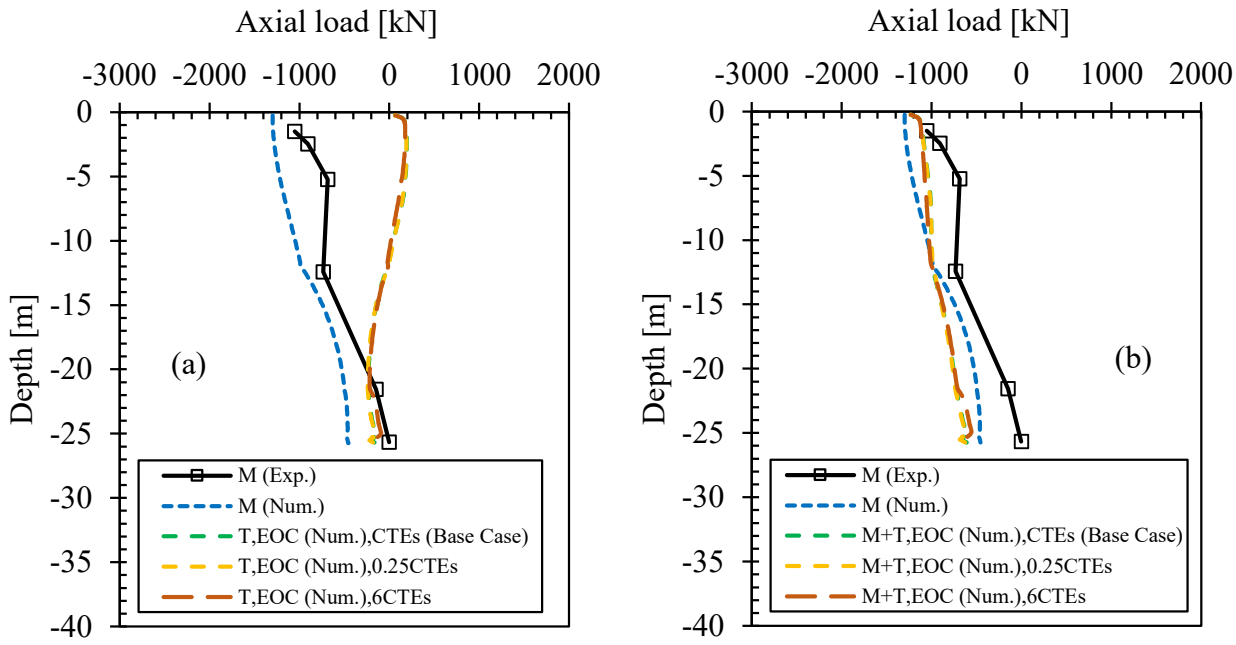

Figure B.5. Axial load profiles (a) thermal (T) and (b) thermo-mechanical (M+T) at the end of cooling (EOC) for the Lausanne energy pile: Test 7 (change in CTEs)

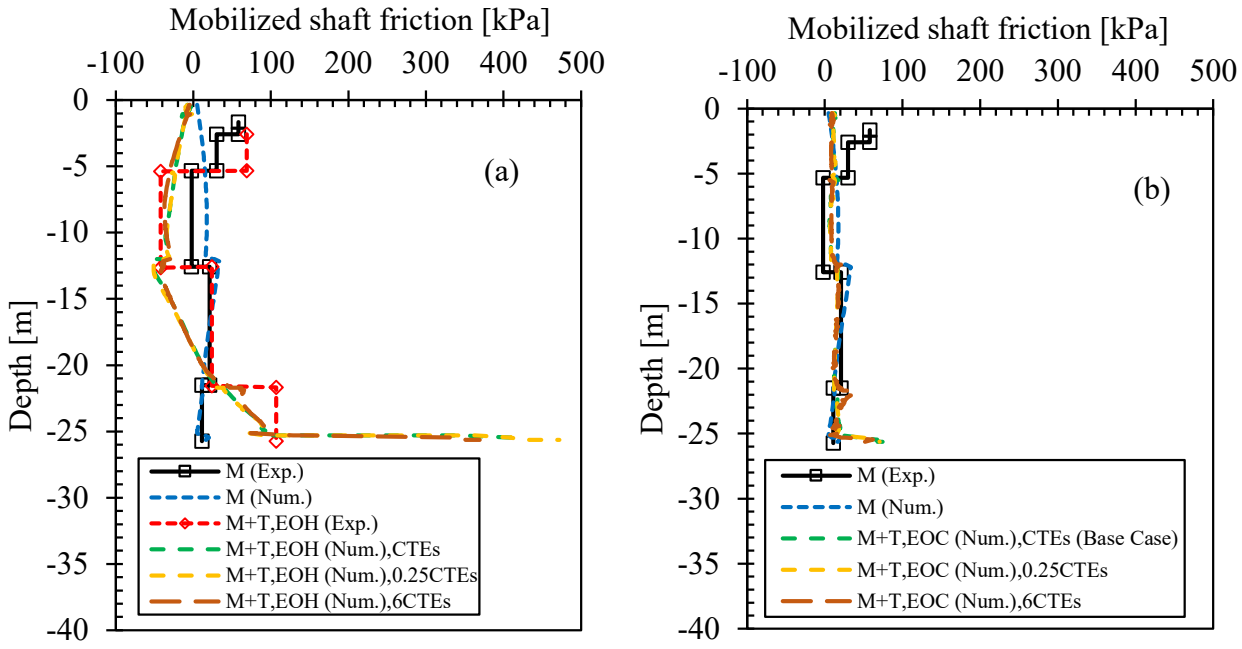

Figure B.6. Mobilized shaft friction along the pile-soil interface (a) at the end of heating (EOH) and (b) at the end of cooling (EOC) for the Lausanne energy pile: Test 7 (change in CTEs)

B.3. Lausanne Energy Pile: Test 7 with changes in soil stiffness (Es)

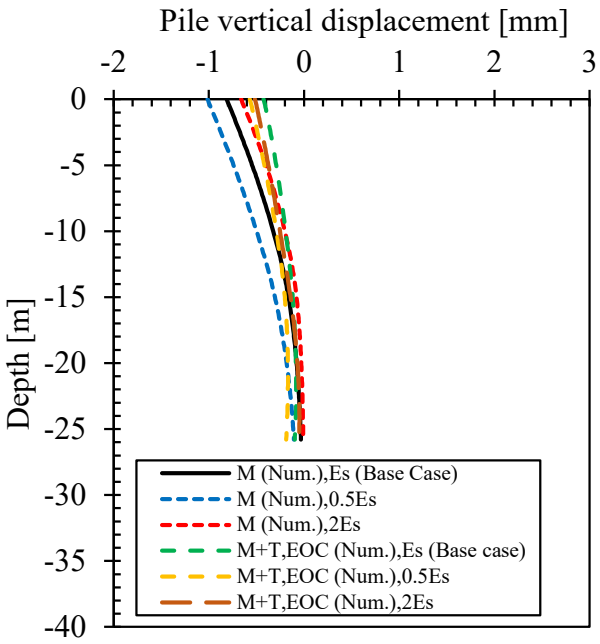

Figure B.7. Pile vertical displacement profiles at the end of cooling (EOC) for the Lausanne energy pile: Test 7 (change in Es)

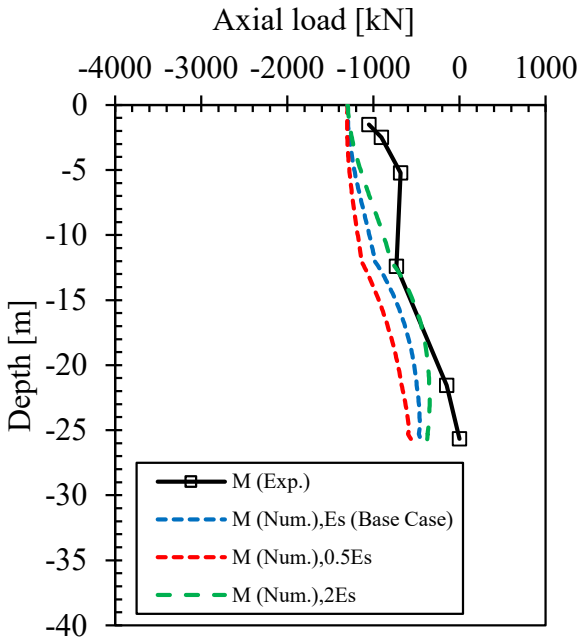

Figure B.8. Axial load profiles due to the mechanical (M) load only for the Lausanne energy pile (change in Es)

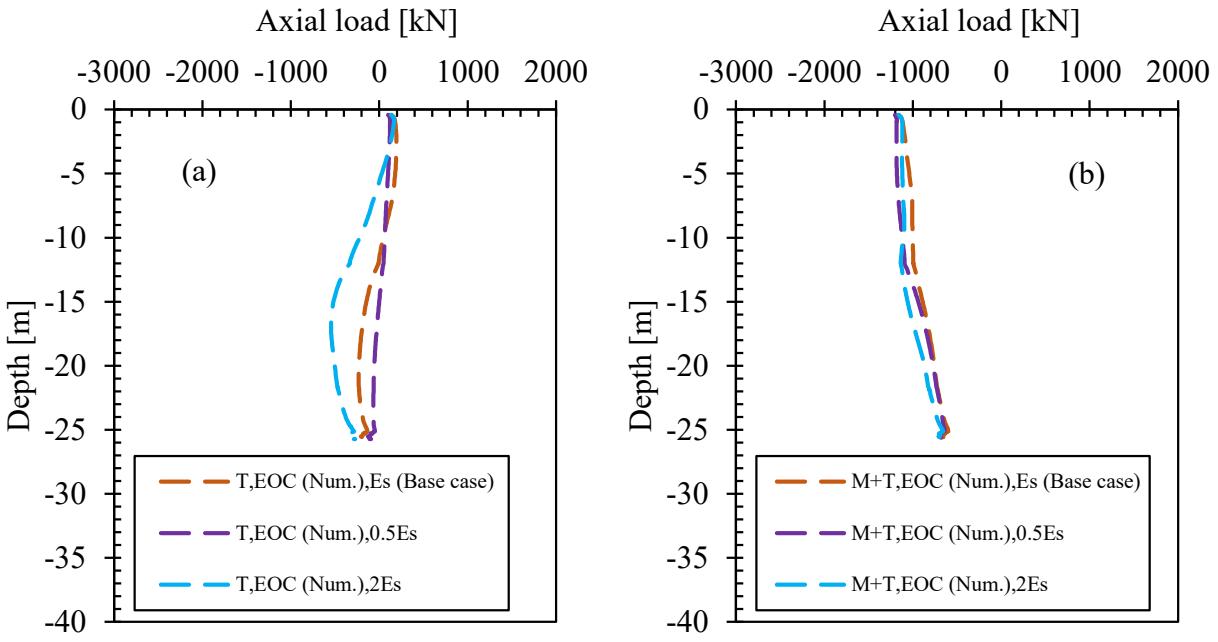

Figure B.9. Axial load profiles (a) thermal (T) and (b) thermo-mechanical (M+T) at the end of cooling (EOC) for the Lausanne energy pile: Test 7 (change in Es)

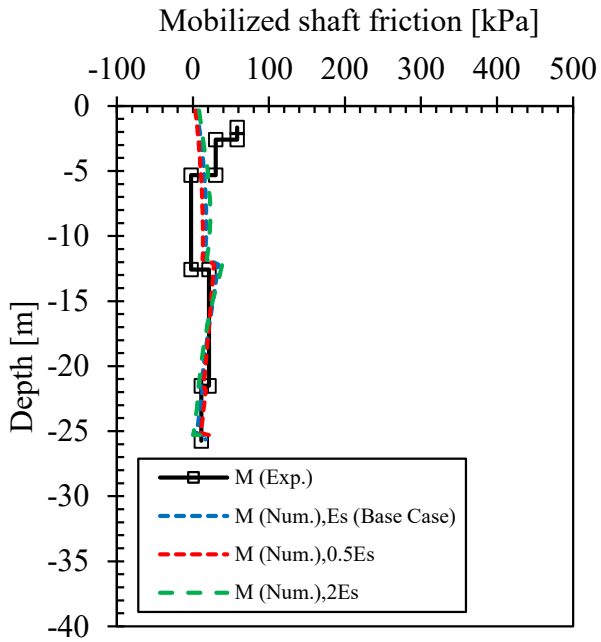

Figure B.10. Mobilized shaft friction along the pile-soil interface due to the mechanical load only (M) for the Lausanne energy pile: Test 7 (change in Es)

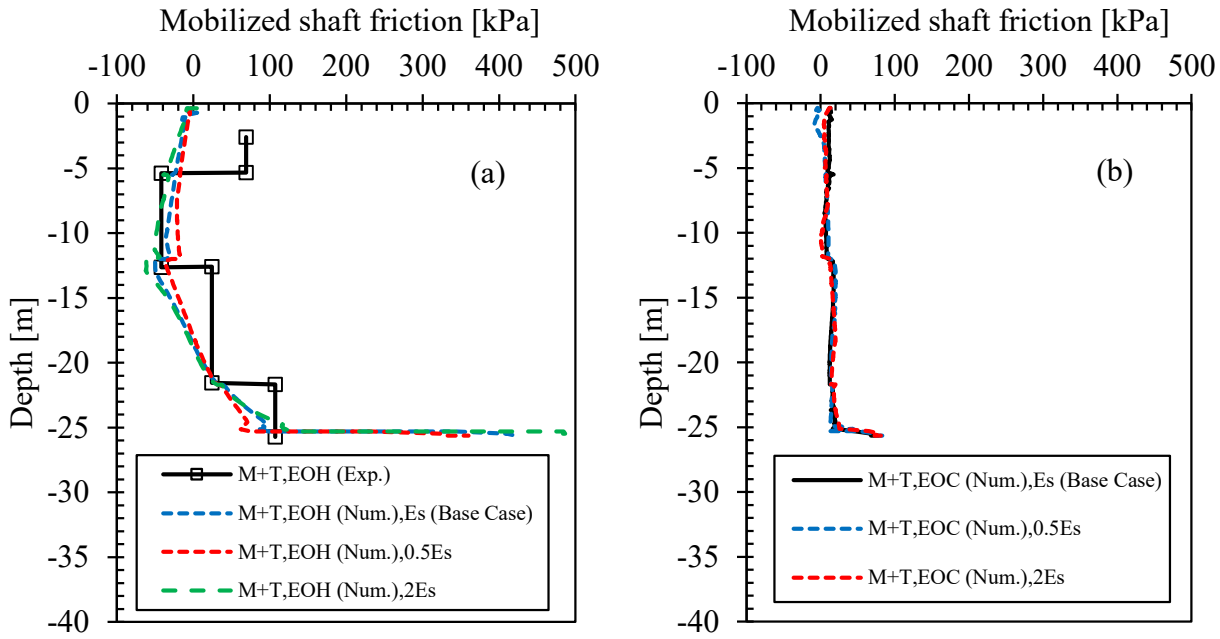

Figure B.11. Mobilized shaft friction along the pile-soil interface (a) at the end of heating (EOH) and (b) at the end of cooling (EOC) for the Lausanne energy pile: Test 7 (change in Es)

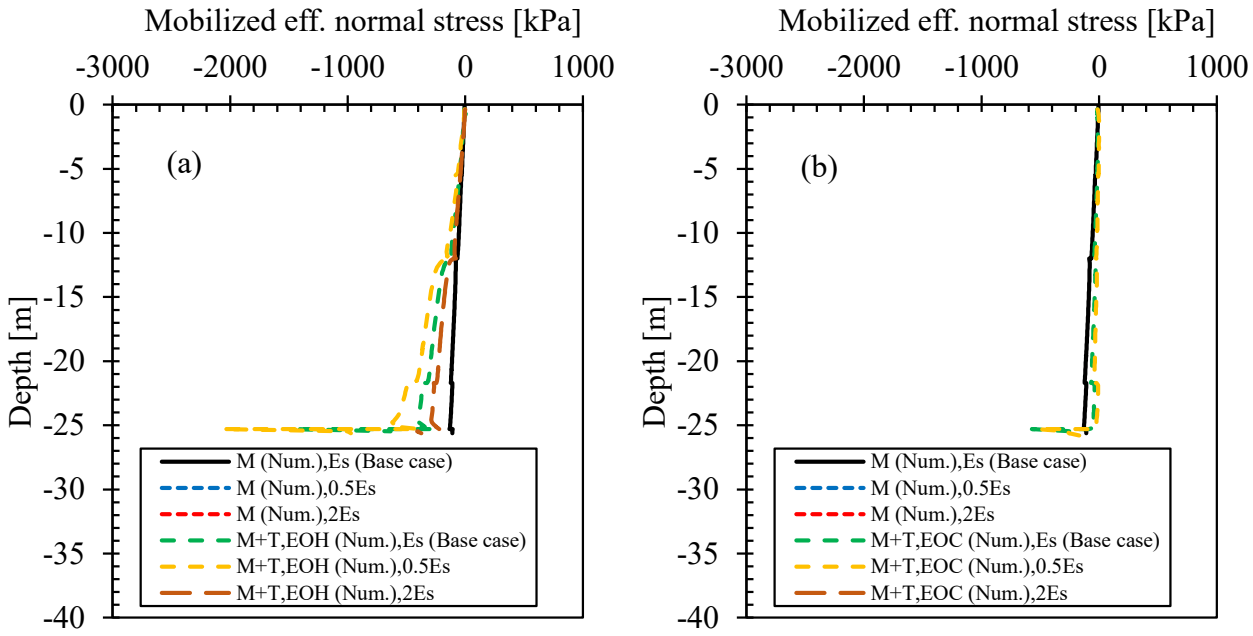

Figure B.12. Mobilized effective radial (normal) stress at the pile-soil interface along the pile length (a) at the end of heating (EOH) and (b) at the end of cooling (EOC) for the Lausanne energy pile: Test 7 (change in Es)

B.4. Lausanne Energy Pile: Test 7 with changes in the thermal conductivity of soil (TCs)

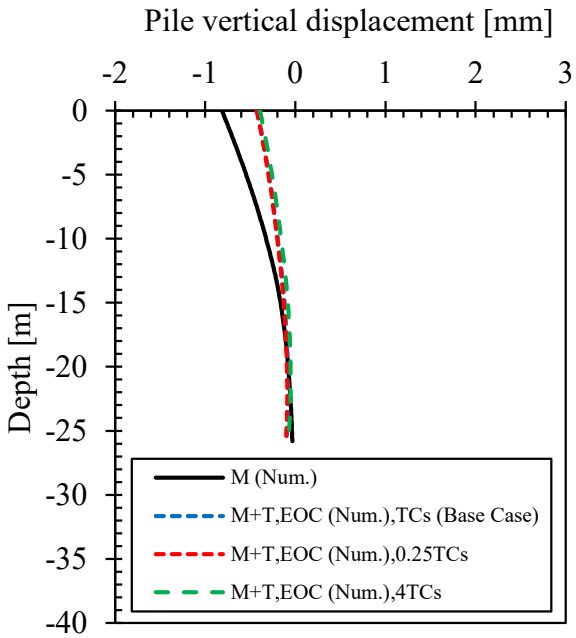

Figure B.13. Pile vertical displacement profiles at the end of cooling (EOC) for the Lausanne energy pile: Test 7 (change in TCs)

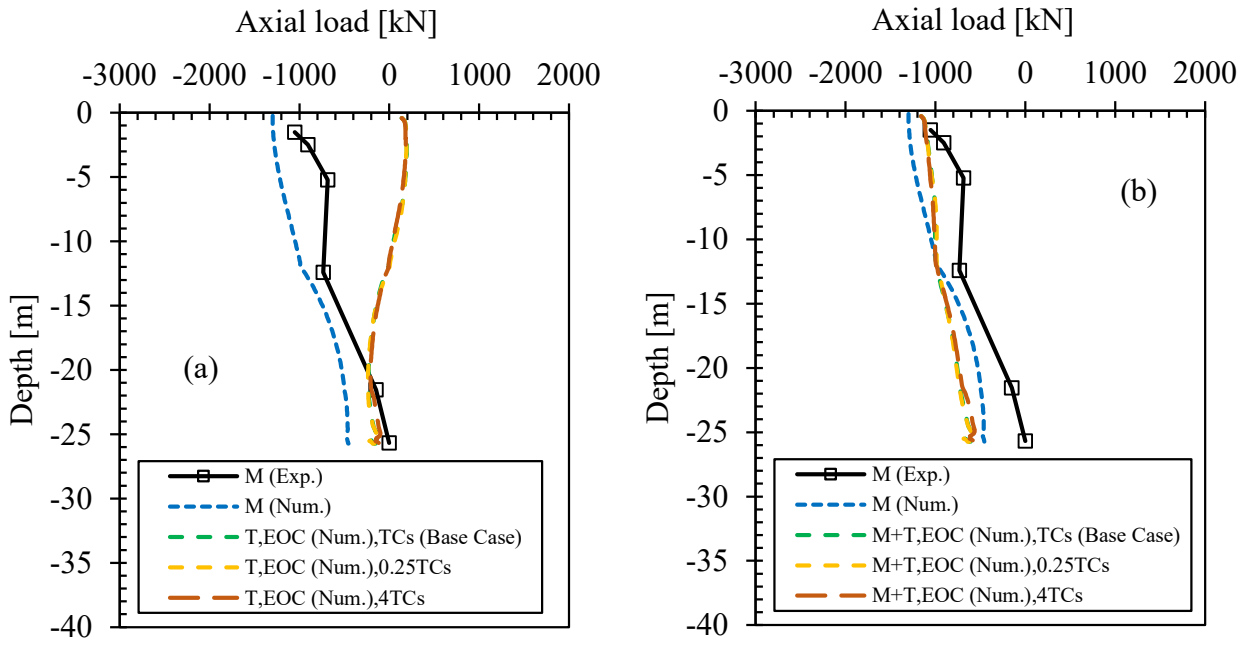

Figure B.14. Axial load profiles (a) thermal (T) and (b) thermo-mechanical (M+T) at the end of cooling (EOC) for the Lausanne energy pile: Test 7 (change in TCs)

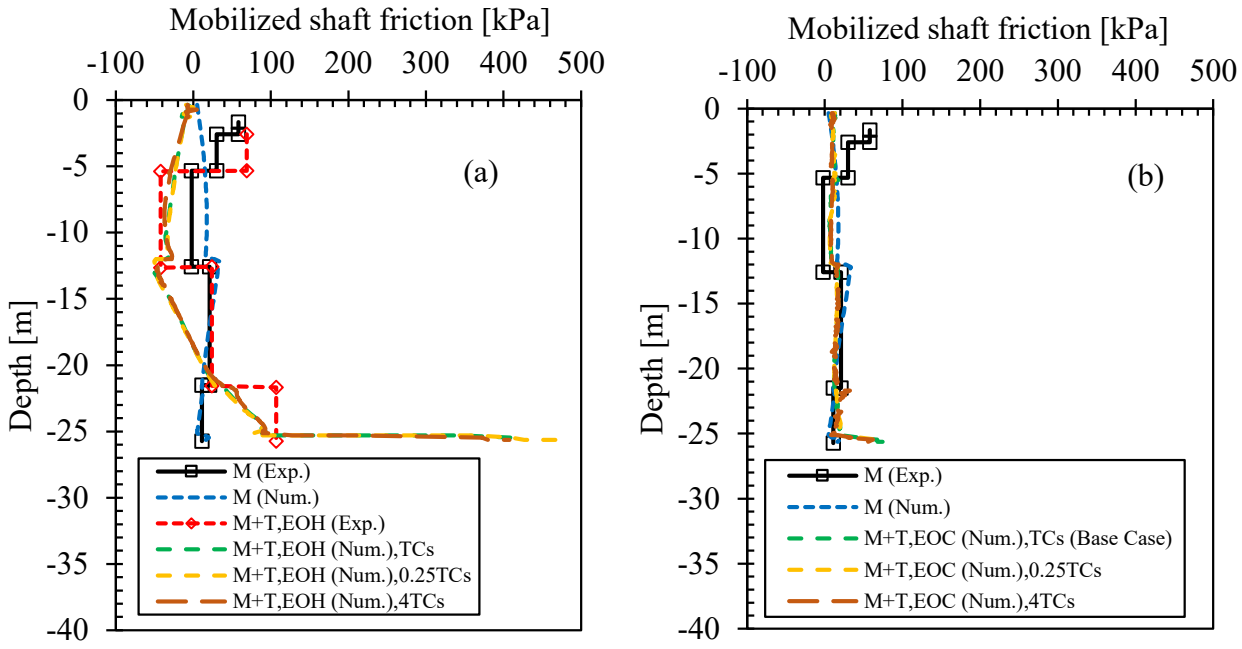

Figure B.15. Mobilized shaft friction along the pile length (a) at the end of heating (EOH) and (b) at the end of cooling (EOC) for the Lausanne energy pile: Test 7 (change in TCs)

B.5. Lausanne Energy Pile: Test 7 with changes in the specific heat capacity of soils (SHCs)

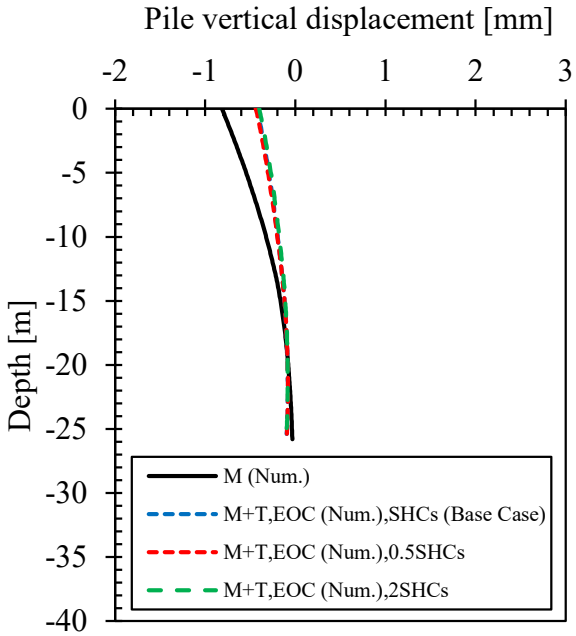

Figure B.16. Pile vertical displacement profiles at the end of cooling (EOC) for the Lausanne energy pile: Test 7 (change in SHCs)

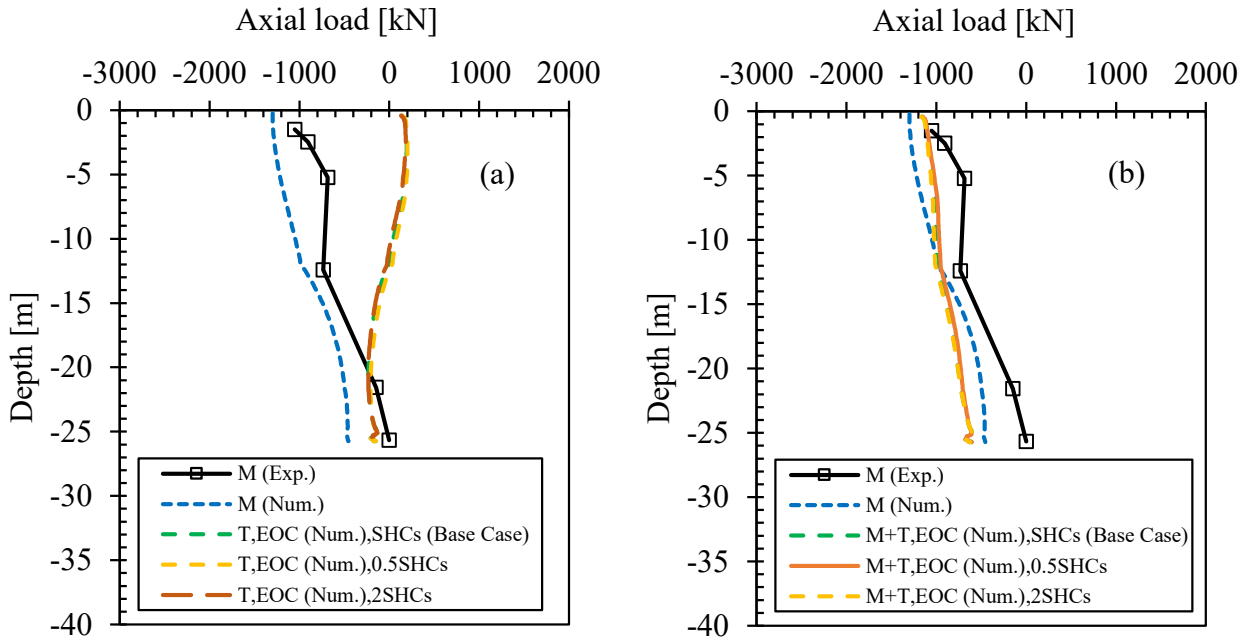

Figure B.17. Axial load profiles (a) thermal (T) and (b) thermo-mechanical (M+T) at the end of cooling (EOC) for the Lausanne energy pile: Test 7 (change in SHCs)

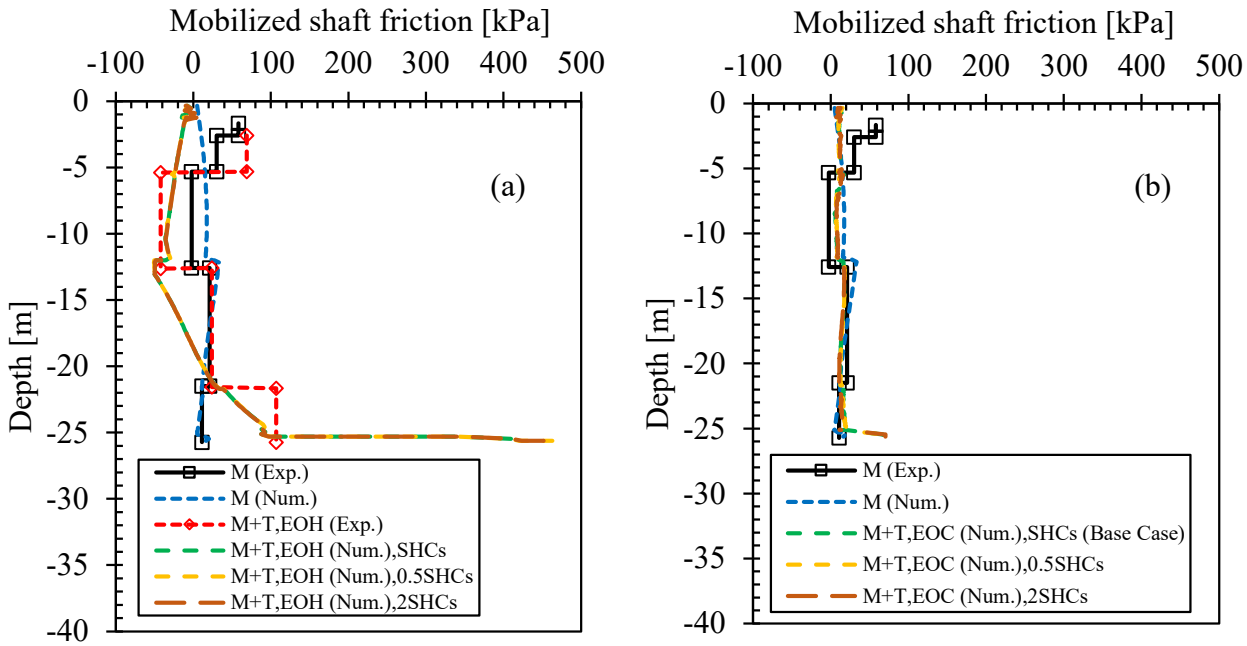

Figure B.18. Mobilized shaft friction along the pile length (a) at the end of heating (EOH) and (b) at the end of cooling (EOC) for the Lausanne energy pile: Test 7 (change in SHCs)

B.6. Lausanne Energy Pile: Test 7 with changes in head restrained conditions of the pile (HRC)

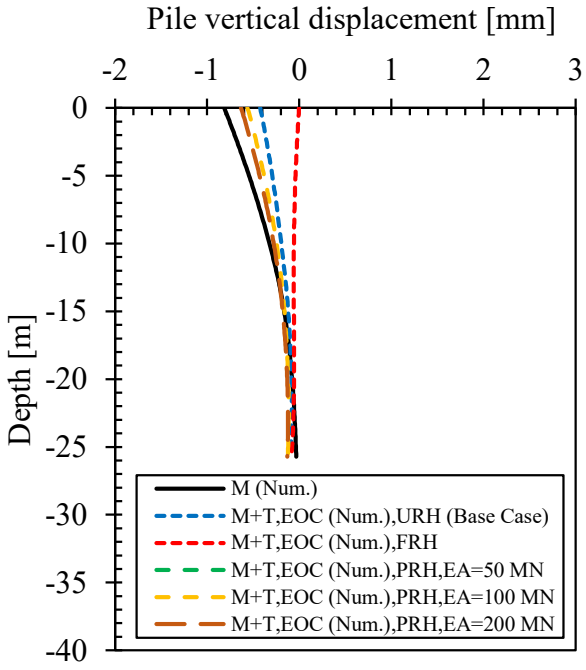

Figure B.19. Pile vertical displacement profiles (a) at the end of heating (EOH) and (b) at the end of cooling (EOC) for the Lausanne energy pile: Test 7 (change in HRC)

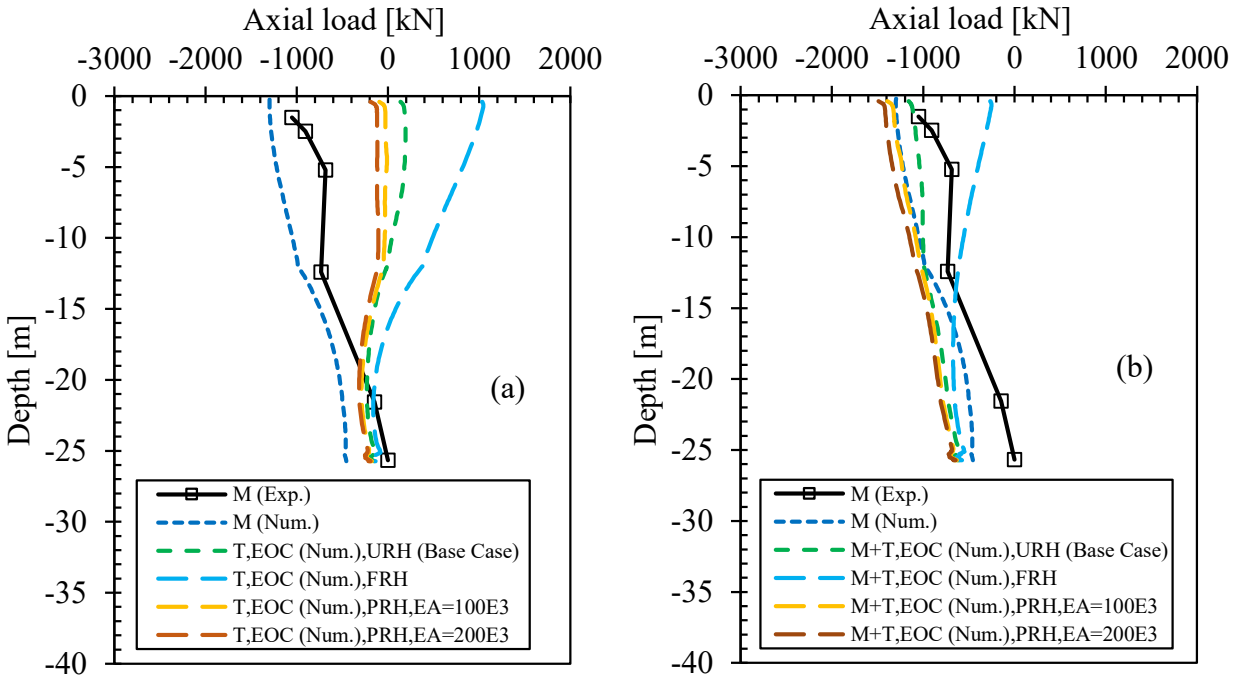

Figure B.20. Axial load profiles (a) thermal (T) and (b) thermo-mechanical (M+T) at the end of cooling (EOC) for the Lausanne energy pile: Test 7 (change in HRC)

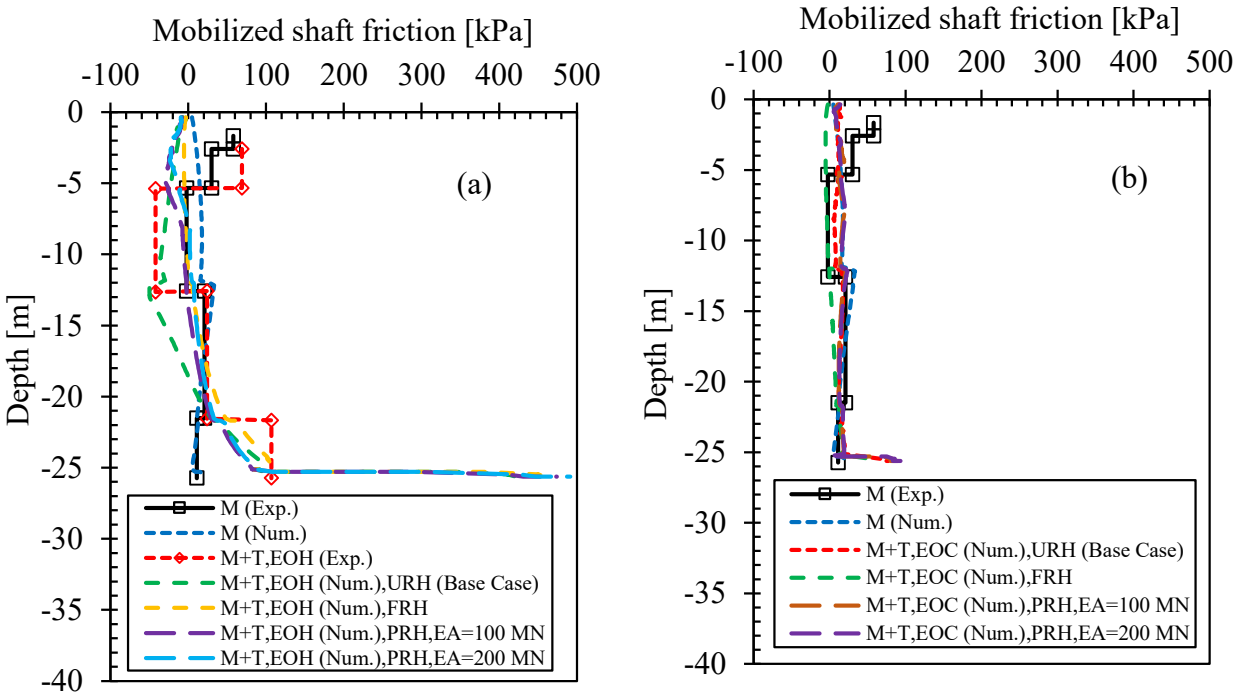

Figure B.21. Mobilized shaft friction along the pile length (a) at the end of heating (EOH) and (b) at the end of cooling (EOC) for the Lausanne energy pile: Test 7 (change in HRC)

Appendix C : Additional Numerical Results for the Friction Energy Pile in Winnipeg

C.1. Winnipeg Friction Energy Pile: Base case

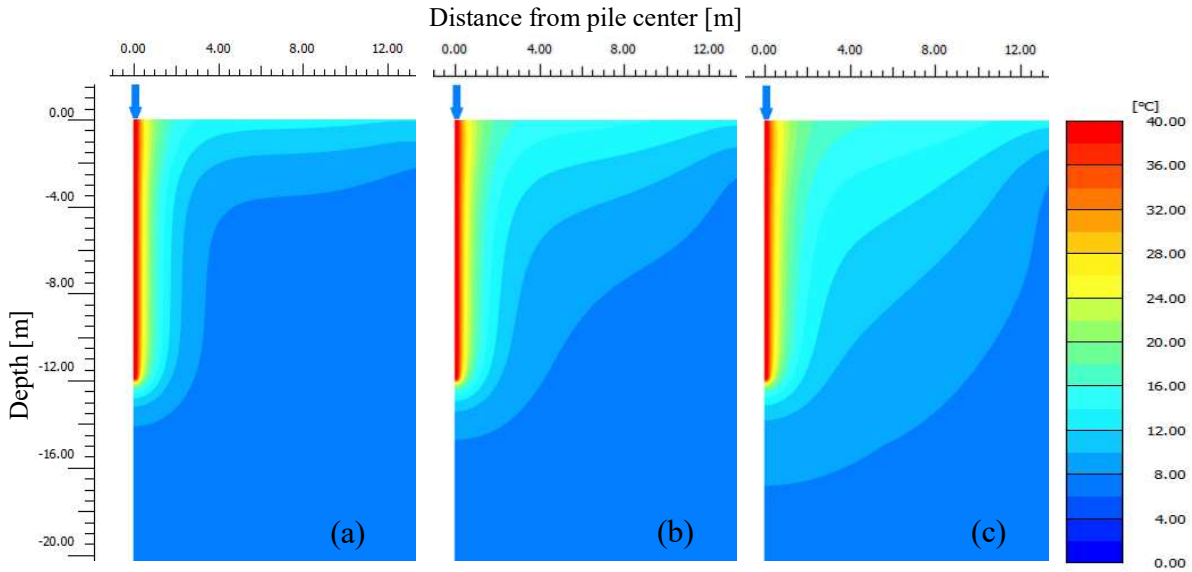

Figure C.1. Temperature distributions in the pile and surrounding ground at the end of heating (EOH): (a) 1st year, (b) 2nd year, and (c) 6th year for the friction energy pile (base case)

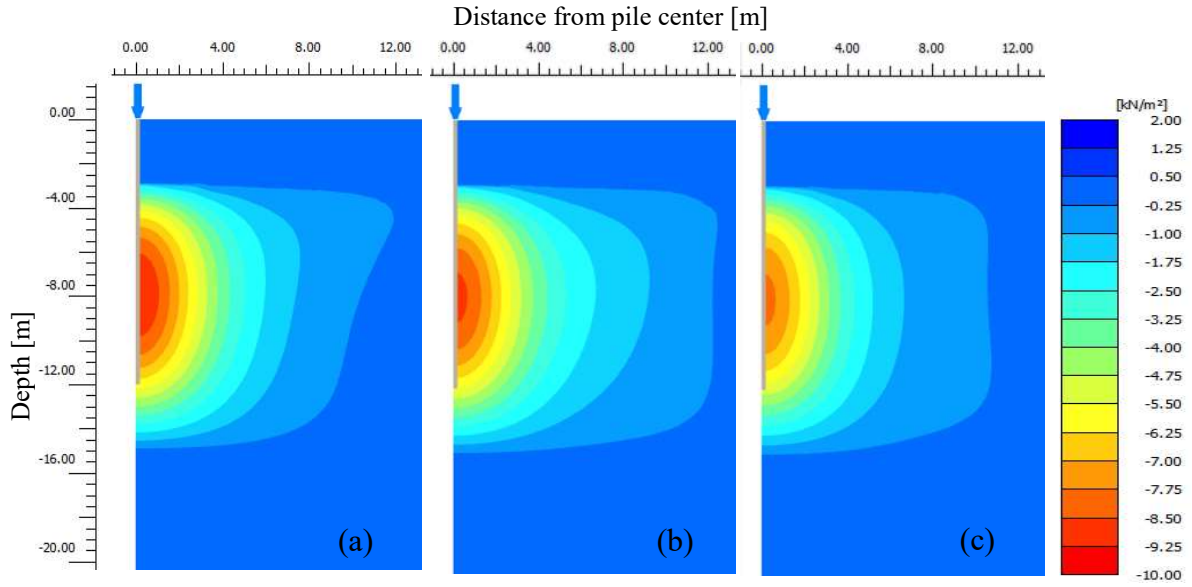

Figure C.2. Thermally induced excess porewater pressures (EPWP) in the ground at the end of heating (EOH): (a) 1st year, (b) 2nd year, and (c) 6th year for the friction energy pile (base case)

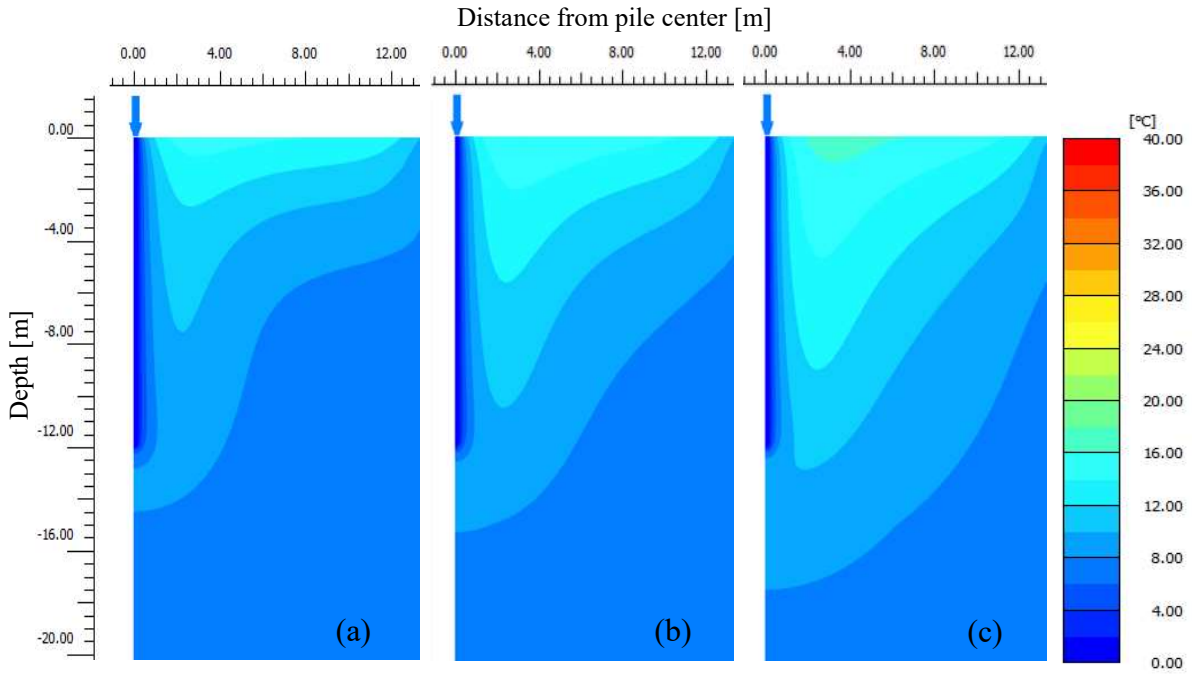

Figure C.3. Temperature distributions in the pile and surrounding ground at the end of cooling (EOC): (a) 1st year, (b) 2nd year, and (c) 6th year for the friction energy pile (base case)

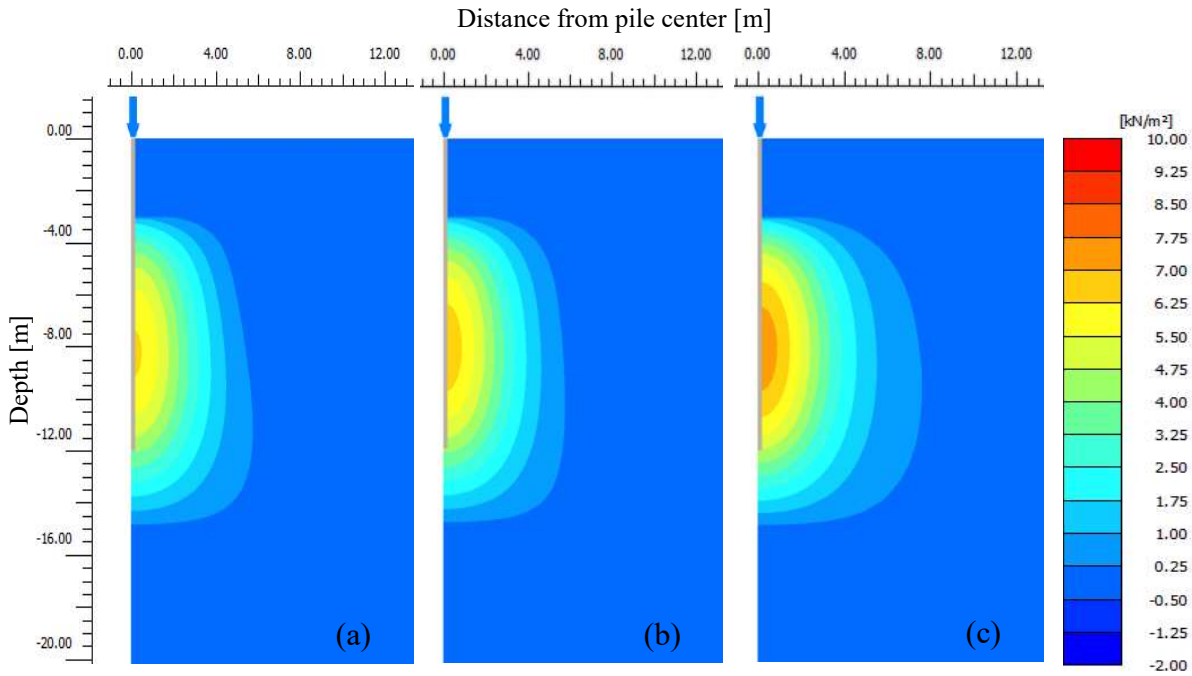

Figure C.4. Thermally induced excess porewater pressures (EPWP) in the ground at the end of cooling (EOC): (a) 1st year, (b) 2nd year, and (c) 6th year for the friction energy pile (base case)

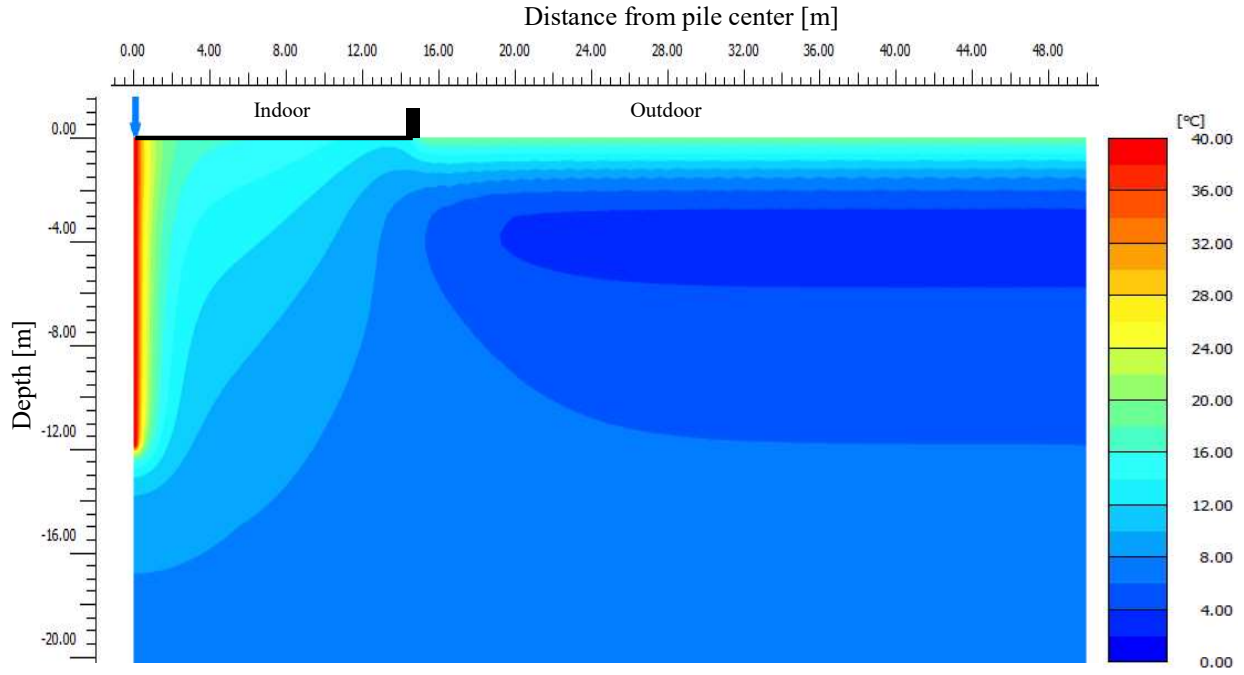

Figure C.5. Temperature distributions in the pile and surrounding ground at the end of heating (EOH): 6th year for the friction energy pile (base case)

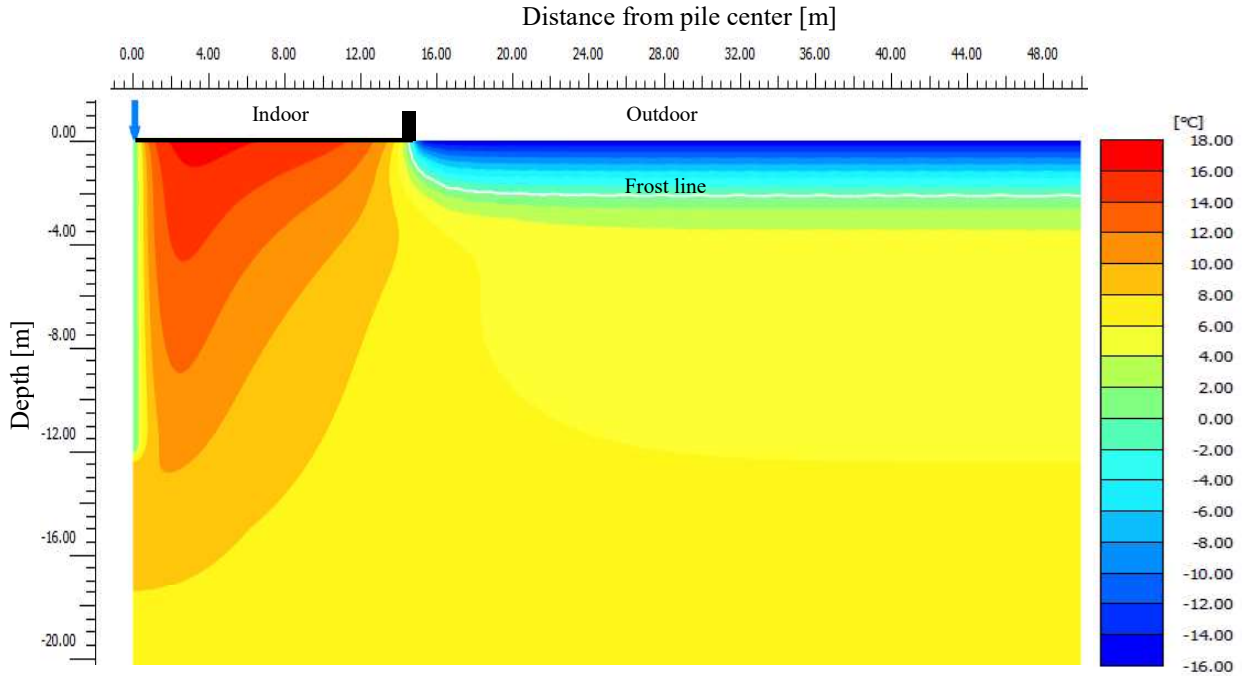

Figure C.6. Temperature distributions in the pile and surrounding ground at the end of cooling (EOC): 6th year for the friction energy pile (base case)

C.2. Winnipeg Friction Energy Pile: Change in thermal load ranges (T)

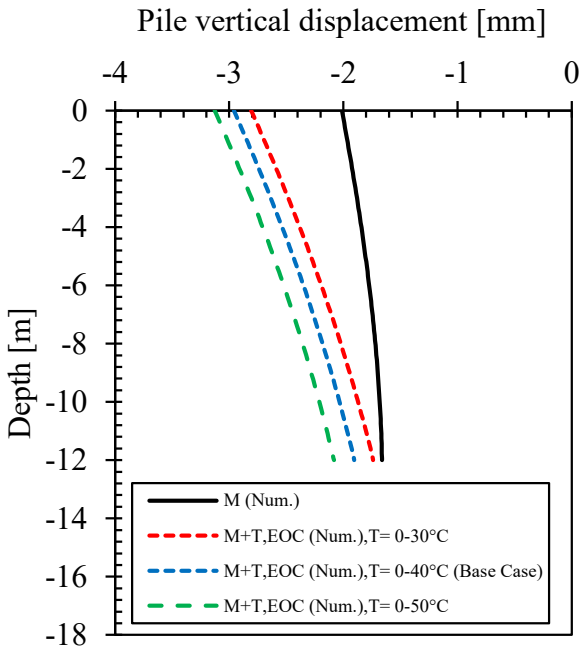

Figure C.7. Pile vertical displacement profiles along its length at the end of cooling (EOC) in the 6th year for the friction energy pile (change in thermal load ranges)

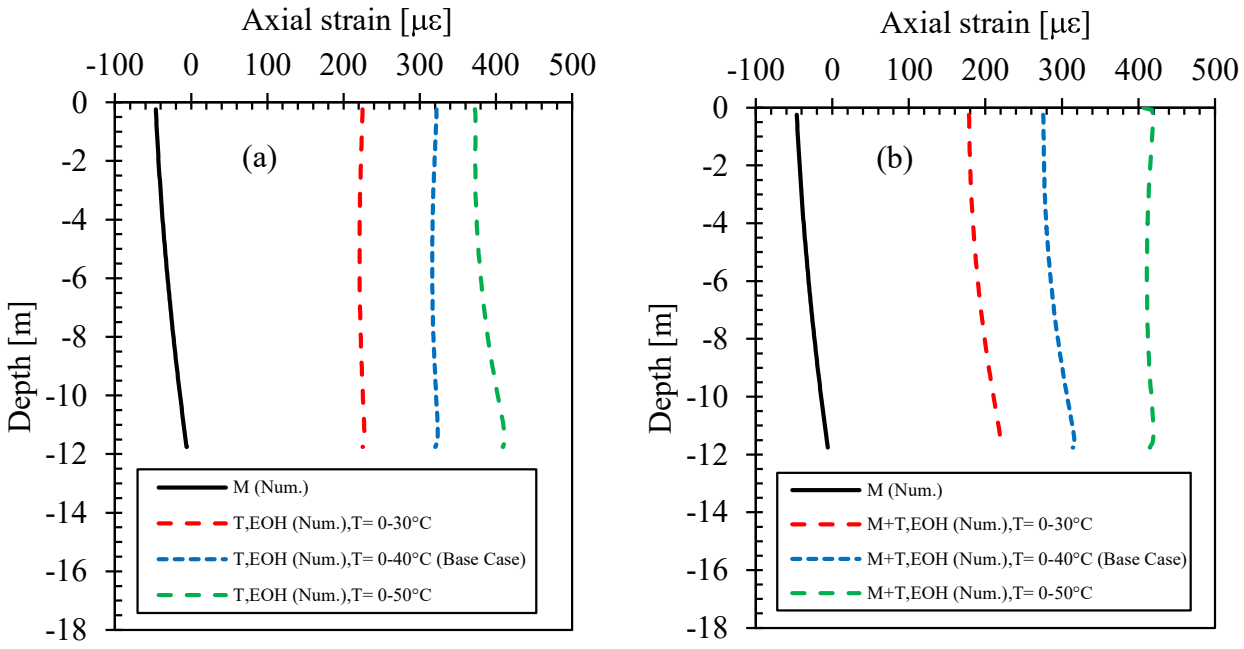

Figure C.8. Axial strain profiles (a) thermal (T) and (b) thermo-mechanical (M+T) at the end of heating (EOH) in the 6th year for the friction energy pile (change in thermal load ranges)

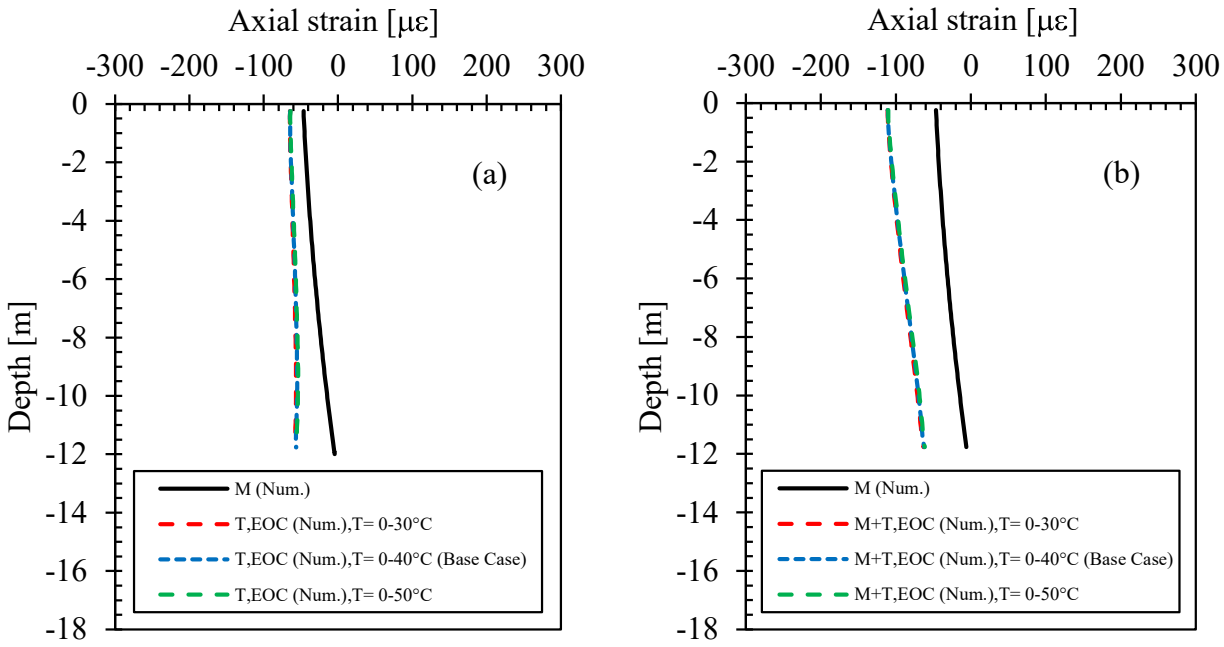

Figure C.9. Axial strain profiles (a) thermal (T) and (b) thermo-mechanical (M+T) at the end of cooling (EOC) in the 6th year for the friction energy pile (change in thermal load ranges)

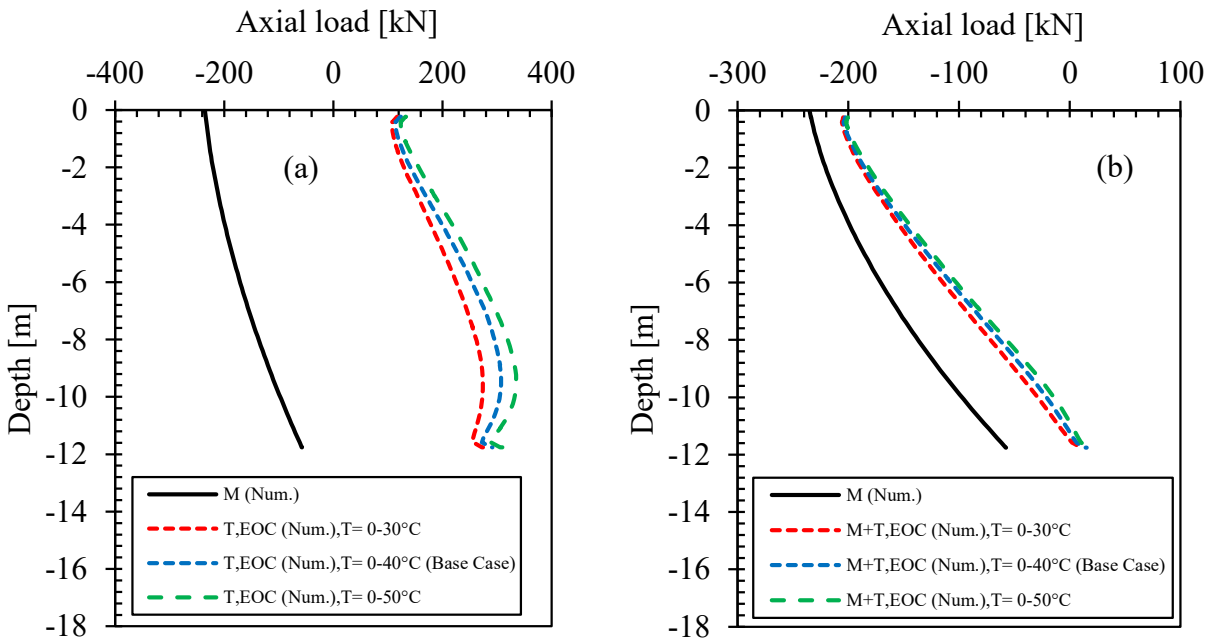

Figure C.10. Axial load profiles (a) thermal (T) and (b) thermo-mechanical (M+T) at the end of cooling (EOC) in the 6th year for the friction energy pile (change in thermal load ranges)

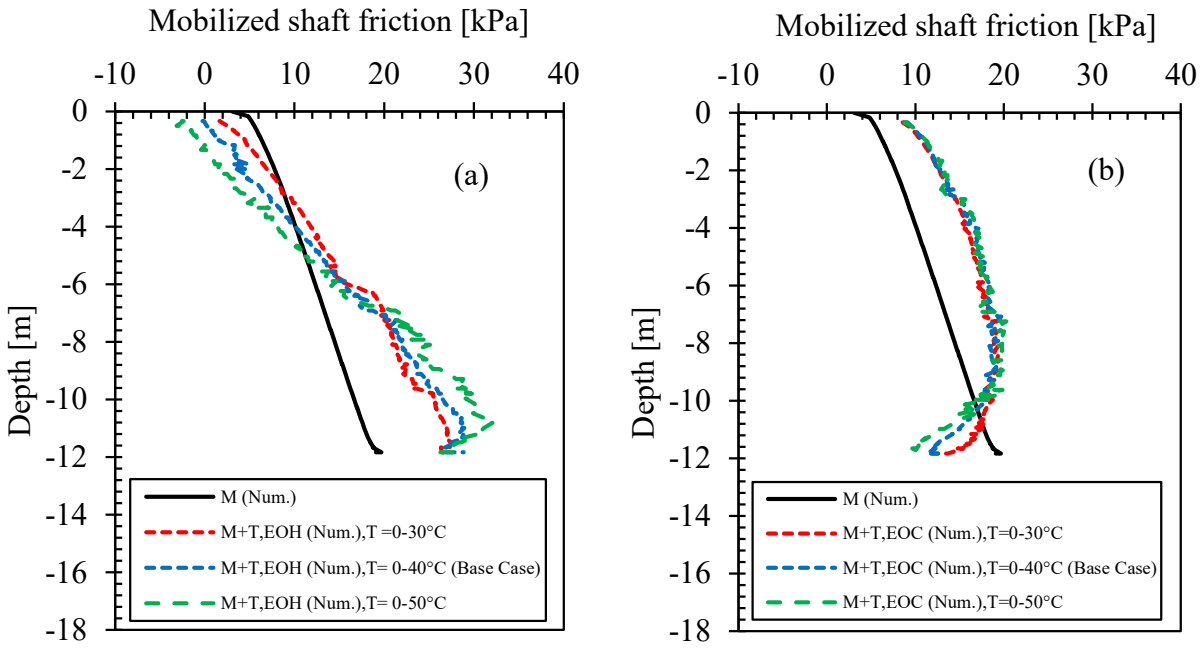

Figure C.11. Mobilized shaft friction along the pile-soil interface (a) at the end of heating (EOH) and (b) at the end of cooling (EOC) in the 6th year for the friction energy pile (change in thermal load ranges)

Appendix D : Additional Numerical Results for the End-Bearing Energy Pile in Winnipeg

D.1. Winnipeg End-Bearing Pile: Base case

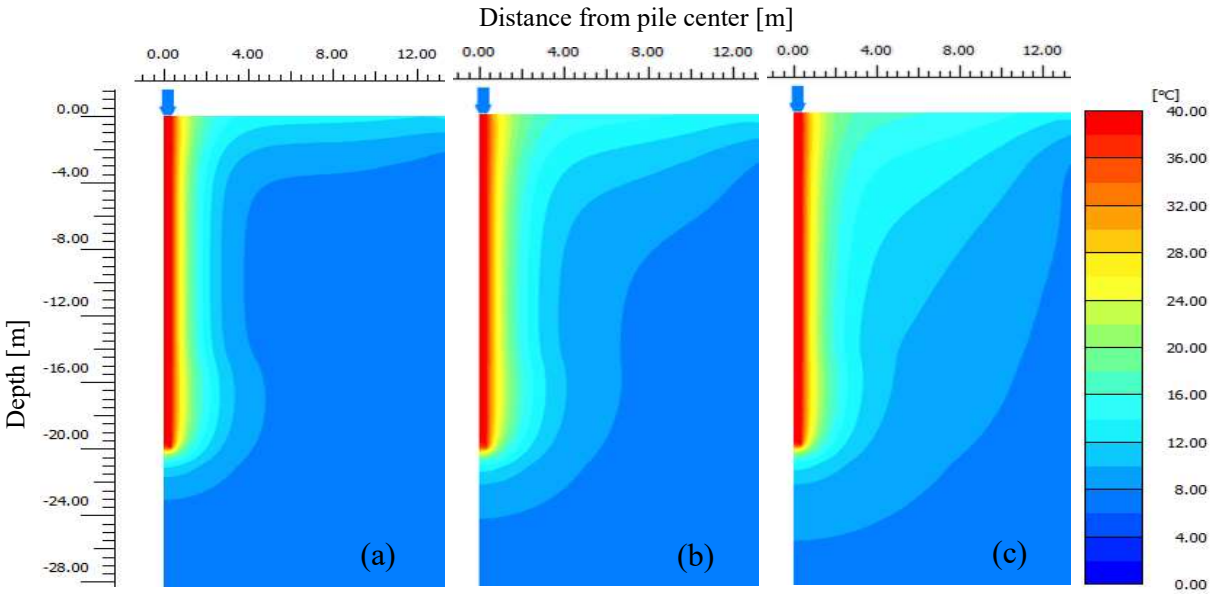

Figure D.1. Temperature distributions in the pile and surrounding ground at the end of heating (EOH): (a) 1st year, (b) 2nd year, and (c) 6th year for the end-bearing energy pile (base case)

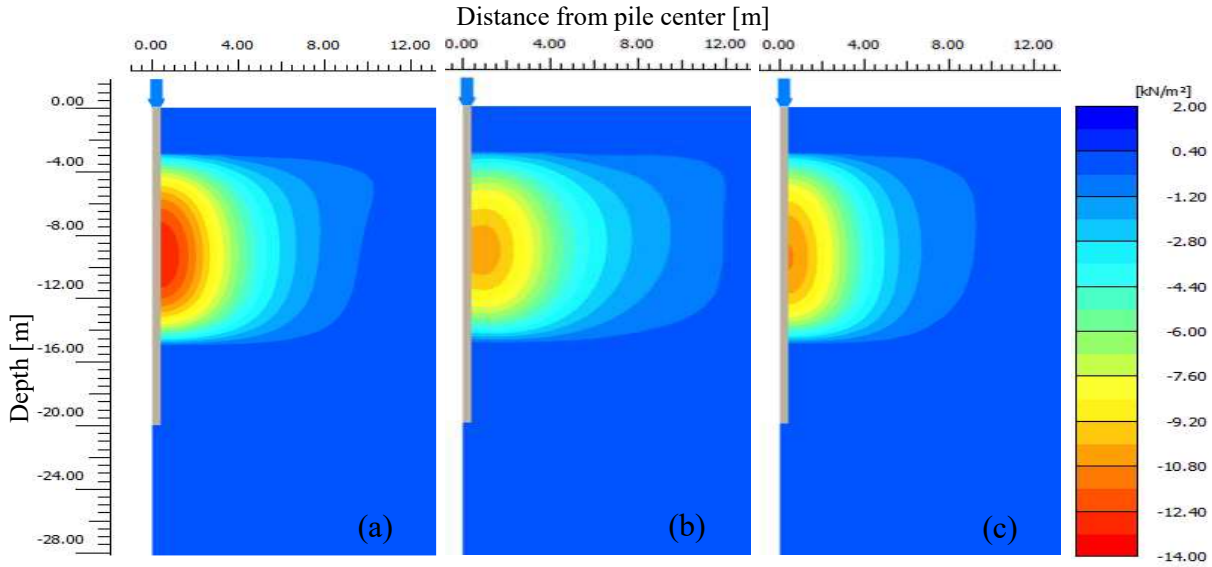

Figure D.2. Thermally induced excess porewater pressures (PWP) in the ground at the end of heating (EOH): (a) 1st year, (b) 2nd year, and (c) 6th year for the end-bearing energy pile (base case)

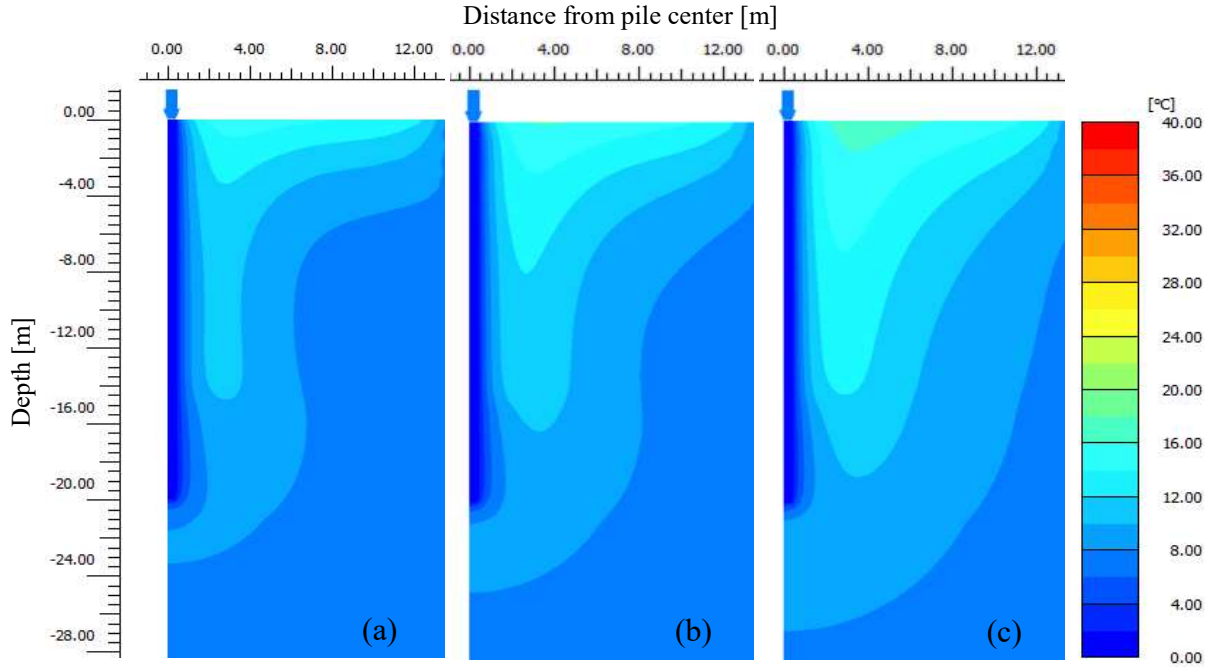

Figure D.3. Temperature distributions in the pile and surrounding ground at the end of cooling (EOC): (a) 1st year, (b) 2nd year, and (c) 6th year for the end-bearing energy pile (base case)

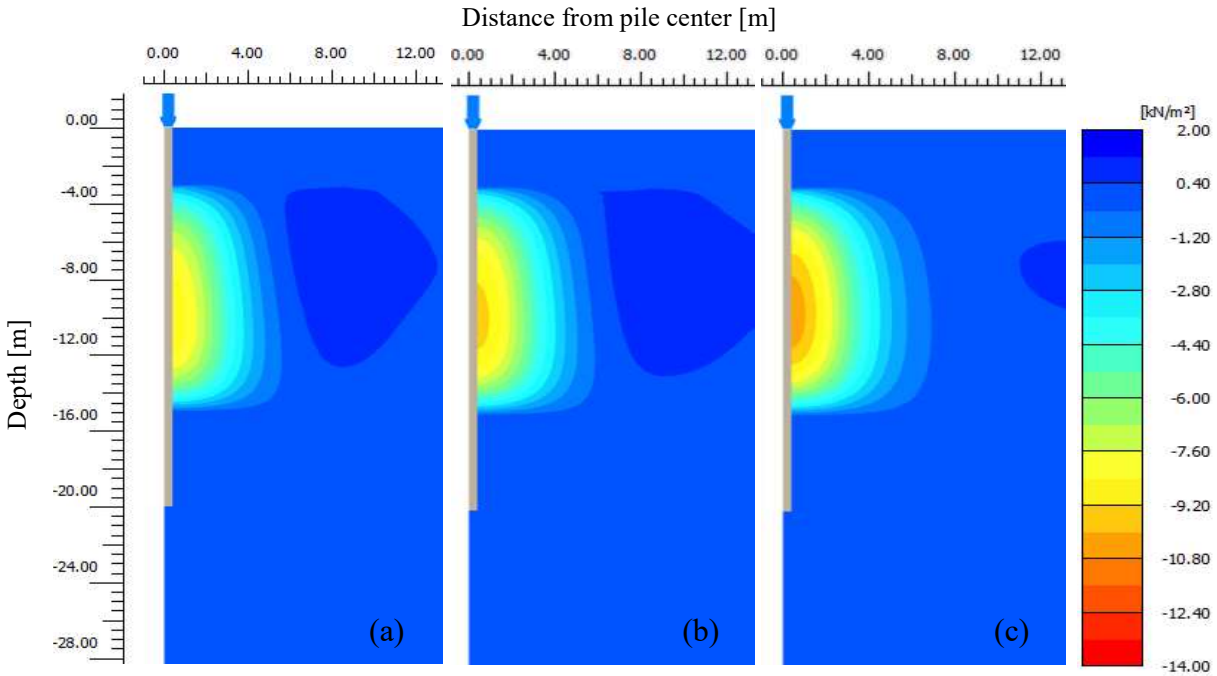

Figure D.4. Thermally induced excess porewater pressures (PWP) in the ground at the end of cooling (EOC): (a) 1st year, (b) 2nd year, and (c) 6th year for the end-bearing energy pile (base case)

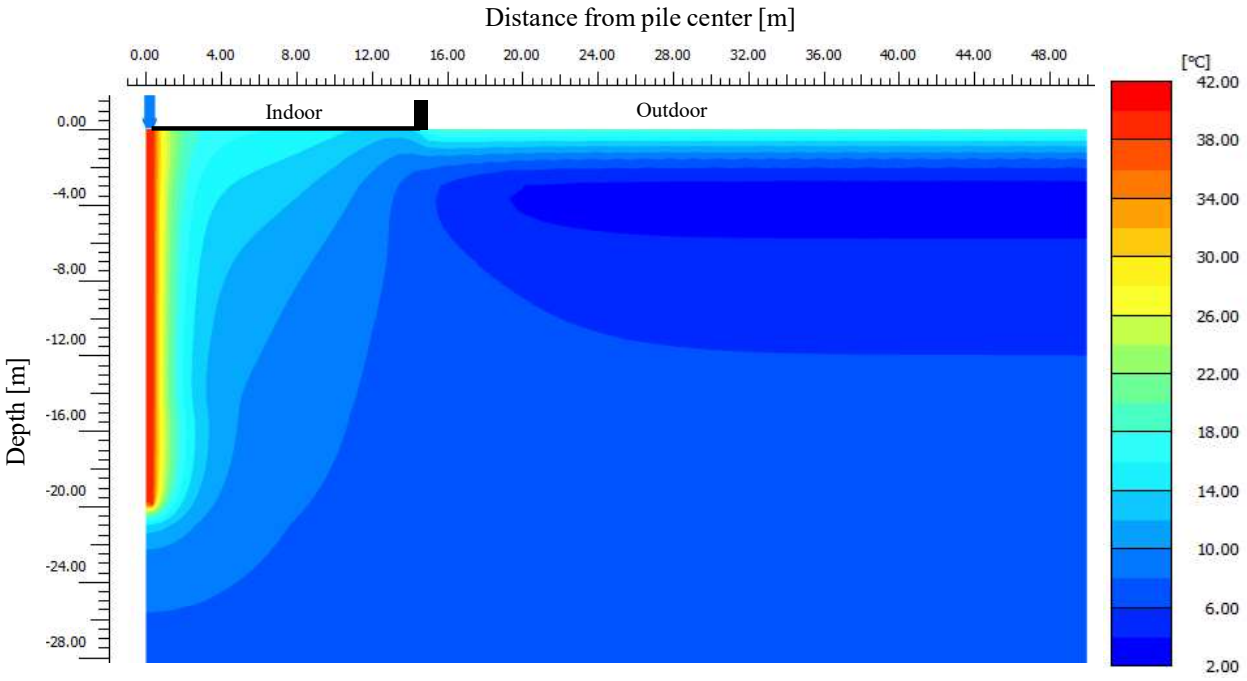

Figure D.5. Temperature distributions in the pile and surrounding ground at the end of heating (EOH): 6th year for the end-bearing energy pile (base case)

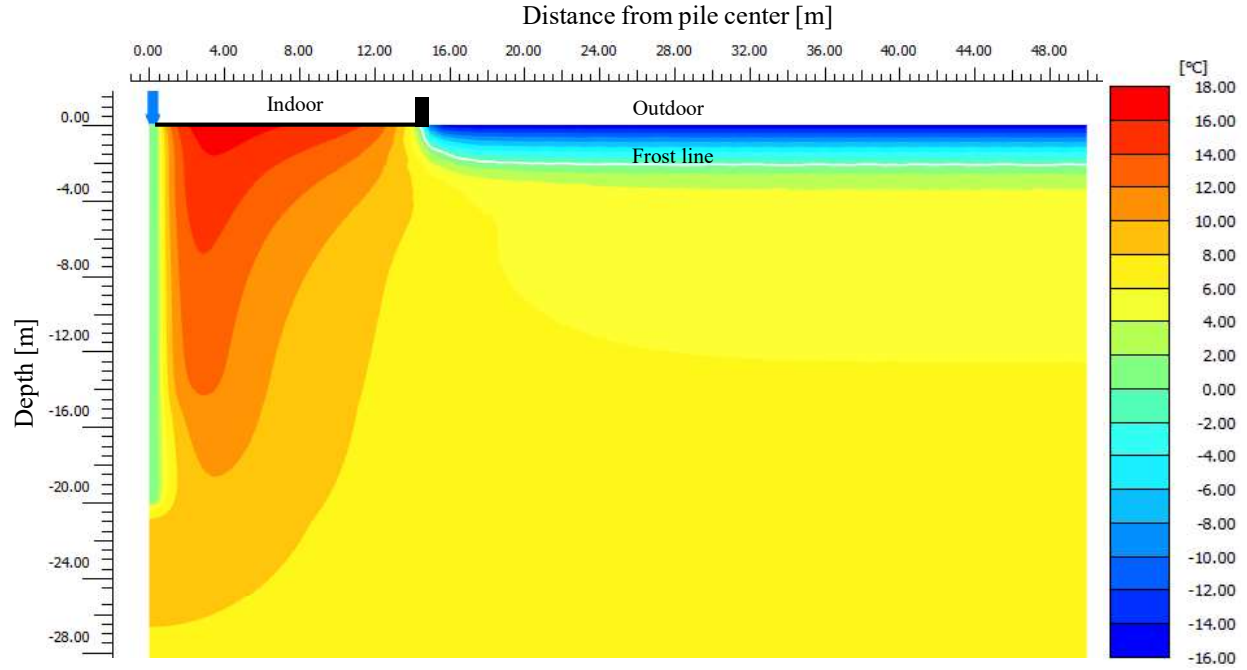

Figure D.6. Temperature distributions in the pile and surrounding ground at the end of cooling (EOC): 6th year (a) for the end-bearing energy pile (base case)

D.2. Winnipeg End-Bearing Energy Pile: Change in thermal load ranges (T)

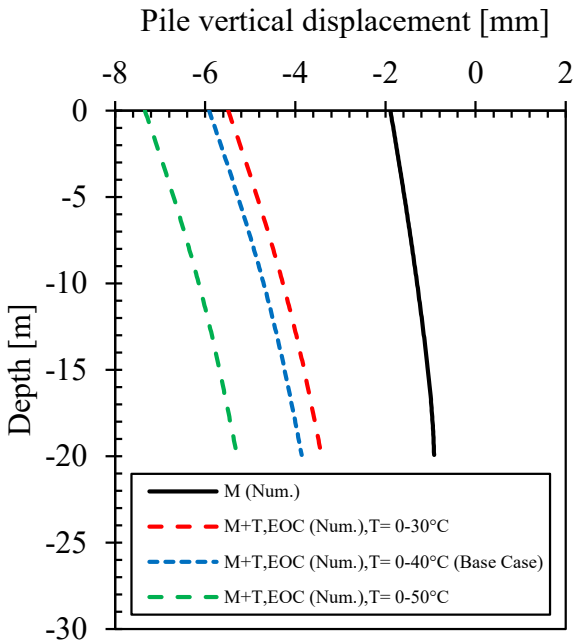

Figure D.7. Pile vertical displacement profiles along its length at the end of cooling (EOC) in the 6th year for the end-bearing energy pile (change in thermal load ranges)

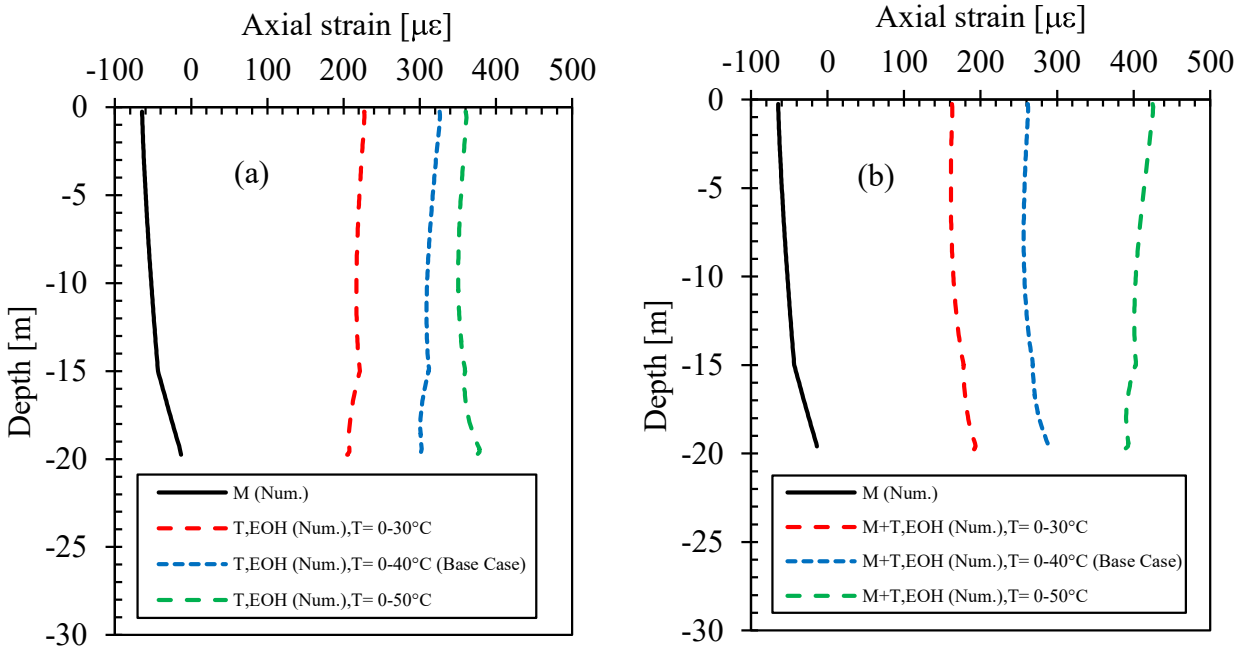

Figure D.8. Axial strain profiles (a) thermal (T) and (b) thermo-mechanical (M+T) at the end of heating (EOH) in the 6th year for the end-bearing energy pile (change in thermal load ranges)

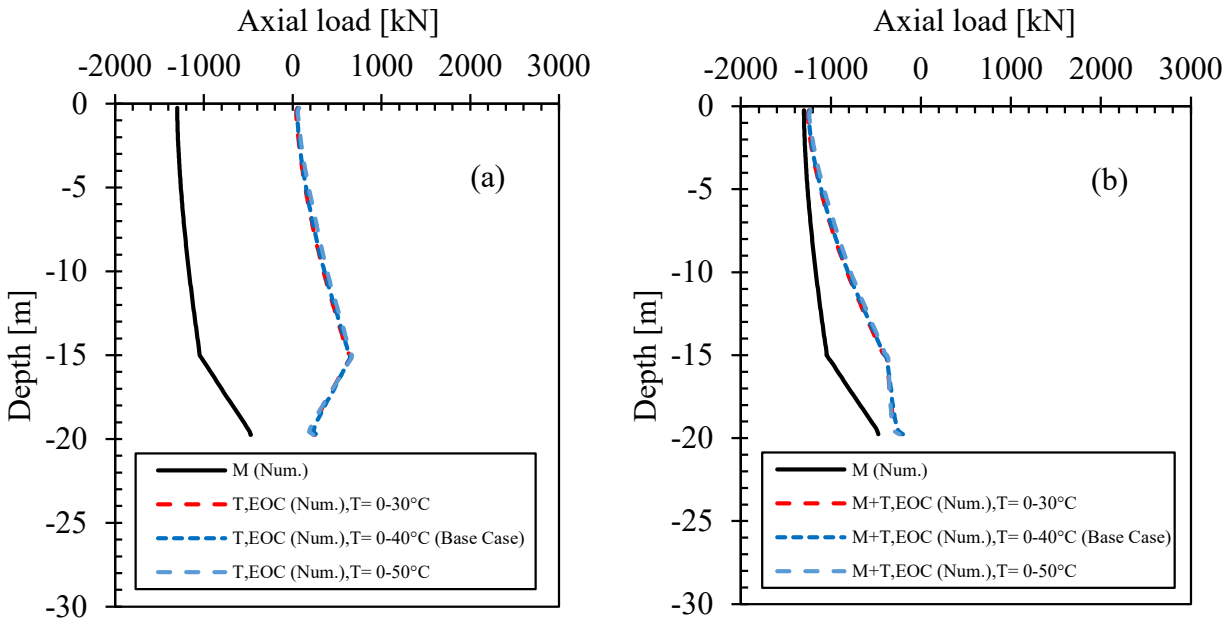

Figure D.9. Axial load profiles (a) thermal (T) and (b) thermo-mechanical (M+T) at the end of cooling (EOC) in the 6th year for the end-bearing energy pile (change in thermal load ranges)

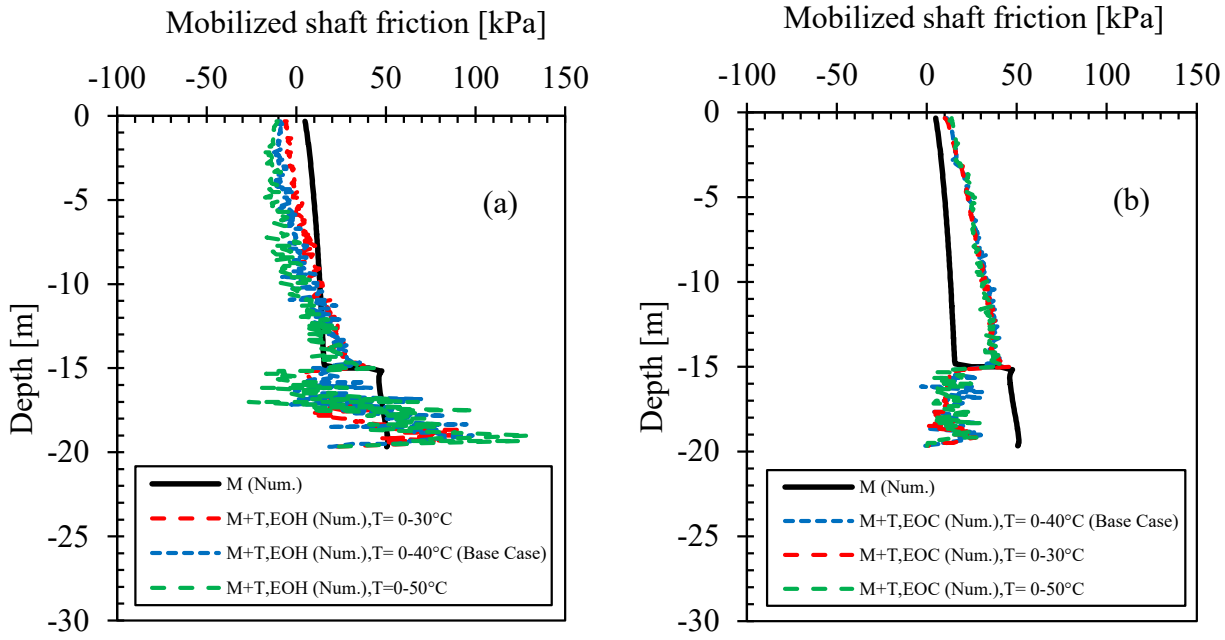

Figure D.10. Mobilized shaft friction along the pile-soil interface (a) at the end of heating (EOH) and (b) at the end of cooling (EOC) in the 6th year for the end-bearing energy pile (change in thermal load ranges)

Appendix E : Properties of Soils related to the Soils found in the London Energy Pile Site (Case Study 1)

Table E.1. General properties of soils related to the soils found in the London energy pile site

Material	Unit weight γ / γ_{sat} [kN/m^3]	Density ρ_s x10^3[kg/m^3]	Porosity n [%]	Void ratio e [-]	Source
Fill	18/20.5	-	-	-	Rigby-Jones & Milne (2010)
Terrace gravels	21/23	-	-	-	Rigby-Jones & Milne (2010)
Granular fill / sand and gravel (made ground & river terrace deposits)	19	-	-	-	Amatya et al. (2012)
Made ground (sand & gravel)	19	-	-	-	Yavari et al. (2014)
Made ground	18	-	-	-	Gawecka et al. (2017)
Terrace gravel	20	-	-	-	Gawecka et al. (2017)
Granular and coarse material	17/20	-	-	-	De Santos et al. (2012)
London clay	18/20	-	-	-	De Santos et al. (2012)
London clay	19.8/19.8	-	-	-	Rigby-Jones & Milne (2010)
London clay (stiff, fissured silty clay)	20	-	-	-	Amatya et al. (2012)
London clay	20	-	-	-	Yavari et al. (2014)
London clay	20	-	-	-	Gawecka et al. (2017)

Table E.2. Strength and stiffness of soils related to the soils found in the London energy pile site

Material	Elastic modulus		Poisson's ratio		Undrained shear strength	Cohesion	Friction angle	Dilatancy angle	Source
	E' [MPa]	E_u [MPa]	ν' [-]	ν_u [-]	s_u (c_u) [kPa]	c' [kPa]	ϕ' (φ') [°]	ψ [°]	
Fill	18	-	0.15	-	-	0.2[#]	33	3	Rigby-Jones & Milne (2010)
Terrace gravels	140	-	0.15	-	-	0.2[#]	39	9	Rigby-Jones & Milne (2010)
Granular fill / sand and gravel	36	-	0.20	-	-	-	-	-	Ouyang et al. (2011)
Granular fill / sand and gravel (made ground & river terrace deposits)	-	-	-	-	-	0	35	-	Amatya et al. (2012)
Made ground (sand & gravel)	13	-	0.30	-	-	0	35	0	Yavari et al. (2014)
Made ground	10	-	0.20	-	-	0	30	0	Gawecka et al. (2017)
Terrace gravel	-	-	-	-	-	0	35	17.5	Gawecka et al. (2017)
Gravel & coarse material	5.28	-	0.32	-	-	-	35	0	De Santos et al. (2012)
London clay	20 + 3.2z	-	0.20	-	-	15	25	0	De Santos et al. (2012)
London clay (stiff, fissured silty clay)	-	-	-	-	-	7, 15, 31	20	-	Terzaghi et al. (1996), p.154
London clay (stiff, fissured silty clay)	-	-	-	-	-	0 - 20	20	-	Hight et al. (2003)
London clay	86.67 [a]	100	-	0.495	100	-	-	-	Rigby-Jones & Milne (2010)
London clay (stiff, fissured silty clay)	93.60 [a]	600*s_u ≈ 108	-	0.50	180 @ top to 190 @ 30 m	-	-	-	Ouyang et al. (2011)
London clay (stiff, fissured silty clay)	-	-	-	-	65 + 8.2 z*	-	-	-	Amatya et al. (2012)
London clay	70	-	0.30	-	-	20	25	0	Yavari et al. (2014)
London clay	-	-	-	-	-	5	22	0	Gawecka et al. (2016)
London clay	-	-	-	-	-	5	25	12.5	Gawecka et al. (2017)
London clay	110	-	0.20	-	-	-	26	12.5	Bot (2017), p.27
Concrete (pile)	40000	-	-	-	-	-	-	-	Bourne-Webb et al. (2009)
Concrete (pile)	40000	-	-	-	-	-	-	-	Ouyang et al. (2011)
Concrete (pile)	40000	-	-	-	-	-	-	-	Knellwolf et al. (2011)
Concrete (pile)	20000	-	0.15	-	-	-	-	-	Gawecka et al. (2016)
Concrete (pile)	40000	-	0.20	-	-	-	-	-	Bot (2017), p.27
Concrete (pile)	40000	-	0.30	-	-	-	-	-	Gawecka et al. (2017)

[a] estimated using Eu = 3 E' / 2(1+ν') or E'= Eu [2 (1+ν')]/3

* z is depth below top of clay layer (m)

[#] a small cohesion is applied to avoid numerical complications

Table E.3. Hydraulic conductivity of soils related to the soils found in the London energy pile site

Material	Hydraulic conductivity k [cm/s]	[m/s]	[m/day]	Source
Gravel and coarse material	-		1	De Santos et al. (2012)
London clay	-		1E-5 (hor.), 5E-4 (vert.)	De Santos et al. (2012)
London clay	-	1.00E-11 to 8.80E-9	8.64E-7 to 7.60E-4	Ratnam et al. (2005)
London clay	-	2.00E-10	1.73E-05	Gawecka et al. (2016)

underlined values are converted

Table E.4. Thermal properties of soils related to the soils found in the London energy pile site

Material	Unit weight γ [kN/m^3]	Density ρ_s x10^3[kg/m^3]	Thermal conductivity λ_s [W/(m. K)]	Specific heat capacity C_s x10^3[J/(kg. K)]	Volumetric heat capacity $\rho_s C_s$ x10^6[J/(m^3.K)]	Linear thermal expansion coefficient α_{sL} x10^{-6}[1/K]	Volumetric thermal expansion coefficient α_{sV} x10^{-6}[1/K]	Source
Made ground	18	1.83 [a]	1.4	1.036 [b]	1.90	17	-	Gawecka et al. (2017)
Terrace gravel	20	2.04 [a]	1.4	0.932 [b]	1.90	17	-	Gawecka et al. (2017)
London clay (stiff, fissured silty clay)	-	-	1.5	-	-	-	-	Amis et al. (2008)
London clay (stiff, fissured silty clay)	-	-	1.5	-	-	-	-	Bourne-Webb et al. (2009)
London clay	20	2.04 [a]	2	1.457 [b]	2.97	12	-	Gawecka et al. (2016)
London clay	20	2.04 [a]	1.79	0.893 [b]	1.82	17	-	Gawecka et al. (2017)
London clay	-	2.00	1.79	0.910 [b]	1.82	0.5	-	Bot (2017), p.27
Concrete (pile)	-	-	-	-	-	8.5	-	Bourne-Webb et al. (2009)
Concrete (pile)	-	-	-	-	-	8.5	-	Ouyang et al. (2011)
Concrete (pile)	-	-	-	-	-	8.5	-	Knellwolf et al. (2011)
Concrete (pile)	-	-	-	-	-	8.5	25.5	Yavari et al. (2014)
Concrete (pile)	-	2.5	2.33	0.768 [b]	1.92	8.5	-	Bot (2017), p.27
Concrete (pile)	-	-	-	-	-	12	-	Gawecka et al. (2016)
Concrete (pile)	24	2.45 [a]	2.33	0.785 [b]	1.92	8.5	-	Gawecka et al. (2017)

[a] estimated using $\rho_s = \gamma / g$

[b] estimated from $\rho_s c_s$

underlined values were calculated using $\alpha_{sL} = \alpha_{sV}/3$

Appendix F : Properties of Soils related to the Soils found in the Lausanne Energy Pile Site (Case Study 2)

Table F.1. General properties of soils related to the soils found in the Lausanne energy pile site

Material	Unit weight γ [kN/m^3]	Density ρ_s x10^3[kg/m^3]	Porosity n [%]	Void ratio e [-]	Source
Soil A1_Alluvial soil (soft clay[a])	19.62 [b]	2	10	0.11 [c]	Laloui et al. (2006)
Soil A1_Alluvial soil	20	-	-	-	Yavari et al. (2014)
Soil A1_Alluvial soil	27.16 [b]	2.769	10	0.11 [c]	Batini et al. (2015)
Soil A1_Alluvial soil	27.16 [b]	2.769	10	0.11 [c]	Di Donna et al. (2016)
Soil A2_Alluvial soil (soft clay[a])	19.13 [b]	1.95	10	0.11 [c]	Laloui et al. (2006)
Soil A2_Alluvial soil	19.5	-	-	-	Yavari et al. (2014)
Soil A2_Alluvial soil	27.16 [b]	2.769	10	0.11 [c]	Batini et al. (2015)
Soil A2_Alluvial soil	27.16 [b]	2.769	10	0.11 [c]	Di Donna et al. (2016)
Soil A (A1+A2)_Alluvial soil	27.16 [b]	2.769	10	0.11 [c]	Rotta Loria & Laloui (2017)
Soil A (A1+A2)_Alluvial soil (soft clay[a])	19.6	-	-	-	Amatya et al. (2012)
Soil B_Sandy-gravelly moraine or till (soft sandy-gravelly clay[a])	19.62 [b]	2	35	0.54 [c]	Laloui et al. (2006)
Soil B_Sandy-gravelly moraine	20	-	-	-	Yavari et al. (2014)
Soil B_Sandy-gravelly moraine	26.83 [b]	2.735	35	0.54 [c]	Batini et al. (2015)
Soil B_Sandy-gravelly moraine	26.83 [b]	2.735	35	0.54 [c]	Di Donna et al. (2016)
Soil B_Sandy-gravelly moraine	26.83 [b]	2.735	35	0.54 [c]	Rotta Loria & Laloui (2017)
Soil B_Sandy-gravelly moraine (soft sandy-gravelly clay[a])	19.1	-	-	-	Amatya et al. (2012)
Soil C_Bottom moraine or till (stiff sandy-gravelly clay[a])	21.58 [b]	2.2	30	0.43 [c]	Laloui et al. (2006)
Soil C_Bottom moraine	22	-	-	-	Yavari et al. (2014)
Soil C_Bottom moraine	26.88 [b]	2.74	30	0.43 [c]	Batini et al. (2015)
Soil C_Bottom moraine	26.88 [b]	2.74	30	0.43 [c]	Di Donna et al. (2016)
Soil C_Bottom moraine	26.88 [b]	2.74	30	0.43 [c]	Rotta Loria & Laloui (2017)
Soil C_Bottom moraine (stiff sandy-gravelly clay[a])	21.6	-	-	-	Amatya et al. (2012)
Soil D_Molasse or sandstone (moderately weak sandstone[a]) considered as impervous layer in their numerical model	25.02 [b]	2.55	-	-	Laloui et al. (2006)
Soil D_Molasse	25.5	-	-	-	Yavari et al. (2014)
Soil D_Molasse	21.26 [b]	2.167	10	0.11 [c]	Batini et al. (2015)
Soil D_Molasse	25.07 [b]	2.556	10	0.11 [c]	Di Donna et al. (2016)
Soil D_Molasse	21.26 [b]	2.167	10	0.11 [c]	Rotta Loria & Laloui (2017)
Soil D_Molasse (moderately weak sandstone[a])	25	-	-	-	Amatya et al. (2012)
Concrete (pile)	24.53 [b]	2.5	-	-	Laloui et al. (2006)
Concrete (pile)	24.53 [b]	2.5	10	0.11 [c]	Batini et al. (2015)
Concrete (pile)	24.53 [b]	2.5	10	0.11 [c]	Di Donna et al. (2016)
Concrete (pile)	26.70 [b]	2.722	10	0.11 [c]	Rotta Loria & Laloui (2017)
Concrete (slab)	24.53 [b]	2.5	10	0.11 [c]	Di Donna et al. (2016)
Concrete (slab)	26.70 [b]	2.722	10	0.11 [c]	Rotta Loria & Laloui (2017)

[a] as described by Amatya et al. (2012) for the same layer

[b] estimated using $\gamma = \rho_s g$

[c] estimated using $e = n / (1-n)$. They were not given in the source documents.

Table F.2. Strength and stiffness of soils related to the soils found in the Lausanne energy pile site

Material	Bulk modulus K [MPa]	Shear modulus G [MPa]	Elastic modulus E' [MPa]	Poisson's ratio ν' [-]	Cohesion c' [kPa]	Undrained shear strength s_u (c_u) [kPa]	Friction angle ϕ' (φ') [°]	Dilatancy angle ψ' [°]	Source
Soil A1_Alluvial soil (soft clay [a])	122	113	259.03 [b]	0.15 [c]	5	15 - 20	30	-	Laloui et al. (2006)
Soil A1_Alluvial soil	-	-	260	0.30	5	-	30	0	Yavari et al. (2014)
Soil A1_Alluvial soil	-	-	190	0.22	-	-	-	-	Batini et al. (2015)
Soil A1_Alluvial soil	-	-	190	0.22	5	-	30	7.5	Di Donna et al. (2016)
Soil A2_Alluvial soil (soft clay [a])	122	113	259.03 [b]	0.15 [c]	3	15 - 20	27	-	Laloui et al. (2006)
Soil A2_Alluvial soil	-	-	260	0.30	3	-	27	0	Yavari et al. (2014)
Soil A2_Alluvial soil	-	-	190	0.22	-	-	-	-	Batini et al. (2015)
Soil A2_Alluvial soil	-	-	190	0.22	3	-	27	7.5	Di Donna et al. (2016)
Soil A (A1+A2)_Alluvial soil	-	-	190	0.22	-	-	-	-	Rotta Loria & Laloui (2017)
Soil A (A1+A2)_Alluvial soil (soft clay [a])	-	-	-	-	-	15 - 20	-	-	Amatya et al. (2012)
Soil B_Sandy-gravelly moraine (soft sandy-gravelly clay [a])	59	1000	451.15 [b]	0.00 [c]	6	20 -30	23	-	Laloui et al. (2006)
Soil B_Sandy-gravelly moraine	-	-	450	0.35	6	-	23	0	Yavari et al. (2014)
Soil B_Sandy-gravelly moraine	-	-	84	0.40	-	-	-	-	Batini et al. (2015)
Soil B_Sandy-gravelly moraine	-	-	84	0.40	6	-	23	7.5	Di Donna et al. (2016)
Soil B_Sandy-gravelly moraine	-	-	84	0.40	-	-	-	-	Rotta Loria & Laloui (2017)
Soil B_Sandy-gravelly moraine (soft sandy-gravelly clay [a])	-	-	-	-	-	20 - 30	-	-	Amatya et al. (2012)
Soil C_Bottom moraine or till (stiff sandy-gravelly clay [a])	83	1400	634.20 [b]	0.00 [c]	20	70 - 150	27	-	Laloui et al. (2006)
Soil C_Bottom moraine	-	-	630	0.35	20	-	27	0	Yavari et al. (2014)
Soil C_Bottom moraine	-	-	90	0.40	-	-	-	-	Batini et al. (2015)
Soil C_Bottom moraine	-	-	90	0.40	20	-	27	-	Di Donna et al. (2016)
Soil C_Bottom moraine	-	-	90	0.40	-	-	-	-	Rotta Loria & Laloui (2017)
Soil C_Bottom moraine (stiff sandy-gravelly clay [a])	-	-	-	-	-	70 - 150	-	-	Amatya et al. (2012)
Soil D_Molasse or sandstone [a]	620 - 3100 (av. 18600)	550 - 2800 (av. 1675)	1273 - 6456 (av. 3865) [b]	0.15 [c]	-	UCS =12000	-	-	Laloui et al. (2006)
Soil D_Molasse	-	-	3000	0.22	4	-	25	0	Yavari et al. (2014)
Soil D_Molasse	-	-	3000	0.20	-	-	-	-	Batini et al. (2015)
Soil D_Molasse	-	-	3000	0.30	2000	-	35	7.5	Di Donna et al. (2016)
Soil D_Molasse	-	-	3000	0.30	-	-	-	-	Rotta Loria & Laloui (2017)
Soil D_Molasse	-	-	-	-	-	UCS =12000	-	-	Amatya et al. (2012)
Concrete (pile)	17381	14313	33690.99 [b]	0.18 [c]	-	-	-	-	Laloui et al. (2006)
Concrete (pile)	-	-	29200	-	-	-	-	-	Knellwolf et al. (2011)
Concrete (pile)	-	-	29200	0.2	-	-	-	-	Yavari et al. (2014)
Concrete (pile)	-	-	28000	0.25	-	-	-	-	Batini et al. (2015)
Concrete (pile)	-	-	28000	0.25	-	-	-	-	Di Donna et al. (2016)
Concrete (pile)	-	-	28000	0.25	-	-	-	-	Rotta Loria & Laloui (2017)
Concrete (slab)	-	-	35000	0.25	-	-	-	-	Di Donna et al. (2016)
Concrete (slab)	-	-	35000	0.25	-	-	-	-	Rotta Loria & Laloui (2017)

[a] as described by Amatya et al. (2012) for the same layer

[b] estimated using E = (9KG / (3K+G). They were not given in the source documents.

[c] estimated using ν = (E / 2G) -1. They were not given in the source documents.

UCS = unconfined compressive strength

Table F.3. Hydraulic conductivity of soils related to the soils found in the Lausanne energy pile site

Material	Hydraulic conductivity k			Source
	[cm/s]	[m/s]	[m/day]	
Soil A1_Alluvial soil (soft clay[a])	-	2.00E-06	0.173	Laloui et al. (2006)
Soil A1_Alluvial soil	-	7.00E-06	0.605	Di Donna et al. (2016)
Soil A2_Alluvial soil (soft clay[a])	-	7.00E-07	0.060	Laloui et al. (2006)
Soil A2_Alluvial soil	-	1.00E-05	0.864	Di Donna et al. (2016)
Soil B_Sandy-gravelly moraine or till (soft sandy-gravelly clay[a])	-	1.00E-06	0.086	Laloui et al. (2006)
Soil B_Sandy-gravelly moraine	-	1.00E-05	0.864	Di Donna et al. (2016)
Soil C_Bottom moraine or till (stiff sandy-gravelly clay[a])	-	1.00E-06	0.086	Laloui et al. (2006)
Soil C_Bottom moraine	-	2.00E-10	0.000017	Di Donna et al. (2016)
Soil D_Molasse or sandstone (moderately weak sandstone[a]), considered as impervous layer in their numerical model	-	-	-	Laloui et al. (2006)
Soil D_Molasse	-	2.00E-10	0.000017	Di Donna et al. (2016)
Concrete (pile)	-	-	-	Laloui et al. (2006)
Concrete (pile)	-	2.00E-10	0.000017	Di Donna et al. (2016)
Concrete (slab)	-	2.00E-10	0.000017	Di Donna et al. (2016)

[a] as described by Amatya et al. (2012) for the same layer

underlined values are converted

Table F.4. Thermal properties of soils related to the soils found in the Lausanne energy pile site

Material	Density ρ_s x10^3[kg/m^3]	Thermal conductivity λ_s [W/(m. K)]	Specific heat capacity C_s x10^3[J/(kg. K)]	Volumetric heat capacity $\rho_s C_s$ x10^6[J/(m^3.K)]	Linear thermal expansion coefficient α_{sL} x10^{-6}[1/K]	Volumetric thermal expansion coefficient α_{sV} x10^{-6}[1/K]	Source
Soil A1_Alluvial soil	2	1.8	1.200 [a]	2.40	3.33	10	Laloui et al. (2006)
Soil A1_Alluvial soil	2.769	1.8	0.880	-	3.3	-	Batini et al. (2015)
Soil A1_Alluvial soil	2.769	3.38	0.880	-	3.33	10	Di Donna et al. (2016)
Soil A2_Alluvial soil	1.95	1.8	1.231 [a]	2.40	3.33	10	Laloui et al. (2006)
Soil A2_Alluvial soil	2.769	1.8	0.880	-	3.3	-	Batini et al. (2015)
Soil A2_Alluvial soil	2.769	3.38	0.880	-	3.33	10	Di Donna et al. (2016)
Soil A (A1+A2)_Alluvial soil	2.769	1.49 adjusted (3.38 initial)	0.880	-	3.3	-	Rotta Loria & Laloui (2017)
Soil B_Sandy-gravelly moraine	2	1.8	1.200 [a]	2.40	33.33	100	Laloui et al. (2006)
Soil B_Sandy-gravelly moraine	2.735	1.8	0.890	-	33	-	Batini et al. (2015)
Soil B_Sandy-gravelly moraine	2.735	4.45	0.890	-	33.33	100	Di Donna et al. (2016)
Soil B_Sandy-gravelly moraine	2.735	3.68 adjusted (4.45 initial)	0.890	-	3.3 adjusted (33 initial)	-	Rotta Loria & Laloui (2017)
Soil C_Bottom moraine or till	2.2	1.8	1.091 [a]	2.40	33.33	100	Laloui et al. (2006)
Soil C_Bottom moraine	2.74	1.8	0.890	-	33	-	Batini et al. (2015)
Soil C_Bottom moraine	2.74	4.17	0.890	-	33.33	100	Di Donna et al. (2016)
Soil C_Bottom moraine	2.74	3.46 adjusted (4.17 initial)	0.890	-	3.3 adjusted (33 initial)	-	Rotta Loria & Laloui (2017)
Soil D_Molasse or sandstone	2.55	1.1	0.784 [a]	2.00	0.33	1.0	Laloui et al. (2006)
Soil D_Molasse	2.167	1.11	0.923	-	0.33	-	Batini et al. (2015)
Soil D_Molasse	2.556	3.38	0.923	-	0.33	1.0	Di Donna et al. (2016)
Soil D_Molasse	2.167	3.82 adjusted (3.38 initial)	0.923	-	2.3 adjusted (0.33 initial)	-	Rotta Loria & Laloui (2017)
Concrete (pile)	2.5	2.1	0.800 [a]	2.00	3.33	10	Laloui et al. (2006)
Concrete (pile)	-	-	-	-	10	-	Knellwolf et al. (2011)
Concrete (pile)	-	-	-	-	10	30	Yavari et al. (2014)
Concrete (pile)	2.5	1.628	0.837	-	10	-	Batini et al. (2015)
Concrete (pile)	2.5	1.628	0.837	-	10	30	Di Donna et al. (2016)
Concrete (pile)	2.722	1.628	0.837	-	10	-	Rotta Loria & Laloui (2017)
Concrete (slab)	2.5	1.628	0.837	-	10	30	Di Donna et al. (2016)
Concrete (slab)	2.722	1.628	0.837	-	10	-	Rotta Loria & Laloui (2017)

[a] estimated from $\rho_s c_s$

___underlined values were calculated using $\alpha_{sL} = \alpha_{sV}/3$

Appendix G : Properties of Soils related to the Soils found in Winnipeg

Table G.1. Typical properties of the Winnipeg lacustrine clay (extracted from Baracos et al., 1983)

Symbol	Soil properties	Lower bound	Upper bound	Unit
E	Deformation modulus	3.5	21	[MPa]
v	Poisson's ratio	0.4	0.5	[-]
q_u	Unconfined compressive strength	50	120	[kPa]
s_u	Undrained shear strength	35	85	[kPa]
ϕ'_r	Residual internal friction angle	8	12	[°]
C_c	Compression index	0.5	1	[-]
K_o	Coefficient of earth pressure at rest	0.6	0.8	[-]
OCR	Overconsolidation ratio	1	5	[-]
γ	Moist unit weight	16.2	18.2	[kN/m^3]
γ_d	Dry unit weight	10.2	13.3	[kN/m^3]
W_n	Moisture content	40	60	[%]
LL	Liquid limit	65	110	[%]
PL	Plastic limit	20	35	[%]
PI	Plasticity index	40	75	[%]
S_t	Sensitivity	2	4	[-]

Table G.2. General properties of Winnipeg soils

Material	Unit weight γ [kN/m^3]	Density ρ_s x10^3[kg/m^3]	Porosity n [%]	Void ratio e [-]	Source
Clay (lacustrine clay)	16.2 - 18.2 (av. 17.2)	-	-	-	Baracos et al. (1983), p.24
Clay (lacustrine clay)	-	-	55 - 60 (av. 58)	1.22 - 1.5 [a] (av. 1.38)	Ferguson & Woodbury (2004)
Clay (lacustrine clay)	17.1	-	-	1.36 [a]	Thiessen (2010), p.93
Clay (lacustrine clay)	17.1	-	-	-	Thiessen et al. (2011)
Till (silt till)	21.2 - 24.3 (av. 22.8)	-	-	-	Baracos et al. (1983), p.25-26
Till (silt till)	-	-	10 - 30 (av. 20)	0.11 - 0.43 [a] (av. 0.25)	Ferguson & Woodbury (2004)
Till (silt till)	23	-	-	Varies	Thiessen (2010), p.93
Till (silt till)	23	-	-	-	Thiessen et al. (2011)
Bedrock (dolomitic limestone)	-	-	4 - 12 (av. 8)	0.042 - 0.14 [a] (av. 0.087)	Baracos et al. (1983), p.27
Bedrock (dolomitic limestone)	-	-	5	0.053 [a]	Ferguson & Woodbury (2004)

[a] estimated using e = n / (1-n). They were not given in the source documents.

Table G.3. Strength and stiffness of Winnipeg soils

Material	Bulk modulus K [MPa]	Shear modulus G [MPa]	Elastic modulus E' [MPa]	Cohesion c' [kPa]	Unconfined compressive strength q_u [MPa]	Undrained shear strength s_u (c_u) [kPa]	Friction angle ϕ'_{cs} [°]	Friction angle ϕ' (φ') [°]	Source
Clay (lacustrine clay)	-	-	-	3	-	-	-	23	Baracos & Graham (1981)
Clay (lacustrine clay)	-	-	3.5 - 21	-	-	35 - 85	-	-	Baracos et al. (1983), p.24
Clay (lacustrine clay)	-	5.1	-	28	-	-	-	14.7	Thiessen (2010), p.92
Clay (lacustrine clay)	-	5.07	13.4	5	-	-	18	-	Thiessen et al. (2011)
Clay (lacustrine clay)	-	-	-	-	-	40 - 60	-	-	Skaftfeld (2014), p.115
Till (silt till)	-	-	170 - 240 (av. 205)	-	3.4 - 3.6	-	-	-	Baracos et al. (1983), p.26
Till (silt till)	-	7.9	-	3	-	-	-	42	Thiessen (2010), p.92
Till (silt till)	-	-	200	-	-	-	-	42	Thiessen et al. (2011)
Bedrock (dolomitic limestone)	-	-	9700 - 12400 (av. 11050)	-	34 - 37 to > 60		-	-	Baracos et al. (1983), p.26-27

Table G.4. Hydraulic conductivity of Winnipeg soils

Material	Hydraulic conductivity k [cm/s]	[m/s]	[m/day]	Permeability $k_{intrinsic}$ [m^2]	Source
Clay (lacustrine clay)	-	2.5E-10 to 1.3E-9 (av. 7.75E-10)	2.16E-5 to 1.12E-4 (av. 6.7E-5)	-	Baracos et al. (1983), p.33
Clay (lacustrine clay)	-	1.00E-07 [a]	0.009	1.00E-14	Ferguson & Woodbury (2004)
Clay (lacustrine clay), brown	-	4E-8 to 1.3E-10 (av. 4.01E-8)	3.46E-3 to 1.12E-5 (av. 1.74E-3)	-	Thiessen (2010), p.94
Clay (lacustrine clay), grey	-	8.60E-11	7.430E-06	-	Thiessen (2010), p.94
Clay (lascustrine clay)	-	8E-11 to 8E-10 (av. 8.8E-10)	6.91E-6 to 6.91E-5 (av. 7.60E-5)	-	Thiessen et al. (2011)
Till (silt till)	-	2.5E-10 to 6.4E-7 (av. 3.2E-7)	2.16E-5 to 0.055 (av. 0.028)	-	Baracos et al. (1983), p.32
Till (silt till)	-	1.00E-03 [a]	86.40	1.00E-10	Ferguson & Woodbury (2004)
Bedrock (dolomitic limestone)	-	0.0001 [a]	8.640	1.00E-11	Ferguson & Woodbury (2004)

[a] estimated using $k_{intr} = k\,(\mu_w / \gamma_w)$, or using aproximate relation k [m/s] = k_{intr} [m^2] x 10^7 for water at 20° C
where μ_w is the dynamic viscosity and γ_w is unit weight of water (see Kresic, 2007, p.35-36)

underlined values are converted

Table G.5. Thermal properties of Winnipeg soils

Material	Density ρ_s x10^3[kg/m^3]	Thermal conductivity λ_s [W/(m. K)]	Specific heat capacity C_s x10^3[J/(kg. K)]	Volumetric heat capacity $\rho_s C_s$ x10^6[J/(m^3.K)]	Thermal diffusivity α_{td} [m^2/s]	Linear thermal expansion coefficient α_{sL} x10^{-6}[1/K]	Source
Clay (lacustrine clay)	1.83 [a]	1.2	0.830 [b]	1.52 [c]	7.90E-07	-	Ferguson & Woodbury (2004)
Till (silt till)	2.34 [a]	1.5	0.720 [b]	1.69 [c]	8.90E-07	-	Ferguson & Woodbury (2004)
Bedrock (dolomitic limestone)	2.45	2.3	1.286 [b]	3.15 [c]	7.30E-07	-	Ferguson & Woodbury (2004)

[a] from Baracos et al. (1983)

[b] estimated from $\rho_s c_s$

[c] estimated using $\alpha_{td} = \lambda_s / \rho_s c_s$ (see Banks, 2012, p.51)

Appendix H : Geotechnical Pile Capacity Estimation of Piles in Winnipeg using the Semi-empirical Static Method

The geotechnical pile capacity in cohesionless (non-plastic) soils such as sands can be estimated using effective stress analysis (ESA). This method is also known as the β-Method of analysis. Whereas, in cohesive soil layers such as clays, the pile capacity is usually estimated using total stress analysis (TSA), also known as the α-Method of analysis.

$$Q_{ult} = Q_s + Q_p \quad \text{[Equation H.1]}$$

$$Q_{all} = \frac{Q_{ult}}{F.S} = \frac{Q_s}{F.S_s} + \frac{Q_p}{F.S_p} \quad \text{[Equation H.2]}$$

$$Q_{ULS} = \varphi_r \, Q_{ult} \quad \text{[Equation H.3]}$$

where, Q_{ult} is the ultimate load-carrying capacity of the pile (kN), Q_s is the shaft capacity or resistance (kN), and Q_p is the point (toe) bearing capacity or resistance (kN). The global factor of safety (F.S) ranges from 2.5-3.0 for the working stress design (WSD). $F.S_s$ = factor of safety on shaft resistance (usually 2.5). $F.S_p$ = factor of safety on point (toe) resistance (usually 3.0). Whereas, for the ultimate limit state (ULS) design the overall resistance factor (φ_r) of 0.4 is generally adopted for the static analysis (CFEM, 2006).

$$Q_s = A_s \, f_s \quad \text{[Equation H.4]}$$

$$A_s = P \, L \quad \text{[Equation H.5]}$$

For cohesionless soils:

$$f_s = (K_s \tan \delta) \, \sigma'_{z0(av.)} \quad \text{[Equation H.6]}$$

$$\beta = K_s \tan \delta \quad \text{[Equation H.7]}$$

For cohesive soils:

$$f_s = \alpha\, c_u \qquad \text{[Equation H.8]}$$

where, A_s is the area of the pile shaft (m^2), f_s is the unit shaft friction stress (kPa), P is the perimeter of the pile (m), L is the pile length considered (m), K_s is the lateral earth pressure coefficient (-), δ is the interface friction angle between soil and pile (°), $\sigma'_{z0(av.)}$ is the average effective stress along the considered pile length (kPa), α is the adhesion factor (-), and $c_u = s_u$ is the undrained shear strength (kPa).

$$Q_P = A_p\, q_p \qquad \text{[Equation H.9]}$$

For cohesionless soils:

$$q_P = \sigma'_{z0}\, N_p^* \qquad \text{[Equation H.10]}$$

For cohesive soils:

$$q_P = N_c^* C_u \qquad \text{[Equation H.11]}$$

where, A_p is the area of the pile point or toe (m^2), q_p is the unit end-bearing stress (kPa), σ'_{z0} is the effective stress at the pile toe (kPa), and N'_p, N'_c is the point bearing capacity factor for the pile for cohesionless and cohesive, respectively.

The calculations were done in spreadsheets using the semi-empirical static method as shown in tables below for the Winnipeg friction pile with the diameter of 0.4 m and the Winnipeg end-bearing pile with the pile toe in the till layer and the diameter of 0.8 m. Figure H.1 and Figure H.2 show the geotechnical pile capacities with varying depths of both the 0.4 m dia. and 0.8 m cast-in-place piles.

Table H.1. Pile capacity estimation with 0.4 m dia. using a semi-empirical static method

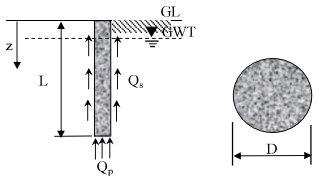

Pile cross-section: D = 0.4 [m]
Pile perimeter, P_p = 1.257 [m]
Cross-sectional area, A_p = 0.126 [m^2] ; note: for the selection of a pile capacity, designers must ensure
Pile cut-off elevation: at: 0.00 [m] that the pile toe is embeded at least 3 B into the bearing stratum.
Groundwater table elevation: at: 3 [m] ; below ground level (bgl)

																						WSD			LSD	
Soil type	Depth	Elevation	Bulk unit weight	Unit weight of water	Total overb. Stress	Water pressure	Eff. overb. stress	Friction angle (drained)	Interface angle	Lateral earth pres. coeff.	Beta value	Undr. shear strength	Alpha value	Unit side-shear stress	Increm. Shaft resistance	Shaft resistance	Bearing capacity factor	Bearing capacity factor	Unit end-bearing (point) stress	End-bearing (point) resistance	Ultimate capacity	Factor of safety		Allow. Capacity	Resistance factor	Ultimate limit state resistance
	z	EL	γ	γ_w	σ_{vo}	u_w	σ'_{vo}	ϕ'	δ	K_s	β	s_u (or c_u)	α	fs	ΔQs	Q_s	Nc*	Nq*	q_p	Q_p	Qult	$F.S_s$	$F.S_p$	Qallow.	RF or φ_r	Q_{ULS}
	[m]	[m]	[kN/m^3]	[kN/m^3]	[kPa]	[kPa]	[kPa]	[°]	[°]	[-]	[-]	[kPa]	[-]	[kPa]	[kN]	[kN]	[-]	[-]	[kPa]	[kN]	[kN]	[-]	[-]	[kN]	[-]	[kN]
	0		17.0	0.00	0.0	0.0	0.0																			
	-0.5		17.0	0.00	8.5	0.0	8.5																			
	-1		17.0	0.00	17.0	0.0	17.0																			
	-1.5		17.0	0.00	25.5	0.0	25.5	n/a	n/a	n/a	n/a	60	0.640	38.40	24.13	24.13	9	n/a	540.00	67.86	91.99	2.5	3	32.27	0.40	36.79
	-2		17.0	0.00	34.0	0.0	34.0	n/a	n/a	n/a	n/a	60	0.640	38.40	24.13	48.25	9	n/a	540.00	67.86	116.11	2.5	3	41.92	0.40	46.45
	-2.5		17.0	0.00	42.5	0.0	42.5	n/a	n/a	n/a	n/a	60	0.640	38.40	24.13	72.38	9	n/a	540.00	67.86	140.24	2.5	3	51.57	0.40	56.10
	-3		17.0	0.00	51.0	0.0	51.0	n/a	n/a	n/a	n/a	60	0.640	38.40	24.13	96.51	9	n/a	540.00	67.86	164.37	2.5	3	61.22	0.40	65.75
	-3.5		18.0	9.81	60.0	4.9	55.1	n/a	n/a	n/a	n/a	60	0.640	38.40	24.13	120.64	9	n/a	540.00	67.86	188.50	2.5	3	70.87	0.40	75.40
	-4		18.0	9.81	69.0	9.8	59.2	n/a	n/a	n/a	n/a	60	0.640	38.40	24.13	144.76	9	n/a	540.00	67.86	212.62	2.5	3	80.53	0.40	85.05
	-4.5		18.0	9.81	78.0	14.7	63.3	n/a	n/a	n/a	n/a	60	0.640	38.40	24.13	168.89	9	n/a	540.00	67.86	236.75	2.5	3	90.18	0.40	94.70
	-5		18.0	9.81	87.0	19.6	67.4	n/a	n/a	n/a	n/a	60	0.640	38.40	24.13	193.02	9	n/a	540.00	67.86	260.88	2.5	3	99.83	0.40	104.35
	-5.5		18.0	9.81	96.0	24.5	71.5	n/a	n/a	n/a	n/a	60	0.640	38.40	24.13	217.15	9	n/a	540.00	67.86	285.01	2.5	3	109.48	0.40	114.00
	-6		18.0	9.81	105.0	29.4	75.6	n/a	n/a	n/a	n/a	60	0.640	38.40	24.13	241.27	9	n/a	540.00	67.86	309.13	2.5	3	119.13	0.40	123.65
	-6.5		18.0	9.81	114.0	34.3	79.7	n/a	n/a	n/a	n/a	60	0.640	38.40	24.13	265.40	9	n/a	540.00	67.86	333.26	2.5	3	128.78	0.40	133.30
Winnipeg	-7		18.0	9.81	123.0	39.2	83.8	n/a	n/a	n/a	n/a	60	0.640	38.40	24.13	289.53	9	n/a	540.00	67.86	357.39	2.5	3	138.43	0.40	142.96
lacustrine	-7.5		18.0	9.81	132.0	44.1	87.9	n/a	n/a	n/a	n/a	60	0.640	38.40	24.13	313.66	9	n/a	540.00	67.86	381.52	2.5	3	148.08	0.40	152.61
clay	-8		18.0	9.81	141.0	49.1	92.0	n/a	n/a	n/a	n/a	60	0.640	38.40	24.13	337.78	9	n/a	540.00	67.86	405.64	2.5	3	157.73	0.40	162.26
	-8.5		18.0	9.81	150.0	54.0	96.0	n/a	n/a	n/a	n/a	60	0.640	38.40	24.13	361.91	9	n/a	540.00	67.86	429.77	2.5	3	167.38	0.40	171.91
	-9		18.0	9.81	159.0	58.9	100.1	n/a	n/a	n/a	n/a	60	0.640	38.40	24.13	386.04	9	n/a	540.00	67.86	453.90	2.5	3	177.04	0.40	181.56
	-9.5		18.0	9.81	168.0	63.8	104.2	n/a	n/a	n/a	n/a	60	0.640	38.40	24.13	410.17	9	n/a	540.00	67.86	478.02	2.5	3	186.69	0.40	191.21
	-10		18.0	9.81	177.0	68.7	108.3	n/a	n/a	n/a	n/a	60	0.640	38.40	24.13	434.29	9	n/a	540.00	67.86	502.15	2.5	3	196.34	0.40	200.86
	-10.5		18.0	9.81	186.0	73.6	112.4	n/a	n/a	n/a	n/a	60	0.640	38.40	24.13	458.42	9	n/a	540.00	67.86	526.28	2.5	3	205.99	0.40	210.51
	-11		18.0	9.81	195.0	78.5	116.5	n/a	n/a	n/a	n/a	60	0.640	38.40	24.13	482.55	9	n/a	540.00	67.86	550.41	2.5	3	215.64	0.40	220.16
	-11.5		18.0	9.81	204.0	83.4	120.6	n/a	n/a	n/a	n/a	60	0.640	38.40	24.13	506.68	9	n/a	540.00	67.86	574.53	2.5	3	225.29	0.40	229.81
	-12		18.0	9.81	213.0	88.3	124.7	n/a	n/a	n/a	n/a	60	0.640	38.40	24.13	530.80	9	n/a	540.00	67.86	598.66	2.5	3	234.94	0.40	239.46
	-12.5		18.0	9.81	222.0	93.2	128.8	n/a	n/a	n/a	n/a	60	0.640	38.40	24.13	554.93	9	n/a	540.00	67.86	622.79	2.5	3	244.59	0.40	249.12
	-13		18.0	9.81	231.0	98.1	132.9	n/a	n/a	n/a	n/a	60	0.640	38.40	24.13	579.06	9	n/a	540.00	67.86	646.92	2.5	3	254.24	0.40	258.77
	-13.5		18.0	9.81	240.0	103.0	137.0	n/a	n/a	n/a	n/a	60	0.640	38.40	24.13	603.19	9	n/a	540.00	67.86	671.04	2.5	3	263.89	0.40	268.42
	-14		18.0	9.81	249.0	107.9	141.1	n/a	n/a	n/a	n/a	60	0.640	38.40	24.13	627.31	9	n/a	540.00	67.86	695.17	2.5	3	273.54	0.40	278.07
	-14.5		18.0	9.81	258.0	112.8	145.2	n/a	n/a	n/a	n/a	60	0.640	38.40	24.13	651.44	9	n/a	540.00	67.86	719.30	2.5	3	283.20	0.40	287.72
	-15		18.0	9.81	267.0	117.7	149.3	n/a	n/a	n/a	n/a	60	0.640	38.40	24.13	675.57	9	n/a	540.00	67.86	743.43	2.5	3	292.85	0.40	297.37

Ignored load-carrying capacity for this 1.5 m for seasonal effects

Table H.1. (Cont.)

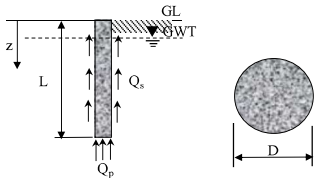

Pile cross-section: D = 0.4 [m]
Pile perimeter, P_p = 1.257 [m]
Cross-sectional area, A_p = 0.126 [m^2] ; note: for the selection of a pile capacity, designers must ensure
Pile cut-off elevation: at: 0.00 [m] that the pile toe is embeded at least 3 B into the bearing stratum.
Groundwater table elevation: at: 3 [m] ; below ground level (bgl)

																						WSD			LSD	
Soil type	Depth	Elevation	Bulk unit weight	Unit weight of water	Total overb. Stress	Water pressure	Eff. overb. stress	Friction angle (drained)	Interface angle	Lateral earth pres. coeff.	Beta value	Undr. shear strength	Alpha value	Unit side-shear stress	Increm. Shaft resistance	Shaft resistance	Bearing capacity factor	Bearing capacity factor	Unit end-bearing (point) stress	End-bearing (point) resistance	Ultimate capacity	Factor of safety		Allow. Capacity	Resistance factor	Ultimate limit state resistance
	z	EL	γ	γ_w	σ_{vo}	u_w	σ'_{vo}	ϕ'	δ	K_s	β	s_u (or c_u)	α	f_s	ΔQ_s	Q_s	N_c*	N_q*	q_p	Q_p	Qult	$F.S_s$	$F.S_p$	Qallow.	RF or φ_r	Q_{ULS}
	[m]	[m]	[kN/m^3]	[kN/m^3]	[kPa]	[kPa]	[kPa]	[°]	[°]	[-]	[-]	[kPa]	[-]	[kPa]	[kN]	[kN]	[-]	[-]	[kPa]	[kN]	[kN]	[-]	[-]	[kN]	[-]	[kN]
	-15.5		23.0	9.81	278.5	122.6	155.9	40	28	0.8	(a) 0.43	n/a	n/a	67.71	42.54	718.11	n/a	(b) 100	(c) 2160.00	271.43	989.54	2.5	3	377.72	0.40	395.82
	-16		23.0	9.81	290.0	127.5	162.5	40	28	0.8	0.43	n/a	n/a	70.51	44.30	762.41	n/a	100	2160.00	271.43	1033.85	2.5	3	395.44	0.40	413.54
	-16.5		23.0	9.81	301.5	132.4	169.1	40	28	0.8	0.43	n/a	n/a	73.32	46.07	808.48	n/a	100	2160.00	271.43	1079.91	2.5	3	413.87	0.40	431.97
	-17		23.0	9.81	313.0	137.3	175.7	40	28	0.8	0.43	n/a	n/a	76.12	47.83	856.31	n/a	100	2160.00	271.43	1127.74	2.5	3	433.00	0.40	451.10
	-17.5		23.0	9.81	324.5	142.2	182.3	40	28	0.8	0.43	n/a	n/a	78.93	49.59	905.90	n/a	100	2160.00	271.43	1177.34	2.5	3	452.84	0.40	470.93
Silt till	-18		23.0	9.81	336.0	147.2	188.9	40	28	0.8	0.43	n/a	n/a	81.73	51.35	957.26	n/a	100	2160.00	271.43	1228.69	2.5	3	473.38	0.40	491.48
	-18.5		23.0	9.81	347.5	152.1	195.4	40	28	0.8	0.43	n/a	n/a	84.54	53.12	1010.37	n/a	100	2160.00	271.43	1281.81	2.5	3	494.63	0.40	512.72
	-19		23.0	9.81	359.0	157.0	202.0	40	28	0.8	0.43	n/a	n/a	87.34	54.88	1065.25	n/a	100	2160.00	271.43	1336.69	2.5	3	516.58	0.40	534.67
	-19.5		23.0	9.81	370.5	161.9	208.6	40	28	0.8	0.43	n/a	n/a	90.15	56.64	1121.90	n/a	100	2160.00	271.43	1393.33	2.5	3	539.24	0.40	557.33
	-20		23.0	9.81	382.0	166.8	215.2	40	28	0.8	0.43	n/a	n/a	92.57	58.16	1180.06	n/a	100	2160.00	271.43	1451.49	2.5	3	562.50	0.40	580.60
	-20.5		23.0	9.81	393.5	171.7	(d) 220.0	40	28	0.8	0.43	n/a	n/a	93.58	58.80	1238.86	n/a	100	2160.00	271.43	1510.29	2.5	3	586.02	0.40	604.12
	-21		23.0	9.81	405.0	176.6	220.0	40	28	0.8	0.43	n/a	n/a	93.58	58.80	1297.65	n/a	100	2160.00	271.43	1569.09	2.5	3	609.54	0.40	627.63

Groundwater table (GWT): 3 m below ground level (bgl)
Minimum pile length in the Winnipeg area is about 6 m

(a) CFEM (2006, p. 263) gives values from 0.4 - 0.6 for dense sand and 0.4 - 0.7 for gravel.

(b) Nq* from Poulos & David (1980, p. 27) and CFEM (2006, p. 263) gives value in the range from 50 - 100 for dense sand and 100 - 150 for gravel.

(c) Local practice in Winnipeg (Baracos et al., 1983) reported that the allowable unit end-bearing, $q_{p(all)}$ = 720 kPa, has been commonly used for dense till. Considering local practice, this value was set as a limiting value for the allowable unit end-bearing calculated given in the table. Using the assumed F.Sp = 3, the limiting ultimate unit end-bearing would be equal to 720 x 3 = 2160 kPa.

(d) Effective overburden stress used for calculation of the pile capacity is limited to 220 kPa (Randolph et al. 1994)

Table H.2. Pile capacity estimation with 0.8 m dia. using a semi-empirical static method

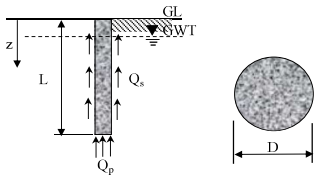

Pile cross-section: D = 0.8 [m]
Pile perimeter, P_p = 2.513 [m]
Cross-sectional area, A_p = 0.503 [m^2] ; note: for the selection of a pile capacity, designers must ensure
Pile cut-off elevation: at: 0.00 [m] that the pile toe is embeded at least 3 B into the bearing stratum.
Groundwater table elevation: at: 3 [m] ; below ground level (bgl)

																						WSD		LSD	
Soil type	Depth	Elevation	Bulk unit weight	Unit weight of water	Total overb. Stress	Water pressure	Eff. overb. stress	Friction angle (drained)	Interface angle	Lateral earth pres. coeff.	Beta value	Undr. shear strength	Alpha value	Unit side-shear stress	Increm. Shaft resistance	Shaft resistance	Bearing capacity factor	Bearing capacity factor	Unit end-bearing (point) stress	End-bearing (point) resistance	Ultimate capacity	Factor of safety	Allow. Capacity	Resistance factor	Ultimate limit state resistance
	z	EL.	γ	γ_w	σ_{vo}	u_w	σ'_{vo}	ϕ'	δ	K_s	β	s_u (or c_u)	α	fs	ΔQs	Q_s	Nc*	Nq*	q_p	Q_p	Qult	$F.S_s$	$F.S_p$	Qallow.	RF or φ_r	Q_{ULS}
	[m]	[m]	[kN/m^3]	[kN/m^3]	[kPa]	[kPa]	[kPa]	[°]	[°]	[-]	[-]	[kPa]	[-]	[kPa]	[kN]	[kN]	[-]	[-]	[kPa]	[kN]	[kN]	[-]	[-]	[kN]	[-]	[kN]
	0		17.0	0.00	0.0	0.0	0.0																			
	-0.5		17.0	0.00	8.5	0.0	8.5																			
	-1		17.0	0.00	17.0	0.0	17.0																			
	-1.5		17.0	0.00	25.5	0.0	25.5	n/a	n/a	n/a	n/a	60	0.640	38.40	48.25	48.25	9	n/a	540.00	271.43	319.69	2.5	3	109.78	0.40	127.88
	-2		17.0	0.00	34.0	0.0	34.0	n/a	n/a	n/a	n/a	60	0.640	38.40	48.25	96.51	9	n/a	540.00	271.43	367.94	2.5	3	129.08	0.40	147.18
	-2.5		17.0	0.00	42.5	0.0	42.5	n/a	n/a	n/a	n/a	60	0.640	38.40	48.25	144.76	9	n/a	540.00	271.43	416.20	2.5	3	148.38	0.40	166.48
	-3		17.0	0.00	51.0	0.0	51.0	n/a	n/a	n/a	n/a	60	0.640	38.40	48.25	193.02	9	n/a	540.00	271.43	464.45	2.5	3	167.69	0.40	185.78
	-3.5		18.0	9.81	60.0	4.9	55.1	n/a	n/a	n/a	n/a	60	0.640	38.40	48.25	241.27	9	n/a	540.00	271.43	512.71	2.5	3	186.99	0.40	205.08
	-4		18.0	9.81	69.0	9.8	59.2	n/a	n/a	n/a	n/a	60	0.640	38.40	48.25	289.53	9	n/a	540.00	271.43	560.96	2.5	3	206.29	0.40	224.39
	-4.5		18.0	9.81	78.0	14.7	63.3	n/a	n/a	n/a	n/a	60	0.640	38.40	48.25	337.78	9	n/a	540.00	271.43	609.22	2.5	3	225.59	0.40	243.69
	-5		18.0	9.81	87.0	19.6	67.4	n/a	n/a	n/a	n/a	60	0.640	38.40	48.25	386.04	9	n/a	540.00	271.43	657.47	2.5	3	244.89	0.40	262.99
	-5.5		18.0	9.81	96.0	24.5	71.5	n/a	n/a	n/a	n/a	60	0.640	38.40	48.25	434.29	9	n/a	540.00	271.43	705.73	2.5	3	264.20	0.40	282.29
	-6		18.0	9.81	105.0	29.4	75.6	n/a	n/a	n/a	n/a	60	0.640	38.40	48.25	482.55	9	n/a	540.00	271.43	753.98	2.5	3	283.50	0.40	301.59
	-6.5		18.0	9.81	114.0	34.3	79.7	n/a	n/a	n/a	n/a	60	0.640	38.40	48.25	530.80	9	n/a	540.00	271.43	802.24	2.5	3	302.80	0.40	320.89
Winnipeg	-7		18.0	9.81	123.0	39.2	83.8	n/a	n/a	n/a	n/a	60	0.640	38.40	48.25	579.06	9	n/a	540.00	271.43	850.49	2.5	3	322.10	0.40	340.20
lacustrine	-7.5		18.0	9.81	132.0	44.1	87.9	n/a	n/a	n/a	n/a	60	0.640	38.40	48.25	627.31	9	n/a	540.00	271.43	898.75	2.5	3	341.40	0.40	359.50
clay	-8		18.0	9.81	141.0	49.1	92.0	n/a	n/a	n/a	n/a	60	0.640	38.40	48.25	675.57	9	n/a	540.00	271.43	947.00	2.5	3	360.71	0.40	378.80
	-8.5		18.0	9.81	150.0	54.0	96.0	n/a	n/a	n/a	n/a	60	0.640	38.40	48.25	723.82	9	n/a	540.00	271.43	995.26	2.5	3	380.01	0.40	398.10
	-9		18.0	9.81	159.0	58.9	100.1	n/a	n/a	n/a	n/a	60	0.640	38.40	48.25	772.08	9	n/a	540.00	271.43	1043.51	2.5	3	399.31	0.40	417.40
	-9.5		18.0	9.81	168.0	63.8	104.2	n/a	n/a	n/a	n/a	60	0.640	38.40	48.25	820.33	9	n/a	540.00	271.43	1091.77	2.5	3	418.61	0.40	436.71
	-10		18.0	9.81	177.0	68.7	108.3	n/a	n/a	n/a	n/a	60	0.640	38.40	48.25	868.59	9	n/a	540.00	271.43	1140.02	2.5	3	437.91	0.40	456.01
	-10.5		18.0	9.81	186.0	73.6	112.4	n/a	n/a	n/a	n/a	60	0.640	38.40	48.25	916.84	9	n/a	540.00	271.43	1188.28	2.5	3	457.21	0.40	475.31
	-11		18.0	9.81	195.0	78.5	116.5	n/a	n/a	n/a	n/a	60	0.640	38.40	48.25	965.10	9	n/a	540.00	271.43	1236.53	2.5	3	476.52	0.40	494.61
	-11.5		18.0	9.81	204.0	83.4	120.6	n/a	n/a	n/a	n/a	60	0.640	38.40	48.25	1013.35	9	n/a	540.00	271.43	1284.79	2.5	3	495.82	0.40	513.91
	-12		18.0	9.81	213.0	88.3	124.7	n/a	n/a	n/a	n/a	60	0.640	38.40	48.25	1061.61	9	n/a	540.00	271.43	1333.04	2.5	3	515.12	0.40	533.22
	-12.5		18.0	9.81	222.0	93.2	128.8	n/a	n/a	n/a	n/a	60	0.640	38.40	48.25	1109.86	9	n/a	540.00	271.43	1381.30	2.5	3	534.42	0.40	552.52
	-13		18.0	9.81	231.0	98.1	132.9	n/a	n/a	n/a	n/a	60	0.640	38.40	48.25	1158.12	9	n/a	540.00	271.43	1429.55	2.5	3	553.72	0.40	571.82
	-13.5		18.0	9.81	240.0	103.0	137.0	n/a	n/a	n/a	n/a	60	0.640	38.40	48.25	1206.37	9	n/a	540.00	271.43	1477.81	2.5	3	573.03	0.40	591.12
	-14		18.0	9.81	249.0	107.9	141.1	n/a	n/a	n/a	n/a	60	0.640	38.40	48.25	1254.63	9	n/a	540.00	271.43	1526.06	2.5	3	592.33	0.40	610.42
	-14.5		18.0	9.81	258.0	112.8	145.2	n/a	n/a	n/a	n/a	60	0.640	38.40	48.25	1302.88	9	n/a	540.00	271.43	1574.31	2.5	3	611.63	0.40	629.73
	-15		18.0	9.81	267.0	117.7	149.3	n/a	n/a	n/a	n/a	60	0.640	38.40	48.25	1351.14	9	n/a	540.00	271.43	1622.57	2.5	3	630.93	0.40	649.03

Ignored load-carrying capacity for this 1.5 m for seasonal effects

Table H.2. (Cont.)

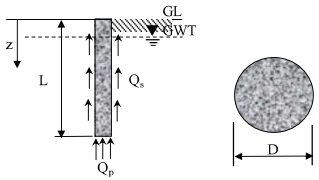

Pile cross-section: D = 0.8 [m]
Pile perimeter, P_p = 2.513 [m]
Cross-sectional area, A_p = 0.503 [m^2] ; note: for the selection of a pile capacity, designers must ensure
Pile cut-off elevation: at: 0.00 [m] that the pile toe is embeded at least 3 B into the bearing stratum.
Groundwater table elevation: at: 3 [m] ; below ground level (bgl)

																						WSD			LSD	
Soil type	Depth	Elevation	Bulk unit weight	Unit weight of water	Total overb. Stress	Water pressure	Eff. overb. stress	Friction angle (drained)	Interface angle	Lateral earth pres. coeff.	Beta value	Undr. shear strength	Alpha value	Unit side-shear stress	Increm. Shaft resistance	Shaft resistance	Bearing capacity factor	Bearing capacity factor	Unit end-bearing (point) stress	End-bearing (point) resistance	Ultimate capacity	Factor of safety		Allow. Capacity	Resistance factor	Ultimate limit state resistance
	z	EL	γ	γ_w	σ_{vo}	u_w	σ'_{vo}	ϕ'	δ	K_s	β	s_u (or c_u)	α	fs	ΔQs	Q_s	Nc*	Nq*	q_p	Q_p	Qult	$F.S_s$	$F.S_p$	Qallow.	RF or φ_r	Q_{ULS}
	[m]	[m]	[kN/m^3]	[kN/m^3]	[kPa]	[kPa]	[kPa]	[°]	[°]	[-]	[-]	[kPa]	[-]	[kPa]	[kN]	[kN]	[-]	[-]	[kPa]	[kN]	[kN]	[-]	[-]	[kN]	[-]	[kN]
	-15.5		23.0	9.81	278.5	122.6	155.9	40	28	0.8	(a) 0.43	n/a	n/a	67.71	85.08	1436.22	n/a	(b) 100	(c) 2160.00	1085.73	2521.95	2.5	3	936.40	0.40	1008.78
	-16		23.0	9.81	290.0	127.5	162.5	40	28	0.8	0.43	n/a	n/a	70.51	88.61	1524.83	n/a	100	2160.00	1085.73	2610.56	2.5	3	971.84	0.40	1044.22
	-16.5		23.0	9.81	301.5	132.4	169.1	40	28	0.8	0.43	n/a	n/a	73.32	92.13	1616.96	n/a	100	2160.00	1085.73	2702.69	2.5	3	1008.70	0.40	1081.08
	-17		23.0	9.81	313.0	137.3	175.7	40	28	0.8	0.43	n/a	n/a	76.12	95.66	1712.62	n/a	100	2160.00	1085.73	2798.35	2.5	3	1046.96	0.40	1119.34
	-17.5		23.0	9.81	324.5	142.2	182.3	40	28	0.8	0.43	n/a	n/a	78.93	99.18	1811.80	n/a	100	2160.00	1085.73	2897.54	2.5	3	1086.63	0.40	1159.01
Silt till	-18		23.0	9.81	336.0	147.2	188.9	40	28	0.8	0.43	n/a	n/a	81.73	102.71	1914.51	n/a	100	2160.00	1085.73	3000.25	2.5	3	1127.72	0.40	1200.10
	-18.5		23.0	9.81	347.5	152.1	195.4	40	28	0.8	0.43	n/a	n/a	84.54	106.23	2020.75	n/a	100	2160.00	1085.73	3106.48	2.5	3	1170.21	0.40	1242.59
	-19		23.0	9.81	359.0	157.0	202.0	40	28	0.8	0.43	n/a	n/a	87.34	109.76	2130.51	n/a	100	2160.00	1085.73	3216.24	2.5	3	1214.11	0.40	1286.50
	-19.5		23.0	9.81	370.5	161.9	208.6	40	28	0.8	0.43	n/a	n/a	90.15	113.28	2243.79	n/a	100	2160.00	1085.73	3329.53	2.5	3	1259.43	0.40	1331.81
	-20		23.0	9.81	382.0	166.8	215.2	40	28	0.8	0.43	n/a	n/a	92.57	116.32	2360.11	n/a	100	2160.00	1085.73	3445.85	2.5	3	1305.96	0.40	1378.34
	-20.5		23.0	9.81	393.5	171.7	(d) 220.0	40	28	0.8	0.43	n/a	n/a	93.58	117.60	2477.71	n/a	100	2160.00	1085.73	3563.44	2.5	3	1353.00	0.40	1425.38
	-21		23.0	9.81	405.0	176.6	220.0	40	28	0.8	0.43	n/a	n/a	93.58	117.60	2595.31	n/a	100	2160.00	1085.73	3681.04	2.5	3	1400.03	0.40	1472.42

Groundwater table (GWT): 3 m below ground level (bgl)
Minimum pile length in the Winnipeg area is about 6 m

(a) CFEM (2006, p. 263) gives values from 0.4 - 0.6 for dense sand and 0.4 - 0.7 for gravel.

(b) Nq* from Poulos & David (1980, p. 27) and CFEM (2006, p. 263) gives value in the range from 50 - 100 for dense sand and 100 - 150 for gravel.

(c) Local practice in Winnipeg (Baracos et al., 1983) reported that the allowable unit end-bearing, $q_{p(all)}$ = 720 kPa, has been commonly used for dense till. Considering local practice, this value was set as a limiting value for the allowable unit end-bearing calculated given in the table. With the assumed F.Sp = 3, the limiting ultimate unit end-bearing would be equal to 720 x 3 = 2160 kPa.

(d) Effective overburden stress used for calculation of the pile capacity is limited to 220 kPa (Randolph et al. 1994)

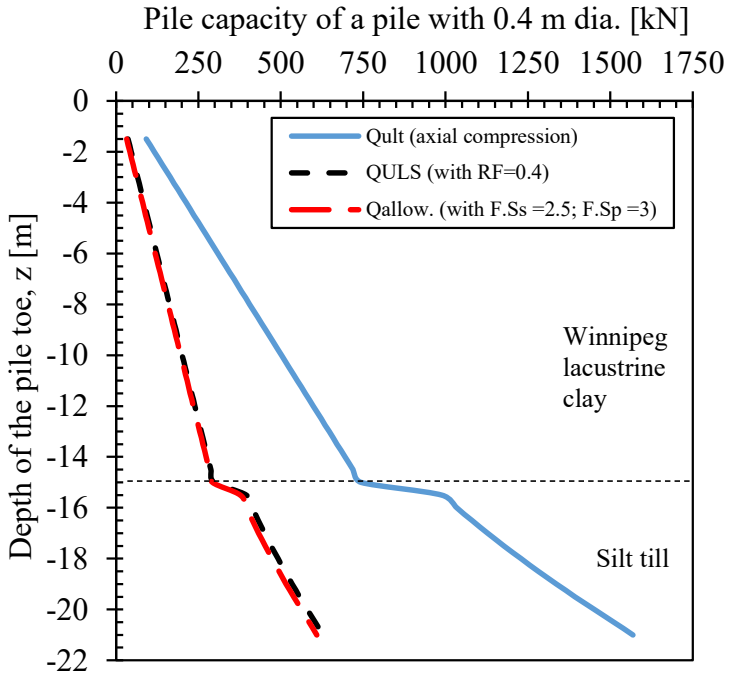

Figure H.1. Geotechnical pile capacity with varying depths of the 0.4 m dia. cast-in-place pile

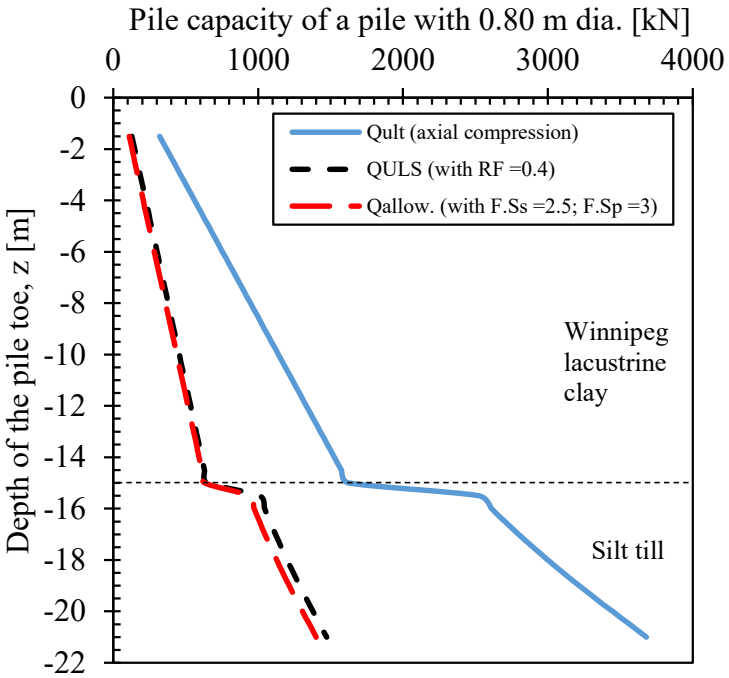

Figure H.2. Geotechnical pile capacity with varying depths of the 0.8 m dia. cast-in-place pile

Appendix I : Typical Properties of Geomaterials reported in the Literature

Table I.1. Typical values of porosity and void ratio of some soils

Material	Porosity n [%]			Void ratio e [-]				Source
	from	to	av.	from	to	av.		
Clay, very organic, soft	75			3				Terzaghi et al. (1996), p.22
Clay, slightly organic, soft	66			1.9				Terzaghi et al. (1996), p.22
Glacial clay, soft	55			1.2				Terzaghi et al. (1996), p.22
Glacial clay, stiff	37			0.6				Terzaghi et al. (1996), p.22
Clay	34	60	47	0.52	1.50	1.01	a	Dominico & Schwartz (1998), p.14
Clay	33	60	47	0.49	1.50	1.00	a	Fetter(2001), p.75
Clay	30	60	45	0.43	1.50	0.96	a	Banks (2012), p.204
Clay	40	70	55	0.67	2.33	1.50	a	Karamouz et al. (2011), p.43
Silt	34	61	48	0.52	1.56	1.04	a	Dominico & Schwartz (1998), p.14
Silt	35	50	43	0.54	1.00	0.77	a	Fetter(2001), p.75
Silt	35	50	43	0.54	1.00	0.77	a	Banks (2012), p.204
Silt	35	50	43	0.54	1.00	0.77	a	Karamouz et al. (2011), p.43
Sand, uniform, loose	46			0.85				Terzaghi et al. (1996), p.22
Sand, uniform, dense	34			0.51				Terzaghi et al. (1996), p.22
Sand, mixed-grained, loose	40			0.67				Terzaghi et al. (1996), p.22
Sand, mixed-grained, dense	30			0.43				Terzaghi et al. (1996), p.22
Sand, fine	26	53	40	0.35	1.13	0.74	a	Dominico & Schwartz (1998), p.14
Sand, coarse	31	46	39	0.45	0.85	0.65	a	Dominico & Schwartz (1998), p.14
Sands	25	50	38	0.33	1.00	0.67	a	Banks (2012), p.204
Sand	25	40	33	0.33	0.67	0.50	a	Karamouz et al. (2011), p.43
Sand & gravel, mixed	20	30	25	0.25	0.43	0.34	a	Fetter(2001), p.75
Sand or gravel, well-sorted	25	50	38	0.33	1.00	0.67	a	Fetter(2001), p.75
Gravel, fine	25	38	32	0.33	0.61	0.47	a	Dominico & Schwartz (1998), p.14
Gravel, coarse	24	36	30	0.32	0.56	0.44	a	Dominico & Schwartz (1998), p.14
Gravel	20	40	30	0.25	0.67	0.46	a	Banks (2012), p.204
Gravel	25	40	33	0.33	0.67	0.50	a	Karamouz et al. (2011), p.43
Soils, coarse-grained, very loose	>	80		>	4.00			Budhu (2011), p.53
Soils, coarse-grained, loose	60	80	70	1.50	4.00	2.75	a	Budhu (2011), p.53
Soils, coarse-grained, m. dense or firm	30	60	45	0.43	1.50	0.96	a	Budhu (2011), p.53
Soils, coarse-grained, dense	15	30	23	0.18	0.43	0.30	a	Budhu (2011), p.53
Soils, coarse-grained, very dense	<	15		<	0.18			Budhu (2011), p.53
Glacial till, very mixed-grained	20			0.25				Terzaghi et al. (1996), p.22
Glacial till	10	20	15	0.11	0.25	0.18	a	Fetter(2001), p.75

[a] estimated using e = n / (1- n)

Table I.2. Typical values of porosity and void ratio of some rocks

Material	Porosity n [%] from	to	av.	Void ratio e [-] from	to	av.		Source
Shale	0	10	5	0	0.11	0.06	a	Dominico & Schwartz (1998), p.14
Shale	0	10	5	0	0.11	0.06	a	Karamouz et al. (2011), p.43
Limestone	0	20	10	0	0.25	0.13	a	Al-Khoury (2012), p.15
Limestone, dolomite	0	40	20	0	0.67	0.33	a	Dominico & Schwartz (1998), p.14
Limestone, dolomite	0	20	10	0	0.25	0.13	a	Karamouz et al. (2011), p.43
Karst limestone	0	40	20	0	0.67	0.33	a	Dominico & Schwartz (1998), p.14
Karst limestone	5	50	27.5	0.05	1.00	0.53	a	Karamouz et al. (2011), p.43
British chalk	10	45	27.5	0.11	0.82	0.46	a	Banks (2012), p.204
Siltstone	21	41	31	0.27	0.69	0.48	a	Dominico & Schwartz (1998), p.14
Sandstone	5	30	17.5	0.05	0.43	0.24	a	Dominico & Schwartz (1998), p.14
Sandstone	5	30	17.5	0.05	0.43	0.24	a	Banks (2012), p.204
Sandstone	5	30	17.5	0.05	0.43	0.24	a	Karamouz et al. (2011), p.43
Sandstone	5	30	17.5	0.05	0.43	0.24	a	Al-Khoury (2012), p.15
Basalt	3	35	19	0.03	0.54	0.28	a	Dominico & Schwartz (1998), p.14
Basalt	1	50	25.5	0.01	1.00	0.51	a	Banks (2012), p.204
Basalt, fractured	5	50	27.5	0.05	1.00	0.53	a	Karamouz et al. (2011), p.43
Granite, weathered	34	57	45.5	0.52	1.33	0.92	a	Dominico & Schwartz (1998), p.14
Gabbro, weathered	42	45	43.5	0.72	0.82	0.77	a	Dominico & Schwartz (1998), p.14
Crystalline rocks, fractured	0	10	5	0	0.11	0.06	a	Dominico & Schwartz (1998), p.14
Crystalline rocks, dense	0	5	2.5	0	0.05	0.03	a	Dominico & Schwartz (1998), p.14
Crystalline rock, fractured	0	10	5	0	0.11	0.06	a	Karamouz et al. (2011), p.43
Crystalline rock, dense	0	5	2.5	0	0.05	0.03	a	Karamouz et al. (2011), p.43
Most unweathered crystalline	<	1		<	0.01			Banks (2012), p.204
silicate rocks (granites,	0.1			0.001				Banks (2012), p.204
schists, gneisses)	<	0.05		<	0.001			Banks (2012), p.204
Concrete	0.12			0.001				Di Donna & Laloui (2015)

[a] estimated using e = n / (1- n)

Table I.3. Typical values of strength and stiffness of some geomaterials (soils and rocks)

Material	Elastic modulus		Poisson's ratio		Cohesion	Undrained shear strength	Friction angle		Source
	E' [MPa]	E_u [MPa]	ν' [-]	ν_u [-]	c' [kPa]	s_u (c_u) [kPa]	ϕ'_{cs} [°]	ϕ' (φ') [°]	
Clay, saturated	-	-	0.4 - 0.5	-	-	-	-	-	Bowles (1996), p.123
Clay, unsaturated	-	-	0.1 - 0.3	-	-	-	-	-	Bowles (1996), p.123
Clays	-	-	-	-	-	-	15 - 30	20 - 30	Budhu (2011), p.724
Clay (very soft)	2 - 15	-	-	-	-	-	-	-	Bowles (1996), p.125
Clay (soft)	5 - 25	-	-	-	-	-	-	-	Bowles (1996), p.125
Clay (soft)	1 - 15	-	0.3 - 0.4	-	-	-	-	-	Budhu (2011), p.724
Clay (medium/firm)	15 - 50	-	-	-	-	-	-	-	Bowles (1996), p.125
Clay (medium)	15 - 30	-	0.3 - 0.35	-	-	-	-	-	Budhu (2011), p.724
Clay (stiff)	30 - 100	-	0.2 - 0.3	-	-	-	-	-	Budhu (2011), p.724
Clay (hard)	50 - 100	-	-	-	-	-	-	-	Bowles (1996), p.125
Clay, sandy	25 - 250	-	-	-	-	-	-	-	Bowles (1996), p.125
Clay, sandy	-	-	0.2 - 0.3	-	-	-	-	-	Bowles (1996), p.123
Silt	2 - 20	-	-	-	-	-	-	-	Bowles (1996), p.125
Silt	-	-	0.3 - 0.35	-	-	-	-	-	Bowles (1996), p.123
Silt or silty sand	-	-	-	-	-	-	24 - 32	27 - 35	Budhu (2011), p.724
Sand (silty)	5 - 20	-	-	-	-	-	-	-	Bowles (1996), p.125
Sand	-	-	-	-	-	-	27 - 37	32 - 50	Budhu (2011), p.724
Sand (loose)	10 - 20	-	0.15 - 0.25	-	-	-	-	-	Budhu (2011), p.724
Sand (loose)	10 - 25	-	-	-	-	-	-	-	Bowles (1996), p.125
Sand (medium)	20 - 40	-	0.25 - 0.3	-	-	-	-	-	Budhu (2011), p.724
Sand (dense)	40 - 80	-	0.2 - 0.35	-	-	-	-	-	Budhu (2011), p.724
Sand (dense)	50 - 81	-	-	-	-	-	-	-	Bowles (1996), p.125
Sand, gravelly sand	50 - 150	-	-	-	-	-	-	-	Bowles (1996), p.125
Sand & gravel (loose)	100 - 200	-	-	-	-	-	-	-	Bowles (1996), p.125
Sand & gravel (dense)	-	-	0.3 - 0.4	-	-	-	-	-	Bowles (1996), p.123
Gravel & sand mixture w/ fine-grained soils	-	-	-	-	-	-	28 - 33	30 - 40	Budhu (2011), p.724
Gravel	-	-	-	-	-	-	30 - 35	30 - 50	Budhu (2011), p.724
Glacial till (loose)	10 - 150	-	-	-	-	-	-	-	Bowles (1996), p.125
Glacial till (dense)	150 - 720	-	-	-	-	-	-	-	Bowles (1996), p.125
Glacial till (very dense)	500 - 1440	-	-	-	-	-	-	-	Bowles (1996), p.125
Glacial till (cohesiveless) (Toronto, Ontario, Canada)	-	-	-	-	0 - 50	-	-	31 - 45	Manzari et al. (2014)
Till (Toronto, Ontario, Canada)	0.9 N [a]	-	-	-	-	-	-	32.5+0.09 N [a]	Cao et al. (2015)
Shale	150 - 5000	-	-	-	-	-	-	-	Bowles (1996), p.125
Rock (depends somewhat on rock types)	-	-	0.1 - 0.4	-	-	-	-	-	Bowles (1996), p.123
Concrete	-	-	0.15	-	-	-	-	-	Bowles (1996), p.123

[a] SPT N value

Table I.4. Typical values of hydraulic conductivity of some soils

Material	Hydraulic conductivity (coefficient of permeability) k						Source
	[cm/s]		[m/s]		[m/day]		
	from	to	from	to	from	to	
Clays (intact)	-	-	1.0E-12	1.0E-08	8.6E-08	8.6E-04	Head (1994), p.100
Clay, marine (unweathered)	-	-	8.0E-13	2.0E-09	6.9E-08	1.7E-04	Domenico & Schwartz (1998), p.39
Clays, homogeneous (CL, CH)	<	1.0E-07	-	-	<	8.6E-05	Budhu (2011), p.724
Clays, intact (practically impermeable)	-	-	<	1.0E-09	<	8.6E-05	Cashman & Preene (2013), p.35
Clay	-	-	1.0E-11	4.7E-09	8.6E-07	4.1E-04	Domenico & Schwartz (1998), p.51
Clay	1.0E-09	1.0E-06	-	-	8.6E-07	8.6E-04	Fetter (2001), p.85
Clay	-	-	1.0E-12	1.0E-08	8.6E-08	8.6E-04	Banks (2012), p.204
Clay	<	1.0E-06	-	-	<	8.6E-04	Das & Sobhan (2014), p.203
Clays (fissured and weathered)	-	-	1.0E-08	1.0E-04	8.6E-04	8.6E+00	Head (1994), p.100
Clays, silt, silty clay (MH, ML), weathered and fissured	1.0E-07	1.0E-05	-	-	8.6E-05	8.6E-03	Budhu (2011), p.724
Clays (fissured or laminated)	-	-	1.0E-09	1.0E-07	8.6E-05	8.6E-03	Cashman & Preene (2013), p.35
Silty clay	1.0E-05	1.0E-03	-	-	8.6E-03	8.6E-01	Das & Sobhan (2014), p.203
Silt, loess	-	-	1.0E-09	2.0E-05	8.6E-05	1.7E+00	Domenico & Schwartz (1998), p.39
Silt	-	-	1.0E-09	1.0E-05	8.6E-05	8.6E-01	Banks (2012), p.204
Silty sands, fine sands	1.0E-05	1.0E-03	-	-	8.6E-03	8.6E-01	Fetter (2001), p.85
Silty sands	-	-	1.0E-06	1.0E-04	8.6E-02	8.6E+00	Cashman & Preene (2013), p.35
Sandy silts, very silty fine sands, and laminated or mixed strata of silt/sand/clay	-	-	1.0E-08	1.0E-05	8.6E-04	8.6E-01	Cashman & Preene (2013), p.35
Very fine or silty sands	-	-	1.0E-08	1.0E-05	8.6E-04	8.6E-01	Head (1994), p.100
Fine sand	-	-	2.0E-07	2.0E-04	1.7E-02	1.7E+01	Domenico & Schwartz (1998), p.39
Fine sand	1.0E-03	1.0E-02	-	-	8.6E-01	8.6E+00	Das & Sobhan (2014), p.203
Fine sands, silts, mixtures comprising sands, silts, and clays (SM-SC)	1.0E-05	1.0E-03	-	-	8.6E-03	8.6E-01	Budhu (2011), p.724
Fine and medium sands	-	-	1.0E-04	5.0E-04	8.6E+00	4.3E+01	Cashman & Preene (2013), p.35
Medium sand	-	-	9.0E-07	5.0E-04	7.8E-02	4.3E+01	Domenico & Schwartz (1998), p.39
Coarse sand	-	-	9.0E-07	6.0E-03	7.8E-02	5.2E+02	Domenico & Schwartz (1998), p.39
Coarse sand	1.0E-02	1.0E+00	-	-	8.6E+00	8.6E+02	Das & Sobhan (2014), p.203
Well-sorted sands, glacial outwash	1.0E-03	1.0E-01	-	-	8.6E-01	8.6E+01	Fetter (2001), p.85
Sand	-	-	1.0E-07	1.0E-03	8.6E-03	8.6E+01	Banks (2012), p.204
Clean sands	-	-	1.0E-05	1.0E-02	8.6E-01	8.6E+02	Head (1994), p.100
Clean sands, clean sand and gravel mixture (SW, SP)	1.0E-03	1.0E+00	-	-	8.6E-01	8.6E+02	Budhu (2011), p.724
Clean sand and sand-gravel mixtures	-	-	5.0E-04	1.0E-03	4.3E+01	8.6E+01	Cashman & Preene (2013), p.35
Gravels	-	-	1.0E-02	1.0E+00	8.6E+02	8.6E+04	Head (1994), p.100
Gravel	-	-	3.0E-04	3.0E-02	2.6E+01	2.6E+03	Domenico & Schwartz (1998), p.39
Gravel	-	-	1.0E-04	1.0E-01	8.6E+00	8.6E+03	Banks (2012), p.204
Well-sorted gravel	1.0E-02	1.0E+00	-	-	8.6E+00	8.6E+02	Fetter (2001), p.85
Clean gravel (GW, GP)	>	1.0E+00	-	-	>	8.6E+02	Budhu (2011), p.724
Clean gravels	-	-	>	1.0E-03	>	8.6E+01	Cashman & Preene (2013), p.35
Clean gravel	1.0E+00	-	-	-	8.6E+02	8.6E+04	Das & Sobhan (2014), p.203
Silt, sandy silts, clayey sands, till	1.0E-06	1.0E-04	-	-	8.6E-04	8.6E-02	Fetter (2001), p.85
Till	-	-	1.0E-12	2.0E-06	8.6E-08	1.7E-01	Domenico & Schwartz (1998), p.39

Table I.5. Typical values of hydraulic conductivity of some rocks and concrete

Material	Hydraulic conductivity (coefficient of permeability) k						Source
	cm/s		[m/s]		[m/day]		
	from	to	from	to	from	to	
Shale	-	-	1.0E-13	2.0E-09	8.6E-09	1.7E-04	Domenico & Schwartz (1998), p.39
British chalk	-	-	1.0E-10	1.0E-06	8.6E-06	8.6E-02	Banks (2012), p.204
Limestone, dolomite	-	-	1.0E-09	6.0E-06	8.6E-05	5.2E-01	Domenico & Schwartz (1998), p.39
Karst and reef limestone	-	-	1.0E-06	2.0E-02	8.6E-02	1.7E+03	Domenico & Schwartz (1998), p.39
Sandstone	-	-	1.0E-10	6.0E-06	8.6E-06	5.2E-01	Domenico & Schwartz (1998), p.39
Sandstone	-	-	1.0E-09	1.0E-04	8.6E-05	8.6E+00	Banks (2012), p.204
Siltstone	-	-	1.0E-11	1.4E-08	8.6E-07	1.2E-03	Domenico & Schwartz (1998), p.39
Most unweathered crystalline sillicate rocks (granites, schists, gneisses)	-	-	1.0E-13 depends on degree of fracturing	1.0E-05	8.6E-09	8.6E-01	Banks (2012), p.204
Basalt	-	-	2.0E-11	4.2E-07	1.7E-06	3.6E-02	Domenico & Schwartz (1998), p.39
Basalt	-	-	1.0E-13	1.0E-02	8.6E-09	8.6E+02	Banks (2012), p.204
Permeable basalt	-	-	4.0E-07	2.0E-02	3.5E-02	1.7E+03	Domenico & Schwartz (1998), p.39
Fractured igneous and metamorphic rocks	-	-	8.0E-09	3.0E-04	6.9E-04	2.6E+01	Domenico & Schwartz (1998), p.39
Weathered granite	-	-	3.3E-06	5.2E-05	2.9E-01	4.5E+00	Domenico & Schwartz (1998), p.39
Weathered gabbro	-	-	5.5E-07	3.8E-06	4.8E-02	3.3E-01	Domenico & Schwartz (1998), p.39
Unfractured igneous and metamorphic rocks	-	-	3.0E-14	2.0E-10	2.6E-09	1.7E-05	Domenico & Schwartz (1998), p.39
Concrete	-	-	-	1.0E-09	-	8.6E-05	Di Donna & Laloui (2015)
Concrete	-	-	1.0E-12	1.0E-09	8.6E-08	8.6E-05	Di Donna (2014), p.12

Table I.6. Typical values of thermal conductivity and heat capacity of some soils

Material	Porosity n [%]	Density ρ_s $x10^3$[kg/m^3]	Thermal conductivity λ_s [W/(m. K)]	Specific heat capacity C_s $x10^3$[J/(kg. K)]	Volumetric heat capacity $\rho_s C_s$ $x10^6$[J/(m^3.K)]	Source
Peat, soft lignite	-	-	0.2 - 0.7	-	-	Loveridge et al. (2013)
Clay soil (40% pore space), dry	40	1.6	0.25	0.89	1.42	Oke (1987), p.44
Clay, dry	-	-	0.2 - 0.3	0.24 [a]	0.3 - 0.6	Di Donna (2014), p.12
Clay soil (40% pore space), saturated	40	2	1.58	1.55	3.1	Oke (1987), p.44
Clay, saturated	-	-	1.1 - 1.6	1.40 [a]	2.1 - 3.2	Di Donna (2014), p.12
Clay	-	-	0.84 - 1.26	-	-	Domenico & Schwartz (1998), p.193
Clay	33 - 60	1.07 - 1.6	0.15 - 2.5	0.92 - 2.2	-	Al-Khoury (2012), p.15
Clay	-	2.5	1.5	1.0	-	Allani et al. (2017)
Clay (London)	-	-	1.5	-	-	Amis et al. (2008)
Clay (London)	-	-	1.5	-	-	Bourne-Webb et al. (2009)
Silty clay (Thompson, Manitoba)	-	-	1.24	-	-	Flynn et al. (2016)
Clayey silt w/ organics (Thompson, Manitoba)	-	-	1.42	-	-	Flynn et al. (2016)
Clay/silt, dry	-	-	0.4 - 1.0	-	-	Loveridge et al. (2013)
Silt, dry	-	-	0.2 - 0.3	0.42 [a]	0.6 -1.0	Di Donna (2014), p.12
Clay/silt, saturated	-	-	0.9 - 2.3	-	-	Loveridge et al. (2013)
Silt, saturated	-	-	1.2 - 2.5	1.18 [a]	2.1 - 2.4	Di Donna (2014), p.12
Sandy soil (40% pore space), dry	40	1.6	0.3	0.8	1.28	Oke (1987), p.44
Sand, dry	-	-	0.3 - 0.8	-	-	Loveridge et al. (2013)
Sand, dry	-	-	0.3 - 0.4	0.61 [a]	1.0 - 1.3	Di Donna (2014), p.12
Sandy soil (40% pore space), saturated	40	2	2.2	1.48	2.96	Oke (1987), p.44
Sand, saturated	-	-	1.5 - 4.0	-	-	Loveridge et al. (2013)
Sand, saturated	-	-	1.7 - 3.2	1.21 [a]	2.2 - 2.4	Di Donna (2014), p.12
Sand	20 - 60	1.28 - 2.15	0.15 - 4	0.8 - 1.48	-	Al-Khoury (2012), p.15
Sand	-	2.5	2	1.0	-	Allani et al. (2017)
Made ground, Cardiff, Wales, UK	-	1.5	1.5	2	-	Thomas & Rees (2009)
Sand and gravel, Cardiff, Wales, UK	-	1.5	2	1.35	-	Thomas & Rees (2009)
Gravel, dry	-	-	0.3 - 0.4	-	-	Loveridge et al. (2013)
Gravel, dry	-	-	0.3 - 0.4	0.74 [a]	1.2 - 1.6	Di Donna (2014), p.12
Gravel, dry (Thompson, Manitoba)	-	-	1.5	-	-	Flynn et al. (2016)
Gravel, saturated	-	-	1.6 - 2.0	-	-	Loveridge et al. (2013)
Gravel, saturated	-	-	1.8 - 3.3	1.21 [a]	2.2 - 2.4	Di Donna (2014), p.12
Gravel, saturated (Thompson, Manitoba)	-	-	2.7	-	-	Flynn et al. (2016)
Soil	30 - 50	1.6 - 2.05	0.4 - 0.6	1.8 - 1.9	-	Al-Khoury (2012), p.15
Soil	-	-	1.112	0.82	1.5	Bodas Freitas et al. (2013)

[a] estimated using the density of 1.9 x 10 ^{3} kg/m^3

Table I.7. Typical values of thermal conductivity and heat capacity of some rocks

Material	Porosity n [%]	Density ρ_s $x10^3$[kg/m^3]	Thermal conductivity λ_s [W/(m.K)]	Specific heat capacity C_s $x10^3$[J/(kg.K)]	Volumetric heat capacity $\rho_s C_s$ [J/(m^3.K)]	Source
Coal	-	-	0.3	0.78 [a]	1.80	Banks (2012), p.43
Marl	-	-	1.5 - 3.5	-	-	Loveridge et al. (2013)
Shale	-	-	1.5 - 3.5	1.0 [a]	2.30	Banks (2012), p.43
Limestone	-	-	1.5 - 3.0	0.83 - 1.04 [a]	1.9 - 2.4	Banks (2012), p.43
Limestone	-	-	2.09	-	-	Dominico & Schwartz (1998), p.193
Limestone (massive)	-	-	2.8	1.0 [a]	2.3	Eskilson et al., as cited in Banks (2012), p.43
Limestone	-	-	2.0 - 3.0	-	-	GSHPA (2012), p.78
Limestone	0.0 - 20	2.3 - 2.5	1.2 - 2.15	0.8 - 0.9	-	Al-Khoury (2012), p.15
Basalt	-	-	1.3 - 2.3	1.04 - 1.13 [a]	2.4 - 2.6	Banks (2012), p.43
Diorite	-	-	1.7 - 3.0	1.26 - 1.43 [a]	2.9 - 3.3	Banks (2012), p.43
Dolomite	-	-	1.67 - 4.18	-	-	Dominico & Schwartz (1998), p.193
Dolomite/dolostone	-	-	3.8 - 5.0	-	-	GSHPA (2012), p.78
Siltstone	-	-	3.5 - 5.2	-	-	GSHPA (2012), p.78
Siltstone (dry), av.	-	2.32	1.23	-	-	Barry-Macaulay et al. (2013)
Siltstone (saturated), av.	-	-	2.14	-	-	Barry-Macaulay et al. (2013)
Sandstone	-	-	3.77	-	-	Dominico & Schwartz (1998), p.193
Sandstone	-	-	2.0 - 6.5	0.87 - 0.91 [a]	2.0 - 2.1	Banks (2012), p.43
Sandstone	-	-	2.3	-	-	Eskilson et al., as cited in Banks (2012), p.43
Sandstone	-	-	3.0	-	-	GSHPA (2012), p.78
Sandstone	5 - 30	2.16 - 2.3	1.8 - 2.9	0.7 - 0.8	-	Al-Khoury (2012), p.15
Sandstone (dry), av.	-	2.25	1.3	-	-	Barry-Macaulay et al. (2013)
Sandstone (saturated), av.	-	-	2.64	-	-	Barry-Macaulay et al. (2013)
Sandstone	-	-	1.3 - 5.0	-	-	Loveridge et al. (2013)
Gneiss	-	-	2.5 - 4.5	0.91 - 1.13 [a]	2.1 - 2.6	Banks (2012), p.43
Granite	-	-	3.0 - 4.0	0.70 - 1.35 [a]	1.6 - 3.1	Banks (2012), p.43
Quartzite	-	-	5.5 - 7.5	0.83 - 1.20 [a]	1.9 - 2.7	Banks (2012), p.43

[a] estimated using the density of 2.3 x 10 ^{3} kg/m^3

Table I.8. Typical values of thermal conductivity and heat capacity of concrete

Material	Density ρ_s x10^3[kg/m^3]	Thermal conductivity λ_s [W/(m. K)]	Specific heat capacity C_s x10^3[J/(kg. K)]	Volumetric heat capacity $\rho_s C_s$ [J/(m^3.K)]	Source
Grout	1.1 - 1.4	0.8 - 1.5	2.0 - 2.2	-	Al-Khoury (2012), p.15
Neat cement paste	-	1.20	-	-	GSHPA (2012), p.77
Neat cement paste	-	1.2	-	-	Loveridge et al. (2013)
Concrete	-	0.8 - 1.7	0.72 [a]	1.80	Banks (2012), p.43
Concrete	-	1.6	-	-	Eskilson et al., as cited in Banks (2012), p.43
Concrete	-	1.0 - 4.0	-	-	GSHPA (2012), p.77
Concrete (pile)	-	2.34	0.78 [a]	1.95	Bodas Freitas et al. (2013)
Concrete	-	0.9 - 2.0	0.86 [a]	1.8 - 2.0	Di Donna (2014), p.12
Concrete (bored pile)	2.5	2.5	0.8	-	Allani et al. (2017)
Concrete (depending on aggregate types)	-	1.8 - 2.9	-	-	GSHPA (2012), p.78
Concrete (depending on aggregate types)	-	1.0 - 2.9	-	-	Loveridge et al. (2013)
Concrete (pile)	2.45	2.0	-	-	Bourne-Webb et al. (2016)
Concrete (slab-on-grade), Cardiff, Wales, UK	2.4	1.37	0.88	-	Thomas & Rees (2009)
Concrete (slab-on-grade), Sendai, Japan	2.2	1.63	0.8	-	Yoshino et al., as cited in Thomas & Rees (2009), p.370

[a] estimated using the density of 2.5 x 10 ^{3} kg/m^3

Table I.9. Typical values of thermal conductivity and heat capacity of other materials

Material	Density ρ_s x10 ^{3}[kg/m^3]	Thermal conductivity λ_s [W/(m. K)]	Specific heat capacity C_s x10^3[J/(kg. K)]	Volumetric heat capacity $\rho_s C_s$ x10^6[J/(m^3.K)]	Source
Air (at 10°C), still	0.0012	0.025	1.01	0.0012	Oke (1987), p.44
Air (at 10°C), turbulent	0.0012	≈125	1.01	0.0012	Oke (1987), p.44
Air	-	0.0251	-	-	Dominico & Schwartz (1998), p.193
Air	-	0.024	-	1.29x10^{-3} at 1atm.	Banks (2012), p.43
Air (standard lab conditions)	0.001225	0.026	1.005	-	Pasquale et al. (2014), p.32
Air	-	0.025	-	4.186	Di Donna (2014), p.12
Air	-	0.03	-	-	Horai, as cited in Abuel-Naga et al. (2015)
Water (at 4°C), still	1.0	0.57	4.18	4.18	Oke (1987), p.44
Water	-	0.4602	-	-	Dominico & Schwartz (1998), p.193
Water (at 20°C)	-	0.6	-	4.18	Banks (2012), p.43
Water	1.0	0.56	4.18	-	Al-Khoury (2012), p.15
Water (standard lab conditions)	1.0	0.6	4.186	-	Pasquale et al. (2014), p.32
Water	-	0.57	-	0.0012	Di Donna (2014), p.12
Water	-	0.6	-	-	Horai, as cited in Abuel-Naga et al. (2015)
Water+25% Ethylene glycol	1.05	0.5	3.795	-	Al-Khoury (2012), p.15
Snow (fresh)	0.1	0.08	2.09	0.21	Oke (1987), p.44
Snow (old)	0.48	0.42	2.09	0.84	Oke (1987), p.44
Ice (at 0°C), pure	0.92	2.24	2.1	1.93	Oke (1987), p.44
Ice	-	1.7 - 2.0	-	1.9	Banks (2012), p.43
Ice	-	2.2	-	-	Eskilson et al., as cited in Banks (2012), p.43
Polyethylene	0.96	0.33	2.1	-	Al-Khoury (2012), p.15
Glass	-	0.8 - 1.3	-	1.6 - 1.9	Banks (2012), p.43
Steel	-	14 - 16	-	3.12	Di Donna (2014), p.12

Table I.10. Typical values of thermal conductivity and heat capacity of some minerals

Material	Density	Thermal conductivity λ_s	Specific heat capacity C_s	Volumetric heat capacity $\rho_s C_s$	Source
	$x10^3$[kg/m^3]	[W/(m. K)]	$x10^3$[J/(kg. K)]	$x10^6$[J/(m^3.K)]	
Plagioclase	-	1.5 - 2.3	-	1.64 - 2.21	Banks (2012), p.43
Plagioclase	2.642	1.97	0.837	-	Pasquale et al. (2014), p.32
Mica	-	2.0 - 2.3	-	2.2 - 2.3	Banks (2012), p.43
Mica	-	2.3	-	-	Horai, as cited in Abuel-Naga et al. (2015)
K-feldspar	-	2.3 - 2.5	-	1.6 - 1.8	Banks (2012), p.43
K-feldspar	2.562	2.4	0.7	-	Pasquale et al. (2014), p.32
Olivine	-	3.1 - 5.1	-	2.0 - 3.6	Banks (2012), p.43
Quartz	-	7.7	-	1.9 - 2.0	Banks (2012), p.43
Quartz	2.647	7.69	0.74	-	Pasquale et al. (2014), p.32
Quartz	-	7.8	-	-	Horai, as cited in Abuel-Naga et al. (2015)
Calcite	-	3.6	-	2.24	Banks (2012), p.43
Calcite	2.721	3.59	0.815	-	Pasquale et al. (2014), p.32
Calcite	-	3.4	-	-	Horai, as cited in Abuel-Naga et al. (2015)
Kaolinite	-	2.8	-	-	Horai, as cited in Abuel-Naga et al. (2015)
Smectite	-	1.8	-	-	Horai, as cited in Abuel-Naga et al. (2015)
Illite	-	1.8	-	-	Horai, as cited in Abuel-Naga et al. (2015)
Gypsum	2.32	1.3	1.07	-	Pasquale et al. (2014), p.32

Table I.11. Thermal expansion coefficient of some soils

Material	Porosity n [%]	Density ρ_s $x10^3$[t/m^3]	Linear thermal expansion coefficient α_{sL} $x10^{-6}$[1/K]	Volumetric thermal expansion coefficient α_{sV} $x10^{-6}$[1/K]	Source
Peat	-	2.20	5	-	Allani et al. (2017)
Clay	-	2.50	5	-	Allani et al. (2017)
Boom clay	-	-	13.33 to 20	40 to 60	Bodas Freitas et al. (2013)
Opalinus clay	-	-	13.33 to 20	40 to 60	Bodas Freitas et al. (2013)
Clay (assumed)	-	-	0, 5, 20	0, 15, 60	Bodas Freitas et al. (2013)
Sandy fill, Colorado, USA	-	-	6	-	Khosravi et al. (2016)
Dense sand, Colorado, USA	-	-	5	-	Khosravi et al. (2016)
Sand	-	2.5	5	-	Allani et al. (2017)

underlined values were calculated using $\alpha_{sL} = \alpha_{sV}/3$. They were not given in the source documents.

Table I.12. Thermal expansion coefficient of some rocks

Material	Porosity	Density	Linear thermal expansion coefficient	Volumetric thermal expansion coefficient	Source
	n [%]	ρ_s x10^3[kg/m^3]	α_{sL} x10^{-6}[1/K]	α_{sV} x10^{-6}[1/K]	
Slates	-	-	9 ± 1	-	Huotari & Kukkonen (2004), p.37
Slates	-	-	4.7 ± 0.2	-	Huotari & Kukkonen (2004), p.37
Basalts, gabbros & diabases	-	-	5.4 ± 1	-	Huotari & Kukkonen (2004), p.37
Limestone, dense	-	-	3.42	-	Harvey (1967), p.3
Limestone, dense, mottled	-	-	3.96	-	Harvey (1967), p.3
Limestone, cherty	-	-	3.24	-	Harvey (1967), p.3
Limestone, argillaceous with laminate structure	-	-	9.36	- -	Harvey (1967), p.3
Limestone, argillaceous with globular structure	-	-	6.3	- -	Harvey (1967), p.3
Limestone	-	-	3.42	-	Harvey (1967), p.3
Dolomite gravel	-	-	7.92	-	Harvey (1967), p.3
Sandstone	-	-	13 ± 1	-	Kirk & Williamson (2012)
Sandstone	-	-	15	-	Somerton, as cited in Kirk & Williamson (2012)
Sandstone, Colorado, USA	-	-	6	-	Khosravi et al. (2016)
Sandstone, Lausanne, Switzerland	-	2.55	0.33	1.0	Laloui et al. (2006)
Sandstone, Lausanne, Switzerland	-	2.556	0.33	1.0	Di Donna et al. (2016)
Sandstone, Lausanne, Switzerland	-	2.167	2.3	-	Rotta Loria & Laloui (2017)
Granites & rhyolites	-	-	8 ± 3	-	Huotari & Kukkonen (2004), p.37
Granites series	-	-	5 ± 1.6	-	Huotari & Kukkonen (2004), p.37
Andersites & diorites	-	-	7 ± 2	-	Huotari & Kukkonen (2004), p.37
Gabbro	-	-	2.95 ± 0.05	-	Huotari & Kukkonen (2004), p.37
Diabases	-	-	3.3 ± 0.2	-	Huotari & Kukkonen (2004), p.37
Gneisses	-	-	3.8 ± 0.6	-	Huotari & Kukkonen (2004), p.37
Quartzites	-	-	11	-	Huotari & Kukkonen (2004), p.37
Quartzites	-	-	6.05 ± 0.05	-	Huotari & Kukkonen (2004), p.37

underlined values were calculated using $\alpha_{sL} = \alpha_{sV}/3$

Table I.13. Thermal expansion coefficient of concrete

Material	Density ρ_s x10^3[kg/m^3]	Linear thermal expansion coefficient α_{sL} x10^{-6}[1/K]	Volumetric thermal expansion coefficient α_{sV} x10^{-6}[1/K]	Source
Concrete (bored pile), Lausanne, Switzerland	2.5	3.33	10	Laloui et al. (2006)
Concrete (pile)	-	10	-	Knellwolf et al. (2011)
Concrete	2.5	12	36	Di Donna (2014)
Concrete (bored pile), Lausanne, Switzerland	2.5	10	30	Di Donna (2014)
Concrete (bored pile & slab)	-	12	36	Di Donna & Laloui (2015)
Concrete	2.5	10	30	Di Donna et al. (2016)
Concrete (bored pile & slab), Lausanne, Switzerland	2.722	10	-	Rotta Loria & Laloui (2017)
Concrete (bored pile), Lausanne, Switzerland	-	10	-	Amatya et al. (2012)
Concrete (bored pile), Bad Schallerbach, Austria	-	10	-	Amatya et al. (2012)
Concrete	-	6.67 to 13.33	20 to 40	Bodas Freitas et al. (2013)
Concrete	-	10	30	Bodas Freitas et al. (2013)
Concrete (bored pile), Lambeth College, London, UK using limestone aggregates	-	8.5	-	Bourne-Webb et al. (2009)
Concrete, typical values w/ limestone aggregates	-	6.35 to 9.35	-	Bourne-Webb et al. (2009)
Concrete (bored pile), Lambeth College, London, UK	-	8.5	-	Amatya et al. (2012)
Concrete (pile)	2.5	10	-	Olgun et al. (2014)
Concrete (pile)	1.73	8.5	-	Adinolfi et al. (2016)
Concrete (pile)	2.5	12	-	Allani et al. (2017)
Concrete (pile)	-	8.5	-	GSHPA (2012), p.72
Concrete (pile)	2.45	10	-	Bourne-Webb et al. (2016)

___underlined values were calculated using $\alpha_{sL} = \alpha_{sV}/3$